

Diet-dependent regulation of TGF β impairs reparative innate immune responses after demyelination

Investigating a therapeutic approach to enhance remyelination

Mar Bosch Queralt



Graduate School of
Systemic Neurosciences
LMU Munich



Dissertation at the
Graduate School of Systemic Neurosciences
Ludwig-Maximilians-Universität München

April 2020

Supervisor: Prof. Dr. Mikael Simons
Institute of Neuronal Cell Biology,
Technical University Munich
German Centre for Neurodegenerative Diseases
(DZNE)

First Reviewer: Prof. Dr. Mikael Simons

Second Reviewer: Prof. Dr. Thomas Misgeld

External Reviewer: Prof. Dr. med. Christine Stadelmann-Nessler

Date of Submission: 08th of April 2020

Date of Defense: 08th of September 2020

Table of contents

Table of contents	3
Abstract	7
Introduction	9
1. Macrophages in the central nervous system	9
1.1. Microglia: the parenchymal CNS macrophage.....	9
1.2. Non-parenchymal CNS macrophages: perivascular, meningeal and choroid plexus macrophages.....	14
1.3. Infiltrating myeloid cells contribute to the CNS macrophage pool during injury.....	15
1.4. Epigenetics and CNS macrophages	15
1.5. Neurodegeneration- or disease- associated microglia	17
1.6. Microglia in ageing.....	18
2. Demyelinating diseases of the central nervous system	20
2.1. Myelin	20
2.2. Multiple sclerosis is a demyelinating disease of the CNS	20
2.3. Remyelination.....	22
3. Lipid buffering and processing in macrophages	26
3.1. Myelin debris phagocytosis and degradation.....	26
3.2. The LXR Pathway	26
3.3. The PPAR Pathway	28
3.4. The effect of myelin internalisation on the phenotype of CNS macrophages	30
3.5. The LXR and PPAR pathways in the CNS in health and disease	31
4. Obesity	34
4.1. Obesity is associated with peripheral inflammation.....	34
4.2. Alterations in lipid storage and metabolism in obesity	34
4.3. Peripheral abnormalities cause inflammation in the CNS.....	35
4.4. Obesity as a risk factor for multiple sclerosis.....	38
5. Hypothesis and aim of this project	39
Materials and Methods	41

Table of contents

1. Materials	41
1.1. Consumables.....	41
1.2. Mouse lines	41
1.3. Antibodies	41
1.4. Commercial kits	42
1.5. Primers.....	42
1.6. Buffers and solutions.....	43
1.7. Software.....	48
2. Methods	48
2.1. Mouse procedures.....	48
2.2. Histological analysis of lesioned and unlesioned mouse CNS tissue	56
2.3. Electron Microscopy	59
2.4. In vitro analysis	60
2.5. Tissue processing and cell isolation	61
2.6. Molecular Biology analysis of tissue and cells	62
2.7. Lipidomics analysis	63
2.8. Short- and medium-length fatty acid analysis.....	64
2.9. Bulk RNA sequencing analysis of microglia.....	64
2.10. Statistical analysis	65
Results	67
1. Characterisation of western diet-fed mice	67
1.1. The consequences of WD consumption on the lipid profile in plasma and in the CNS....	67
1.2. Microglia in the white matter are altered by western diet feeding	72
2. The influence of western diet on the pro-repair function of microglia	78
2.1. Obesity causes poor recovery after demyelinating injury	78
2.2. Persistent demyelination is associated with accumulation of lipids within microglia/macrophages.....	79
2.3. Stimulation of lipid processing pathways in WD-fed mice improves recovery from demyelinating injury.....	81
2.4. Stimulation of LXR and PPAR pathways enhances lipid processing in microglia and macrophages.....	83
3. Why do microglia in WD-fed mice poorly induce the LXR pathway?	86

Table of contents

3.1. Increased chromatin acetylation as the cause of poor LXR pathway induction	86
3.2. Are LXR ligands sufficiently produced in the lesions of WD-fed mice?.....	87
3.3. Insufficient early-phase microglia activation upon demyelination in WD-fed mice.....	87
3.4. TGF β signalling in the CNS of western diet-fed mice	89
3.5. TGF β blocks LXR target gene induction after myelin uptake	91
4. Finding a way to rescue the phenotype	93
4.1. Genetic deletion of <i>Tgfb2</i> in microglia of WD-fed mice promotes recovery from demyelinating injury.....	93
4.2. Galunisertib treatment enhances microglia's reparative immune responses in WD-fed mice but not in old mice.....	94
4.3. Enhancing TREM2 activity improves lipid clearance by microglia and macrophages after demyelinating injury.....	96
Discussion	99
1. Remyelination is impaired in obese mice.....	99
1.1. WD intake and leptin deficiency cause poor myelin regeneration.....	99
1.2. Impaired lipid processing by phagocytes as the underlying mechanism of poor myelin regeneration.....	101
1.3. Translational potential of lipid-processing stimulating drugs.....	102
2. Excess TGFβ signalling perturbs cholesterol efflux.....	103
2.1. TGF β is increased in the brain of WD-fed mice.....	103
2.2. Excess TGF β signalling perturbs microglia's response to myelin damage.....	103
2.3. TGF β blocks the induction of the LXR pathway upon myelin intake	106
3. Western diet intake alters the brain lipidome and causes white matter neuroinflammation	108
3.1. The plasma lipid profile is profoundly altered by western diet intake	108
3.2. The lipid alterations in plasma are associated with lipid alterations in the brain.....	109
3.3. Lipid alterations associate with low-grade neuroinflammation in the white matter	110
4. Conclusion	111
Appendix	113
1. Summary figures	113
2. Generation of recombinant anti-TREM2 antibodies	116
3. Custom-made macros in Fiji	117

Table of contents

4. Protocols	139
References	159
List of figures	173
List of tables	175
List of abbreviations	177
List of publications	179
Copyright of figures taken from publications	181
Acknowledgements	185
Affidavit/Eidesstattliche Versicherung	187
Author contributions	189

Abstract

Multiple sclerosis (MS) is one of the most common causes of chronic disability in young adults. In 85% of the cases, the disease starts with a relapsing-remitting course but, as age advances, the majority of patients enter a progressive phase of the disease characterized by neurological decline and brain atrophy. Treatments that delay, prevent or reverse this progression phase are an unmet need in MS research. The cause of progressive MS is not known, but remyelination failure may contribute. Hence, large efforts have been directed into identifying strategies to enhance endogenous remyelination, which can prevent neuronal death. Microglia are the immune cells of the central nervous system (CNS) and play a crucial role in orchestrating remyelination. With ageing, microglia do not respond adequately to myelin damage, leading to failed remyelination. Apart from ageing, clinical observations suggest that also obesity increases the risk of progression in MS. However, whether and how obesity might influence remyelination is not known.

In this study, we use western diet (WD) to induce obesity in mice and investigate the impact of WD on microglia's response to demyelination. With this, we aim to understand how obesity might affect the pro-regenerative functions of microglia. Since the metabolism of myelin-derived lipids by microglia is an essential step for successful remyelination, we further examine how WD changes the lipid composition of the plasma and brain and whether these changes have consequences on microglia's response to demyelination.

We find that WD consumption leads to impaired remyelination after toxin-induced demyelination due to deficient cholesterol efflux by microglia. Furthermore, we show that WD intake alters the lipid profile of the brain white and grey matter, is associated with modest microgliosis in the corpus callosum, and causes an increase in transforming growth factor- β (TGF β) in the brain. Such excess TGF β signalling leads to insufficient microglia response to damage and impaired cholesterol efflux, which ultimately prevents inflammation resolution and remyelination. By blocking TGF β signalling or enhancing microglia activation through triggering-receptor expressed on myeloid cells 2 (TREM2), we could promote adequate microglia activation and successful resolution of damage in the CNS. Hence, we unravel a microglia immune checkpoint mechanism as a potential therapeutic target to promote a reparative inflammatory response after demyelinating injury.

In conclusion, our study demonstrates that obesity leads to failed remyelination by disturbing the pro-regenerative functions of microglia. In addition, our findings expand the spectrum of potential therapeutic strategies to enhance endogenous remyelination.

Introduction

This project is at the crossroad of four main topics. First, neuroimmunology, since our cell of interest is microglia, the immune cell of the central nervous system (CNS). Second, multiple sclerosis (MS), as we study remyelination, the regenerative response that occurs after myelin damage in demyelinating diseases such as MS. Third, lipid processing by macrophages, because the cellular process that we examine is how macrophages process and buffer lipids after myelin intake. Fourth, obesity, since we want to understand its influence on microglia's orchestration of myelin regeneration.

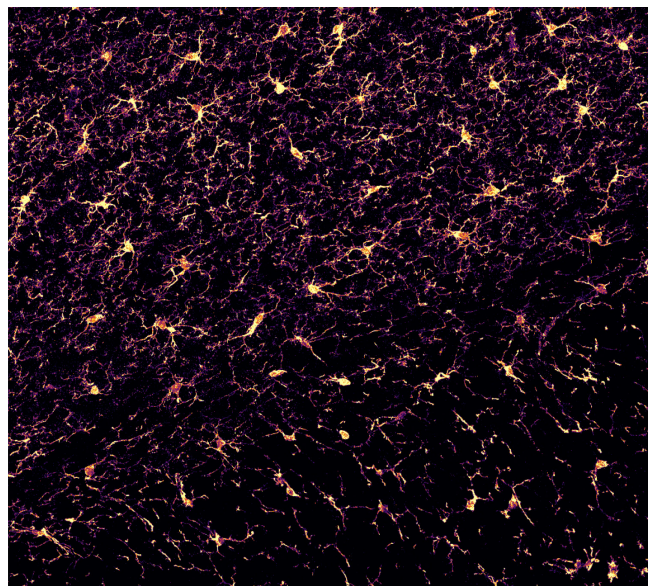
1. Macrophages in the central nervous system

Immune surveillance of the CNS is provided by microglia in the CNS parenchyma and non-parenchymal macrophages in the different CNS barriers. Additionally, circulating monocytes can infiltrate the CNS upon damage. In recent years, technological advances have allowed a highly detailed understanding of microglia function during development, homeostasis, ageing and damage. These exciting findings allow a better evaluation of microglia responses in a particular context and, surely, will support more precise targeting of particular processes.

1.1. Microglia: the parenchymal CNS macrophage

In 1913, Santiago Ramon y Cajal described “the third element” of the CNS, which we now know included oligodendrocytes and microglia, but it was not until a couple of years later when Pío del Río-Hortega fully characterized and named microglia (Sierra et al., 2016). Microglia are the only true tissue-resident macrophages of the CNS and the only immune cells found in the CNS parenchyma. Although they only constitute 5-10% of the total number of cells in the CNS, they have a crucial role in maintaining tissue integrity and normal brain function, which they achieve by continuously scanning the entire brain parenchyma and interacting with essentially all CNS components (Nimmerjahn et al., 2005) (Fig. 1.1).

Figure 1.1: Microglia cover the entire brain parenchyma. With their highly branched ramifications, microglia scan the entire brain parenchyma. In this picture of the mouse brain cortex (top left) and corpus callosum (bottom right), you can observe the high density of microglial ramifications in the cortex, where microglia continuously control neurological function, and the strategic position of microglia along the myelin sheaths in the corpus callosum.



1.1.1. Ontogeny

As demonstrated by fate-mapping analysis, parabiosis experiments and neonatal bone marrow transplantations, microglia do not derive from the neuroectoderm, like all other neural cells, but from the mesoderm. Precisely, microglia derive from primitive c-kit⁺ erythromyeloid yolk sac precursor cells (Ginhoux et al., 2010; Li and Barres, 2018). These precursors appear as early as 3 weeks of estimated gestational age in humans (Prinz and Priller, 2014) and embryonic day 8-9.5 (E8-E9.5) in mice (Ginhoux et al., 2010; Kierdorf et al., 2013). This occurs at the same time as the development of neurons and before the development of astrocytes and oligodendrocytes. Thus, microglia can participate in developmental processes such as neurogenesis, programmed cell death and synapse pruning (Li and Barres, 2018).

Once inside the CNS parenchyma, microglial precursors sense different cues from the CNS environment that instruct them to differentiate. They develop from an initial amoeboid morphology to a ramified morphology, which appears by E14.5 (Kierdorf et al., 2013; Swinnen et al., 2013). Microglia maintain a highly proliferative capacity until the first postnatal week (Bennett et al., 2016). Only by postnatal day 14 (P14), microglia are fully mature and express adult-signature genes (Bennett et al., 2016; Butovsky et al., 2014; Prinz and Priller, 2014). These phases are defined by a stepwise developmental gene program (Matcovitch-Natan et al., 2016), which ensures that microglia's function is adapted to each step of development. These discrete transitions are controlled by several transcription factors, including SALL1, MAFB and IRF8 (find full names at list of abbreviations).

After microglial precursors have invaded the brain and differentiated into microglia, they do not require replenishment by neither the foetal liver-derived or the circulating monocytic precursors (Ajami et al., 2007), because they are capable of self-renewal. This is performed by coupling proliferation and apoptosis in a context-dependent manner, so that cell expansion is ensured, and region-specific densities are kept constant (Askew et al., 2017; Prinz and Priller, 2014). Nevertheless, bone marrow-derived cell recruitment has an important role in pathological conditions that affect the integrity of the CNS such as stroke (Kim and Cho, 2016), MS (Floris et al., 2004), amyotrophic lateral sclerosis (ALS) (Vaknin et al., 2011) and others.

1.1.2. Microglia signature

Transcriptomic and single-cell RNA-sequencing (scRNAseq) studies demonstrated that microglia in the healthy wild-type mouse brain show a relatively consistent homeostatic transcriptional signature (Butovsky et al., 2014; Galatro et al., 2017; Gosselin et al., 2017; Li et al., 2019). Microglia's unique transcriptional signature is defined by the expression of the following markers: CX₃CR1, CD11b, CD45^{low}, TMEM119, P2RY12, SALL1, MHCII^{low}, MER and FCGR1 (for full names, see list of abbreviations) (Gautier et al., 2012; Li and Barres, 2018). The core expression signature for human microglia has also been studied (Galatro et al., 2017; Gosselin et al., 2017) and, interestingly, it partly overlaps with the mouse microglia core signature, suggesting a certain degree of conservation between human and mouse microglia function (Galatro et al., 2017). Microglia's identity is actively maintained by cytokines such as macrophage colony-stimulating factor 1 (CSF1) and transforming growth factor- β (TGF β), transcription factors such as SALL1 and molecules such as cholesterol

(Bohlen et al., 2017; Li and Barres, 2018), though more studies are necessary to define the spectrum of molecules ensuring microglial transcriptomic signature.

The development of the microglia population depends on the interaction between CSF1 and its receptor CSF1R, which induces the differentiation of microglial precursors by activating the myeloid lineage-determining transcription factors PU.1 and interferon-regulating factor 8 (IRF8) (Kierdorf et al., 2013). The microglia-specific genes SALL1 and SALL3 start to be expressed by the colonized precursor cells as early as E10.25 (Mass et al., 2016), demonstrating possible roles for these genes in precursor maturation. On the other hand, neither CX₃CR1 nor P2RY12, which are established microglia markers, are necessary for the entry of microglia into the developing CNS (Squarzoni et al., 2014). The brain environment further shapes the acquisition of the microglial signature by secreting tissue-specific cues. For example, TGF β seems to be a brain-derived factor crucial for microglia specification (Butovsky et al., 2014; Gosselin et al., 2014). Nonetheless, TGF β is insufficient to reproduce the ability of the brain environment to induce full microglial differentiation (Bohlen et al., 2017; Gosselin et al., 2017), demonstrating a role for other brain-derived factors on defining the microglial signature. Indeed, brain-engrafting macrophages do not recapitulate microglia's transcriptional signature or function (Butovsky et al., 2014; Cronk et al., 2018; Gautier et al., 2012; Gosselin et al., 2014), thereby indicating that microglia origin plays an essential role in defining the transcriptional identity of microglia (Bennett et al., 2018; Cronk et al., 2018).

Different brain regions seem to cause age- and region-dependent differences on microglial transcriptomic profile (De Biase et al., 2017; Grabert et al., 2016). In an elegant combination of single-cell analysis, single-molecule fluorescence in situ hybridisation, advanced immunohistochemistry and computational modelling, Masuda et al comprehensively characterised subclasses of microglia in multiple regions in the CNS and revealed region-dependent subtypes of microglia both in mouse and human. Interestingly, the different microglia subpopulations did not appear as distinct clusters, but rather as a transcriptional continuum (Masuda et al., 2019).

1.1.3. Microglia function

Microglia are the only immune cells of the CNS and therefore the endogenous brain defence system. As such, they are responsible for CNS protection against diverse pathogenic factors (Kettenmann et al., 2011). Furthermore, microglia provide trophic support to neurons, remove apoptotic debris and eliminate dysfunctional synapses (Davalos et al., 2005; Nimmerjahn et al., 2005; Schafer et al., 2013; Sierra et al., 2010).

1.1.3.1. Microglia function during development and homeostasis

In homeostatic conditions, microglia display a highly ramified morphology, with a very small cellular body and multiple thin extended processes (Schwartz et al., 2013). Microglia are distributed all over the brain so that each microglial cell has its own territory of around 50 μm of diameter, with very little overlap between neighbouring microglia (Castellano et al., 2016). While the cellular body stays quite still in the assigned territory, microglia's processes are highly mobile and constantly extend and retract, approximately at a speed of 1.5 $\mu\text{m}/\text{min}$. This allows microglia to screen the entire brain

parenchyma every few hours (Davalos et al., 2005; Nimmerjahn et al., 2005) and rapidly sense the presence of tissue damage or infection (Schwartz et al., 2013).

Microglia's processes interact with synapses, neuronal cell bodies, macroglia and blood vessels (Nimmerjahn et al., 2005; Norris and Kipnis, 2019; Šišková and Tremblay, 2013; Wake et al., 2009). In the healthy adult brain, movement of microglia's processes responds to local concentrations of neurotransmitters, neuropeptides and neuromodulators (Castellano et al., 2016; Hanisch and Kettenmann, 2007; Norris and Kipnis, 2019). During developmental stages, microglia control neurogenesis by regulating cell death, axon outgrowth and laminar positioning of neurons. They increase the complexity of the vasculature networks and support the survival and differentiation of oligodendrocyte progenitor cells (OPCs). In later stages, they remodel neural networks by pruning immature synapses. During adult homeostasis, microglia phagocytose myelin and promote OPC survival, phagocytose adult neural precursor cells (NPCs) and monitor neuronal activity (Li and Barres, 2018).

1.1.3.2. Microglia activation during CNS disease

Microglia activation is part of neuroinflammation, which is the response of the CNS to disturbed homeostasis and includes reactions from microglia, infiltrating myeloid cells, astrocytes, oligodendrocytes and the blood brain barrier. Microglia are highly plastic cells and respond rapidly to danger signals released by injured cells. Upon activation, microglia retract their processes, acquire an amoeboid shape with highly motile protrusions (Biber et al., 2014; Stence et al., 2001) and rapidly move towards the lesion site (Davalos et al., 2005). Furthermore, microglia proliferate, release a plethora of inflammatory mediators and enhance antigen presentation (Graeber and Streit, 2010; Prinz, 2014).

Microglia activation can adopt a multidimensional spectrum of polarizations depending on environmental cues (Mosser and Edwards, 2008; Murray and Wynn, 2011; Stout et al., 2005; Xue et al., 2014). Different activation states of microglia have been associated with different functions of microglia during CNS disease, some of which are detrimental and some of which are beneficial. On one hand, amyloid- β deposits seem to upregulate the expression of complement component C1q, which tags synapses and mediates synapse elimination by microglia (Hong et al., 2016). Furthermore, the secretion of pro-inflammatory cytokines such as tumour necrosis factor α (TNF α) and interleukin 1 α (IL1 α) by microglia upon activation can polarize astrocytes into the A1 state, in which they promote toxicity to neurons and oligodendrocytes (Liddelow et al., 2017). On the other hand, microglia can promote proliferation and differentiation of OPCs, thereby demonstrating beneficial effects.

1.1.4. Regulation of microglia's activation

Excessive microglial immune response can potentially cause damage to the surrounding tissue. Thus, the transition from support-oriented functions to immune activation must be tightly regulated. Microglia is equipped with a set of systems that prevent or trigger microglia's immune response (Castellano et al., 2016; Deczkowska et al., 2018). These are grouped in two entities: "off-signals" and "on-signals".

Signals that keep microglia in a deactivated phenotype in the healthy CNS are called “off-signals”. There are several systems of off-signals expressed constitutively in the healthy adult brain and include cell-cell interactions such as CX3CL1–CX3CR1, CD200-CD200R, CD47-CD172a and CD22-CD45. All these ligands are expressed on the surface of healthy neurons and are detected by microglial receptors (Biber et al., 2007; Ravichandran, 2010). Furthermore, soluble anti-inflammatory factors such as TGF β and neurotrophins including neurotransmitters, nerve growth factor (NGF), brain-derived neurotrophic factor (BDNF) and neurotrophin-3 (Biber et al., 2007; Deczkowska et al., 2018; Zöller et al., 2018) keep microglia in a homeostatic state. Finally, also the negative regulator of reactive oxygen species (NRROS) seems to promote a quiescent microglial identity (Buttgereit et al., 2016; Wong et al., 2017). Off-signals must be present in the microglia environment so that microglia stay in a deactivated, homeostatic state. If off-signals are lost or downregulated due to changes in the microenvironment, microglial activation is triggered.

On the other hand, “on-signals” are produced on demand to initiate an inflammatory response to damage or injury stimuli. Molecules that promote microglial activation can be classified as PAMPS (Pathogen Associated Molecular Patterns), which warn of the presence of exogenous material, or DAMPs (Damage Associated Molecular Patterns), which warn of internal damage to the own organism. Microglia express a wide range of surface receptors such as toll-like receptors (TLRs), scavenger receptors (SRs) and cytokine and chemokine receptors that detect these signals and trigger activation (Kierdorf and Prinz, 2013). Some on-signals are the so-called “help-me/find-me” signals (Marín-Teva et al., 2011; Panatier and Robitaille, 2012), and include nucleotides, chemokines, cytokines, neuropeptides, neurotransmitters, cannabinoids and morphine (Castellano et al., 2016). In response to these signals, microglia approach the source of the damage to perform close surveillance. If additional “eat-me” signals are present, microglia initiate an intracellular signalling cascade leading to phagocytosis, which is mainly mediated by triggering receptor expressed on myeloid cells (TREM2) (Linnartz-Gerlach et al., 2019).

1.1.4.1. Immune checkpoints might be prejudicial in disease

As described above, microglia are equipped with activation-restraining and activation-promoting mechanisms that allow them to detect and respond to damage only when required. These mechanisms seem to work best in the context of a focal injury in the CNS, which causes transient but robust microglia activation that results in the rapid removal of the damage followed by restoration of brain homeostasis. Nevertheless, under chronic CNS pathological conditions, such “microglial checkpoints” can become counterproductive (Cohen et al., 2014; London et al., 2013). Typically, chronic pathologies cause a slight deviation from homeostasis that is not enough to overcome the restraining mechanisms and trigger full microglial activation. Nevertheless, microglia recognise the persistent pathological condition, and seem to adapt to this new context by readjusting their phenotype to the new homeostatic set point. As the disease progresses, microglia cannot reverse the damage even if a robust microglial immune response is triggered. Likewise, the re-adjusted microglia homeostasis might impair microglial response to a new damaging stimulus. Hence, in CNS chronic pathologies, blocking the restraining mechanisms (i.e. off signals) that keep microglia at homeostasis

and promoting microglial immune activation at early stages could be beneficial (Deczkowska et al., 2018).

1.2. Non-parenchymal CNS macrophages: perivascular, meningeal and choroid plexus macrophages

The interface between the CNS parenchyma and the circulation is surveyed by non-parenchymal CNS macrophages. These support the CNS during both development and homeostasis and are critical effectors and regulators of immune responses at the CNS interfaces during virtually all neuroinflammatory, neurodegenerative and neuro-oncological diseases (Goldmann et al., 2016; Prinz et al., 2017).

Non-parenchymal CNS macrophages include perivascular, meningeal and choroid plexus macrophages, each of which occupies a strategic niche. Perivascular macrophages are found next to endothelial cells, sandwiched between the laminin-positive endothelial and glial basement membranes (Galea et al., 2008), meningeal macrophages are localized in the subdural space, in close proximity to fibroblast-like cells that line the meninges and meningeal vasculature (Kim et al., 2009), and choroid-plexus macrophages are found exclusively in the stroma and epithelial layer of the choroid plexus (Prinz and Priller, 2017).

Non-parenchymal CNS macrophages were thought to originate from short-lived blood monocytes that are quickly replaced by bone marrow-derived cells (Aguzzi et al., 2013; Prinz and Priller, 2014). However, recent fate-mapping studies showed that subdural meningeal, perivascular and, to some extent, choroid-plexus macrophages are derived from embryonic haematopoietic precursor cells and are maintained by self-renewal (Goldmann et al., 2016). Only choroid-plexus macrophages have been found to derive from both embryonic myeloid precursors and adult haematopoietic stem cells and to partly depend on blood-derived immigrating Ly6C^{hi} monocytes for replenishment (Goldmann et al., 2016). These results were confirmed by parabiosis experiments and are consistent with the fact that only choroid plexus macrophages depend on CCR2 for maintenance (Goldmann et al., 2016; Prinz et al., 2017).

Like microglia, the development of non-parenchymal CNS macrophages does not require MYB, the master transcription factor of definitive haematopoiesis (Schulz et al., 2012), instead, the transcription factors PU.1 and IRF8 drive the maturation and diversity of CNS macrophages (Van Hove et al., 2019). Expression profiling of non-parenchymal CNS macrophages reveals that although they share a core signature (Jordão et al., 2019), they consist of distinct subsets with tissue-specific transcriptional signatures (Van Hove et al., 2019) and that they have only limited relation to circulating myeloid cells (Goldmann et al., 2016). Upon neuroinflammation, non-parenchymal CNS macrophages drastically change their transcriptomic profile and generate context-dependent subsets (Jordão et al., 2019). These can infiltrate damaged areas and contribute to the innate immune response, together with microglia, thereby gaining relevance for the study of neuroinflammation.

1.3. Infiltrating myeloid cells contribute to the CNS macrophage pool during injury

The CNS contains an extensive vasculature network, in which circulating myeloid cells, such as monocytes, granulocytes and dendritic cells reside. Upon breach of the blood-brain barrier due to CNS disease or injury, these cells can infiltrate the CNS parenchyma and contribute to disease. In particular, monocytes differentiate into macrophages, thereby giving rise to monocyte-derived macrophages (MDMs). In these circumstances, MDMs intermingle with the resident microglia population and contribute in coping with the CNS damage, which makes their study in this project also relevant.

Monocytes belong to the mononuclear phagocyte system lineage (Prinz, 2014) and continuously differentiate from bone marrow haematopoietic stem cells under the control of the transcription factor MYB (Yamasaki et al., 2014). Monocytes display at least two distinct identities in mice: Ly6C^{hi}CCR2^{hi} classical inflammatory monocytes (CCR2^{hi}CD14^{hi}CD16^{lo} monocytes in human), and Ly6C^{lo}CX₃CR1^{hi} non-classical patrolling monocytes (CCR2^{lo}CD14^{hi}CD16^{hi} monocytes in human) (Ingersoll et al., 2010). In healthy conditions, monocytes circulate in the blood, bone marrow and spleen without proliferating. However, under inflammatory conditions (Geissmann et al., 2010), Ly6C^{hi} monocytes are rapidly attracted to the inflammatory chemokine CCL2, while Ly6C^{lo} respond to elevated levels of CX₃CL1 (Nahrendorf et al., 2007; Shechter et al., 2013).

In the CNS parenchyma, monocytes differentiate into macrophages expressing major histocompatibility complex II (MHCII), costimulatory molecules, and pro-inflammatory agents such as IL1 β and TNF α . In addition, they produce proteolytic enzymes and act as potent phagocytes, thereby actively contributing to CNS disease (Jiang et al., 2014; Takahashi et al., 2007; Yamasaki et al., 2014).

1.4. Epigenetics and CNS macrophages

Epigenetic changes are alterations that affect gene activity without altering the nucleotide sequence of DNA. Changing the epigenetic landscape of a cell by introducing modifications into its chromatin can lead to changes in expression of the nearby genes. Although many modifications are ubiquitous, small variations in the global scale generate the distinct chromatin landscape observed between cell types (Lavin et al., 2014). Since epigenetic marks may persist after resolution of the initial stimulus, they provide a mechanism for converting transient signals into potentially persistent cellular responses (Kaminska et al., 2016).

Epigenetic changes are mediated by modification of histones (mainly methylation, acetylation and phosphorylation), by non-coding RNA and by methylation and hydroxymethylation of DNA (Kaminska et al., 2016). The balance of positive and negative histone marks at gene promoters and distal regulatory elements can regulate transcription rates by changing the position of nucleosomes. Nucleosomes consist of 147 bases of DNA wrapped around a histone core. Nucleosome-dense regions are considered “closed chromatin” regions, which are transcriptionally inactive, while nucleosome-depleted regions are known as “open chromatin” and contain regulatory elements such as promoters and enhancers that play a critical role in gene regulation (Lavin et al., 2014).

1.4.1. Epigenetic mechanisms regulating the identity of CNS macrophages

Tissue macrophages have tissue-specific chromatin modifications and enhancer landscapes that allow them to express unique genes. Such epigenetic modifications are shaped by both ontogeny and environmental cues and define their identity. In CNS macrophages, the major regulator of the epigenetic landscape is the lineage-determining factor PU.1, a transcription factor that binds to the vast majority of accessible sites. Subsequently, PU.1 recruits lineage-specific and CNS-specific co-factors and epigenetic modifiers, which will incorporate CNS-specific signals to select subsets of microglia-restricted enhancers, genomic elements that modulate the spatial and temporal expression of genes (Saeed et al., 2014). For example, myocyte-specific enhancer factor 2C (MEF2C) and SMAD3 are brain environment-triggered factors that may have a role in microglial specification (Gosselin et al., 2014; Lavin et al., 2014). Moreover, IRF8 is one of the factors that determine the regulatory network involved in maturation of microglia (Hagemeyer et al.; Kierdorf and Prinz, 2013). Recently, it was shown that the local CNS environment establishes epigenetic modifications of the epigenetic enhancers, which orchestrate microglial stepwise developmental program and define mouse and human microglia identity and function (Gosselin et al., 2017; Matcovitch-Natan et al., 2016).

1.4.2. Epigenetic mechanisms underlying microglia activation

Epigenetic marks established by ontogeny and the environment can be modified by newly introduced environmental cues, thereby leading to changes in gene expression and functional response. Although it is not yet clear which epigenetic modifications underlie microglia activation, we can learn from the epigenetic modifications underlying the activation of inflammatory macrophages. Studies with human macrophages show that the transcriptional regulator network of inflammatory macrophages is defined by accessible promoters (i.e. open chromatin) (Schmidt et al., 2016). This accessible state of chromatin was present independent of the activation signal (Schmidt et al., 2016). Furthermore, the chromatin remodelling and transcription factor binding following macrophage activation seems to be independent of PU.1 (Heinz et al., 2010; Mancino et al., 2015).

Some of the most dynamic epigenetic marks were shown to be histone acetylations at enhancer sites. The state of histone acetylation depends on histone acetyltransferases (HATs) and histone deacetylases (HDACs), enzymes responsible for acetylation and deacetylation, respectively. Histone deacetylation promotes chromatin condensation and makes DNA less accessible for transcription factors (Kaminska et al., 2016). In neurodegenerative diseases, there is a loss of the acetylation equilibrium due to decreased HAT activity. Accordingly, inhibiting HDACs to promote histone acetylation has beneficial effects in animal models of Alzheimer's disease (AD), Huntington's disease (HD), MS, trauma and stroke (Kaminska et al., 2016). Thus, a state of accessible enhancers and promoters seems to be necessary and beneficial for macrophage activation and function, and this seems to apply to microglia as well.

1.4.3. Innate Immune Memory in microglia

Innate immune memory is the long-lasting change in the responsiveness of an innate immune cell induced by a first immune stimulus, leading to increased (trained) or decreased (tolerant) responses

to a secondary stimulus (Neher and Cunningham, 2019). Direct evidence for innate immune memory in adult microglia was recently obtained by demonstrating that one intraperitoneal lipopolysaccharide (LPS) injection caused immune training in the brain one day later, as evidenced from increased production of several cytokines. Contrarily, repeated LPS injections on four consecutive days induced immune tolerance, as shown by decreased production of cytokines (Wendeln et al., 2018). These changes had consequences on brain pathology in mouse models of stroke and AD and were demonstrated to be driven by epigenetic modifications. Together, these findings highlight the consequences that either acute or chronic inflammatory insults can have on microglia's epigenetic landscape and function.

1.5. Neurodegeneration- or disease- associated microglia

In a variety of neurodegenerative settings, microglia acquire features of activated microglia; less ramifications, more amoeboid morphology and increased expression of activation markers. Such activated microglia were first detected and profiled at a single-cell level in mouse models of AD, where it was observed that these activated microglia had a conserved transcriptional signature across different AD models (Keren-Shaul et al., 2017; Orre et al., 2014; Wang et al., 2015). Thereafter, these cells were named “disease-associated microglia” (DAM), although the refined term “microglial neurodegenerative phenotype” (MgnD) was also suggested to better define the disease context of microglia activation (Krasemann et al., 2017; Prinz et al., 2019). DAM were found in other standard mouse models of neurodegeneration, such as the SOD1^{G93A} model of ALS (Chiu et al., 2013), and in other non-neurodegenerative states, such as cuprizone models of demyelination (Poliani et al., 2015) or ageing (Holtman et al., 2015). Although the functions of DAM are still under investigation, both positive and negative effects have been detected in different mouse models of disease so far.

The transcriptional signature of DAM involves the upregulation of genes such as *Axl*, *Clec7a*, *Cst7*, *Spp1*, *Gpmb*, *Lpl*, *Lgals3*, *ApoE* and *Trem2* and the downregulation of the homeostatic signature of microglia, mainly *P2ry12*, *Tmem119* and *Selplg*. Furthermore, DAMs express surface proteins such as CD11c, MHCII, CD44, CD14, CD86, CD39, CD90 and CD274 (Ajami et al., 2018; Keren-Shaul et al., 2017; Mrdjen et al., 2018). In more general terms, the upregulated gene modules are involved in stress response, interferon response, lysosomal function and lipid metabolism.

DAM can be induced by a variety of stimuli; including protein aggregates, apoptotic cells and myelin debris, and seem to require intracellular signalling by type I and II interferons. The acquisition of the DAM signature is TREM2-independent in the early stages of activation; but depends on TREM2 for full activation in later stages. Once activated, DAM decrease the expression of homeostatic genes, trigger the expression of the DAM signature, and secrete several factors. These include CSF1, apolipoprotein E (APOE) and secreted phosphoprotein 1 (SPP1), which can form an autocrine loop by activating the DAM-expressed receptors CSF1R, TREM2 and CD44, respectively. On the other hand, CNS-derived homeostatic signals such as TGF β and NRROS normally suppress the DAM signature. This model of activation and control of DAM induction thus suggests that TREM2 and TGF β /NRROS are opposing signalling forces controlling microglial activation status during neurodegenerative diseases (Fig. 1.2) (Song and Colonna, 2018).

It is important to note that the DAM signature is not simply the default response to any stimulus to the CNS. For example, the microglial response to experimental autoimmune encephalitis (EAE) (Jordão et al., 2019), to lysolecithin (LLC)-induced demyelination (Hammond et al., 2019) or to systemic injection of LPS (Holtman et al., 2015) lead to surface-marker, cytokine and signalling profiles that are markedly distinct both between them and from those of DAM (Song and Colonna, 2018). Nevertheless, such single-cell transcriptomic studies have significantly advanced our understanding of CNS macrophages and revealed disorder-specific activation states of microglia, which will allow for context-dependent treatment options (Prinz et al., 2019).

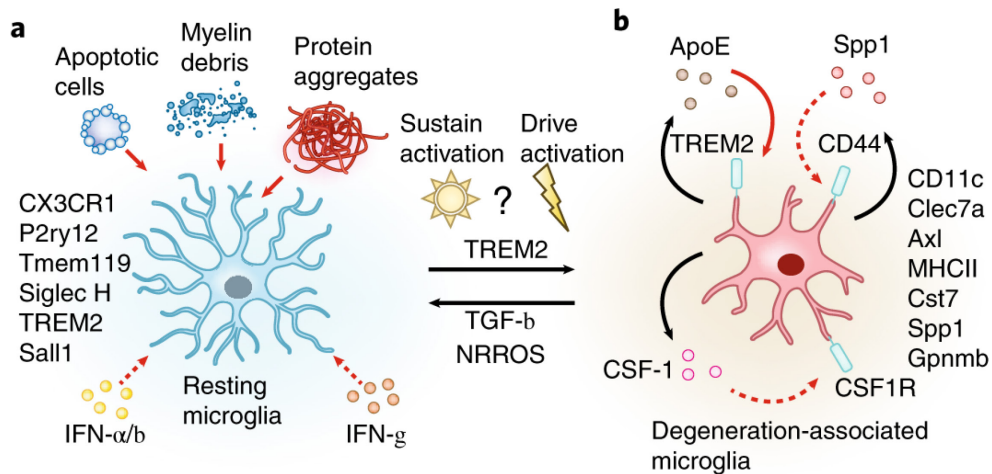


Figure 1.2: DAM represent a unique response to various neuropathologies. **a.** Homeostatic microglia are characterized by the expression of genes such as *Tmem119*, *Sall1* and *P2ry12*. Various stimuli, including protein aggregates, myelin debris, apoptotic cells, can induce a DAM response by microglia. This requires interferon and TREM2 signalling. On the other hand, TGF β and NRROS signalling normally suppress the transition to DAM. **b.** DAM downregulate the homeostatic microglia signature genes and upregulate a common activation signature dependent on TREM2. They secrete several factors, including CSF1, APOE and SPP1, which can form an autocrine loop by activating their own receptors. Dashed arrows indicate links that have not been formally proven. DAM: disease-associated microglia, TREM2: triggering receptor expressed on myeloid cells 2, TGF β : transforming growth factor β , NRROS: negative regulator of reactive oxygen species, CSF1: macrophage colony stimulating factor 1, APOE: apolipoprotein E, SPP1: secreted phosphoprotein 1, IFN: interferon. Figure from Song & Colonna, 2018, replicated with permission.

1.6. Microglia in ageing

Upon ageing, the CNS becomes an increasingly challenging environment, characterized by increased inflammation, accumulation of oxygen-free radicals, compromise of the blood-brain barrier integrity, and loss of functional synapses (Hammond et al., 2019). Such environment results in an abundance of microglia activators, and; indeed, microglia activation in the aged brain has been widely reported both in the human and mouse CNS (Hammond et al., 2019; Luo et al., 2010; Raj et al., 2017; Streit, 2006; Zrzavy et al., 2017).

Aged microglia exhibit signs of microglial dystrophy (partially or completely broken processes), enlarged processes, cytoplasmic hypertrophy and a less ramified appearance (Streit, 2006). They also accumulate phagocytic-intake material such as insoluble, lipofuscin-like lysosomal inclusions

(Safaiyan et al., 2016). Furthermore, aged microglia have elevated immunoreactivity for markers of inflammatory processes, phagocytosis and lipid homeostasis (such as CD68, TLRs, MHCII, matrix metalloprotease 12 (MMP12), CD11b and CD11c (Luo et al., 2010)). Particularly, microglia in the white matter show abundant expression of phagocytic markers including MAC2 (Galectin-3), AXL, CD16/32, C-type lectin domain family 7 (CLEC7A) and CD36 (Raj et al., 2017). In white matter from human brain tissue, the first signs of inflammatory activity are detected already during middle age and are characterized by increased CD68 and human leukocyte antigen (HLA)-DR expression (Raj et al., 2017). Changes in the epigenetic landscape are also detected in ageing microglia, such as demethylation of the promoters of TNF α and IL1 β , which lead to increased expression of both cytokines (Cheray and Joseph, 2018).

The transcriptional signature of ageing microglia has recently been characterized at a single-cell level (Hammond et al., 2019). Notably, ageing didn't lead to the appearance or disappearance of any cell clusters, but rather caused an expansion of two clusters that have few cells during adulthood. One of the clusters enriched expressed a number of inflammatory signals that were not expressed by other populations of microglia in vivo, including *Lgals3*, *Cst7*, *Ccl4*, *Ccl3* and *Il1b* as well as transcription factors *Id2* and *Atf3*. The other cluster that was expanded included interferon-response genes such as *Ifitm3*, *Rtp4* and *Oasl2*, which are produced in response to DAMPs such as high mobility group box 1 (HMGB1) and cell-free nucleic acids. In short, this study shows that a small fraction of the microglia respond to ageing, while the vast majority of microglia are unaltered or only slightly altered (Hammond et al., 2019).

Changes in microglia upon ageing associate with functional dysregulation. Impaired regulation of phagocytosis in aged microglia causes microglia to excessively prune synapses (Morrison and Baxter, 2012) or insufficiently phagocytose apoptotic bodies, protein aggregates and myelin (Safaiyan et al., 2016). In addition, upon peripheral LPS injection, aged mice had a more pronounced inflammatory response than young mice (Godbout et al., 2005; Sierra et al., 2007). With ageing, microglia also show delayed responses to demyelination, which result in impaired remyelination (see chapter 2.3.1 of Introduction). Also MDMs undergo changes during ageing; however, their particularities seem to be slightly different to the ones of ageing microglia (Rawji et al., 2016), which can modify the CNS macrophage response to age-associated diseases that involve recruitment of MDMs.

2. Demyelinating diseases of the central nervous system

Myelin can be either primarily or secondarily damaged in many CNS diseases, and subsequently; it can be repaired. CNS macrophages are essential for such repair process, because they clear up debris and regulate myelin regeneration. Thus, we are interested in understanding the interplay between CNS macrophages and remyelinating oligodendrocytes in the context of demyelinating diseases.

2.1. Myelin

Myelin is a multi-layered stack of membranes that wraps axons in both the CNS and the peripheral nervous system (PNS). This stack has a uniform thickness and a characteristic period structure that can be visualized by electron microscopy (Aggarwal et al., 2011). In the CNS, myelin is generated by oligodendrocytes, which have multiple extended processes that wrap around axons from multiple neurons. Myelin reduces the transverse capacitance, increases the resistance along the axis of the axonal membrane and establishes a cluster organization of voltage-gated sodium channels at the nodes between adjacent sheaths. This enables nerve impulse conduction at high speeds which would otherwise only be reached by prohibitively large axons (Mount and Monje, 2017). Furthermore, by establishing such protective layer and close contact to the axons, myelin provides metabolic support to neurons and regulates ion and water homeostasis (Stadelmann et al., 2019). Although myelination occurs during development following an innate program that is independent of nervous system activity, myelin continuously adapts throughout life. These myelin alterations seem to respond to various neuronal activities and suggest a new role for myelin in modifying network dynamics in response to experience and learning (Mount and Monje, 2017; Young et al., 2013).

The composition of myelin is unique among biological membranes: in contrast to the plasma membrane, regularly composed of 50% lipids and 50% proteins in dry weight, lipids constitute 73-81% of the total dry weight of myelin (Chrast et al., 2011). Specifically, lipid species such as cholesterol, phospholipids and glycosphingolipids such as galactocerebroside and sulfogalactosylceramide are enriched in myelin (Baumann and Pham-Dinh, 2001; Nonaka and Kishimoto, 1979; Norton and Poduslo, 1973). The remaining 19-27% of the total dry weight of myelin comprises proteins, mainly myelin basic protein, proteolipid proteins and 2',3'-cyclic nucleotide 3'-phosphodiesterase (de Monasterio-Schrader et al., 2012; Pfeiffer et al., 1993).

2.2. Multiple sclerosis is a demyelinating disease of the CNS

MS is the most common demyelinating disease in high-income countries and one of the most common causes of neurological disability in young adults (Gilden, 2005). In most cases; around 85% of newly diagnosed patients, MS initially presents as a relapsing-remitting disease that starts between 20 and 30 years of age and affects women two times more frequently than men (Klineova and Lublin, 2018; Lublin et al., 2014). Over time, most patients enter a progressive form of the disease, characterized by slowly progressive neurological decline and CNS atrophy. Patients usually have oligoclonal immunoglobulin G in the cerebrospinal fluid and transient gadolinium-enhancing lesions on magnetic resonance scans. These lesions are a sign of inflammation and blood-brain barrier breakdown and are confirmed by characteristic perivascular inflammatory infiltrates, myelin

breakdown and axonal degeneration detected in the pathological analysis (Ransohoff et al., 2015; Stys et al., 2012).

MS is considered an inflammatory demyelinating and neurodegenerative disease with a multifactorial origin that includes genetical predisposition and environmental risk factors. Genetical studies demonstrate strong associations with immune regulators, including T cells, B cells and phagocytes (Sawcer et al., 2011). Several systematic reviews and meta-analyses have unravelled environmental risk factors such as Epstein-Barr virus infection, vitamin D deficiency, smoking and latitude; nevertheless, there are still no well-established risk factors to assist disease prevention (Belbasis et al., 2015).

2.2.1. The role of CNS macrophages in multiple sclerosis and experimental autoimmune encephalomyelitis

In MS and EAE, the most commonly used murine model of MS, macrophages dominate the inflammatory infiltrates of demyelinated lesions. Macrophage numbers and activation correlate with tissue damage including axon and oligodendrocyte pathology and are commonly found in areas of active demyelination (Ajami et al., 2011; Ferguson et al., 1997; Henderson et al., 2009; Huitinga et al., 1990, 1993). These macrophages include both microglia and infiltrating monocyte-derived macrophages. Despite the difficulties of differentiating microglia-derived from monocyte-derived macrophages, recent studies analysing the expression of the microglia-specific marker TMEM119 (Bennett et al., 2016) demonstrated that, on average, 45% of the macrophage-like cells in active MS lesions are derived from the resident microglia pool (Zrzavy et al., 2017).

Activated macrophages in actively demyelinating lesions contain degenerated myelin and axonal products, display a high expression of MHCII and co-stimulatory molecules and secrete a plethora of inflammatory and neurotoxic mediators (Boven et al., 2006; Butovsky et al., 2012; Hendriks et al., 2005; Nikić et al., 2011; Vogel et al., 2013). Due to the accumulation of lipids in their cytoplasm, these cells acquire a foamy appearance. Thus, they are often named foamy phagocytes or foamy macrophages in the literature.

As in many other diseases, CNS macrophages have a double-edged behaviour that can promote both neurotoxicity and neuroprotection in the context of demyelination (Aguzzi et al., 2013; Bogie et al., 2014a). The ability of CNS macrophages to promote the recruitment and reactivation of T cells, present antigens and release inflammatory cytokines, free radicals and proteases has been typically associated with toxicity over neurons and OPCs. Mostly, these findings are based on experiments that inhibit macrophage activation and observe attenuated symptoms and lesion development in EAE (Arvin et al., 2002; Bhasin et al., 2007; Goldmann et al., 2013; Heppner et al., 2005; Mejia et al., 2001; Ponomarev et al., 2005; Wells et al., 2003) and on experiments that promote constitutive activation of inflammatory pathways and observe aggravated EAE symptoms (Ellrichmann et al., 2012). Nevertheless, similar experiments demonstrate that although inhibition of macrophage activation results in a delay onset of EAE symptoms, these mice also exhibit higher disease severity and delayed recovery from neurological dysfunction (Lu et al., 2002). Even more, CNS macrophages can promote repair by clearing the myelin debris and producing growth factors such as activin A and insulin-like

growth factor 1 (IGF1) (Butovsky et al., 2006; GrandPré et al., 2000; Kotter, 2006; Miron et al., 2013). Thus, the role of macrophages in MS and EAE seems to be dependent on the perspective from which it is looked at, the specific process studied and the time point of interest.

2.3. Remyelination

After myelin injury, damaged myelin sheaths are phagocytosed and removed by phagocytic cells. This leaves the axon demyelinated, and thus; unprotected and unable to conduct the nerve impulse efficiently. In MS, axonal degeneration is associated with disease progression and correlates with the degree of disability. Nevertheless, the myelin sheath can be regenerated in a process named remyelination. This regenerative response is most clearly seen in young animals following experimental demyelinating lesions (Franklin and Ffrench-Constant, 2017), but also occurs in MS (Chari, 2007). Remyelination seems to be a very frequent event in early MS lesions (Goldschmidt et al., 2009), but it can also occur in some patients with progressive chronic disease (Patrikios et al., 2006). Neuropathological studies of the distribution of remyelinated areas showed that the extent of remyelination depends on the location of the lesion (Patrikios et al., 2006), with subcortical lesions showing more extensive remyelination than periventricular or cerebellar lesions (Goldschmidt et al., 2009; Patrikios et al., 2006).

Remyelination could be important to restore metabolic support to the axon, which will limit the axon degeneration responsible for progressive disability. Moreover, remyelination re-establishes the ionic channel organization necessary to facilitate impulse conduction, hence; it allows for successful neuronal communication and CNS function (Franklin and Ffrench-Constant, 2017). Despite re-establishing these myelin functions, the remyelinated myelin sheaths do not fully recapitulate normal myelination. They are too thin for the axons they surround and establish shorter internodes (Fig. 1.3). This reduction in myelin sheath thickness is only apparent when large-diameter axons are remyelinated, which makes the distinction between normally myelinated and remyelinated myelin sheaths challenging (Blakemore and Franklin, 2008). However, it is unknown whether these morphological differences have functional consequences.

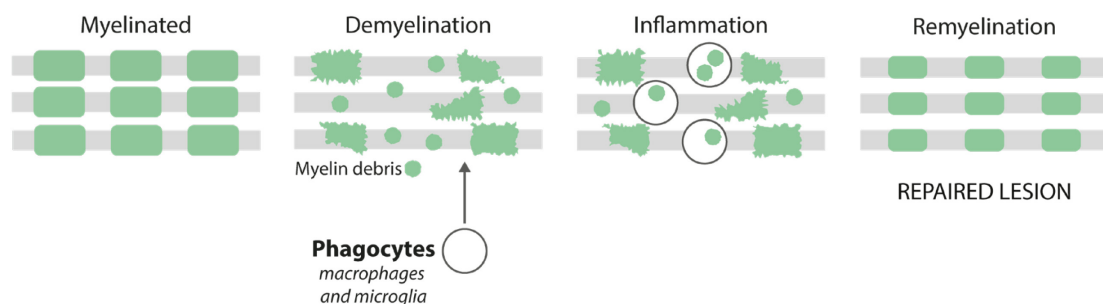


Figure 1.3: Remyelination re-establishes myelin sheaths around demyelinated axons. Myelin damage results in the release of myelin fragments or myelin debris, which are phagocytosed and cleared away by microglia and macrophages. After clearance of myelin debris, oligodendrocyte precursor cells will create new myelin sheaths around demyelinated axons. The new myelin sheaths never attain the length and thickness of the original myelin sheaths.

To establish a new myelin sheath after demyelinating injury, adult OPCs become activated and start proliferating to create new oligodendrocytes. Both progenitors within the lesion and those around the lesion can contribute to the regeneration of the lesion, which they populate by migrating into it after activation. Once in the lesion, new oligodendrocytes can differentiate and form new myelin sheaths. In unusual cases, CNS remyelination can also be achieved by Schwann cells, the myelinating cells in the PNS. This phenomenon frequently occurs at sites close to spinal roots or deficient in astrocytes. Surprisingly, fate-mapping studies have proven that the CNS remyelinating Schwann cells can be both of PNS and CNS origin (Franklin and Ffrench-Constant, 2017).

2.3.1. Remyelination failure underlies disease progression

In many patients with MS, remyelination ultimately fails. As stated above, failed remyelination contributes to axonal degeneration and hence to the progressive disability that characterizes the later stage of MS (Nave, 2010; Patani et al., 2007). Thus, many investigations have focused on understanding the reasons underlying remyelination failure with the aim to find effective therapies for MS. Since the transition into the progressive phase of MS normally occurs in advanced ages, it is apparent that age can have a profound influence on remyelination efficiency. Indeed, many studies of the age-associated decline in remyelination efficiency have yielded numerous interesting findings regarding the mechanisms of remyelination failure.

The first cause of decreased remyelination rate is a decline in the efficiency of OPCs recruitment and differentiation into remyelinating oligodendrocytes (Sim et al., 2002). This seems to result from intrinsic changes in the OPCs and extrinsic changes in the signalling environment. The intrinsic changes in OPCs reflect epigenetic changes within the ageing OPCs characterized by poor HDAC recruitment that leads to persistence of oligodendrocyte differentiation inhibitors (Shen et al., 2008). On the other hand, the signalling environment during remyelination is controlled by inflammatory cells; most prominently, by CNS macrophages. In aged murine models of remyelination, macrophage recruitment into the lesion is slower (Hinks and Franklin, 2000) and results in a decline in the phagocytic removal of myelin debris (Hinks and Franklin, 2000; Ruckh et al., 2012). Myelin debris contain proteins that inhibit the differentiation of new oligodendrocytes, thus; slower myelin debris clearance leads to inhibition of OPC differentiation (Kotter, 2006; Shields et al., 1999). Furthermore, the dynamic regulation of the inflammatory environment that accompanies and is necessary for remyelination is dysregulated in aged models, as demonstrated by differences in the expression of inflammatory mediators such as IGF1, TGF β , platelet-derived growth factor α (PDGF α) (Hinks and Franklin, 2000) and the slower switch from a pro-inflammatory to a pro-regeneration macrophage phenotype (Miron et al., 2013). Recently, our study highlighted the role of cholesterol efflux by macrophages in regulating the pro-repair environment necessary for successful remyelination (Cantuti-Castelvetri et al., 2018).

2.3.2. Macrophage function in remyelination

The revealed mechanisms of remyelination failure underline the importance of CNS macrophages in orchestrating remyelination. Indeed, remyelination occurs most efficiently when it is closely linked to the process of demyelination, most likely because the inflammatory response associated with

demyelination provides the necessary environment for remyelination to occur efficiently. Dysregulations of this temporal associations might lead to chronic inflammation and unrepaired tissue damage.

Macrophages are necessary for the remyelination process because they remove inhibitory myelin debris and extracellular matrix components and secrete growth factors that stimulate axonal re-growth and oligodendrocyte differentiation (Kigerl et al., 2009; Miron et al., 2013; Ruckh et al., 2012; Setzu et al., 2006; Zhao et al., 2006). Studies in toxin-induced demyelination models have demonstrated that reducing the number or activation of macrophages by administration of minocycline or toxin-encapsulated liposomes inhibits remyelination (Kotter et al., 2001; Li et al., 2005; Miron et al., 2013). Likewise, stimulating macrophage function with amphotericin B and macrophage-colony stimulating factor (MCSF) promotes remyelination (Döring et al., 2015). Macrophage activation and recruitment seems to be crucial in early stages of CNS remyelination, since delayed macrophage depletion does not affect remyelination (Kotter et al., 2001). Among the plethora of inflammatory mediators that macrophages upregulate and secrete, IL1 β , TNF α , Activin-A, MAC2, MHCII, BDNF, IL10 and ferritin appear to be the most important remyelination mediators (Franklin and Ffrench-Constant, 2008; Lloyd and Miron, 2019; Rawji and Yong, 2013). The phagocytic function of macrophages is also of outmost importance; since myelin debris present in demyelinated lesions exerts potent inhibitory effects on the ability of adult oligodendrocyte progenitors to generate remyelinating oligodendrocytes (Gitik et al., 2011; Kotter, 2006). Efficient clearance of myelin debris is CX₃CR1-dependent, demonstrating a more preferential role of microglia and perivascular macrophages in myelin debris clearance (Lampron et al., 2015). After myelin phagocytosis, myelin-derived cholesterol has to be expelled from the macrophage cytoplasm into apolipoproteins, a process named cholesterol efflux (Cantuti-Castelvetri et al., 2018).

The activation of macrophages is dynamically regulated during efficient remyelination. For successful regeneration, macrophages must switch from a pro-inflammatory to a pro-resolution phenotypes. Such dynamic regulation indicates that timed coordination of particular macrophage phenotypes and functions is essential for efficient remyelination. Several studies have characterized the distinct macrophage populations that orchestrate remyelination. Findings by Miron et al. (Miron et al., 2013) demonstrated that an early iNOS⁺CD16/32⁺TNF α ⁺ (iNOS: inducible nitric oxygen synthase) population stimulates oligodendrocyte progenitor recruitment, while a later-appearing ARG1⁺IGF1⁺CD206⁺ population promotes oligodendrocyte differentiation (ARG1: arginase 1). This polarization seems to occur both in microglia and MDMs, as demonstrated by fate-mapping studies (Miron et al., 2013). Experiments using parabiosis to link the circulatory systems of young and aged mice demonstrated that the enhanced remyelination observed in aged animals results from the recruitment of young macrophages that promote the conversion of macrophages to the ARG1⁺CD206⁺ population (Ruckh et al., 2012). Post-mortem MS tissue also demonstrated an abundance of iNOS⁺ macrophages in chronic inactive lesions, which are poorly remyelinated, and an increase of the CD206⁺ macrophage population in actively remyelinating lesions (Vogel et al., 2013).

The cues dictating macrophage phenotype transition are still unknown (Lloyd and Miron, 2016, 2019). Interestingly, a recent study reported that the switch from pro-inflammation to pro-resolution is driven by pro-inflammatory microglia necroptosis and repopulation by a pro-regeneration population of microglia (Lloyd et al., 2019). In this view, necroptosis would shut down pro-inflammatory microglia to support remyelination. Nevertheless, more studies will be necessary to confirm this finding and further elucidate the mechanisms underlying macrophage phenotype switch. For now, it is clear that the temporal regulation of the activation of CNS macrophages is an essential aspect of efficient regeneration.

3. Lipid buffering and processing in macrophages

Considering the high lipid content of myelin, macrophages take in very high amounts of lipids upon myelin phagocytosis. The way macrophages buffer and process these lipids determines the phagocytosis efficiency and the macrophage phenotype, both of which must be tightly regulated to ensure remyelination. Thus, this chapter reviews how macrophages phagocytose myelin debris, how they process the lipids contained in these debris and the transcriptional and signalling pathways controlling this process.

3.1. Myelin debris phagocytosis and degradation

Microglia and MDMs detect myelin debris via MAC2, TREM2, Fc γ receptors, complement receptors such as CR3 and scavenger receptors such as SRII (Smith, 2001; Takahashi et al., 2005). These receptors stimulate phosphoinositide 3-kinase (PI3K)-dependent signalling pathways that cause a rearrangement of the actin filaments and the phagocytic intake of myelin debris. One of the most relevant components of myelin debris is free cholesterol. In diseases such as atherosclerosis, over-accumulation of cholesterol in macrophages is detrimental for the atherosclerotic plaque, in that it will promote inflammation and plaque necrosis (Moore and Tabas, 2011). Thus, many efforts have been directed in understanding how cholesterol is processed in the macrophage after intake. Initially, the newly formed phagosome containing myelin debris traffics into the cytoplasm and enter the endosome network. At the late endosome stage, lysosomal hydrolases derived from the Golgi apparatus are incorporated and immediately activated due to the low pH in the endosome, thereby causing the release of free cholesterol and fatty acids contained in myelin debris (Maxfield, 2014). Free cholesterol is very poorly soluble in water and needs to be transported out of the late endosome/lysosome through the cooperative action of two proteins (NPC1 and NPC2, identified through their association with Niemann Pick disease type C, an inherited lysosomal storage disease). Free cholesterol is transferred to a cytoplasmic cholesterol-binding protein (Maxfield, 2014) and trafficked to the endoplasmic reticulum (Boadu et al., 2008). In the endoplasmic reticulum, free cholesterol can be esterified by the action of the enzyme acetyl-CoA acetyltransferase 1 (ACAT1) and, together with fatty acids, start forming lipid droplets, which will bud off the endoplasmic reticulum to become an independent structure surrounded by a single layer of membrane that safely buffers cholesterol and fatty acids. The overload of lipid droplets in a macrophage results in the typical foam cell morphology found both in atherosclerotic plaques and demyelinating lesions (Tabas and Bornfeldt, 2016). Neural cholesteryl ester hydrolases nCEH and nCEH1 are involved in a secondary hydrolysis of cholesterol esters to liberate free cholesterol that could be then out flowed from macrophages into lipoproteins by cholesterol transporters ATP-binding cassette transporter A1 (ABCA1) and G1 (ABCG1) (Chistiakov et al., 2016) (see Fig. 5.1 in the Appendix).

3.2. The LXR Pathway

The study of the macrophage phenotype after internalization of myelin demonstrates an enhancement in pathways involved in lipid metabolism, proliferation, chemotaxis, phagocytosis and inflammation (Bogie et al., 2012). One of the specific pathways involved in lipid metabolism that is upregulated by myelin intake is the Liver-X Receptor (LXR) pathway. The LXR pathway is generally

activated when cells accumulate excess cholesterol and it works as a regulatory system for the elimination of excess cholesterol via promotion of reverse cholesterol transport. In this chapter, we will analyse the LXR pathway from the point of view of each of its components: ligands, transcription factor, and targets.

3.2.1. LXR ligands

The ligands for LXR are naturally occurring desmosterol and oxysterols. Desmosterol is the main endogenous LXR ligand accumulating in response to cholesterol loading. It also is the final intermediate in the Blotch pathway of cholesterol biosynthesis, which is downregulated by cholesterol accumulation (Spann and Glass, 2013). Oxysterols, instead, are produced by the oxidation of cholesterol. The most abundant oxysterol in the brain is 24S-hydroxycholesterol, whose levels are elevated in plasma upon active demyelination in MS patients and EAE models (Moutinho et al., 2015; Wang et al., 2002). Other typical oxysterols are 27-hydroxycholesterol, 22-hydroxycholesterol, and 24,25-hydroxycholesterol (Janowski et al., 1996; Lehmann et al., 1997; Wang et al., 2002). In addition to activating LXRs, desmosterol and oxysterols potently suppress the activation of the sterol regulatory element-binding protein (SREBP) pathway to prevent its promotion of cholesterol and fatty acid biosynthesis (Jeon and Osborne, 2012; Spann and Glass, 2013) (see Fig. 5.1 in the Appendix).

Synthetic agonists for LXR have been developed and include components such as T1317 (Schultz et al., 2000) and GW3965 (Collins et al., 2002). Both compounds are anti-atherogenic in mice, however; they do not suppress the processing of SREBPs, and therefore lead to undesirable effects due to increasing plasma and liver triacylglycerides (Spann and Glass, 2013; Xu et al., 2013).

3.2.2. The transcription factor LXR

The LXR is a lipid-activated transcription factor part of a nuclear receptor family composed of 48 ligand-activated transcription factors. These predominantly form heterodimers with the retinoid X receptor (RXR) and control metabolism homeostasis, development and cell growth (Yang et al., 2007). The LXR/RXR heterodimers are permissive, which implies that either an RXR or an LXR agonist can activate the complex, and that binding by agonists for both partners could have synergistic effects (Rószler et al., 2013). In the absence of ligand, LXR/RXR complexes are bound to the DNA in specific sites considered their DNA response elements. There, they repress gene expression via interactions with co-repressor and histone deacetylases (Kidani and Bensinger, 2012). Upon ligand binding, a conformational change to the LXR/RXR complex causes the exchange of the co-repressors for co-activators and the initiation of target gene transcription (Kidani and Bensinger, 2012).

There are two isoforms of the LXR: LXR α ; produced by the gene *Nr1h3*, and LXR β ; produced by the gene *Nr1h2*. LXR α is primarily expressed in metabolically active tissues and cells such as adipose tissue, liver, intestine and macrophages. By contrast, LXR β is nearly ubiquitously expressed (Edwards et al., 2002; Schultz et al., 2000). Although the same ligands bind to both isoforms, single-isoform KO models suggest that each isoform has a distinct set of target genes and might have non-overlapping roles (Edwards et al., 2002; Lehmann et al., 1997).

3.2.3. LXR Target genes

The target genes for LXR are involved in processes such as dietary cholesterol absorption, cellular cholesterol efflux, reverse cholesterol transport, lipoprotein metabolism, conversion of excess cholesterol into bile acids and fatty acid synthesis and esterification (Valledor et al., 2004). The most prominent LXR target genes are the following:

- *Abca1* and *Abcg1*: These ABC-type transporters mediate cholesterol efflux by transporting free cholesterol from the cell cytoplasm into lipoproteins. ABCA1 preferentially binds to lipid-poor APOA1-containing lipoproteins, while ABCG1 rather effluxes cholesterol into APOE-containing lipoproteins.
- *Apoa1* and *ApoE*: apolipoproteins required for lipoprotein formation, cholesterol efflux and reverse cholesterol transport (Cummins and Mangelsdorf, 2006; Traversari et al., 2014).
- *Srebp1c*: this transcription factor upregulates fatty acid synthesis and other lipogenic genes (Hong and Tontonoz, 2014).
- *Npc1* and *Npc2*: proteins that regulate the intracellular trafficking of cholesterol (Rigamonti et al., 2005).

It is important to note that passive diffusion driven by the cholesterol gradient established between the cell surface and the APOE/APOA1-containing lipoproteins in contact with the cell surface further drives cholesterol efflux. This is facilitated by SRBI, a scavenger receptor of the family of CD36 receptors (Phillips, 2014).

3.2.4. The LXR pathway controls lipid metabolism and inflammatory status

The LXR pathway protects cells from lipid overload by activating the cholesterol efflux pathway, thus contributing to lipid metabolism and maintaining whole-body sterol homeostasis. In macrophages, LXR contributes to handling lipids after phagocytosis, together with storage in lipid droplets and beta-oxidation pathways. Interestingly, the LXR pathway also antagonizes the expression of a battery of inflammatory genes in activated macrophages (Joseph et al., 2003) and reduces inflammation in several models of disease in murine models (Fowler et al., 2003; Ito et al., 2015; Lee and Tontonoz, 2015; Valledor, 2005). Thus, the LXR pathway is a common regulator of lipid metabolism and immune functions in macrophages (Joseph et al., 2003), which promotes macrophage survival and inflammation resolution in an array of diseases (Valledor, 2005).

3.3. The PPAR Pathway

Another pathway prominently activated in myelin-phagocytosing macrophages is the peroxisome proliferator-activated receptor (PPAR) pathway (Bogie et al., 2012). This pathway was identified in the early 1990s and termed PPAR because of its ability to bind chemicals known to induce peroxisome proliferation. PPARs are also members of the nuclear receptor superfamily and form permissive heterodimers with RXR (Röszer et al., 2013). Similar to the LXR, the PPAR/RXR heterodimer also binds to specific DNA regions and upon ligand binding is dissociated from its co-repressors and binds to co-activators to initiate gene transcription. PPARs are lipid sensors and are activated by dietary fatty acids and their metabolic derivatives in the body. In particular, several unsaturated fatty acids (UFAs) bind to PPARs, whereas saturated fatty acids (SFAs) are poor PPARs

ligands. Upon activation, they redirect metabolism by controlling lipid and glucose metabolism, energy homeostasis and adipocyte and macrophage differentiation.

There are three PPAR subtypes; PPAR α , PPAR γ , and PPAR β/δ . These share high homology but differ in tissue distribution, ligand specificity and function.

3.3.1. PPAR α

PPAR α is the predominant subtype in tissues with high catabolic rates of fatty acids; namely, the liver and brown adipose tissue, as well as the heart and muscle to a lesser extent. Its endogenous ligands include polyunsaturated fatty acids (PUFAs) such as arachidonic acid and fatty acid-derived compounds such as members of the 15-hydroxycosatetraenoic acid family (Bernardo and Minghetti, 2006). PPAR α is the target of fibrate drugs used to treat hypertriglyceridemia, which reduce plasma triacylglycerides, reduce adiposity and improve hepatic and muscle steatosis, consequently improving insulin sensitivity.

PPAR α activation promotes fatty acid catabolism, gluconeogenesis, ketogenesis and lipoprotein assembly. Its activation typically occurs after an overnight of prolonged fast, when fatty acids are released from adipose tissue and transported into the liver, where PPAR α is potently induced and generates ketone bodies to provide an energy source for peripheral tissues. Mice devoid of PPAR α are unable to meet the energy demands during fasting and suffer from hypoglycaemia, hyperlipidaemia, hypoketonaemia and a fatty liver. In macrophages and microglia, PPAR α inhibits inflammatory activation and promotes antioxidative actions (Chinetti et al., 2001; Wang et al., 2010).

3.3.2. PPAR γ

PPAR γ predominates in adipose tissue and to a lower extent in colon, immune system (macrophages and lymphocytes) and retina. In peripheral monocytes, the expression of PPAR γ is induced during extravasation from blood vessels into tissue and in macrophages and microglia, activation by pro-inflammatory stimuli also induce PPAR γ expression (Bernardo and Minghetti, 2006).

Similar to the other PPARs, the natural agonists for PPAR γ are PUFAs and its derivatives. In this case, arachidonic acid derivatives and lipoxygenase products have a higher affinity for PPAR γ (Bernardo and Minghetti, 2006). Two major groups of synthetic compounds also activate PPAR γ . The first group are thiazolidinediones or glitazones, which were originally identified as improving insulin sensitivity of diabetic animals. The other group are some non-steroidal anti-inflammatory drugs, such as ibuprofen, fenoprofen and flufenamic acid. These need to be in a high micromolar range to activate PPAR γ , thereby largely exceeding those required for *in vivo* inhibition of cyclooxygenases (Canfora et al., 2015; Feinstein et al., 2002; Kidani and Bensinger, 2012).

PPAR γ is the master regulator of adipocyte differentiation, maturation and function. It induces the storage of lipids in lipid droplets, as demonstrated by experiments where the forced expression of PPAR γ in non-adipogenic cells effectively converts these cells in mature adipocytes. Insights gained from studies with thiazolidinediones demonstrated that PPAR γ activation also leads to insulin sensitization. Several mechanisms have been proposed for this effect, in which the ability of PPAR γ to promote lipid storage in adipose tissue and prevent the release of far-reaching inflammatory

molecules can have metabolic effects on other tissues and promote insulin sensitivity (Hyong et al., 2008).

In microglia and macrophages, PPAR γ also has a very strong anti-inflammatory action. PPAR γ activation blocks the selective removal of co-repressor from gene targets of the inflammatory pathways nuclear factor κ of activated B cells (NF κ B), activator protein 1 (AP1) and signal transducer and activator of transcription 1 (STAT1) and competes for the same co-activators as these pathways. Strong inflammatory insults, such as LPS stimulation, can downregulate PPAR γ expression, thereby making the co-activators available for inflammatory pathways and releasing the co-repressors from their target genes (Chawla et al., 2001).

3.3.3. PPAR β/δ

PPAR β/δ is expressed throughout the body, with higher levels in the gut, kidney and heart and low levels in the liver. Although PPAR β/δ has a narrower ligand binding domain compared to the other PPAR subtypes, a variety of natural ligands bind PPAR β/δ , such as arachidonic and linoleic acid and their metabolites (Liu et al., 2018). PPAR β/δ was the latest subtype to be studied, therefore, not so many synthetic agonists are available. Most experimental studies have used GW501516, which lowers triglyceride levels in obese monkeys and is currently under clinical trials (Dressel et al., 2003).

PPAR β/δ is a key regulator of fat burning, thereby opposing the fat-storing function of PPAR γ . Therefore, PPAR β/δ tightly regulates serum lipid profiles by promoting fatty acid β -oxidation in the muscle and adipose tissue (Bordet et al., 2006). Mice expressing an activated form of PPAR β/δ in adipose tissue are resistant to diet- and genetically- induced obesity. In macrophages, PPAR β/δ seems to also regulate both lipid metabolism and inflammation (Bogie et al., 2012).

3.4. The effect of myelin internalisation on the phenotype of CNS macrophages

Myelin internalisation profoundly changes the morphology and phenotype of CNS macrophages. Initially, several studies focused on the pro-inflammatory profile that microglia and MDMs acquire after myelin intake, where they increase the production of pro-inflammatory and toxic mediators (Van Der Laan et al., 1996; Williams et al., 1994). More recently, it has become apparent that these macrophages can also obtain a rather pro-resolution and healing-promoting identity following (Boven et al., 2006; Liu et al., 2006; van Rossum et al., 2008). These apparent contradictions have been resolved by the model of biphasic temporal pattern of microglial and macrophage activation (Fig. 1.4). Following this model, the pro-inflammatory profile of microglia and macrophages is triggered after rapid activation of receptor-mediated signalling pathways. Here, complement, Fc and scavenger receptors activate signalling pathways after contacting their ligands and promote the release of pro-inflammatory and toxic mediators. After myelin is internalised, it is digested into its constituents, which, in turn, are or produce LXR and PPAR pathway agonists. As explained above, the activation of these pathways skews the macrophage phenotype towards a less inflammatory phenotype (Bogie et al., 2012, 2014b; Grajchen et al., 2018). This pro-resolution phenotype may partially underlie the role of microglia and macrophages in the EAE model and in MS, where they can suppress neuroinflammation and neurodegeneration and promote CNS repair (Kotter, 2006; Ruckh et al., 2012).

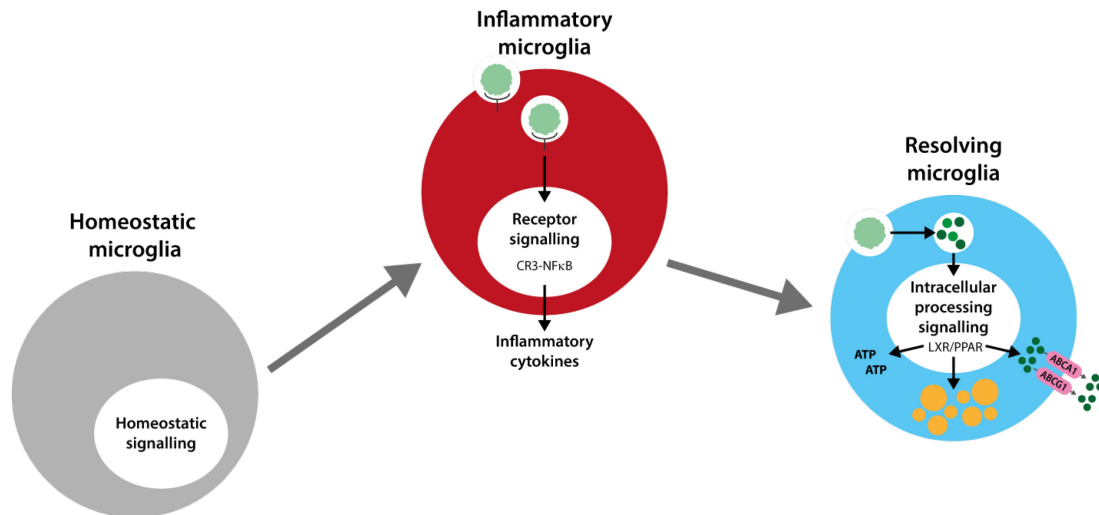


Figure 1.4: Illustration of the model of biphasic temporal pattern of microglial and macrophage activation. After myelin intake, microglia and macrophages initially trigger a pro-inflammatory response mediated by complement, Fc and scavenger receptors. After myelin processing, its lipid constituents activate the LXR and PPAR pathways, which activate lipid handling pathways and skew the macrophage phenotype towards a pro-resolving phenotype. LXR: liver-X receptor, PPAR: peroxisome proliferation activating receptor, CR3: complement receptor 3, NFκB: nuclear factor κ of activated B cells, ABCA1/G1: ATP-binding cassette transporter A1/G1.

Despite these findings, it must be noted that the phenotype of myelin-loaded phagocytes is further determined by the balance between cholesterol ester storage and efflux of free cholesterol. Upon long-term lipid overload and saturation of the storage and efflux mechanisms, free cholesterol levels can be increased in the cytoplasm of foam cells (Moore and Tabas, 2011). This can lead to pathological free cholesterol-induced lipotoxicity (Katz et al., 1976), which leads to release of pro-inflammatory mediators, promotes endoplasmic reticulum stress and subsequent calcium leakage into the cytosol, causes lysosome dysfunction and affects cell signalling by changing membrane fluidity (Tabas and Bornfeldt, 2016). Furthermore, lipotoxicity-derived mitochondrial dysfunction triggers further inflammation, esterification of oxysterols (which renders them unable to bind LXR) and programmed cell death (Hubler and Kennedy, 2016). Accumulation of unbuffered free cholesterol also leads to the formation of cholesterol crystals. These are highly cytotoxic and may impair cholesterol metabolism, further enhance the release of pro-inflammatory cytokines through inflammasome activation and ultimately lead to cell death, which releases the cholesterol crystals in the extracellular matrix of the damaged tissue (Cantuti-Castelvetri et al., 2018; Tall and Yvan-Charvet, 2015) (see Fig. 5.1 and 5.2 in the Appendix).

3.5. The LXR and PPAR pathways in the CNS in health and disease

Although the LXR and PPAR pathways were first mostly studied in peripheral contexts such as atherosclerosis, hyperlipidemia and diabetes, they have now also been broadly studied in the CNS and, indeed, they seem to be involved in most neuroinflammatory and neurodegenerative diseases.

Both LXR isoforms are expressed in the brain, but particularly LXR β is broadly expressed in all cell types of the developing and adult rodent CNS (Gilardi et al., 2009; Kainu et al., 1996; Nelissen et al., 2012). Global LXR deficiency results in a severe CNS phenotype, indicating that the LXR pathway contributes to CNS development and homeostasis (Wang et al., 2002). Furthermore, these mice spontaneously develop lupus-like autoimmune disease, underlying the role of LXR in regulating the immune system (Kidani and Bensinger, 2012). Indeed, stimulation of the LXR pathway using synthetic agonists has proved beneficial for treatment of EAE by suppressing the polarization of mouse CD4⁺ T cells into the T cell helper 17 (Th17) phenotype (Cui et al., 2011), reducing the secretion of pro-inflammatory cytokines by microglia and astrocytes (Xu et al., 2009; Zhang-Gandhi and Drew, 2007) and preventing antigen presentation via MHCII (Kidani and Bensinger, 2012). Likewise, LXR deficiency results in exacerbated EAE disease course (Cui et al., 2011; Kidani and Bensinger, 2012).

It is apparent that these studies mostly focused on how the regulation of inflammation by LXR influences the course of a neuroinflammatory disease such as MS. Nevertheless, a more recent study from our laboratory focused on the regulation of lipid metabolism by LXR and how this can affect remyelination (Cantuti-Castelvetri et al., 2018). In this study, we found that the aged microglia and macrophages accumulated excessive amounts of myelin debris. This triggered cholesterol crystal formation and led to lipotoxicity, inflammasome activation and the perpetuation of inflammation. Stimulation of the LXR pathway was sufficient to enhance reverse cholesterol transport by microglia and macrophages and restore the capacity of old mice to remyelinate the lesioned tissue. Hence, the LXR pathway is an essential step to promote the resolution of inflammation and tissue regeneration. LXR pathway agonism is also beneficial in other neurological diseases, such as AD, Parkinson's Disease (PD), HD and NPC1 disease, among others (Cermenati et al., 2013).

Less is known about the physiological role of PPARs for CNS development and homeostasis. All three PPAR subtypes are expressed in the CNS, but PPAR β/δ seems to be the dominant form present in all cell types of the murine brain (Basu-Modak et al., 1999). The distribution of PPAR β/δ is widespread throughout the CNS, whereas the distributions of PPAR α and γ are more restricted (Bordet et al., 2006). PPAR α is most expressed in astrocytes (Basu-Modak et al., 1999) and PPAR γ is most present in microglia and oligodendrocytes (Heneka and Landreth, 2007). Transgenic mouse models provide evidence that PPARs play pivotal roles for CNS development and function (Heneka and Landreth, 2007). For instance, PPAR β/δ null mice exhibit an altered myelination of the corpus callosum, indicating that PPAR β/δ participates in the regulation of oligodendrocyte differentiation in the CNS. Moreover, activation of PPAR in neurons can directly influence neuron cell viability and differentiation (Heneka and Landreth, 2007).

In EAE, the activation of PPARs, particularly PPAR γ , suppresses the secretion of pro-inflammatory mediators and chemoattractant chemokines, prevents T-cell proliferation and hinders Th1 polarization of CD4⁺ T-cells. Likewise, PPAR γ -deficient heterozygous mice develop an exacerbated phenotype in the EAE model. Stimulation of PPAR β/δ and PPAR α pathways also exert beneficial effects in the EAE model, by reducing astrocytic and microglial activation and decreasing lymphocyte

proliferation, respectively (Heneka and Landreth, 2007; Zolezzi et al., 2017). PPAR pathway agonism can also have beneficial effects in other neurological diseases, such as AD, PD and ALS (Heneka and Landreth, 2007; Zolezzi et al., 2017).

4. Obesity

Obesity is a worldwide health problem that has reached epidemic proportions and is associated to a cluster of disorders collectively known as metabolic syndrome. Despite its separation from peripheral organs by the blood-brain barrier, the CNS is likewise affected by obesity: obese patients have a 74% increased risk of dementia (Whitmer et al., 2005). In this project, we study the influence of obesity on the regenerative process of remyelination. Therefore, this chapter reviews all aspects of obesity that influence microglia function and its ability to orchestrate remyelination.

4.1. Obesity is associated with peripheral inflammation

Obesity is associated with chronic low-grade systemic inflammation that appears to be both a cause and a consequence of obesity. Dietary factors such as fatty acids stimulate the free fatty acid receptor TLR4 on immune cells, which initiates an inflammatory cascade (Miller and Spencer, 2014). Furthermore, obesity is associated with infiltration of macrophages into the white adipose tissue, apoptosis of adipocytes, and reduced white adipose tissue vascularity. Such macrophage proliferation further leads to an increase in the proinflammatory cytokine profile. The adipose tissue itself can also act as an endocrine organ releasing adipocytokines such as leptin, which further promotes the production of cytokines and increases macrophage phagocytic activity (Procaccini et al., 2014). Excessive adipose tissue also increases the number and activity of mast cells, neutrophils, and lymphocytes in the circulation (Court and Alvarez, 2016).

The establishment of this circulating inflammatory status can have downstream effects on the liver and muscle that contribute to the establishment of systemic insulin resistance. For instance, pro-inflammatory cytokines such as TNF α activate serine kinases that directly and indirectly phosphorylate insulin receptor substrate (IRS) 1 and 2, resulting in a reduced ability of insulin to stimulate PI3K-dependent pathways that normally result in glucose uptake and metabolism. Additionally, feeding-related pathways in the hypothalamus are also disrupted by inflammation, with insulin and leptin less able to suppress hunger and feeding, further contributing to the maintenance of a HFD and thus obesity. This establishment of inflammation in peripheral tissues finally promotes the progression and development of a wide range of obesity-associated co-morbidities (Gregor and Hotamisligil, 2011; Miller and Spencer, 2014).

4.2. Alterations in lipid storage and metabolism in obesity

In a healthy human, triacylglycerides (TAGs) stored in adipocytes can undergo lipolysis to provide peripheral tissues with free fatty acids to generate energy. This lipolysis is hormonally controlled, thus; the level of free fatty acids in plasma is balanced by energy demands. In obesity, adipocytes have altered sensitivity to regulating hormones and increase their lipolysis rate, generating abnormally high plasma levels of free fatty acids. These lead to pathological fat storage in other organs such as liver or muscle and contribute to obesity-associated metabolic complications characterized by insulin resistance and diabetes (Quehenberger and Dennis, 2011).

The lipid species circulating in plasma are profoundly altered by obesity. Several individual TAG and diacylglyceride (DAG) species are specifically increased by obesity and correlate with biomarkers of

acquired obesity (Pietiläinen et al., 2007). Interestingly, rather than the total amounts of TAGs, the length and the number of double bonds seem to be altered by obesity. Indeed, TAGs containing saturated or monounsaturated fatty acids correlate positively to insulin resistance, while TAGs containing PUFAs correlate negatively to insulin resistance (Kotronen et al., 2009). A decrease in the amounts of TAGs containing odd-chain-length fatty acids has also been reported (Sysi-Aho et al., 2011). Obesity has also been associated with increases in lysophosphatidylcholines (LPC), lipids found in proinflammatory and proatherogenic conditions, and to decreases in ether phospholipids, which are known to have antioxidant properties (Pietiläinen et al., 2007).

The serum lipidome has also been analysed in mouse models of diet-induced obesity (DIO), which are generally based on the feeding of either a high-fat diet (HFD), which contains a defined high percentage of fat or a western diet (WD), which is a high-sugar, high-fat and high-calorie diet. It is challenging to generalize these results due to the divergence of type and duration of diet, however, these studies led to the discovery of particular lipid species that are associated with obesity (Eisinger et al., 2014; Li et al., 2014).

4.3. Peripheral abnormalities cause inflammation in the CNS

In 2005, de Souza and colleagues first suggested that DIO can result in neuroinflammation by detecting an elevated expression of pro-inflammatory cytokines in the hypothalamus upon HFD consumption in mouse (De Souza et al., 2005). Since then, the causes of obesity-induced hypothalamic inflammation have been widely studied. Indeed, the arcuate nucleus of the hypothalamus and other circumventricular organs lack an effective blood-brain barrier and are therefore in a prime position to respond directly to circulating factors such as nutrients and inflammatory mediators including cytokines (Miller and Spencer, 2014). This way, circulating free fatty acids can activate TLR4 on microglia and astrocytes and initiate an inflammatory cascade. Interestingly, myeloid differentiation primary response 88 (MYD88) knock-out mouse models, where signalling downstream of TLR4 is abolished, are resistant not only to neuroinflammation induced by obesity but also to the actual obesity associated with a HFD (Miller and Spencer, 2014). Neuroinflammation resulting from HFD intake has also been reported in other areas of the CNS; for instance, in the amygdala, hippocampus, cortex and cerebellum during obesity (Guillemot-Legrís and Muccioli, 2017).

4.3.1. Characteristics of obesity-induced central inflammation

The main feature of HFD-induced neuroinflammation in rodents is the activation of microglia and astrocytes (Buckman et al., 2013; Thaler et al., 2012; Yi et al., 2012). This results in proliferation and morphological changes in these cells that are accompanied by an increase in the secretion of inflammatory mediators such as reactive oxygen species (ROS), IL1 β or TNF α (Guillemot-Legrís and Muccioli, 2017; Miller and Spencer, 2014). The blood-brain barrier as well as the choroid plexus can also be altered by obesity: HFD and WD increase their permeability in several areas of the brain (Guillemot-Legrís and Muccioli, 2017). Nevertheless, the affection of these areas is not homogenous, thus; future studies will need to unravel the precise effects of HFD and WD on these barriers. It has also been suggested that peripheral immune cells infiltrate the CNS during obesity (Buckman et al.,

2014; Lee et al., 2019; Valdearcos et al., 2017), however; there are still discrepancies on this matter because other studies show no infiltration (Baufeld et al., 2016). The reason for the discrepancies is not clear, but it could be due to different cell sorting methods that might have included other CNS resident macrophage populations (Guillemot-Legrís and Muccioli, 2017). It is important to note that the type of diet (e.g. HFD, WD), its duration and the age of the organism are crucial determinants of the consequences of DIO on neuroinflammation. Furthermore, not all CNS structures are affected to the same degree, hence stressing the importance of studying neuroinflammation in defined structures as opposed to in the whole brain.

In humans, obesity-induced neuroinflammation has been less studied. Nevertheless, Schur and colleagues used diffusion tensor imaging and MRI in obese individuals and identified that insulin resistance was associated with gliosis in the mediobasal hypothalamus (Schur et al., 2015). Interestingly, obesity indicators such as the body mass index or waist circumference seem to be associated with decreased brain volume in elderly individuals (Raji et al., 2010), decreased grey matter volume in elderly and morbidly obese patients (Karlsson et al., 2013) and white matter atrophy in morbidly obese patients (Karlsson et al., 2013). These modifications support the links between obesity and CNS pathologies in humans (Guillemot-Legrís and Muccioli, 2017).

4.3.2. Consequences of central inflammation

Several studies suggest that hypothalamic inflammation can cause an interruption of the normal feeding- and metabolism-related signalling that further promotes obesity (Kälín et al., 2015; Miller and Spencer, 2014). Central inflammation can contribute to leptin and insulin resistance, favouring overconsumption, weight gain and the maintenance an elevated body weight (Miller and Spencer, 2014; Valdearcos et al., 2017). Indeed, reduction in the NF- κ B inflammatory signalling cascade through targeted deletion of inhibitor of nuclear factor kappa- β (IKK β) or infusion of a TNF α neutralizing antibody in the CNS of mice led to a reduction in weight gain on HFD, improved glucose tolerance and higher insulin sensitivity in the liver (Milanski et al., 2012; Zhang et al., 2008).

Deficits in cognitive function caused by obesity have also been reported (Kanoski and Davidson, 2011; Miller and Spencer, 2014). For instance, 10 days of WD consumption decreased the hippocampal GLUT1 glucose transporter that provides the CNS with glucose, and this was associated with learning and memory deficits (Hargrave et al., 2015). Other mechanisms linking obesity and cognitive impairment are reduced levels of BDNF, altered glutamatergic signalling, and impaired insulin regulation (Hargrave et al., 2015; Hsu and Kanoski, 2014). Chronic neuroinflammation can also cause anxiety and anhedonia (Guillemot-Legrís and Muccioli, 2017), possibly due to its affection of the amygdala. In humans, low-grade inflammation assessed by levels of C-reactive protein is linked to impaired cognitive function and attention (Lasselin et al., 2016). It is here also necessary to highlight that the duration of the HFD or WD is pivotal in mediating differences in cognition.

4.3.3. The role of microglia in obesity

As explained above, microglia quickly react to a HFD. Despite *in vitro* evidence that both microglia and astrocytes can be activated by fatty acids, *in vivo* studies show that microglia, and not astrocytes, are specifically activated by SFAs (Guillemot-Legrís and Muccioli, 2017; Valdearcos et al., 2014).

Additionally, Valdearcos and colleagues (Valdearcos et al., 2017) demonstrated that microglia inflammatory signalling determines the immunologic response of the mediobasal hypothalamus to high-fat diet. Interestingly, either inhibiting CSF1R to deplete microglia or restraining microglial NF κ B signalling reduced microgliosis and limited weight gain (Valdearcos et al., 2017). Recently, the role of mitochondria on the control of HFD-induced microgliosis was uncovered, revealing that the mitochondrial protein uncoupling protein 2 (UCP2) is fundamental for the HFD-induced microgliosis (Kim et al., 2019). Together, these results indicate that microglia are the key players orchestrating the neuroinflammatory response caused by HFD. Nevertheless, whether and how obesity influences microglia's response upon acute damage to the CNS is still unknown.

4.3.4. Obesity results in microbiome changes that can influence microglia function

Our gut and its resident microbiota regulate energy and substrate metabolism and play a crucial role in the development of cardiometabolic diseases in rodent models and humans. Transfer of intestinal microbiota from lean donors to individuals with metabolic syndrome or antibiotic treatment against gram-positive bacteria in obese humans can improve insulin sensitivity (Vrieze et al., 2012, 2014). Although many mechanisms exist that underlie the microbiome effects on energy regulation, the main mediators are short-chain fatty acids (SCFA). SCFA are a side product of the fermentation of dietary components by our gut microbiota and they include acetate, butyrate and propionate (Topping and Clifton, 2001). Acetate is absorbed in the highest amount in the liver and reaches the highest peripheral concentrations (19-160 μ mol/l) compared with propionate (1-13 μ mol/l) and butyrate (1-12 μ mol/l) (Bloemen et al., 2010). These SCFA have key functional roles in the pathophysiology of obesity and related disorders by affecting control of body weight via regulation of energy intake, energy harvesting and substrate metabolism (Canfora et al., 2015). In addition, several mechanisms that link SCFA to insulin sensitivity have been proposed, including effects on adipose tissue function and lipid storage capacity, inflammatory profile and liver and skeletal muscle substrate metabolism (Al-Lahham et al., 2012, 2010; den Besten et al., 2015). Nevertheless, the currently available data are still controversial, hence, long-term human dietary intervention studies will need to examine the chronic effect of SCFA supplementation on the control of body weight (Canfora et al., 2015).

Microglia maturation and immune response can also be modulated by microbiota (Erny et al., 2015; Mosher and Wyss-Coray, 2015; Thion et al., 2018), as demonstrated by the generation of mice devoid of any microbiota (germ-free mice). Such mice present global defects in microglia function, which show altered cell proportions and an immature phenotype (Erny et al., 2015). The regulation of microglia by microbiota is mediated by SCFA, as mice deficient for the SCFA receptor free fatty acid receptor 2 (FFAR2) mirrored the microglia defects found under germ-free conditions. Consistently, SCFA treatment impacted microglial activation in a model of stroke and improved post-stroke recovery via effects on systemic and CNS resident immune cells (Sadler et al., 2020). Furthermore, SCFA have protective effects on EAE, and blood levels of major SCFAs are significantly decreased in long-term active progressive multiple sclerosis patients (Park et al., 2019). Indeed, microbiota derived from MS patients induces a significantly higher incidence of autoimmunity than the healthy

twin-derived microbiota (Berer et al., 2017). Thus, it appears that the microbiome and SCFA can regulate both obesity and microglia function, making this an interesting mechanism to consider.

4.4. Obesity as a risk factor for multiple sclerosis

Clinical data have demonstrated that obesity-associated parameters such as increased body mass index increase the risk of MS (Hedström et al., 2012; Langer-Gould et al., 2013; Mokry et al., 2015). Obesity during childhood and adolescence have a stronger influence, but also obesity in adulthood increases the risk, and although the increased risk applies to both females and males, females seem to be more susceptible (Altowajri et al., 2017). Furthermore, obesity worsens treatment response and progression in MS (De et al., 2016). High levels of leptin are present in the serum of MS patients and, indeed, leptin worsens the disease course in the EAE mouse model of MS (Matarese et al., 2010). The mechanisms by which obesity leads to higher MS risk, poor treatment response, and worse disease progression are still unclear. Possibly, the inflammatory changes caused by obesity can interact with other environmental factors such as vitamin D levels or with genetic factors such as the human leukocyte antigen isoforms to increase the risk (Altowajri et al., 2017). It has also been suggested that a HFD can promote the loss of oligodendrocyte progenitors, thereby altering remyelination potential (Langley et al., 2020). Furthermore, the systemic inflammation induced by a WD induces long-lasting trained immunity in myeloid cells by changing their epigenetic landscape, which might alter the response of these cells upon demyelination (Christ et al., 2018).

So far, few studies have studied the influence of caloric restriction on multiple sclerosis. In 2008, Piccio and colleagues (Piccio et al., 2008) demonstrated that calorie restriction in mice ameliorated clinical EAE by decreasing inflammation, demyelination and axonal injury. More recently, Neumann and colleagues focused on remyelination and demonstrated that intermittent fasting can rejuvenate remyelination in aged rodents (Neumann et al., 2019). Indeed, these studies suggest that obesity might not only worsen MS, but also directly impair remyelination.

4.4.1. Parallelisms between obesity and ageing

Obesity and ageing are both considerable risk factors for MS progression. Interestingly, obesity and ageing share some commonalities that make the comparison between these two states relevant. Most importantly, in both cases there is a generalized, systemic state of chronic, low-grade inflammation that can have consequences on CNS homeostasis and function. Furthermore, it appears that ageing is also associated with adipose tissue malfunction, where age-induced cellular stress induces cellular senescence, impaired adipogenesis, increase of circulating free fatty acids and cytokine generation (Tchkonina et al., 2010). Likewise, as stated above, intermittent fasting led to improved myelin regeneration in ageing mouse models (Neumann et al., 2019), indicating a role for feeding-related pathologies in the age-related remyelination deficiency. These findings indicate that comparing mechanisms underlying obesity and ageing can be useful to unravel on how both of these pathologies impact metabolism and neuroimmunological functions.

5. Hypothesis and aim of this project

Remyelination failure in MS patients contributes to axonal damage and progressive disability. Hence, it is essential to identify the molecular mechanisms contributing to poor remyelination so that we can design therapies to promote remyelination. In previous investigations, we observed that stimulation of the LXR pathway in old mice promoted cholesterol efflux by microglia and MDMs and improved myelin regeneration after toxin-induced demyelination (Cantuti-Castelvetri et al., 2018). Thus, we concluded that lipid processing by microglia and MDMs is the bottleneck for successful remyelination. Apart from ageing, risk factors that contribute to poor remyelination are unclear. Previous studies indicate that obesity may increase the risk of developing MS and accelerate the progression of MS (Barcellos, 2016; Munger et al., 2009). However, whether and how obesity might influence remyelination is unknown. Considering that the consumption of a WD is one of the main causes of obesity in the developed world, we hypothesized that WD may influence remyelination by perturbing the brain microenvironment and microglia metabolic functions.

To test our hypothesis, we studied the microglia response to demyelination and the efficiency of remyelination in WD-fed mice using a mouse model of toxin-induced demyelination. We also characterized the consequences of WD intake on the lipid profile of the brain and on microglia function under homeostatic conditions by using a combination of lipidomics, immunostainings and transcriptomics. In addition, we used genetical and pharmacological approaches both in WD-fed and in old mice to further investigate the mechanistic reasons of poor lipid processing in macrophages.

In short, we were interested in understanding the influence of WD on microglia's function in the context of demyelination. We believed that an improved understanding of this influence could further elucidate the cellular and molecular mechanisms underlying remyelination failure, and therefore unravel new targets for remyelination-promoting therapies.

Materials and Methods

1. Materials

In the following sections, all materials and methods used for this study will be outlined. For each material, the catalogue number, the company and the country of origin are written between brackets.

1.1. Consumables

Consumables were purchased from Greiner bio-one (Germany), Falcon (Becton Dickinson Labware Europe, France), Omnilab (Germany), neoLab (Germany), VWR (Germany), Sarstedt (Germany), Millipore (Germany), Fine Science Tools (Germany), Science Services (Germany) and Eppendorf (Germany).

1.2. Mouse lines

The following mouse lines were used for this study (Table 1):

Table 1: Name, source and purpose of all mouse lines used in this study.

Mouse line	Source	Purpose
C57BL/6J	Janvier Labs, France	Diet-induced obesity
Leptin ^{ob/ob}	Jackson Labs, United States	Genetically induced obesity
CX ₃ CR1-GFP x CCR2-RFP	Prof. Martin Kerschensteiner Lab, Germany	Differential labelling of microglia and MDMs
ARG1-YFP x iNOS-tdTomato	Prof. Martin Kerschensteiner Lab, Germany	Differential labelling of different activation status of macrophages
CX ₃ CR1 ^{CreERT2} x TGFBR2 ^{fllox}	Prof. Marco Prinz Lab, Freiburg	Inducible genetic deletion of TGFβ signalling in microglia

1.3. Antibodies

1.3.1. Primary antibodies

The following antibodies were used for immunohistochemistry and western blot analysis in this study (Table 2):

Table 2: Species, concentration and catalogue details of all primary antibodies used in this study.

Target	Host species	Concentration	Catalogue number	Company, country of origin
IBA1	Rabbit	1:1000	019-19741	Wako, Japan
IBA1	Guinea Pig	1:500	234004	Synaptic Systems, Germany
MAC2	Rat	1:400	125402	BioLegend, USA
MHCII	Rat	1:100	14-5321	Affymetrix-eBioscience, Thermo Fisher Scientific, Germany
CLEC7A	Rat	1:30	Mabg-mdect	InvivoGen, USA
AXL	Goat	1:100	AF854-SP	R&D Systems, USA
CD68	Rat	1:400	MCA1957	Bio-Rad, USA
LAMP1	Rat	1:100	sc-19992	Santa Cruz, USA
GFAP	Guinea Pig	1:400	173004	Synaptic Systems, Germany
pSMAD2	Rabbit	1:1000	AB-3349-I	Millipore, Germany

PLIN2	Guinea Pig	1:500	GP40	Progen, Germany
ALDH1L1	Mouse	1:300	WH0010840M1	Sigma-Aldrich, Germany
TREM2	Mouse	1:500	AF1729	R&D Systems, USA
Tubulin	Mouse	1:5000	T6557	Sigma-Aldrich, Germany

1.3.2. Secondary antibodies

Fluorescence secondary antibodies including Alexa Fluor 488, 555 and 647 were purchased from Invitrogen and used at a concentration of 1:1000, 1:750 or 1:500 depending on the experimental instructions. Fluoromyelin (F34651, 1:400, Fluoromyelin Green Fluorescent Myelin Stain, Life Technologies, Thermo Fisher Scientific, Germany) and DAPI (4',6-diamidino-2-phenylindole, 1:1000, D1306, Thermo Fisher Scientific, Germany) were also used.

1.4. Commercial kits

The following commercial kits were used according to the manual's instructions (Table 3):

Table 3: Application and catalogue details of all commercial kits used in this study.

Kit	Application	Catalogue number	Company, country of origin
Nucleospin Tissue Kit	DNA isolation from tissue	740952250	Macherey-Nagel, Germany
Neural Tissue Dissociation Kit (P)	Brain dissociation	130-092-628	Miltenyi Biotech, Germany
RNeasy Plus Mini Kit	RNA isolation from cells and tissue	74134	Qiagen, Germany
Superscript III First-Strand Synthesis	cDNA synthesis	18080051	Invitrogen, Thermo Fisher Scientific, Germany
RNAscope Multiplex Fluorescent v2 Assay	Fluorescent in Situ Hybridisation	323100	Advanced Cell Diagnostics Inc., United States

1.5. Primers

1.5.1. Primer design and preparation

All primers were designed using NCBI's free tool Primer Blast. The product size was set to 80-250 bp and the melting temperature between 58°C and 61°C, with maximum 1°C of difference. Primers had to expand an exon-exon junction, be specific for *mus musculus*, be no longer than 13 bp and contain 1 GC clamp and between 45 and 75% of GC content. The adequate primers were then synthesized by Sigma-Aldrich (Germany).

Primers were prepared by adding the corresponding volume of Tris-EDTA buffer to the lyophilised powder and mixing thoroughly. Both the forward and reverse primer of one same primer pair were combined with water (40 µL F primer, 40 µL R primer, 720 µL ddH₂O) to achieve a concentration of 5 µM of each primer.

1.5.2. Primers used for genotyping

The following table contains the sequence of all primers used for genotyping (Table 4):

Table 4: Sequence details of all primers used for genotyping.

Gene name		Sequence (5'→3')
<i>Cx3cr1</i>	F	CCTCTAAGACTCACGTGGACCTG
	R	GACTTCCGAGTTGCGGAGCAC
	Specific	GCCGCCACGACCCGGCAAAC
<i>Tgfb2</i>	F	TAAACAAGGTCCGGAGCCCA
	R	ACTTCTGCAAGAGGTCCCCT
<i>Cx3cr1-GFP</i>	F wild-type	GTCTTCACGTTCCGGTCTGGT
	F mutant	CTCCCCCTGAACCTGAAAC
	R common	CCCAGACACTCGTTGTCCTT
<i>Ccr2-RFP</i>	F common	TAAACCTGGTCACCACATGC
	R wild-type	GGAGTAGAGTGGAGGCAGGA
	R mutant	CTTGATGACGTCCTCGGAG
<i>Arginase1-YFP</i>	F wild-type	AGAGCAAGCACCCCGTTTCTTCTC
	F mutant	TGAGCAAAGACCCCAACGAGAAGC
	R common	GCTGTGATGCCCCAGATGGTTTTC
<i>iNOS-tdTomato</i>	Cre30F	GCATTACCGGTCGATGCAACGAGTGATGAG
	Cre30R	GAGTGAACGAACCTGGTTCGAAATCAGTGCG

1.5.3. Primers used for RT-qPCR

The following table contains all details of the primers used for RT-qPCR analysis (Table 5):

Table 5: Sequence details of all primers used for RT-qPCR analysis.

Gene name		Sequence (5'→3')
<i>ApoE</i>	F	CTGACAGGATGCCTAGCC
	R	TCCCAGGGTTGGTTGCITTG
<i>Abca1</i>	F	TGTCTGAAAAAGGAGGACAGTG
	R	TGTCACITTCATGGTCGCTG
<i>Abcg1</i>	F	CAGACGAGAGATGGTCAAAGA
	R	TCAAAGAACATGACAGGCCG
<i>Tgfb1</i>	F	CTGCTGACCCCACTGATAC
	R	AAGCCCTGTATTCCGTCTCC
<i>Tgfb2</i>	F	TCCCCTCCGAAAATGCCATC
	R	TGCTATCGATGTAGCGCTGG
<i>Arginase 1</i>	F	CTGGCCTTTGTTGATGTCCC
	R	AGCACCACACTGACTCTTCC
<i>iNOS</i>	F	TCCCTTCCGAAGTTTCTGGC
	R	CTCTCTTGCAGGACCATCTCC
<i>Rplp0</i>	F	AAACTGCTGCCTCACATCCG
	R	AGCAGCTGGCACCTTATTGG
<i>Cyc1</i>	F	ATGGGGAGATGTTTCATGCGG
	R	CTGAGGTCAGGGGGTAAGC

1.6. Buffers and solutions

1.6.1. For lysolecithin injections

1.6.1.1. Lysolecithin solution

A solution of 1% lysolecithin (LLC) (L4129, Sigma-Aldrich, Germany) was prepared under a laminar flow hood by mixing 25 mg of LLC in 2.5 mL of sterile 1X PBS (10010-056, Thermo Fisher Scientific, Germany). The solution was sonicated in an ultrasonic cleaner at 40 kHz for 15 minutes to ensure complete dissolution. The solution was aliquoted in 20 µL aliquots and stored at -20°C until use.

Once one aliquot was thawed, it was used and discarded. During use, the solution was kept at 37°C to prevent precipitation.

1.6.1.2. Monastral blue solution

A solution of 3% monastral blue (274011, Sigma-Aldrich, Germany) was prepared by dissolving 1.5 g monastral blue in 50 mL of dH₂O. The solution was then filtered through a whatman filter paper and autoclaved. Just before injection into the brain, we added 0.2 µL monastral blue solution into 20 µL of LLC solution.

1.6.1.3. Mouse anaesthesia and analgesia

For injections into the CNS, mice were anaesthetized via an intraperitoneal injection of MMF solution containing 0.5 mg medetomidin/kgBW, 5.0 mg midazolam/kgBW and 0.05 mg fentanyl/kgBW. To terminate the anaesthesia, mice were injected subcutaneously with AFN solution, containing 2.5 mg atipamezol /kgBW, 1.2 mg naloxon /kgBW and 0.5 mg flumazenil /kgBW. For mouse euthanization by perfusion, mice were anaesthetized with an intraperitoneal injection of 100 µL of 10% ketamine and 2% xylazine. To provide analgesia to mice after surgery, mice were injected with 0.05 mg buprenorphine/kgBW on the day of surgery and 1, 2 and 3 days after surgery.

1.6.2. For histological analysis of mouse tissue

1.6.2.1. Paraformaldehyde solution for histology

Paraformaldehyde (PFA) 16% stock solution was prepared by dissolving 80 g PFA (158127, Sigma-Aldrich, Germany) in 450 mL dH₂O at 65°C, while stirring for 15 to 20 minutes. Then, droplets of 5 N NaOH (6771.1, Roth, Germany) were added until the solution became clear. Afterwards, 50 mL 10X PBS were added and the pH was adjusted to 7.4. Finally, dH₂O was added until the final volume of 500 mL (to compensate for evaporation). Aliquots of the solution were then stored at -20°C. The working solution of 4% PFA in PBS was prepared by diluting 50 mL of PFA stock solution in 150 mL of 1X PBS, filtering the resulting solution with a Steritop 0.22 µm filter system (SCGPT01RE, Merck Millipore, Germany) and storing it at 4 °C.

1.6.2.2. Sucrose solution

To cryoprotect tissues before freezing, a 30% sucrose solution was prepared by mixing 15 g of sucrose (S0389, Sigma-Aldrich, Germany) in 50 mL of 1X PBS.

1.6.2.3. Cryoprotecting solution

A cryoprotecting solution containing 25% of glycerol (65518, Sigma-Aldrich, Germany) and 25% of ethylene glycol (102466, Sigma-Aldrich, Germany) in 1X PBS was used to store free-floating tissue sections at -20°C.

1.6.2.4. 10X Phosphate Buffer Solution (PBS):

10X PBS was prepared by dissolving the following in 1L ddH₂O:

- 80 g NaCl (3957.2, Roth, Germany)
- 2 g KCl (6781.1, Roth, Germany)
- 18.05 g Na₂HPO₄•2H₂O (1.06580.1000, Merck Millipore, Germany)
- 2.4 g KH₂PO₄ (3904.1, Roth, Germany)

The pH was adjusted to 7.4 and the solution stored at RT. To prepare 1X PBS, 10X PBS was diluted 10 times with ddH₂O, the pH value was re-adjusted to 7.4, and the solution was stored at RT.

1.6.2.5. 2X Phosphate buffer (PB)

2X PB was prepared by dissolving the following in 1L of ddH₂O:

- 3.6 g NaH₂PO₄•H₂O (1.06346.1000, Merck Millipore, Germany)
- 10 g NaCl (3957.2, Roth, Germany)
- 31 g Na₂HPO₄•2H₂O (1.06580.1000, Merck Millipore, Germany)

The pH value was adjusted to 7.4 and the solution stored at RT. To prepare 1X PB, 2X PB was diluted 2 times with ddH₂O, the pH value was re-adjusted to 7.4, and the solution was stored at RT.

1.6.2.6. Blocking and staining solution for immunohistochemistry

The blocking solution for immunohistochemistry was prepared by mixing the following in 500 mL of 1X PBS:

- 12.5 mL bovine calf serum (BCS) (SH30073.03HI, GE Healthcare Life Sciences, USA)
- 12.5 g bovine serum albumin (BSA) (A2153, Sigma-Aldrich, Germany)
- 12.5 mL fish gelatine (G7765, Sigma-Aldrich, Germany)

The solution was aliquoted and kept at -20°C. To prepare the staining solution, I diluted the blocking solution 1:4 in 1X PBS.

1.6.2.7. Citrate buffer for antigen retrieval

Citrate buffer was prepared by diluting 2.941 g of tri-sodium citrate dehydrate (C₆H₅Na₃O₇•2H₂O, 1.06448.0500, Merck Millipore, Germany) in 1L of ddH₂O. The pH value was adjusted at 6.0 using HCl.

1.6.2.8. Mowiol solution

Mowiol was used as the mounting medium after immunocytochemistry and immunohistochemistry. The solution was prepared by stirring 2.4 g mowiol (0713.2, Roth, Germany), 6 g glycerol (65518, Sigma-Aldrich, Germany) and 6 mL ddH₂O for several hours at RT. After addition of 12 mL 0.2 M Tris-HCl (pH 8.5), the solution was incubated at 60°C for 10 minutes and then centrifuged at 4,000 g for 15 min. Finally, mowiol was aliquoted and kept at -20°C until further use.

1.6.3. For electron microscopy

1.6.3.1. Fixative for electron microscopy

To prepare fixative for electron microscopy, the following components were mixed to prepare 40 mL of fixative, which is enough for perfusion of 1 mouse:

- 10 mL 0.4 M cacodylate buffer. This, in turn, was prepared as follows:
 - o Dissolve 85.6 g sodium cacodylate trihydrate (C0250, Sigma-Aldrich, Germany) in 1 L ddH₂O
 - o Adjust pH value to 7.4 by adding 1 N HCl
- 40 µL 2 M calcium chloride solution. This, in turn, was prepared as follows:
 - o Mix 222 g CaCl₂ (1.02378.0500, Merck Millipore, Germany) in 1 L ddH₂O

- 4 mL 25% glutaraldehyd (electron microscopy grade, 16220, Electron Microscopy Sciences, USA)
- 5 mL 16% PFA (electron microscopy grade, 15710, Electron Microscopy Sciences, USA)
- 20.96 mL ddH₂O

The solution was filtered through a Steritop 0.22 µm filter system (SCGPT01RE, Merck Millipore, Germany). The solution was prepared freshly each day.

In cases where one same brain was used for histology and electron microscopy, the mouse was perfused with a 4% PFA solution prepared in 1X PB, and then fixed in electron microscopy fixative by immersion for 48 hours.

1.6.3.2. Gelatine solution

To embed small tissues such as the spinal cord for sectioning with a vibratome, we prepared a gelatine solution by mixing 15 g of gelatine (104070-0500, Merck Millipore, Germany) in 100 mL sterile 1X PBS (10010-056, Thermo Fisher Scientific, Germany) under continuous rotation at around 60-80°C. The solution can be kept at 4 or -20°C.

1.6.3.3. Osmium solution

A solution of 2% osmium was used to contrast samples for electron microscopy and prepared as follows:

- 2 mL 4% osmium in water stock solution: 0.5 g OsO₄ (E19120, Science Services, Germany) in 12.5 mL ddH₂O
- 1 mL 0.4 M cacodylate buffer
- 1 mL ddH₂O

1.6.3.4. Uranyl acetate in water

A solution of uranyl acetate was used to contrast samples for electron microscopy. It was prepared by combining 1 mL of 4% uranyl acetate in water (0.5 g uranyl acetate (E22400, Science Services, Germany) in 12.5 mL ddH₂O) with 3 mL of ddH₂O. The solution was then filtered.

1.6.3.5. Mixture for staining semithin sections

A 1:1 mixture of methylene blue solution and azur blue solution was used to stain semithin sections. This was prepared by mixing the following freshly before use:

- 1% (1g) methylene blue (M9140, Sigma-Aldrich, Germany) in 100 mL sodium tetraborat (i.e. borax)
- 1% (1g) azur blue (861065, Sigma-Aldrich, Germany) in 100 mL ddH₂O

Before use, the solution was filtered.

1.6.3.6. Epon

Epon was used to embed samples for electron microscopy in blocks to allow for sectioning. This was prepared as follows:

- Combine:
 - o 20 g glycid ether (21045.02, Serva, Germany)
 - o 13.5 g 2-dodecenylsuccinic acid anhydride (DDSA) (20755.02, Serva, Germany)

- 10.6 g methylnadic anhydride (MNA) (29452.05, Serva, Germany)
- Mix by stirring 10 min
- Add 0.79 g of 2,4,6-Tris(dimethylaminomethyl)phenol (DMP-30) (36975.01, Serva, Germany)
- Mix by stirring for 20 min

1.6.4. Other purposes

1.6.4.1. Tris-HCl Buffer

To prepare Tris-HCl Buffer, 60.57 g of Tris Base (A1379,5000AppliChem, Germany) were dissolved into 350 mL of ddH₂O by stirring. Then, under pH monitoring, 12 M HCl (258148, Sigma-Aldrich, Germany) was added until the pH reached a pH value of 7.4. Finally, ddH₂O was added to fill up to 500 mL and the solution was filtered and stored at 4°C.

1.6.4.2. Tris-EDTA Buffer

A solution of 10 mM Tris-EDTA Buffer was prepared by combining the following:

- 5 mL of 1M Tris (A1379.5000, AppliChem, Germany) pH 8
- 1 mL of 0.5M EDTA (AM9261, Invitrogen, Thermo Fisher Scientific, Germany pH 8
- 496 mL ddH₂O

The solution was autoclaved to sterilize.

1.6.4.3. TBS and TBST Buffers

1X TBS Solution was prepared by dissolving the following in 800 mL of ddH₂O:

- 6.05 g Tris (A1379.5000, AppliChem, Germany)
- 8.76 g NaCl (3957.2, Roth, Germany)

The pH value was adjusted 7.6 with 1 M HCl. The volume was then filled up to 1L with ddH₂O. Once prepared, TBS is stable at 4°C for 3 months. To prepare TBST, 1 mL of Tween 20 (8.22184.0500, Merck Millipore, Germany) was added to 1 L of 1X TBS.

1.6.4.4. RIPA Buffer

RIPA buffer was prepared by making a solution of 150 mM NaCl (3957.2, Roth, Germany), 1% Triton-X100 (T8787, Sigma-Aldrich, Germany), 0.5% sodium deoxycholate (3483.1, Roth, Germany), 0.1% SDS (2326.2, Roth, Germany) and 50 mM Tris (A1379.5000, AppliChem, Germany). The pH value was adjusted to 8.0.

1.6.4.5. Blocking solution for western blot

The blocking solution for western blot contained 3% milk (T145.3, Roth, Germany) and 0.05% Tween 20 (8.22184.0500, Merck Millipore, Germany) in TBS Buffer.

1.6.4.6. Sample buffer for western blot

The sample buffer for western blot contained 1% BSA (A2153, Sigma-Aldrich, Germany) and 0.05% Tween-20 in PBS (8.22184.0500, Merck Millipore, Germany). The pH value was adjusted to 7.4.

1.6.4.7. TAE Buffer for agarose gels

A 10X TAE Buffer was prepared by combining the following in 1L of ddH₂O:

- 48.4 g Tris base (A1379.5000, AppliChem, Germany)
- 11.4 mL Acetic acid (3738.4, Roth, Germany)
- 20.0 mL 0.5 M EDTA (AM9261, Invitrogen, Thermo Fisher Scientific, Germany)

The pH value was adjusted to 8.5.

1.7. Software

All software used in this study are detailed in Table 6.

Table 6: Application and source of all software used in this study.

Software	Application	Source
FIJI-ImageJ	Image processing and analysis	http://imagej.nih.gov/ij/
CaseViewer	Image visualization and analysis	3DHISTEC, Germany
Imaris v9.2	Image processing and analysis	Bitplane, United Kingdom
Adobe Illustrator 2019	Data visualization	Adobe Systems, Inc, USA
GraphPad Prism 8	Data analysis	http://www.graphpad.com/scientific-software/prism/
Leica Application Suite AF	Image acquisition and processing	Leica, Germany
LightCycler 480 SW 1.5.1	RT-qPCR data acquisition and processing	Roche, Switzerland
iPython 2.7	Data analysis	Reference (Pérez, 2007)

2. Methods

In this chapter, I would like to briefly discuss the methods that were used in this study. Detailed protocols describing all the steps to follow for several of the following methods can be found in the section 4 of the Appendix.

2.1. Mouse procedures

All mouse procedures were carried out with approval and according to the District Government of Upper Bavaria. All mice were housed at the mouse facility in the German Centre for Neurodegenerative Diseases (DZNE) in Munich or at the mouse facility in the Biomedical Centre (BMC) in Martinsried in a standard, pathogen-free, 12h light/12h dark cycles.

2.1.1. Genotyping of mouse lines

The tissue lysis and DNA extraction from mouse tissue for genotyping was performed with the NucleoSpin Tissue Kit (740952250, Macherey-Nagel, Germany) according to the manufacturer's instructions. Genotyping of the transgenic lines was performed in a standard PCR reaction with 5 µL of extracted DNA using the primers described in section 1.5.1 of Materials and Methods, a Biometria TRIO thermocycler (Analytik Jena, Germany) and according to the following instructions.

2.1.1.1. Genotyping of the CX₃CR1-GFP x CCR2-RFP mouse line

The following thermocycler steps were performed to amplify the *Cx3cr1-gfp* gene:

Step	Temperature (°C)	Time	Notes
1	94	2 minutes	
2	94	15 seconds	
3	60	15 seconds	
4	72	30 seconds	Repeat step 2-4 for 35 cycles
5	72	2 minutes	
6	10		

The genotype was decided based on the presence of bands of different molecular weight:

- 500 bp: mutant, GFP/GFP
- 410 bp and 500 bp: heterozygote, +/GFP
- 410bp: wild-type, +/+

The following thermocycler steps were performed to amplify the *Ccr2-rfp* gene:

Step	Temperature (°C)	Time	Notes
1	94	2 minutes	
2	94	20 seconds	
3	65	15 seconds	-1.5°C decrease per cycle
4	68	10 seconds	Repeat step 2-4 for 10 cycles
5	94	20 seconds	
6	50	15 seconds	
7	72	10 seconds	Repeat step 5-7 for 25 cycles
8	72	2 minutes	
9	10		

The genotype was decided based on the presence of bands of different molecular weight:

- 320 bp: mutant, RFP/RFP
- 320 bp and 494 bp: heterozygote, RFP/+
- 494 bp: wild-type, +/+

2.1.1.2. Genotyping of the ARG1-YFP x iNOS-tdTomato mouse line

The following thermocycler steps were performed to amplify the *iNOS-tdTomato* gene:

Step	Temperature (°C)	Time	Notes
1	93	1 minute	
2	93	20 seconds	
3	68	3 minutes	Repeat step 2-3 for 29 cycles
4	10		

The genotype was decided based on the presence of bands of different molecular weight:

- Approx. 230 bp: positive
- No bands: negative

The following thermocycler steps were performed to amplify the *Arginase1-yfp* gene:

Step	Temperature (°C)	Time	Notes
1	94	2 minutes	
2	94	20 seconds	
3	65	15 seconds	-0.5°C decrease per cycle
4	68	10 seconds	Repeat step 2-4 for 10 cycles
5	94	20 seconds	
6	60	15 seconds	
7	72	10 seconds	Repeat step 5-7 for 28 cycles
8	72	2 minutes	
9	10		

The genotype was decided based on the presence of bands of different molecular weight:

- 186 bp: mutant, YFP/YFP
- 186 bp and 363 bp: heterozygote, YFP/+
- 363 bp: wild-type, +/+

2.1.1.3. Genotyping of the $CX_3CR1^{CreERT2} \times TGFBR2^{flox}$ mouse line

The following thermocycler steps were performed to amplify the *Cx3cr1^{CreERT2}* gene:

Step	Temperature (°C)	Time	Notes
1	94	5 minutes	
2	94	30 seconds	
3	58	45 seconds	
4	72	45 seconds	Repeat step 2-4 for 35 cycles
5	72	5 minutes	
6	10		

The genotype was decided based on the presence of bands of different molecular weight:

- 304 bp: mutant, cre/cre
- 304 bp and 750 bp: heterozygote, cre/wt
- 750 bp: wild-type, wt/wt

The following thermocycler steps were performed to amplify the *Tgfb^{r2}^{flox}* gene:

Step	Temperature (°C)	Time	Notes
1	95	5 minutes	
2	95	30 seconds	
3	58	30 seconds	
4	72	1 minute	Repeat step 2-4 for 39 cycles
5	72	5 minutes	
6	10		

The genotype was decided based on the presence of bands of different molecular weight:

- 540 bp: mutant, flox/flox
- 540 bp and 420 bp: heterozygote, flox/wt
- 420 bp: wild-type, wt/wt

2.1.1.4. Gel electrophoresis

The PCR products were run for 1 hour and 10 minutes on a 1% agarose (Seakem LE Agarose, 50004, Lonza, US) gel at 125 V with a Powerpac HC (Biorad, USA). For DNA labelling in the gel, we used GelRed (41003-1, Biotium, USA) and A 100 bp or 1000 bp ladder (SM0241, Thermo Fisher Scientific, Germany) was added to interpret the results.

2.1.2. Experimental paradigm for western diet-induced obesity

To generate diet-induced obese mice, C57BL/6J male mice were fed either control diet (CD) (CD88137, Ssniff, Germany) or western diet (WD) (TD88137, Ssniff, Germany) from 6 weeks of age and during a period of 8 to 10 weeks (Fig. 2.1a). Both diets were formulated using the same nutritionally defined and purified ingredients to control for diet refinement and abolish confounding factors (Fig. 2.1b). We specifically controlled for fibre content, which was set to 5% cellulose in both diets. The WD contained 19.1 MG/kg of metabolizable energy, of which 42% came from fat, while the CD contained 15.7 MG/kg in metabolizable energy, of which 13% came from fat (Fig. 2.1c). WD-fed mice rapidly increased their weight to 34.76 g in average after 10 weeks of feeding, while mice on CD weighed 27.74 g in average (Fig. 2.1d,e).

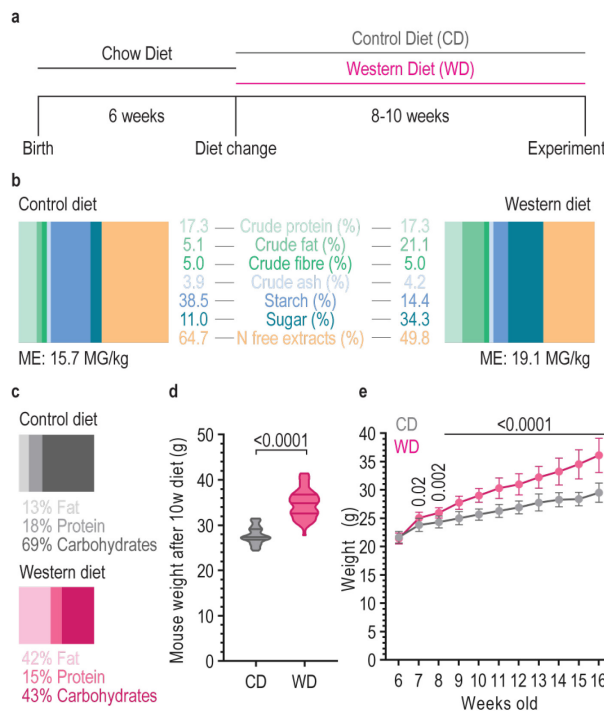


Figure 2.1: Experimental paradigm used to induce obesity by diet. a, Schematic representation of the diet timeline. **b,** Illustration showing the percentage of crude nutrients in control and Western diet. Exact percentages are shown for each component. **c,** Illustration of the percentage of metabolizable energy contained in fat, proteins and carbohydrates. **d,** Violin plot of the body weight of mice fed western or control diet for 10 weeks. Solid lines indicate the 25%, 50% and 75% quartiles. For CD; n=52, for WD; n=54 (two-tailed Welch’s t-test). **e,** Body weight increase over time either under the control or western diet (n=10 for both groups, data represent mean±SD, two-tailed Welch’s t-test). CD: control diet, WD: western diet, ME: metabolizable energy.

2.1.3. Experimental timelines for special diets, treatments and tamoxifen-induced gene deletion

For the experiments using LXR and PPAR agonists, WD (for diet-induced obese mice) or chow diet (for 12-month-old mice) were supplemented with fenofibrate (F6020, Sigma-Aldrich, Germany), rosiglitazone (R2408, Sigma-Aldrich, Germany) and GW3965 (S2630m, Selleckchem, Germany) at a concentration of 2,000 mg fenofibrate/kg diet, 100 mg rosiglitazone/kg diet, and 100 mg GW3965/kg diet. Considering an average mouse weight of 32 g and a food consumption of 4 g/day,

the doses of treatment were 250 mg fenofibrate/kgBW*day, 12.5 mg rosiglitazone/kgBW*day, and 20 mg GW3965/kgBW*day.

Diet containing fenofibrate/rosiglitazone was supplied to animals at the day of injection and for the whole duration of the experiment, while diet containing GW3965 was supplied from two days before injection and for the whole duration of the experiment (Fig. 2.2a,d). The weight of all WD-fed or all old mice was comparable on the day of injection (Fig. 2.2b,e). Treatment with fenofibrate, but not with rosiglitazone or GW3965, caused weight loss in both WD-fed and old mice (Fig. 2.2c,f).

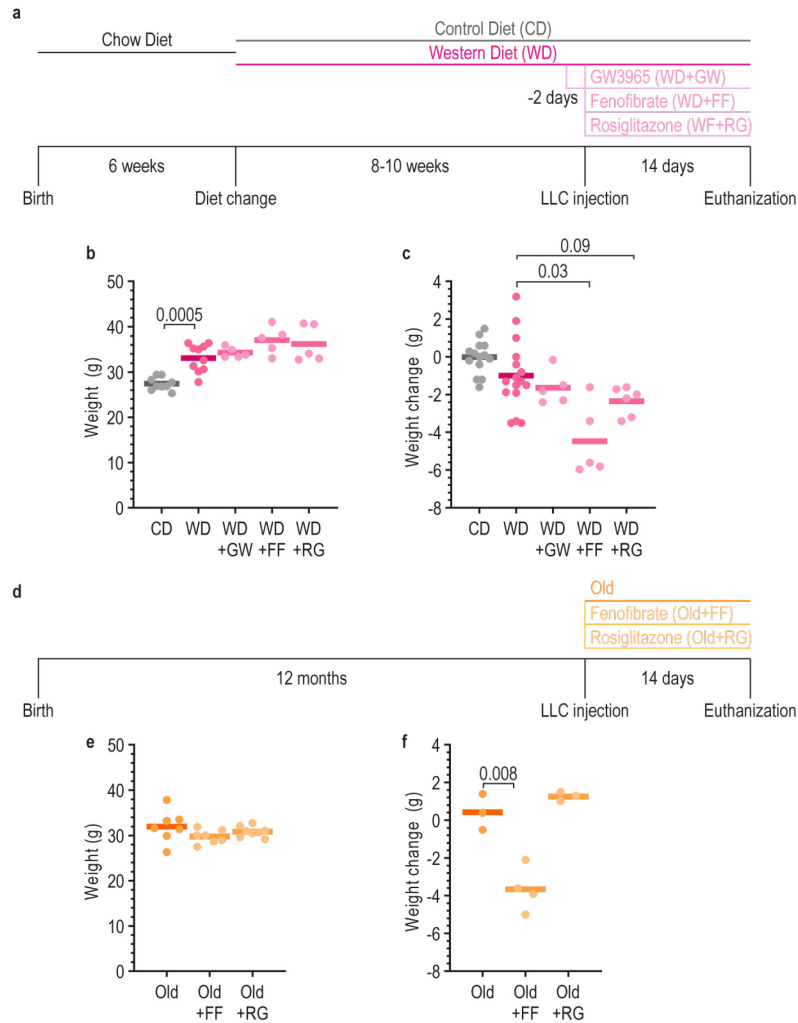


Figure 2.2: Timeline used for pharmacological treatments. **a**, Timeline followed to treat WD-fed mice with GW, FF and RG. **b**, Average weight in the different treatment groups (one-way Brown-Forsythe and Welch ANOVA tests with multiple comparisons corrected by Dunnett T3 test, all groups were compared to WD group). **c**, Quantification of the weight loss from beginning of the treatment to end of experiment in the different groups (one-way Brown-Forsythe and Welch ANOVA tests with multiple comparisons corrected by Dunnett T3 test, all groups were compared to WD group). **d**, Timeline followed to treat old mice with FF and RG. **e**, Average weight in the different treatment groups (one-way Brown-Forsythe and Welch ANOVA tests with multiple comparisons corrected by Dunnett T3 test, all groups were compared to old group). **f**, Quantification of the weight loss from beginning of the treatment to end of experiment in the different groups (one-way Brown-Forsythe and Welch ANOVA tests with multiple comparisons corrected by Dunnett T3

test, all groups were compared to old group. GW: GW3965, FF: Fenofibrate, RG: rosiglitazone, LLC: lysolecithin, CD: control diet, WD: western diet.

Treatment of both WD-fed and old mice with sodium butyrate (303410, Roth, Germany) was achieved through addition of the component to the drinking water 5 days before the injection and for the whole duration of the experiment (Fig. **2.3a,b**). A concentration of 100 mM of sodium butyrate was chosen considering that it is lower than the threshold for lower water consumption due to water saltiness (>200 mM) and enough to achieve effects (which are observed from concentrations of 0.6 g sodium butyrate/kgBW*day). The same concentration (100 mM) of sodium chloride (3957.2, Roth, Germany) was added to the untreated group, to control for the effects of salt consumption. The water solution was prepared freshly and provided to the mice every 5 days. Considering an average mouse weight of 30 g, the doses were 2.3 g sodium butyrate/kgBW*day and 1.23 g sodium chloride/kgBW*day.

The double reporter mouse line ARG1-YFP x iNOS-tdTomato was used to visualize different activation status of microglia and macrophages upon LLC-induced demyelination (Locatelli et al., 2018). Mice were fed CD or WD from 6 to 16 weeks of age, then injected in the spinal cord with LLC and analysed at 4 dpi (Fig. **2.3c**).

To induce obesity in CX₃CR1^{CreERT2} x TGFBR2^{lox} mice, 6-weeks old mice were given WD for 4 weeks before LLC injection. To induce recombination in the *Tgfb^r2^{lox}* locus, tamoxifen (T5648, Sigma-Aldrich, Germany) was dissolved in corn oil to make a solution of 20 mg/mL. The solution was protected from light and placed on a shaker to dissolve overnight at 37°C. 8-weeks old mice were administered 200 µl of tamoxifen solution via intraperitoneal injection 3 times separated by 48 hours 2 weeks before the LLC injection (Fig. **2.3d**). For all experiments, littermates carrying the respective loxP-flanked alleles but lacking expression of Cre recombinase were used as controls. Same ratios of male and female mice were used for this part of the study.

For galunisertib treatment, 175 mg of galunisertib (HY-13226, Hycultec, Germany) were first dissolved in 5 mL of DMSO and then added to 245 mL of drinking water, resulting in a concentration of 0.7 mg galunisertib/mL water. Considering an average weight of 30 g and a water consumption of 6.5 mL/day, the dose of treatment was 150 mg/kgBW*day (Bueno et al., 2008). Control mice were administered the same dose of DMSO in the drinking water. The treatment was started on the same day of LLC injection, and the water solution was prepared freshly and provided to the mice every 5 days (Fig. **2.3e,f**).

For the experiment with the TREM2-enhancing antibody 4D9, we induced focal demyelinating lesions in the spinal cord of WD-fed and old mice, and concomitantly dosed 4D9 antibody or an isotype control for 14 or 21 days (Fig. **2.3g,h**). We had previously determined that intraperitoneal doses of 100 mg/kgBW at the day of LLC injection and at 3, 7 and 14 days after injection were necessary to obtain sufficient concentration of 4D9 within the CNS (Schlepckow et al., 2020). For these experiments, the 4D9 antibody was cloned into a mouse backbone. For details on the

production and characterization of the isotype and the 4D9 antibody, please refer to section 2 of the Appendix.

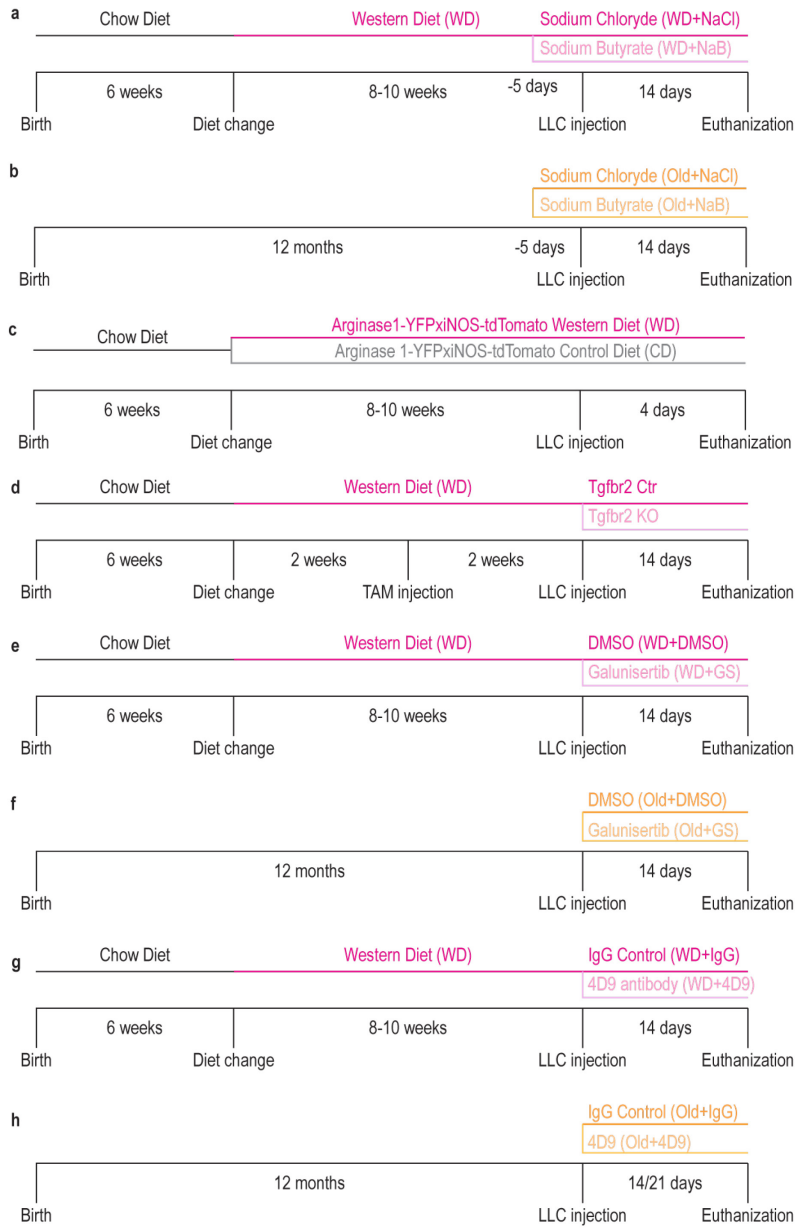


Figure 2.3: Timeline used for pharmacological treatments and induction of knock-outs. a,b, Timeline followed to treat WD-fed mice (**a**) and old mice (**b**) with Sodium Butyrate or its vehicle control, Sodium Chloride. **c,** Timeline followed to treat ARG1-YFPxiNOS-tdTomato mice with CD and WD. **d,** Timeline followed to induce the knock-out of *Tgfr2* in microglia from WD-fed mice. **i,j,** Timeline followed to treat WD-fed mice (**i**) and old mice (**j**) with Galunisertib or its vehicle control DMSO. **k,l,** Timeline followed to treat WD-fed mice (**k**) and old mice (**l**) with the TREM2 enhancing antibody 4D9 or its IgG isotype control. 4D9: TREM2-enhancing antibody, LLC: lysolecithin, CD: control diet, WD: western diet, GS: galunisertib, TAM: tamoxifen.

2.1.4. Lysolecithin Injections

2.1.4.1. The lysolecithin model of de- and remyelination

In this study, we make ample use of the LLC model of remyelination. LLC is a demyelinating chemical that non-specifically disrupts lipids by integrating into cellular membranes and increasing cell membrane permeability (Plemel et al., 2018). Administration of LLC into white matter tracts such as the corpus callosum or the spinal cord white matter through a stereotactic injection creates a focal demyelinated lesion. In this model, noticeable demyelination occurs within hours after the injection, significant demyelination lasts for 7 to 10 days, until the repair process of remyelination follows demyelination. Remyelination is maximal between 14 to 21 dpi and requires rapid clearance of damaged myelin by microglia and macrophages (Jeffery and Blakemore, 1995).

The LLC injection causes a disruption of the blood-brain barrier, thereby promoting the infiltration of MDMs into the demyelinating lesion. To determine whether microglia or MDMs had a more relevant role in this model, we injected CX3CR1-GFP x CCR2-RFP mice with LLC in the spinal cord. This reporter mouse line is commonly used to differentiate microglia from MDMs based on the differential expression of chemokine receptors (Saederup et al., 2010). Through quantification of the percentage of IBA1⁺ cells that were GFP⁺RFP⁻ versus the IBA1⁺ cells that were RFP⁺, we could examine the prevalence of microglia and MDMs, respectively. Both at 4 and 14 dpi, more than 80% of the IBA1⁺ population was derived from microglia, while only 10-20% was derived from MDMs (Fig 2.4a,b). These findings are consistent with previous reports demonstrating a main role of microglia in lesion repair after LLC injection (Lloyd et al., 2019; Plemel et al., 2020). Thus, our characterization studies focused on microglia rather than on monocytes.

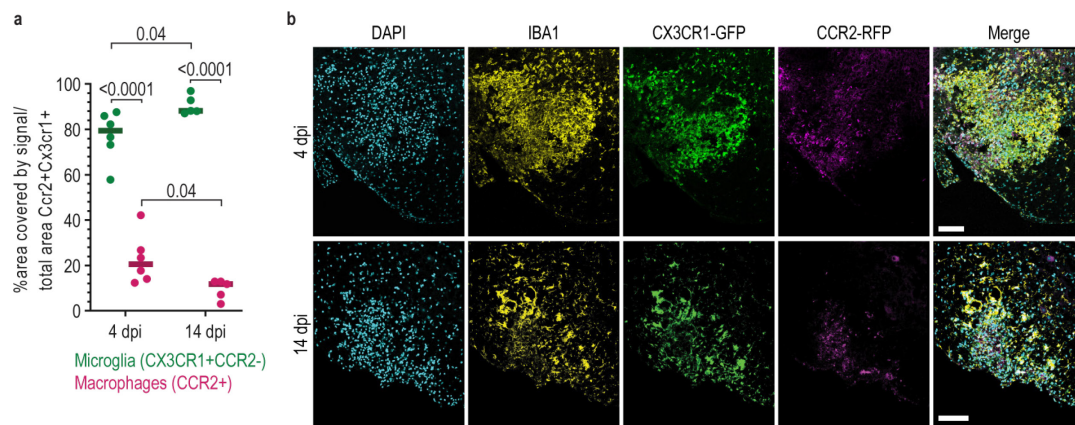


Figure 2.4: Microglia are the predominant CNS macrophage present in lysolecithin-driven demyelinated lesions. **a**, Quantification of the area covered by the CX3CR1+CCR2⁻ or CCR2⁺ signal in the demyelinated area at 4 and 14 dpi (one-way ANOVA followed by Sidak test to correct for multiple comparisons). **b**, Images of demyelinated spinal cord lesions from CX3CR1-GFP/CCR2-RFP reporter mice labelled with IBA1 and DAPI at 4 and 14 dpi. Scale bar: 100 μ m.

2.1.4.2. Methodology for lysolecithin injection in the corpus callosum

A solution of 1% LLC was prepared by mixing LLC (L4129, Sigma-Aldrich, Germany) with sterile 1X PBS. Monastral blue (274011, Sigma-Aldrich, Germany) was added to the LLC solution at a

concentration of 0.03% just before use to aid with visualization of the lesion during tissue processing. Mice were anaesthetized with an intraperitoneal injection of MMF solution. Then, head fur was cut away, the eyes were protected with bepanthene cream (1578847, Bayer, Germany) and a small incision was cut to expose the skull. The mouse was positioned into a stereotactic injection apparatus by accommodating the ears and the snout into the respective holders. A small hole was drilled at the injection coordinates (X: \pm 1.0 mm, Y: -0.1 mm from bregma). A glass capillary containing the LLC/monastral blue solution was then lowered to Z: -1.40 from bregma and 1 μ L was injected at a rate of 100 nL/minute. Two minutes after the delivery of LLC, the capillary was slowly retracted. The mouse was then injected with 0.05 mg buprenorphin/kgBW and the skin was sutured using serafit violet suture (DSS-13, USP4/0, EP1.5, 1088835, Spree Dental, Germany). Anaesthesia was terminated by a subcutaneous injection of AFN solution, containing 2.5 mg/kgBW atipamezol, 1.2 mg/kgBW naloxon and 0.5 mg/kgBW flumazenil.

2.1.4.3. Methodology for lysolecithin injection in the spinal cord

For the injection of LLC in the spinal cord, the mice were anesthetized, and the LLC prepared as above. Then, the mouse dorsal skin was shaved, and a 3 cm incision was performed to expose the thoracolumbar part of the vertebral column. The dorsal muscles and connective tissue between T11 and L2 were removed, thereby exposing the spinal cord. The capillary was positioned 0.5 mm lateral to the dorsal artery and lowered 1.5 mm into the tissue. The delivery of 1 μ L LLC was performed at a rate of 150 nL/min, and the retraction of the capillary was performed as stated above. The mouse was then injected with 0.05 mg buprenorphin/kgBW and the skin and muscle were sutured using serafit violet suture (DSS-13, USP4/0, EP1.5, 1088835, Spree Dental, Germany). Anaesthesia was terminated by a subcutaneous injection of AFN solution.

2.2. Histological analysis of lesioned and unlesioned mouse CNS tissue

2.2.1. Tissue preparation

To prepare samples for immunohistochemistry, mice were anaesthetized with an intraperitoneal injection of 10% ketamine/2% xylazine and perfused intracardially with 4% PFA with a peristaltic pump (Peri-Star PRO, World Precision Instruments, Germany). Either the brain or the spinal cord was removed, post-fixed in 4% PFA overnight and cryoprotected in 30% sucrose in 1X PBS. The tissue was embedded in Tissue-Tek O.C.T (4583, Sakura Europe, Germany), frozen on dry ice and kept at -80°C until sectioning.

To section the injected brains and spinal cords, a cryostat (CryoStar NX70, Thermo Scientific, Germany) was used to cut 16 μ m-thick coronal sections, which were directly mounted on Superfrost Plus slides (10149870, Thermo Scientific, Germany) in a serial manner. The lesions were identified by the presence of monastral blue. To section unlesioned brains, we collected 30 μ m-thick sagittal sections and kept them free-floating in a cryoprotecting solution at -20°C . All sections were kept at -20°C until further processing.

2.2.2. Immunohistochemistry

To stain the sections for lipidic antigens (e.g. PLIN2, Fluoromyelin), the sections were first dried at 37°C for 30 minutes, rinsed with 1X PBS and permeabilized for 10 minutes in 1X PBS containing 0.3% Triton X (T8787, Sigma-Aldrich, Germany). To prevent non-specific binding, sections were incubated for 1 hour with blocking solution. Primary antibodies were diluted in staining solution and incubated overnight at 4°C. The next day, the sections were further incubated with primary antibodies for 1 hour at RT, washed with 1X PBS, and subsequently incubated with secondary antibodies (1:1000) for 2 hours. After washing with 1X PBS, the sections were incubated with Fluoromyelin (1:400, F34651 Invitrogen, Thermo Fisher Scientific, Germany) and DAPI (1:1000, D1306, Thermo Fisher Scientific, Germany) in 1X PBS for 15'. The sections were then washed in 1X PBS, in distilled water and then mounted with mowiol.

To stain the sections with non-lipidic antigens, permeabilization was performed by using 1X PBS with 1% triton X for all solutions (blocking solution, staining solution) and for washes. For stainings with antibodies produced in mice, we added a Fab fragment-blocking step (715-007-003, Jackson ImmunoResearch, Germany) before adding the blocking solution. All steps were performed at room temperature (RT) unless stated otherwise.

2.2.3. Fluorescent in situ hybridization (FISH)

The RNAscope Multiplex Fluorescent v2 Assay (323100, Advanced Cell Diagnostics Inc., USA) was performed according to the manufacturer's instructions for fixed frozen tissue. 16 µm-thick brain sections were hybridized with two mRNA probes (RNAscope Probe-Mm-Tgfb1, Cat. No. 407751; RNAscope Probe-Mm-Tgfb2-C2, Cat. No. 406181-C2, Advanced Cell Diagnostics, Inc. USA) per experiment. Additionally, the negative control probe (RNAscope 3-Plex Negative Control Probe, Cat. No. 320871, Advanced Cell Diagnostics, Inc. USA) and the positive control probe (RNAscope 3-plex Positive Control Probe_Mm, Cat. No. 320881, Advanced Cell Diagnostics, Inc. USA) were used in some sections, to assure the specificity and the sensitivity of the signal. The target probes were also combined with immunofluorescence for IBA1 and GFAP-ALDH1L1, in order to determine which cells express the genes of interest.

2.2.4. Confocal microscopy

Optical sections were acquired with a confocal laser-scanning microscope (Leica TCS SP5, Leica Microsystems, Germany) using the 20xAir/0.75NA and the 63xOil/1.40NA objectives. The z-step in z-stacks was kept at 1 µm. The different fluorophores were stimulated sequentially using the following laser lines: 405 nm for DAPI, 488 nm for Alexa Fluor 488 (AF488) and YFP, 561 nm for Alexa Fluor 555 (AF555) and tdTomato and 633 nm for Alexa Fluor 647 (AF647). The emitted light was collected by photo multiplier tubes (PMT) detectors. For these, the gain was maintained between 700 and 800 V, and the smart offset between -0.05 and -0.35.

The scanning speed was set to 600 Hz and the bit depth to 16 Bit. The pixel size was variable, but the format of the images was either 512x512 or 1024x1024 pixels, with either 1X or 2X zoom. The pinhole was kept at 1 AU, except in the cases where it was necessary to collect more light, where the pinhole was opened to a maximum of 1.3 AU. Furthermore, a 4X line average was used to increase

the signal to noise ratio. The tiles of a tile scan were stitched automatically using the Leica Application Suite AF software (Leica Microsystems, Germany), at the settings of low speed and high precision, and without smoothing the signal between tiles. All settings were kept constant throughout the imaging of one same experiment and were kept similar among similar analysis in different experiments.

To control for possible effects of the monastral blue dye on the stainings, the transmitter light from the laser line 633 nm was also collected. This way, the accumulations of blue dye could be observed, and its signal ignored during manual quantification of myelin- and crystal- loaded cells. To image cholesterol crystals, we acquired the reflected light of the 458 nm laser line sequentially as an additional acquisition channel, as previously described (Duewell et al., 2010).

2.2.5. Image analysis

All analyses were performed in a blinded manner. For all cases, at least three different areas of interest from three different mice were imaged and used for quantification. For details on the custom-made macros, please refer to the section 3 of the Appendix.

The quantifications of microglia density, CLEC7A⁺ microglia, AXL⁺ microglia and MAC2⁺ microglia were performed by manually counting the positive cells in tile scans of the unlesioned corpus callosum. Analysis of the IBA1 signal intensity was performed automatically using a custom-made macro in Fiji. Quantification of lipid droplets within microglia cells was performed manually using Imaris (Bitplane, United Kingdom) in order to be able to observe and analyse the structures in 3D.

To quantify the demyelination volume and the IBA1⁺ volume, the area of demyelination shown by negative Fluoromyelin staining and the area of clustered IBA1⁺ cells, respectively, was measured in consecutive sections of a lesion using a custom-made macro in the Fiji software. Consecutive sections were separated by a known distance thanks to serial sectioning of the tissue. The volume between two consecutive sections was measured according to the truncated cone model. The whole lesion volume was the sum of the single volumes between all sections of the lesion. The formula used for the total volume calculation was the following:

$$V = \sum_{i=1}^{n-1} \frac{1}{3} \pi (r_i^2 + r_{i+1}^2 + r_i r_{i+1}) d$$

Where n is the number of sections.

This formula was applied to the measured lesion areas in an automated fashion using IPython 2.7 (Perez and Granger, 2007). The code is openly available at https://github.com/lenkavaculciakova/lesion_volume.

For the quantification of myelin-loaded IBA1⁺ cells, crystal-loaded IBA1⁺ cells, MAC2⁺IBA1⁺ cells and MHCII⁺IBA1⁺ cells in the demyelinated lesions, the cells were counted manually in high magnification images of the lesion using the Cell Counter plug-in in Fiji. For analysis of pSMAD2,

LAMP1, CD68 and ARG1 signal in the lesions, the percentage area of the lesion occupied by particular signal was quantified in an automated fashion using a custom-made macro in Fiji.

For the quantification of the *Tgfb1* and *Tgfb2* mRNA particles in the fluorescence in situ hybridization, the positive particles were quantified either in the area of interest or in the mask created by the IBA1⁺ or GFAP⁺ALDH1L1⁺ signal using a custom-made macro using Fiji.

2.3. Electron Microscopy

2.3.1. Sample preparation

For electron microscopy (EM), mice were intracardially perfused with EM fixative for 5 minutes, the brain or spinal cord dissected, and then post-fixed overnight in EM fixative. If one same brain was to be used for both histological and EM analysis, mice were perfused with 4% PFA in 1X PB for 5 minutes, the brain or spinal cord were dissected and the sample to be analysed by EM was post-fixed for two nights in EM fixative.

For better infiltration of the tissue with fixative, 200 µm-thick sections were cut with a vibratome (Leica Microsystems, Germany) either freshly or after one day in fixative. For vibratome sectioning of the spinal cord, the tissue was embedded in 15% gelatine to obtain more stability. Two days after perfusion, the EM fixative was washed away with 0.1 M cacodylate buffer. Then, the region of interest was isolated by punching a 1.5 mm-wide circle or cutting a 2 mm x 2 mm square. In cases where the region of interest was a demyelinated lesion, the lesion was recognised thanks to the monastral blue injected together with LLC. Finally, the region of interest was wrapped in a small square of filter paper (from a tea bag) and inserted into the moulds for automatic tissue processing.

Lesion samples were processed in a tissue processor (Lynx, Science Services, Germany) starting with washes in 0.1 M sodium cacodylate buffer and post-fixation in reduced osmium. After several washing steps, the samples were contrasted en bloc with uranyl acetate, dehydrated, infiltrated and embedded in epon resin (Serva, Germany). The samples were flat embedded into gelatine capsules (Science Services, Germany) and cured for 48 hours at 60°C.

2.3.2. Sample sectioning and imaging

Blocks were sectioned on a Leica UC7 ultramicrotome using a 35° ultra diamond knife (Diatome, Switzerland) at thicknesses of 50 nm for transmission EM, 100 nm for scanning EM and 200 nm sections for light microscopy. The latter were stained using a methylene blue and azur blue stain mixed in equal amounts. Sections were imaged on a slide scanner with a 40x objective (Pannoramic MIDI II 2.0.5, 3DHISTOTEC, Germany).

For scanning electron microscopy, sections were collected onto plasma-treated CNT tape (Science Services, Germany) and mounted onto 1-inch silicon wafers (Siegert Wafer, Germany) using adhesive carbon tape (Science Services, Germany). For grounding we attached additional adhesive carbon tape strips (Science Services, Germany) between CNT tape and wafer. EM micrographs were acquired on a Crossbeam Gemini 340 SEM (Zeiss, Germany) with a four-quadrant backscatter detector at 8 kV. In ATLAS5 Array Tomography (Fibics, Canada), the wafer area was scanned at 3000 nm/pixel to

generate an overview map. The entire section areas were scanned at 50x50 nm² and the lesion area at 10x10 nm².

2.3.3. Image analysis from EM micrographs

Sections imaged by light microscopy were used to analyse foam cells in the lesion and lipid droplets in the ventricle. Foam cells were quantified by manual counting and normalized to the lesion area using the CaseViewer software (3DHISTOTEC, Germany). Lipid droplets in the ventricle wall were recognized as green-labelled, circular structures and were manually counted and normalized to ventricle length using the same CaseViewer software (3DHISTOTEC, Germany).

To quantify the amount of foam cells in the lesions in old mice treated with 4D9 or IgG isotype control, which were imaged by scanning EM, the number of foam cells was manually counted using Fiji (Schindelin et al., 2012) and normalized to the lesion area. In the case of WD-fed mice treated with 4D9 or isotype control, it was harder to distinguish one foam cell from the other, thus, the area occupied by lipid droplet-, myelin debris- containing cells was quantified using Fiji (Schindelin et al., 2012) and normalized to the lesion area. To quantify remyelination, the number of axons surrounded by a thin myelin sheath was manually counted and normalized to the lesion area, also using Fiji (Schindelin et al., 2012).

2.4. In vitro analysis

2.4.1. Myelin purification

Myelin was isolated from 8-week-old C57BL/6J mouse brains were homogenized by sonication in 10 mM HEPES buffer (pH 7.4). The homogenate was layered on a sucrose gradient of 0.32 M and 0.85 M sucrose and centrifuged at 25,000 rpm for 38 minutes with a SW32Ti rotor (Beckman Coulter, Germany). The crude myelin fraction was carefully isolated from the interface and subjected to three rounds of osmotic shock by dissolving it in ddH₂O and centrifuging first at 25,000 rpm, then at 10,000 rpm for 18 minutes. The resulting pellet was again laid on a sucrose gradient and the same procedure was repeated to purify myelin. The yield of myelin was calculated by measuring the total amount of protein with the Bradford assay (500-0006, Biorad, USA). Before addition to the cell culture media, myelin was re-suspended by passing the solution through a 25G needle. For further details on buffer preparation, please refer to the protocol in the section 4 of the Appendix.

2.4.2. Preparation of L929-conditioned media

L929 cells are a fibroblast cell line derived from mouse adipose tissue. They secrete MCSF, a factor that is essential for microglia survival and growth in culture after isolation, thus; we normally used L929-conditioned media to culture our microglia. To prepare L929-conditioned media, cells from the L929 cell line were cultured in the DMEM containing 10% BCS (SH30073.03HI, GE Healthcare Life Sciences, USA), 1 mM sodium pyruvate (11360039, Thermo Fisher Scientific, Germany), GlutaMAX™ (35050038, Thermo Fisher Scientific, Germany) and 1% penicillin/streptavidin (15070063, Thermo Fisher Scientific, Germany), and split 3 times to obtain a large-scale L929 culture in 175-cm² flasks. The confluent cells were incubated for 2 weeks. Then, the conditioned medium

was collected, passed through a 0.22 μm vacuum filter (S2GPU05RE, Merck Millipore, Germany) and the aliquots were stored at $-20\text{ }^{\circ}\text{C}$.

2.4.3. Primary microglia cultures

Primary microglia cultures were prepared from p7-p10 C57BL/6J mouse brain. The brains were homogenized using the neural tissue dissociation kit with papain (130-092-628, Miltenyi Biotech, Germany) and the resulting homogenate was filtered through a 70 μm cell strainer (352350, neoLab, Germany) to obtain a single cell suspension. Then, CD11b⁺ cells were labelled using magnetic beads and isolated using a magnetic column. Microglia were kept in DMEM supplemented with 10% bovine calf serum (SH30073.03HI, GE Healthcare Life Sciences, USA), 20% L929-conditioned media, 1% penicillin/streptomycin (15070063, Thermo Fisher Scientific, Germany) and 1% sodium pyruvate (11360039, Thermo Fisher Scientific, Germany) for 4-7 days before using them for experiment.

To analyse the influence of TGF β on the gene expression changes upon myelin treatments, the media was removed, and the microglia washed twice with DMEM. Then, microglia were cultured in DMEM supplemented with 1% penicillin/streptomycin, 1% glutamate and 3 mg/mL of lipoprotein-deficient serum (LP4, Merck, Germany) with or without TGF β 2 (100-35B-2, PreproTech, US) for 16 hours. Next, purified myelin was added to the media at a concentration of 8 $\mu\text{g}/\text{mL}$ for 2 hours. After washing the cells twice, the cells were kept for further 4 or 24 hours with the corresponding media.

To analyse the effect of myelin on TREM2, primary microglia were treated with myelin (5 or 30 $\mu\text{g}/\text{mL}$) or LPS (1 $\mu\text{g}/\text{mL}$) for 24 hours. To analyse the effect of the antibody 4D9 on TREM2, primary microglia cells were pre-treated with 20 $\mu\text{g}/\text{mL}$ of 4D9 cloned into a human backbone and the isotype control antibody for 16 hours. Next, myelin was added to the cells for an additional 24 hours, the media was cleared of debris by centrifugation and 100 μL of the media were collected for the ELISA assay.

2.5. Tissue processing and cell isolation

2.5.1. Tissue processing to isolate lesion material for post-processing

To obtain enough lesion material for downstream RNA and sterol analysis, we injected LLC in four different sites in the corpus callosum. The injection coordinates from bregma were the following: X: -/+ 1.0 mm, Y: -0.1 mm, Z: -1.40 mm and X: -/+ 0.55 mm, Y: -1.22 mm, Z: -1.40 mm. At the desired timepoint, mice were euthanized by cervical dislocation and the brain was isolated. Using a vibratome (Leica Microsystems, Germany), 400 μm sections were cut at a speed of 1 mm/s. The lesion was localized thanks to the monastral blue dye administered together with the LLC during injection. The lesion was then further dissected using fine blades, transferred into a centrifuge tube, flash frozen in dry ice and kept at -80°C .

2.5.2. Microglia isolation from adult mice

To isolate microglia from adult mouse brain for bulk RNA sequencing, mice were euthanized by cervical dislocation, the brain was dissected out and the meninges removed. Then, the brain was dissociated into a single-cell suspension by combining the enzymatic effect of the Neural Tissue Dissociation Kit with papain (130-092-628, Miltenyi Biotech, Germany) and mechanical dissociation

with glass-polished pipettes of three different sizes. Then, the suspension was filtered through a 70 µm cell strainer and centrifuged to pellet the cells. Next, microglia were labelled using magnetically labelled CD11b antibodies and isolated through a magnetic column. Finally, myelin debris was removed by creating a Percoll gradient. Shortly, microglia were re-suspended in 37% Percoll solution (17-0891-01, GE Health Care) in DMEM, overlaid with a 70% Percoll solution in DMEM, and centrifuged at 500 xg for 30 minutes without break or acceleration. Then, the cells were washed with 1X PBS, lysed with RTL Buffer (from the RNeasy Plus Mini Kit, 74134, Qiagen, Germany) and flash-frozen in liquid nitrogen.

To isolate microglia from adult mouse brain for ATAC sequencing, mice were perfused with 1X PBS, the brain dissociated and processed as described above. In this case, the cells were counted after magnetic isolation of microglia and an aliquot containing 50,000 cells was isolated, pelleted and flash-frozen in liquid nitrogen. The samples were sent to our collaborators, who performed the downstream ATAC sequencing analysis.

2.6. Molecular Biology analysis of tissue and cells

2.6.1. RNA isolation and RT-qPCR

Total RNA was isolated from either lesions, unlesioned brain tissue or primary microglia cultures following the manufacturer's instructions of the RNeasy plus mini kit (74134, Qiagen, Germany). The isolated RNA was retrotranscribed with the superscript III first-strand synthesis system (18080051, Invitrogen, Germany) using 100 ng to 1 µg of total RNA and random hexamers as primers. Quantitative PCR was performed using the PowerUp SYBR Green Master Mix (A25742, Applied Biosystems, Germany) on a LightCycler 480 Real-time PCR system (Roche, Germany). All qPCR reactions were run in triplicates. The housekeeping gene *Rplp0* was used for brain samples, while *Cyc1* was used for microglia cultures.

2.6.2. Sterol quantification

Sterols and oxysterols were extracted from isolated lesions by chloroform/methanol (1/1;v/v), dried under nitrogen and the residual sterols/oxysterols were silylated to their corresponding trimethylsilylethers. Cholesterol precursors such as lathosterol, lanosterol, dihydro-lanosterol, and desmosterol, together with the cholesterol metabolite 5 α -cholestanol and the phytosterols, campesterol and sitosterol, were determined by gas chromatography-mass spectrometry selected ion monitoring (GC-MS-SIM), using epicoprostanol as internal standard. 24S- and 27-hydroxycholesterol were measured by isotope dilution mass spectrometry. Data are given as amount of oxysterol/cholesterol per whole sample volume.

2.6.3. Western Blot

Cells were collected and resuspended in RIPA buffer. Cell lysates were cleared of cellular debris by centrifugation at 15,000 rpm for 5 minutes and equal amounts of protein were separated by SDS-PAGE on 12.5% Acrylamide gels and transferred to 0.45 µm nitrocellulose membranes. The membranes were incubated with blocking solution, incubated with primary antibodies overnight at 4°C in blocking solution and washed with TBST three times. The membranes were then incubated

with horseradish peroxidase–conjugated secondary antibodies for 1 hour at room temperature. After washing in TBST, the membranes were visualized using an enhanced chemiluminescence system (32106, Pierce, US).

To measure the amount of soluble TREM2, the media of the treated cells was collected and centrifuged at 3,200g for 20 minutes to remove cell and myelin debris. The media was then concentrated with Amicon Ultra-4 10kDa Centrifugal Filter Units (UFC801024, Merck, Germany) and equal volumes were loaded on 12.5% acrylamide gels and run as described above.

2.6.4. Enzyme-linked immunosorbent assay

Levels of sTREM2 in conditioned media from primary microglia upon treatment with myelin at varying concentrations and 20 µg/mL TREM2-enhancing antibody 4D9 or isotype control antibody were quantified by MSD ELISA as previously described (Schlepckow et al., 2020). Samples were diluted 1:4 in sample buffer before loading onto the MSD plate.

2.7. Lipidomics analysis

To analyse the lipid profile on plasma and brain samples, we performed quantitative shotgun lipidomics. This technology allowed us to quantify around 700 lipid species and their lipid features such as fatty acyl chain length, hydroxylation and number of acyl chain double bonds.

2.7.1. Lipid extraction for mass spectrometry lipidomics

To obtain plasma for lipidomics analysis, we collected blood from the heart using an EDTA-coated 1 mL syringe attached to a 25G needle, which we introduced directly into the left ventricle of the heart. The blood was then transferred into an EDTA-coated tube and centrifuged at 2,000 xg for 10 minutes at 4°C to obtain plasma. We collected all plasma possible and flash-froze it in liquid nitrogen. For lipidomics analysis of white and grey matter of the brain, mice were perfused with sterile 1X PBS (10010-056, Thermo Fisher Scientific, Germany) for 3 minutes. Then, the brain was isolated and transferred into a glass dish with 1X PBS. Under a stereoscope (Leica KL 3000 LED, Leica Microsystems, Germany), the white and grey matter were dissociated using a combination of forceps and blades. Finally, the tissue was weighed and homogenized in sterile 1X PBS (10010-056, Thermo Fisher Scientific, Germany) at a concentration of 5 mg/mL using a Dounce homogenizer. The solution was snap-frozen in liquid nitrogen and kept at -80°C until downstream analysis.

Mass spectrometry-based lipid analysis was performed by Lipotype GmbH (Dresden, Germany) as described elsewhere (Sampaio et al., 2011). Lipids were extracted using a two-step chloroform/methanol procedure (Ejsing et al., 2009). Samples were spiked with internal lipid standard mixture containing: cardiolipin 16:1/15:0/15:0/15:0 (CL), ceramide 18:1;2/17:0 (Cer), diacylglycerol 17:0/17:0 (DAG), hexosylceramide 18:1;2/12:0 (HexCer), lyso-phosphatidate 17:0 (LPA), lyso-phosphatidylcholine 12:0 (LPC), lyso-phosphatidylethanolamine 17:1 (LPE), lyso-phosphatidylglycerol 17:1 (LPG), lyso-phosphatidylinositol 17:1 (LPI), lyso-phosphatidylserine 17:1 (LPS), phosphatidate 17:0/17:0 (PA), phosphatidylcholine 17:0/17:0 (PC), phosphatidylethanolamine 17:0/17:0 (PE), phosphatidylglycerol 17:0/17:0 (PG), phosphatidylinositol 16:0/16:0 (PI), phosphatidylserine 17:0/17:0 (PS), cholesterol ester 20:0 (CE),

sphingomyelin 18:1;2/12:0;0 (SM), triacylglycerol 17:0/17:0/17:0 (TAG) and cholesterol D6 (Chol). After extraction, the organic phase was transferred to an infusion plate and dried in a speed vacuum concentrator. 1st step dry extract was re-suspended in 7.5 mM ammonium acetate in chloroform/methanol/propanol (1:2:4, V:V:V) and 2nd step dry extract in 33% ethanol solution of methylamine in chloroform/methanol (0.003:5:1; V:V:V). All liquid handling steps were performed using Hamilton Robotics STARlet robotic platform with the Anti Droplet Control feature for organic solvents pipetting.

2.7.2. MS data acquisition

Samples were analysed by direct infusion on a QExactive mass spectrometer (Thermo Fisher Scientific, US) equipped with a TriVersa NanoMate ion source (Advion Biosciences). Samples were analysed in both positive and negative ion modes with a resolution of $R_{m/z=200}=280,000$ for mass spectrometry and $R_{m/z=200}=17,500$ for MSMS experiments, in a single acquisition. MSMS was triggered by an inclusion list encompassing corresponding mass spectrometry mass ranges scanned in 1 Da increments (Surma et al., 2015). Both mass spectrometry and MSMS data were combined to monitor CE, DAG and TAG ions as ammonium adducts; PC, PC O-, as acetate adducts; and CL, PA, PE, PE O-, PG, PI and PS as deprotonated anions. Mass spectrometry only was used to monitor LPA, LPE, LPE O-, LPI and LPS as deprotonated anions; Cer, HexCer, SM, LPC and LPC O- as acetate adducts and cholesterol as ammonium adduct of an acetylated derivative (Liebisch et al., 2006).

2.7.3. MS data analysis and post-processing

Data were analysed with an in-house developed lipid identification software based on LipidXplorer (Herzog et al., 2011). Data post-processing and normalization were performed using an in-house developed data management system. Only lipid identifications with a signal-to-noise ratio >5 and a signal intensity 5-fold higher than in corresponding blank samples were considered for further data analysis.

2.8. Short- and medium-length fatty acid analysis

To quantify short- and medium-length fatty acids (SCFA, MCFA), caecum content and plasma from portal vein blood were collected. Portal vein blood was collected as previously described (Goddard et al., 2016) into a EDTA-coated tube and centrifuged at 2,000 xg for 10 minutes at 4°C to obtain plasma. For caecum content, the caecum was cut open and its contents transferred into a centrifuge tube. Both samples were snap frozen in liquid nitrogen and kept at -80°C until analysis.

To analyse the short- and medium-length fatty acids in these samples, we used gas chromatography-mass spectrometry (GC-MS) to quantitatively monitor fatty acid composition according to previously described protocols (Hoving et al., 2018b, 2018a).

2.9. Bulk RNA sequencing analysis of microglia

Bulk RNA sequencing was performed as previously described (Safaiyan et al., *submitted*). Shortly, 1µg of cDNA was used as input for IonXpress™ Plus Fragment Library Kit (ThermoFisher Scientific, Germany) to generate barcoded libraries. Barcoded libraries were then quantified using qRT-PCR (KAPA Library Quantification Kit), pooled, clonally amplified on Ion Spheres (Ion One Touch 200

Template Kit v2, ThermoFisher Scientific, Germany) and sequenced on an Ion Proton sequencer (ThermoFisher Scientific, Germany). Raw reads were sorted based on barcodes and were subjected to quality analysis using FASTQC. The sequences were subsequently aligned to the genome of *Mus musculus* (GRCm38/Mm10) using the TMAP aligner with default parameters. The reads mapping to unique locations were quantified using RefSeq Gene Annotations(v73) into genes. Differential gene expression analysis and hypergeometric pathway analysis using KEGG gene sets was performed using a commercial platform (Partek). Genes with fold change greater than 2 and p-values less than 0.05 were considered for further hypergeometric pathway enrichment analysis.

2.10. Statistical analysis

Statistical analysis was performed with GraphPad Prism (GraphPad Software, Inc.). The number of animals and cell cultures used for the experiments are indicated as single dots in all graphs or indicated in the figure legends. Normality tests confirmed the normal distribution of our data. Thus, to compare two groups, a two-tailed Welch's t-test was applied. For comparison of more than two groups, one-way Brown-Forsythe and Welch ANOVA followed by Dunnett's T3 multiple comparisons post hoc test was performed. For comparing the interference between two variables, we used two-way ANOVA followed by Tukey test for multiple comparison correction. For measuring statistical differences in RT-qPCR results, the DDCT method was employed and the DDCT values were subjected to the test. A p-value of ≤ 0.05 was considered significant in all cases. Measurements were taken from distinct samples; meaning that no samples were measured repeatedly.

Results

In this study, we hypothesized that WD influences remyelination by perturbing the brain microenvironment and microglia metabolic functions. In this section, the results of our analysis are disclosed. First, we focus on characterising the influence of WD intake on the lipid profile of plasma and brain and on microglia function during homeostasis. Second, we examine how WD consumption influences microglia's response to demyelination and remyelination efficiency. Then, we explore different mechanisms that could underlie poor lipid processing by microglia in WD-fed mice. Finally, we describe how different genetical and pharmacological approaches can rescue the phenotype we observe in WD-fed mice.

1. Characterisation of western diet-fed mice

First, we wanted to understand how our model of obesity, based on WD consumption, would affect the CNS. More specifically, we were interested in investigating the changes that WD would cause in the lipid composition of the plasma and brain and in microglia's function during homeostasis.

1.1. The consequences of WD consumption on the lipid profile in plasma and in the CNS

1.1.1. The plasma lipid profile is profoundly altered by western diet

To understand the influence of WD on the plasma lipid profile, we performed quantitative shotgun lipidomics on plasma samples from CD- and WD-fed mice. Indeed, the principal component analysis (PCA) clearly segregated the samples from the two groups, demonstrating a strong influence of WD on the plasma lipidome (Fig. **3.1a**). Plasma from WD-fed mice was characterized by higher proportions of cholesterol esters (CE) and phosphatidylcholine (PC) and lower proportions of triacylglycerides (TAG) (Fig. **3.1b**). Furthermore, the lipid acyl chains from WD-fed mice plasma were of shorter length and increased saturation (Fig. **3.1c,d**), which correlates to the properties of the lipids in WD. The total amount of lipids in the sample was not significantly changed in plasma from WD-fed mice, however; a slight trend could be observed (Fig. **3.1e**). We filtered the top 33 significantly changed lipid species (fold higher than 2.5, p-value smaller than 0.01) and confirmed the high CE and PC content and the low TAG and polyunsaturated lipids content (Fig. **3.1f**) (e.g. TAG_{54:6:0}, TAG_{52:4:0}, TAG_{54:4:0}).

Previous reports have shown that a change of diet can profoundly alter the composition of gut microbiota (Erny et al., 2015; Fleck et al., 2017). One of the functions of gut microbiota is to degrade the fibre content in the diet, which produces SCFAs as side product. Reports have demonstrated that upon HFD or WD consumption, the production of SCFA decreases (den Besten et al., 2015). However, it is important to note that several studies failed to control for the initial amount of fibre in the diet, leading to confounding factors in their results (Dalby et al., 2017). In our case, we controlled for fibre content in the diet by using a CD containing as much fibre as the WD and sought to determine whether the high-calorie, high-sugar and high-fat properties of the WD interfered with SCFA production. For this, we collected portal vein blood plasma and caecum samples from CD-

Results

and WD-fed mice and run a short- and medium-length fatty acid analysis. We found that the production of butyric acid (FA 04:0b) was reduced by half in the caecum samples from WD-fed mice, while the acetic acid (FA 02:0) production was only slightly reduced (Fig. 3.1h). The decrease in butyric acid persisted in the portal vein blood (Fig. 3.1g). Furthermore, we confirmed the high amounts of medium-length saturated fatty acids and low amounts of long-chain unsaturated fatty acids in WD-fed mice that we previously observed in our peripheral blood plasma lipidomics (Fig. 3.1g).

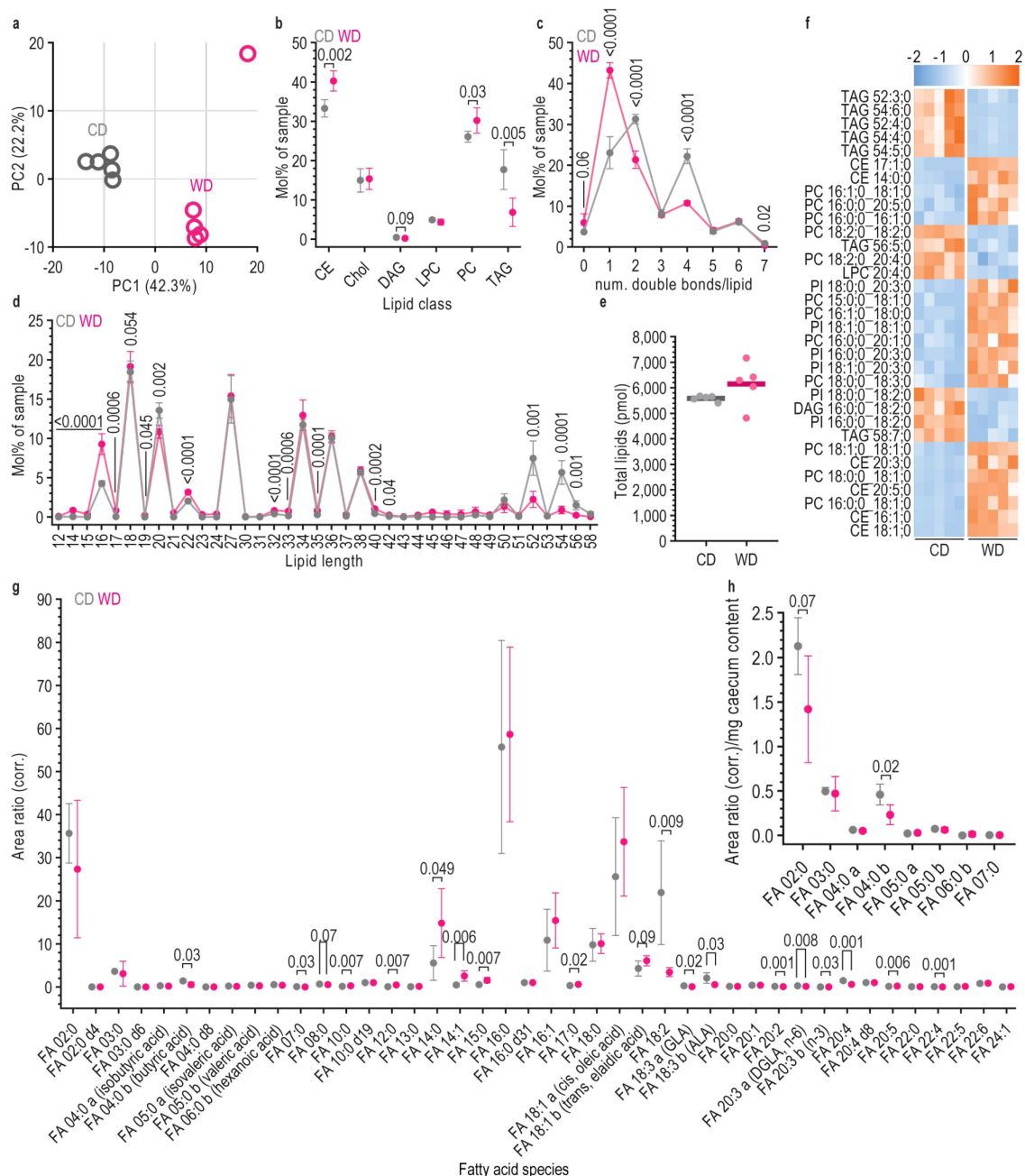


Figure 3.1: The plasma lipidome is profoundly altered by western diet. a, PCA analysis of CD and WD plasma samples. **b**, Percentage of the sample occupied by the different lipid classes in CD- and WD-fed mice (mean±SD, two-tailed Welch's t-test). **c,d**, Percentage of each sample with lipids containing a certain number of double bonds (**c**) or a certain acyl chain length (**d**) (mean±SD, two-tailed Welch's t-test). **e**, Total amount of lipids in plasma from CD- and WD-fed mice (solid lines indicate the mean, two-tailed Welch's t-test). **f**, Heatmap showing the significantly (p value ≤ 0.01 ,

fold ≥ 2.5) changed lipid species in plasma from CD- and WD-fed mice. Scale indicated above the heatmap. Increased values are indicated in orange, while decreased values are in blue. The lipid class label indicates the lipid class, the number of carbons, the number of double bonds, and the number of hydroxyl groups. **g**, Corrected area ratio occupied by each fatty acid species in plasma isolated from portal vein blood (mean \pm SD, two-tailed Welch's t-test). The fatty acid class label indicates the number of carbons and the number of double bonds. **h**, Corrected area ratio of each fatty acid species corrected by the mass of caecum (mean \pm SD, two-tailed Welch's t-test). The fatty acid class label indicates the number of carbons and the number of double bonds, as well as their name between brackets. P-values below 0.1 are indicated in the figure. N numbers are 5 for each group, except for **e** where the n number for WD is 4. PCA: principal component analysis, CD: control diet, WD: western diet, CE: cholesterol esters, Chol: cholesterol, DAG: diacylglycerol, LPC: lysophosphatidylcholine, PC: phosphatidylcholine, TAG: triacylglycerides, PI: Phosphatidylinositol, FA: fatty acid, GLA: γ -linoleic acid, ALA: α -linoleic acid, DGLA: Dihomo- γ -linoleic acid, n-3: ω 3 fatty acid, n-6: ω 6 fatty acid.

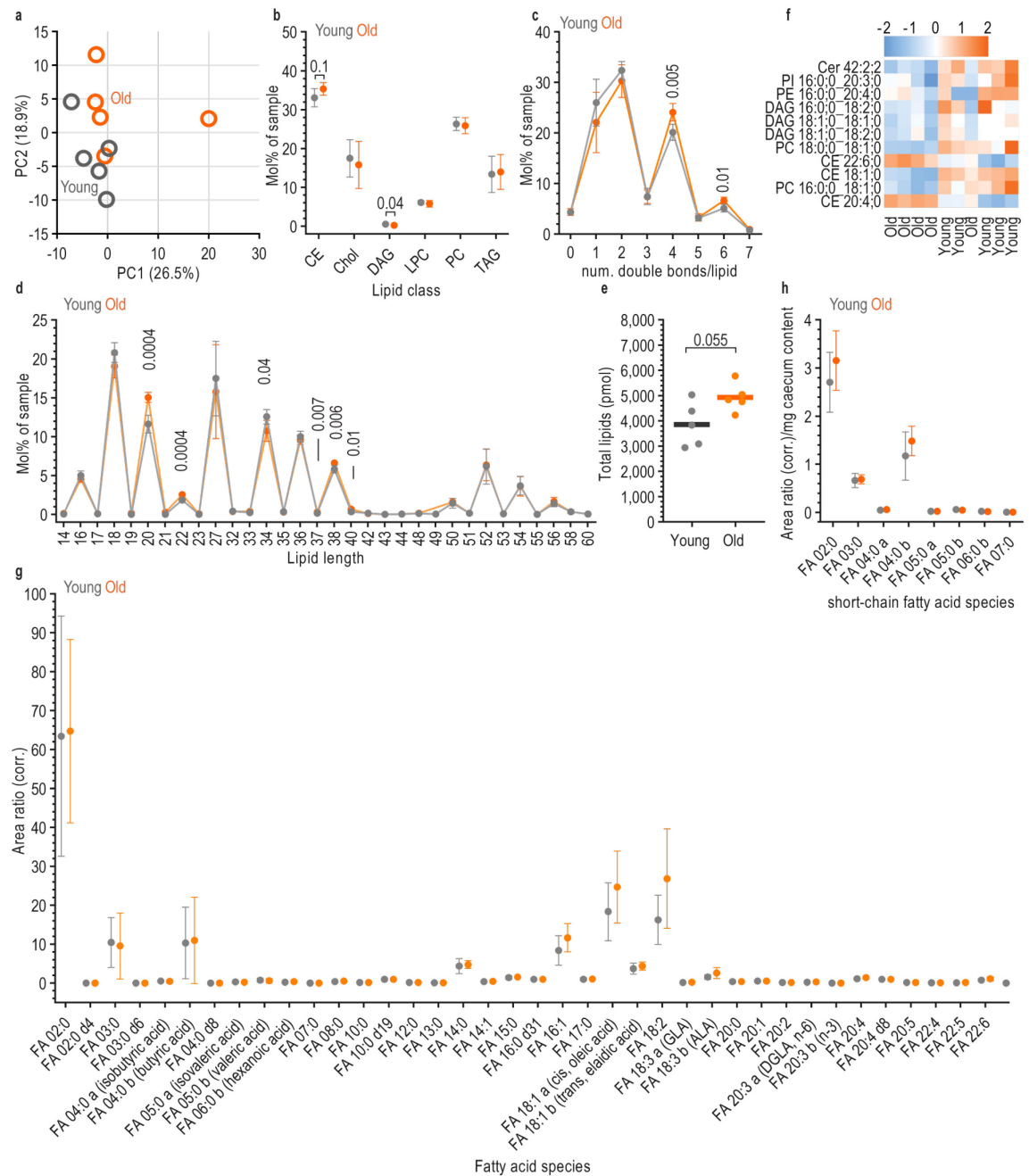


Figure 3.2 (previous page): The plasma lipidome is not altered by age. **a**, PCA analysis of young and old plasma samples. **b**, Percentage of the sample occupied by the different lipid classes in young and old mice (mean \pm SD, two-tailed Welch's t-test). **c,d**, Percentage of each sample with lipids containing a certain number of double bonds (**c**) or a certain acyl chain length (**d**) (mean \pm SD, two-tailed Welch's t-test). **e**, Total amount of lipids in plasma from young and old mice (solid lines indicate the mean, two-tailed Welch's t-test). **f**, Heatmap showing the significantly (p value ≤ 0.05 , fold ≥ 1.3) changed lipid species in plasma from young and old mice. Scale indicated above the heatmap. Increased values are indicated in orange, while decreased values are in blue. The lipid class label indicates the lipid class, the number of carbons, the number of double bonds, and the number of hydroxyl groups. **g**, Corrected area ratio occupied by each fatty acid species in plasma isolated from portal vein blood (mean \pm SD, two-tailed Welch's t-test). The fatty acid class label indicates the number of carbons and the number of double bonds. **h**, Corrected area ratio of each fatty acid species corrected by the mass of caecum (mean \pm SD, two-tailed Welch's t-test). The fatty acid class label indicates the number of carbons and the number of double bonds, as well as their name between brackets. P-values below 0.1 are indicated in the figure. N numbers are 5 for each group. PCA: principal component analysis, CE: cholesterol esters, Chol: cholesterol, DAG: diacylglycerol, LPC: lysophosphatidylcholine, PC: phosphatidylcholine, TAG: triacylglycerides, PI: Phosphatidylinositol, FA: fatty acid, GLA: γ -linoleic acid, ALA: α -linoleic acid, DGLA: Dihomo- γ -linoleic acid, n-3: ω 3 fatty acid, n-6: ω 6 fatty acid.

To understand whether age led to similar changes in the lipid profile in plasma, we analysed the lipidome in plasma samples isolated from 12-month-old (old) mice and compared them to 2-month-old (young) mice. Although we observed no differential clustering in the PCA (Fig. 3.2a), the proportion of diacylglycerol (DAG) was significantly reduced by half in old mice, and the levels of CE were slightly increased, although the differences were not significant (Fig. 3.2b). No clear trends were observed regarding the length or saturation of lipid acyl chains (Fig. 3.2c,d); however, we detected a 1.25 fold increase in the absolute content of lipids in the plasma from old mice (Fig. 3.2e), although this result did not reach significance (p -value = 0.055). Upon analysis of the SCFA content in the portal vein blood plasma and caecum content, we didn't detect any differences (Fig. 3.2g,h). For reference, we demonstrate the significantly increased lipid species (p value ≤ 0.05 , fold ≥ 1.3) in a heatmap, where we also do not observe differential clustering of the samples (Fig. 3.2f).

Hence, consumption of a WD in mice profoundly alters the plasma lipidome and SCFA production, while age seems to have a much more discrete effect on the plasma lipid composition.

1.1.2. The changes in the plasma lipid profile result in changes in the lipid composition in the CNS

Next, we wanted to determine the influence of WD consumption on the lipid profile in the CNS. It is known that WD induces lipid alterations in peripheral organs such as liver and adipose tissue (Aguilera et al., 2008; Fabbrini et al., 2008; Fu et al., 2011). However, it is still unclear whether and how WD affects the lipid composition of the CNS, which is shielded by the blood-brain barrier. Thus, we isolated brain white matter and grey matter from intracardially-perfused CD- and WD-fed mice and performed shotgun lipidomics. Strikingly, the PCA segregated the samples not only by region (white matter vs. grey matter, segregated by PC1) but also by diet (CD vs. WD, segregated by PC2) (Fig. 3.3a). WD-fed mice samples were characterized by increased content of lysophosphatidylcholines (LPC) in the white matter (Fig. 3.3b) and decreased content of phosphatidylglycerol (PG) in the grey matter (Fig. 3.3c), while all other lipid classes remained

unaltered (Fig. 3.3f,g). Next, we determined differences in acyl chain length and degree of saturation of the lipid species that were significantly ($p \leq 0.05$) increased by more than 1.3-fold. These comprised mostly of phosphatidylcholine (PC) and phosphatidylethanolamine (PE) species both in white and grey matter (Fig 3.3d,e). Notably, these species were characterized by a higher percentage of saturated lipids with shorter acyl length both in the white (Fig. 3.3h,i) and the grey matter (Fig. 3.3j,k) from WD-fed mice, which correlated to the changes observed in the plasma.

Together, these findings indicate that WD induced alterations in the brain lipidome that resemble those in the plasma. This suggests that despite the blood-brain barrier, lipids can infiltrate the CNS and change its lipid composition.

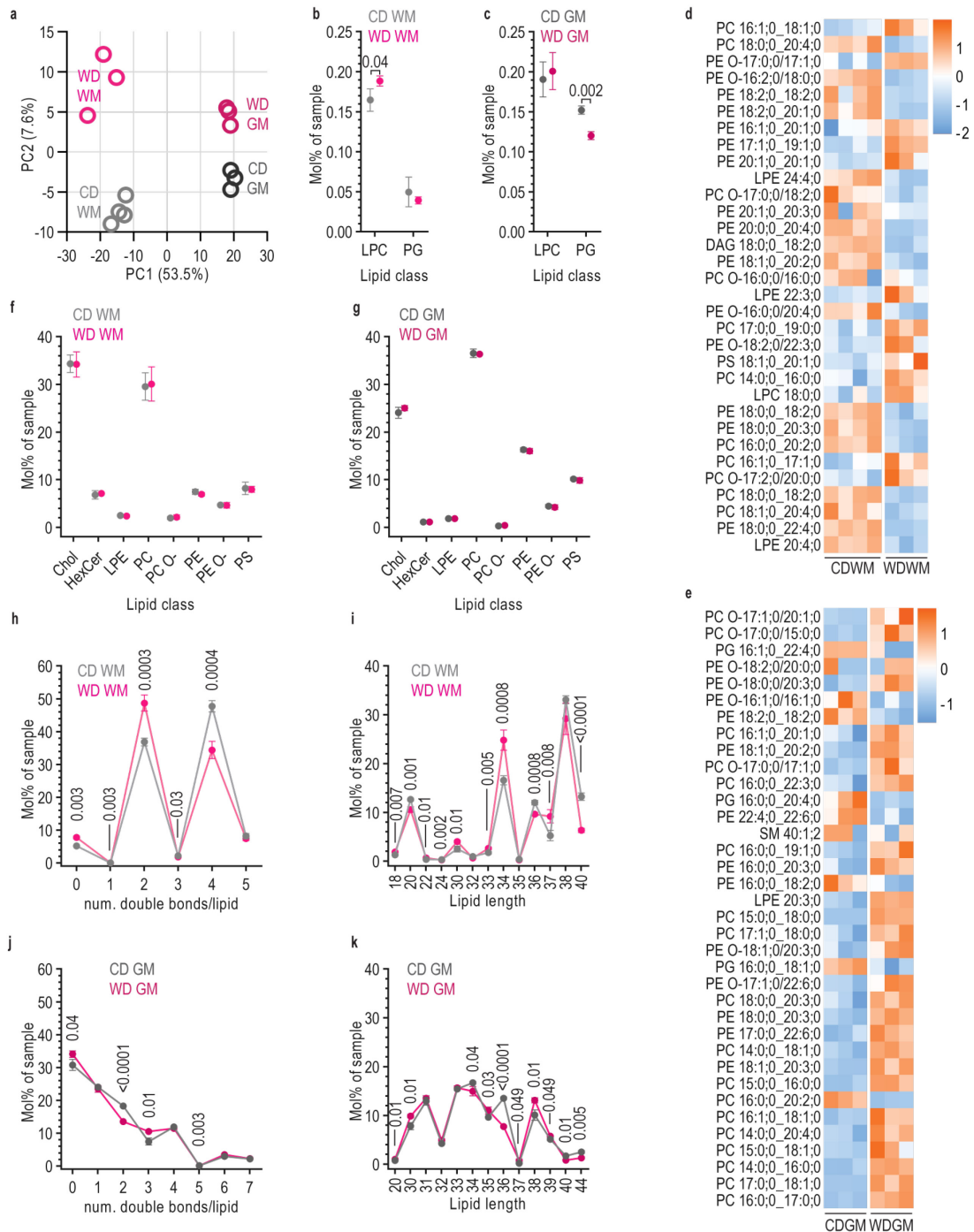


Figure 3.3 (previous page): Western diet feeding alters the brain lipidome of mice. **a**, PCA analysis of white matter and grey matter from brain of WD- and CD-fed mice. **b,c**, Lipid classes changed in brain WM (**b**) and GM (**c**) between CD- and WD-fed mice (mean±SD, two-tailed Welch's t-test). **d,e**, Heatmap showing the significantly (p value ≤ 0.5 , fold ≥ 1.3) changed lipid species in the brain WM (**d**) and in the brain GM (**e**). Scale indicated on the right side of the heatmap. Increased values are indicated in orange, while decreased values are in blue. The lipid class label indicates the lipid class, the number of carbons, the number of double bonds, and the number of hydroxyl groups. **f,g**, Percentage of the sample occupied by the most common lipid classes in the brain WM (**f**) and GM (**g**) in CD- and WD-fed mice (mean±SD, two-tailed Welch's t-test). **f,g**, Percentage of each sample with lipids containing a certain number of double bonds (**f**) or a certain acyl chain length (**g**). **h-k**, Percentage of each sample with lipids containing a certain number of double bonds (**h,j**) or a certain acyl chain length (**i,k**). The data is shown for those lipid species significantly (p value ≤ 0.05 , fold ≥ 1.3) changed in the WM (**h,i**) and GM (**j,k**) from CD- and WD-fed mice. P-values below 0.1 are indicated in the figure. $n=3$ for WD WM, CD GM and WD GM. $n=4$ for CD WM. PCA: principal component analysis, CD: control diet, WD: western diet, WM: white matter, GM: grey matter, CE: cholesterol esters, Chol: cholesterol, DAG: diacylglycerol, LPC: lysophosphatidylcholine, PC: phosphatidylcholine, TAG: triacylglycerides, PI: Phosphatidylinositol, PG: phosphatidylglycerol, PE: phosphatidylethanolamine, PE O-: Phosphatidylethanolamine-ether, LPE: lysophosphatidylethanolamine, DAG: diacylglycerol, PC O-: Phosphatidylcholine-ether, PS: phosphatidylserine.

1.2. Microglia in the white matter are altered by western diet feeding

After recognising that WD led to lipid profile changes in the CNS, we wanted to examine whether microglia were affected by these alterations. We first examined microglia by IBA1⁺ staining in the corpus callosum, a highly myelinated area and therefore a target of demyelinating damage, and found increased microglia density (Fig. 3.4a,c) and IBA1 signal intensity (Fig. 3.4b,c). Considering that, upon activation, microglia proliferate and enhance their immunoreactivity for IBA1⁺, these results indicate a certain reaction of microglia to white matter alterations. Next, we quantified the percentage of microglia containing PLIN2⁺ particles in their cytoplasm. PLIN2 is a lipid droplet-coating protein, thus, PLIN2⁺ particles are an indication of lipid loading in cells. The percentage of IBA1⁺ cells containing PLIN2⁺ particles within their cytoplasm was approximately 50% in the corpus callosum of CD-fed mice, while it was around 70% in the corpus callosum of WD-fed mice (Fig. 3.4d,e), indicating increased lipid loading in microglia from these mice.

To further assess the influence of WD on the activation status of microglia in the corpus callosum, we examined microglia activation markers such as CLEC7A, AXL and MAC2. The expression of such markers typically increases with microglia activation and defines both degeneration-associated microglia (DAM) (Keren-Shaul et al., 2017) and white matter-associated microglia (WAM) (Safaiyan et al., *submitted*). In the corpus callosum of CD- and WD-fed mice, we found generally little expression of these markers in microglia. Nevertheless, the percentage of microglia positive for CLEC7A was significantly increased in WD-fed mice corpus callosum (Fig. 3.4f,i). The number of AXL⁺IBA1⁺ and MAC2⁺IBA1⁺ cells was similar in both groups, although a slight trend to increase was observed for AXL (Fig. 3.4g,h,j,k). Thus, similarly to what has been described for other areas of the CNS (Guillemot-Legris and Muccioli, 2017), microglia in white matter areas of WD-fed mice seemed to be slightly activated.

Dysfunctional aged microglia typically accumulate lipofuscin, a lipidic residue of lysosomal digestion. To evaluate whether microglia from WD-fed mice showed increased lipofuscin accumulation, we imaged the autofluorescent particles in the corpus callosum. Upon quantification of the percentage of microglia containing autofluorescence-positive particles close to the nucleus, we found no differences between the groups (Fig. 3.4l,m). Thus, microglia in the corpus callosum of WD-fed mice didn't seem to show signs of lipid accumulation in the form of lipofuscin.

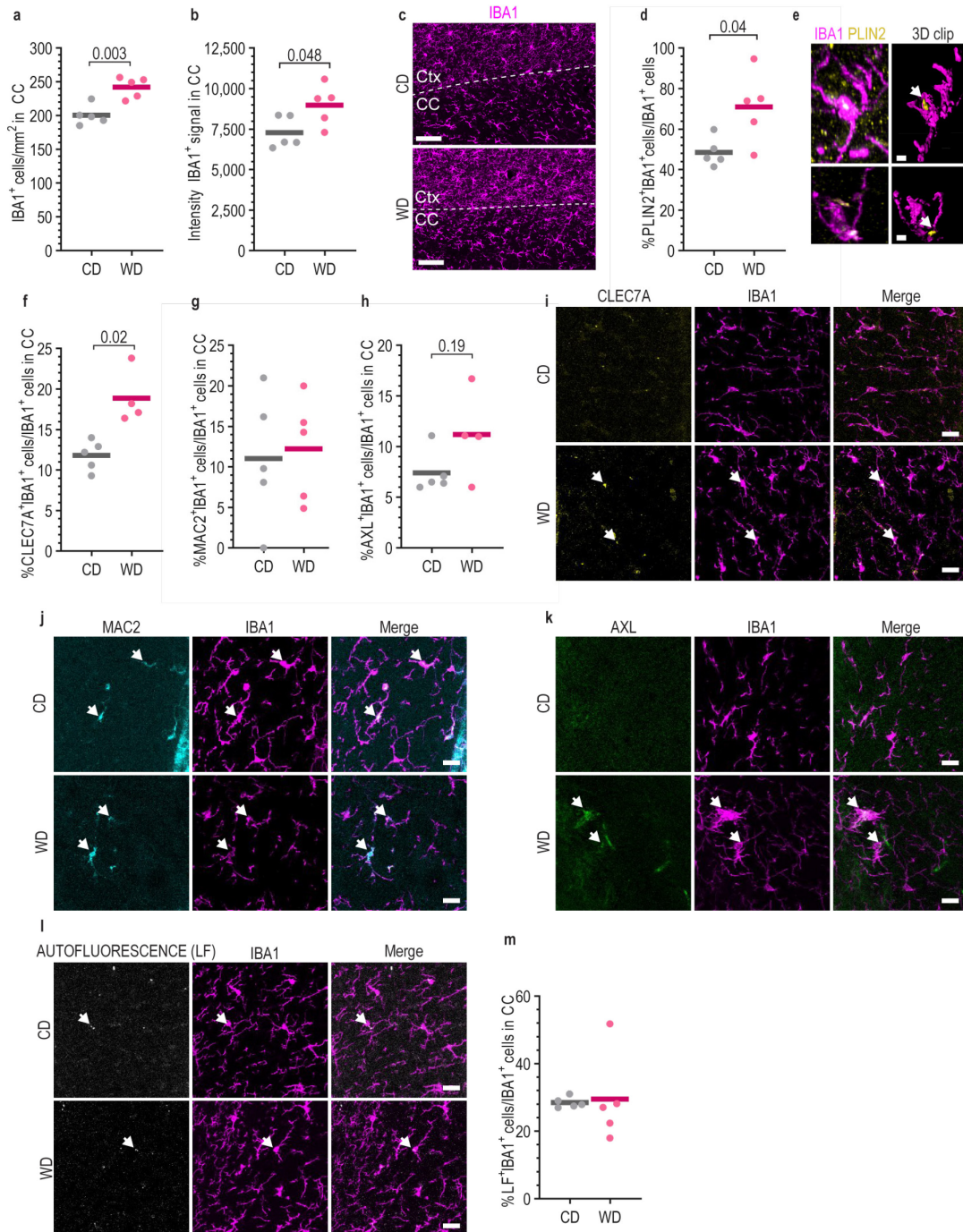


Figure 3.4: Microglia in the white matter are altered by western diet feeding. **a**, Quantification of microglia density in the corpus callosum (two-tailed Welch's t-test). **b**, Measurement of IBA1⁺ signal intensity in the corpus callosum (two-tailed Welch's t-test). **c**, Images of the cortex (Ctx) and corpus callosum (CC) stained with IBA1 to label microglia. Scale bar: 50 μ m. **d**, Quantification of the

percentage of IBA1⁺ cells containing PLIN2⁺ lipid droplets in the corpus callosum (two-tailed Welch's t-test). **e**, Example images of microglia containing PLIN2⁺ lipid droplets in their cytoplasm. On the left side, the raw image is displayed. On the right side, a 3D clip of the corresponding image is displayed, where the PLIN2⁺ signal inside the cell is indicated with a white arrow. Scale bar images above: 3 μm , Scale bar images below: 2 μm . **f,g,h**, Quantification of the percentage of CLEC7A⁺/IBA1⁺ (**f**), MAC2⁺/IBA1⁺ (**g**) and AXL⁺/IBA1⁺ (**h**) cells over all the population of IBA1⁺ cells (two-tailed Welch's t-test). **i,j,k**, Images of microglia in the corpus callosum labelled with IBA1 and the activation markers CLEC7A (**i**), MAC2 (**j**) and AXL (**k**). White arrows indicate cells positive for both IBA1 and the corresponding activation marker. **l**, Images of the autofluorescent particles (labelling LF) in IBA1⁺ microglia in the corpus callosum. White arrows indicate LF particles within microglia. **m**, Quantification of the population of IBA1⁺ cells with LF particles within their cytoplasm (two-tailed Welch's t-test). Scale bars: 20 μm . P-values below 0.2 and n numbers are indicated in the figure. Solid lines in the graphs indicate the mean. CD: control diet, WD: western diet, Ctx: cortex, CC: corpus callosum, LF: lipofuscin.

1.2.1. The epithelial lining of the lateral ventricles could be altered by western diet

While evaluating the PLIN2 staining of the corpus callosum, we noticed that the epithelial lining of the lateral ventricle directly in contact with the corpus callosum contained high numbers of lipid droplets (Fig. 3.5a). To examine whether this epithelium could be a route of entry for lipids into the CNS, we quantified the number of lipid droplets in it. For this, we prepared semithin sections from epon-embedded samples and stained them for a mix of azur and methylene blue, which results in the colouring of lipid accumulations in grey-green. Interestingly, there was a higher density of lipid accumulation in the ventricle lining of WD-fed mice (Fig. 3.5b,c). Next, we examined the characteristics of astrocytes in this area by staining for GFAP. We found that, in WD-fed mice, the area and intensity of GFAP⁺ signal in the ventricle epithelial lining was lower compared to the CD-fed mice (Fig. 3.5d-f). Although we did not explore the functional consequences of this observation, we think that dysfunctional astrocyte sealing of the ventricle lining could lead to a "leaky barrier" that permits lipid entry from the cerebrospinal fluid (CSF) directly into the white matter of the CNS.

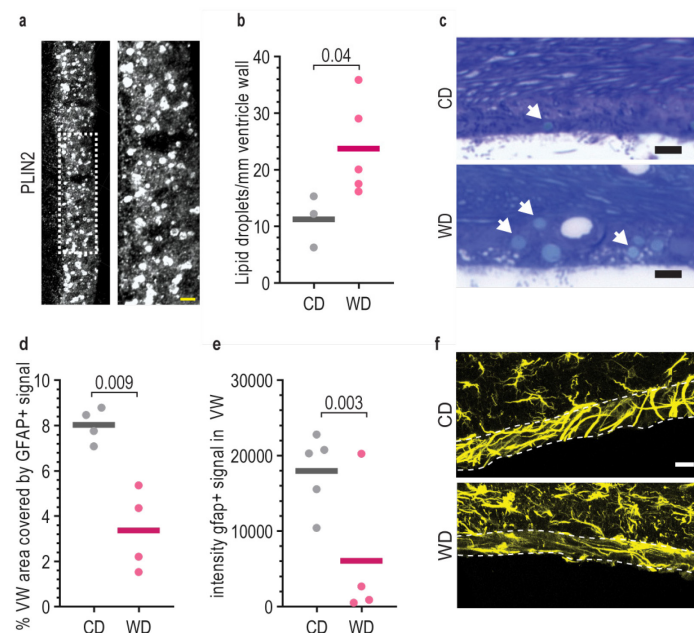


Figure 3.5: The ventricle wall could be a site for lipid trafficking into the CNS. **a**, Images of the ventricle wall labelled with PLIN2. On the left, overview image. On the right, magnification image

of the square delineated with a dotted line. Scale bar: 5 μm . **b**, Quantification of the number of lipid droplets detected in the ventricle wall separating the corpus callosum from the lateral ventricles (two-tailed Welch's t-test). **c**, Images of the ventricle wall separating the corpus callosum from the second ventricle. Lipid droplets are labelled in pale green and marked with white arrows. Scale bar: 5 μm . **d**, Quantification of the percentage area of the ventricle wall covered by GFAP⁺ signal (two-tailed Welch's t-test). **e**, Quantification of the intensity of the GFAP⁺ signal in the ventricle wall (two-tailed Welch's t-test). **f**, Example images of the ventricle wall stained with GFAP. The ventricle wall is delineated with dashed white lines. Scale bar: 20 μm . P-values below 0.1 and n numbers are indicated in the figure. Solid lines in the graphs indicate the mean. CD: control diet, WD: western diet, VW: ventricle wall.

1.2.2. Western diet consumption changes the microglia transcriptomic profile

To evaluate the changes caused by WD on the transcriptome at whole-genome level, we isolated microglia from brains of CD- and WD-fed mice and analysed their mRNA expression. PCA clustering efficiently segregated the microglia samples from CD- and WD-fed mice brain (Fig. 3.6a). Microglia homeostatic signature genes such as *Tmem119*, *Cx3cr1* or *Trem2* were highly expressed, validating the nature of our samples, but were not significantly changed between groups (Fig. 3.6b). Surprisingly, we detected a significant decrease in the expression of typical oligodendrocyte/myelin genes in microglia from WD-fed mice (Fig. 3.6c). This result could have two explanations. One explanation is that WD causes alterations in the contacts between microglia and oligodendrocytes/myelin that lead to less myelin debris being pulled down while isolating microglia. This explanation is further supported by the pathway analysis, where cell-cell adhesion was one of the pathways significantly decreased in microglia from WD-fed mice (Fig. 3.6i). Another explanation is that the myelin debris removal step during the microglia isolation from the WD-fed mice was more efficient than the one in CD-fed mice, thereby leading to less myelin debris in the WD samples and less oligodendrocyte/myelin genes.

Next, we searched genes of pathways of interest for this project (Fig. 3.6d-g). We found that lipid metabolism pathways were mostly decreased in microglia from WD-fed mice, including genes of the PPAR pathway, while inflammatory pathways were changed in both directions. Interestingly, we found that several genes from the TGF β pathway were increased in microglia from WD-fed mice. Further pathway analysis demonstrated that, apart from cell-cell adhesion pathways, also endocytosis, cytokine-cytokine receptor interaction pathways and insulin signalling pathways were altered in microglia from WD-fed mice (Fig. 3.6h-k). Finally, we filtered the most significantly changed genes of high expression (base mean of expression ≥ 500 , fold increase ≥ 0.3 or ≤ -0.3 , p-value ≤ 0.05) to understand where the strongest changes were found.

In short, our RNA sequencing analysis informed us that lipid and sugar metabolism, inflammatory and adhesion pathways seemed to be altered by WD in microglia. Unfortunately, the design of this experiment led to significant batch effects between the CD and WD samples which made it difficult to interpret the significance of the results.

Results

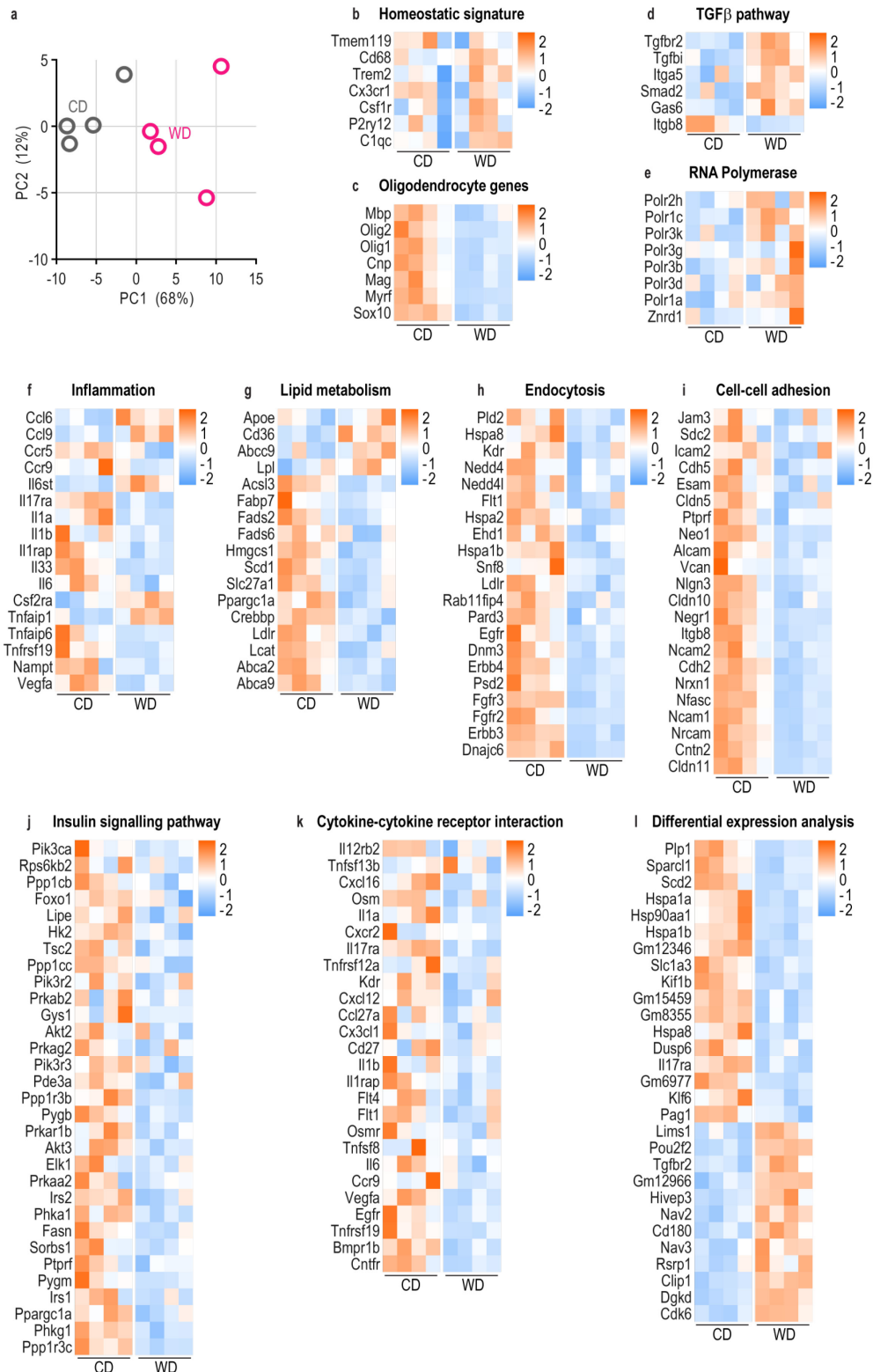


Figure 3.6: The transcriptome of microglia is altered by western diet. **a**, PCA analysis of the transcriptome from microglia isolated from CD- or WD-fed mice brain. **b**, Heatmap showing the standard microglia signature genes. **c**, Heatmap showing standard oligodendrocyte signature genes. **d**, **f**, **g**, Heatmaps showing genes from pathways of interest for this project, namely the TGF β pathway, inflammatory pathways, and lipid metabolism pathways. **e**, Heatmap showing the genes from the KEGG pathway RNA Polymerase (p value 0.039, FDR 0.53), which is enriched in the microglia from WD-fed mice. **h-k**, Heatmaps showing the genes from the KEGG Pathways depleted in microglia from WD-fed mice: endocytosis (p value 0.003, FDR 0.25), cell-cell adhesion (p value 0.0, FDR 0.005), insulin signalling pathway (p value 0.037, FDR 0.38), and cytokine-cytokine receptor

interaction (p value 0.035, FDR 0.43). **1**, Heatmap illustrating the most significantly (Base mean > 500, fold change > 0.3 or < -0.3, adjusted p -value 0.05) changed genes. For all heatmaps, the scale is indicated on the right side of the heatmap. Increased values are indicated in orange, while decreased values are in blue. CD: control diet, WD: western diet.

1.2.3. The microglia epigenome could be altered both by western diet and age

One mechanism by which diet could alter the microglia transcriptome is by changing the epigenetic marks on the DNA. Indeed, such changes have been previously reported and shown to be mediated partly by microbiota products (Erny et al., 2015). Thus, we isolated microglia from CD- and WD-fed mice and analysed their genome-wide chromatin accessibility by Assay for Transposase-Accessible Chromatin using sequencing (ATACseq). Furthermore, we also analysed microglia isolated from young and old mice, to understand whether age led to similar changes in the epigenome. Although we detected areas with different chromatin status in both comparisons (Fig. 3.7a,b), further analysis showed that the differences in chromatin accessibility observed were extremely minor and seemed to follow the same trends for all genes (Fig. 3.7c,d shows the example for the *Il-6* gene), indicating technical problems and inconclusive results. Considering the substantial scope and relevance of this analysis, this project was taken up by Vini Tiwari, another PhD student in our group.

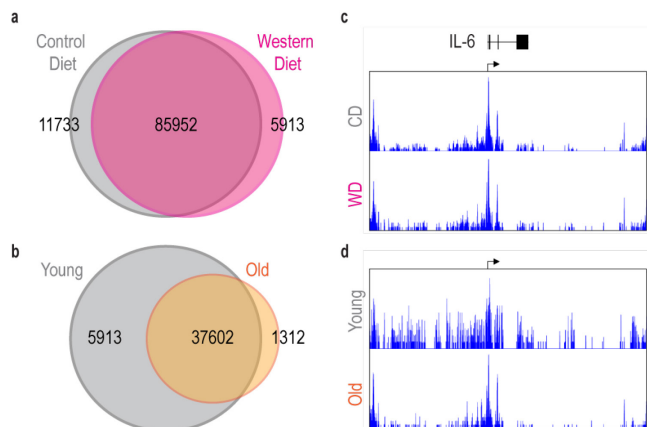


Figure 3.7: Analysis of the epigenome of microglia resulted in similar results in all genes. a,b, Diagrams demonstrating the overlap and differences in the epigenome between microglia from CD- and WD-mice (a) and microglia from young and old mice (b). **c,d**, Comparison of the ATAC sequencing results between CD- and WD-fed mice (c) and young and old mice (d) for the gene *IL-6*. WD: western diet, CD: control diet, *IL-6*: interleukin 6.

2. The influence of western diet on the pro-repair function of microglia

Several studies have focused on understanding the influence of diet on microglia function in the undamaged brain. Nevertheless, how microglia's response to damage is affected by WD is still unknown. In this part of the study, we examined how WD affects microglia's ability to coordinate a regenerative response after demyelinating injury.

2.1. Obesity causes poor recovery after demyelinating injury

To analyse the influence of WD on remyelination, we injected LLC in the corpus callosum of CD- and WD-fed mice and followed lesion development over time. Four days post injection (4 dpi), the volume of demyelination (Fluoromyelin-negative area) and microglia/macrophage-dense area (by IBA1⁺ staining) were similar in both groups (Fig. 3.8a,b,c), indicating similar demyelination and IBA1⁺ phagocyte infiltration properties. We then determined lesion sizes at 14 dpi, when the regenerative process of remyelination has already started. We observed that demyelinated lesions remained large in WD-fed mice, indicating poor recovery (Fig. 3.8a,d). In addition, quantification of the volume occupied by IBA1⁺ cells revealed a sustained immune response in the demyelinated areas (Fig. 3.8b,d).

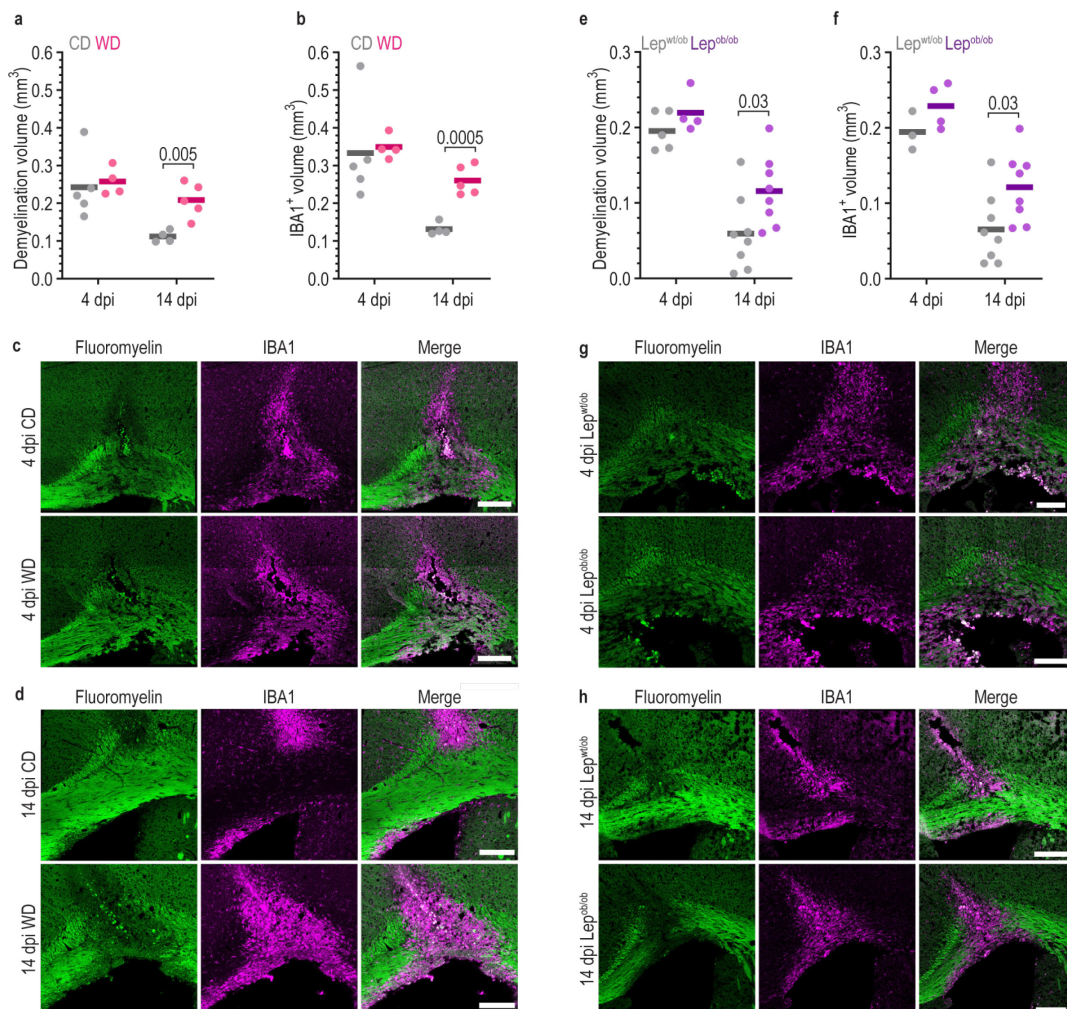


Figure 3.8 (previous page): Obesity impairs lesion recovery after demyelinating injury. a,b, Demyelination (a) and IBA1⁺ (b) volume at 4 and 14 dpi in CD- and WD-fed mice (two-tailed Welch's t-test). **c,d,** Images of corpus callosum lesions in CD- and WD-fed mice at 4 (c) and 14 (d) dpi. Scale bar: 200 μ m. **e,f,** Demyelination (e) and IBA1⁺ (f) volume at 4 and 14 dpi in Leptin^{wt/ob} and Leptin^{ob/ob} mice (two-tailed Welch's t-test). **g,h,** Images of corpus callosum lesions in Leptin^{wt/ob} and Leptin^{ob/ob} mice at 4 (g) and 14 (h) dpi. Scale bar: 200 μ m. P-values below 0.1 and n numbers are indicated in the figure. Solid lines in the graphs indicate the mean. dpi: days post injection, CD: control diet, WD: western diet, Lep: Leptin.

To assess whether genetically induced obesity leads to similar defects in lesion recovery, we followed the same procedure with leptin-deficient mice (Leptin^{ob/ob}). Leptin is a hormone secreted by adipocytes that regulates feeding behaviour, and mice deficient for leptin are hyperphagic and obese (Zhang et al., 1994). Indeed, at 4 dpi, the lesion sizes did not differ; while at 14 dpi, we detected bigger volumes of demyelination and IBA1⁺ phagocyte accumulation in Leptin^{ob/ob} than its control Leptin^{ob/wt} (Fig. 3.8e-h). Thus, both diet-induced and genetic-induced obesity results in poor lesion recovery after demyelinating injury in mice.

2.2. Persistent demyelination is associated with accumulation of lipids within microglia/macrophages

To investigate the reasons underlying poor remyelination in WD-fed mice, we further examined the demyelinated lesions at 14 dpi. We observed myelin-loaded IBA1⁺ cells accumulating in the core of demyelinated lesions, and quantification demonstrated that the density of such cells was higher in the lesions of WD-fed mice (Fig. 3.9a,b). We performed the same quantification in Leptin^{ob/ob} mice and observed similar results (Fig. 3.9c).

We further stained the same lesions for PLIN2 and CD68, to study the content in lipid droplets and the active endolysosomal system, respectively (Fig. 3.9d). We didn't find significant differences in the area occupied by PLIN2⁺ staining (Fig. 3.9e), however; we detected a 1.6-fold increase in the CD68⁺ area in the lesions from WD-fed mice (Fig. 3.9f), indicating that the endolysosomal system of IBA1⁺ cells was highly reactive in these mice. In addition, we imaged cholesterol crystals using reflection microscopy (Fig. 3.9g) and observed significantly increased density of crystal-loaded IBA1⁺ cells in the lesions of WD-fed mice (Fig. 3.9h). We co-stained for myelin debris, crystals and the endolysosomal system marker LAMP1 and confirmed that the myelin debris and crystals were found inside lysosomes (Fig. 3.9i) and that the endolysosomal system was highly reactive in the lesions of WD-fed mice (Fig. 3.9j).

We were also interested in understanding whether the density of IBA1⁺ cells was changed between the groups, but we were not able to detect any differences in density or area in the core of the lesion (Fig. 3.9k, m). However, we detected a strong trend to increased percentage area occupied by IBA1⁺ signal in peripheral areas of the lesion; at the lesion rim, in WD-fed mice (Fig. 3.9l), which further supports persistent microglia and macrophage activation in these mice.

Finally, we imaged semithin sections of spinal cord lesions at 21 dpi, which typically show accumulation of foam cells in the core of the lesions, which typically represent containing very high

Results

numbers of lipid droplets in their cytoplasm (Fig. 3.9n). The quantification of the density of foam cells in the lesions demonstrated that the lesions of WD-fed mice accumulated approximately double amounts of foam cells compared to the lesions of CD-fed mice (Fig. 3.9o).

In conclusion, the characterization of the lesions of CD- and WD-fed mice at 14 dpi confirmed persistent inflammation and indicated that the poor remyelination abilities observed in WD-fed mice could be caused by an impairment in lipid processing by the phagocytic system.

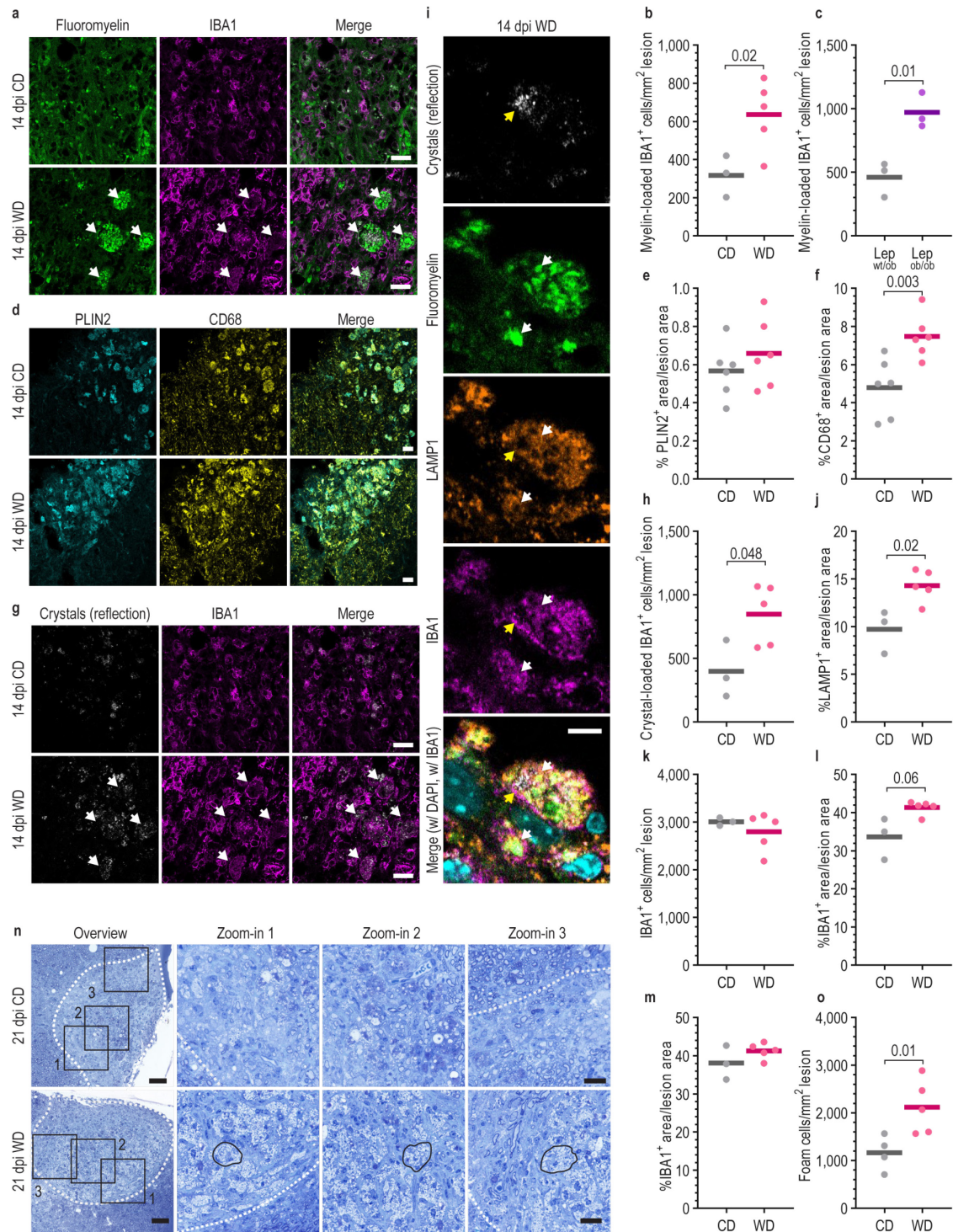


Figure 3.9 (previous page): Persistently demyelinated lesions in WD-fed mice contain lipid-loaded microglia. **a**, Images of the demyelinated lesion in the corpus callosum at 14 dpi exemplifying myelin-loaded-IBA1⁺ cells in CD- and WD-fed mice. White arrows indicate myelin-loaded IBA1⁺ cells. Scale bar: 20 μ m. **b**, Quantification of the number of myelin-loaded IBA1⁺ cells per mm² of lesion (two-tailed Welch's t-test). **c**, Quantification of the number of myelin-loaded cells in Lep^{ob/wt} and Lep^{ob/ob} mice per mm² of lesion (two-tailed Welch's t-test). **d**, Images of demyelinated lesions in the corpus callosum at 14 dpi exemplifying lipid loaded (PLIN2⁺) IBA1⁺ cells with active lysosomal system (CD68⁺). Scale bar: 20 μ m. **e,f**, Quantification of the area occupied by PLIN2⁺ (**e**) and CD68⁺ (**f**) in the demyelinated lesion (two-tailed Welch's t-test). **g**, Images demonstrating the crystal-loaded IBA1⁺ cells accumulating in the demyelinated lesions at 14 dpi. White arrows indicate the crystal-loaded IBA1⁺ cells. Scale bar 20 μ m. **h**, Quantification of the number of crystal-loaded IBA1⁺ cells in the demyelinated lesions (two-tailed Welch's t-test). **i**, Example magnification demonstrating accumulation of myelin debris in lysosomes (LAMP1 staining) of phagocytes (IBA1 staining) in demyelinated lesions at 14 dpi. White arrows point to myelin debris accumulation within LAMP1⁺ organelles of IBA1⁺ cell. Yellow arrows indicate crystal accumulation within an IBA1⁺ cell. Scale bar: 5 μ m. **j**, Quantification of the area occupied by LAMP1⁺ staining in the demyelinated lesion (two-tailed Welch's t-test). **k**, Quantification of the numbers of IBA1⁺ cells in the lesions at 14 dpi. No significant differences were observed (two-tailed Welch's t-test). **l,m**, Quantification of the area occupied by IBA1⁺ signal in the peripheral (**l**) and central (**m**) areas of the lesion (two-tailed Welch's t-test). **n**, Images of demyelinated lesions in the spinal cord of CD- and WD-fed mice at 21 dpi demonstrating foam cell accumulation. Examples of foam cells are circled with a solid black line. The demyelinated area is indicated with a dashed line. The zoom-in regions are indicated in the overview as squares. Scale bar: Overview 50 μ m, zoom-in 20 μ m. **o**, Quantification of the number of foam cells per mm² of lesion in spinal cord lesions at 21 dpi (two-tailed Welch's t-test). P-values below 0.1 and n numbers are indicated in the figure. Solid lines indicate the mean. CD: control diet, WD: western diet, dpi: days post injection.

2.3. Stimulation of lipid processing pathways in WD-fed mice improves recovery from demyelinating injury

One possible explanation for poor lesion recovery in WD-fed mice could be the failure to activate lipid metabolic pathways in microglia such as the LXR and PPARs pathways, which are known to be induced and required in myeloid cells after myelin phagocytosis (Bogie et al., 2012, 2014b; Cantuti-Castelvetri et al., 2018). Previously, we have reported that stimulation of the LXR pathway could promote remyelination in aged mice (Cantuti-Castelvetri et al., 2018), thus, we wanted to confirm whether stimulation of this and other lipid processing pathways could prove beneficial for remyelination in WD-fed mice.

To examine this, we followed different pharmacological approaches. First, we used the small molecule GW3965 (GW) to target LXR, a transcription factor that detects cholesterol derivatives and promotes cholesterol efflux. Indeed, treatment of WD-fed mice with GW led to smaller volumes of demyelination and IBA1⁺ phagocytes at 14 dpi (Fig. 3.10a-e), indicating improved recovery from demyelination upon stimulation of cholesterol efflux. Then, we examined the role of PPAR α , which stimulates fatty acid oxidation, and PPAR γ , which enhances lipid buffering within the cell in the form of lipid droplets, in regulating inflammation (Fig. 3.10a). We treated WD-fed mice and old mice with fenofibrate (FF), a PPAR α agonist, and rosiglitazone (RG), a PPAR γ agonist. Treatment of WD-fed mice with the agonists led to improved recovery at 14 dpi compared to the untreated group as shown by smaller demyelination and IBA1⁺ volumes (Fig. 3.10b-e), however; treatment of old mice had no effect on lesion recovery. Hence, it appears that the LXR pathway, but not the PPAR α / γ pathway, is

a common bottleneck for remyelination in both WD- and age-induced remyelination failure (see Fig. 5.2 in the Appendix).

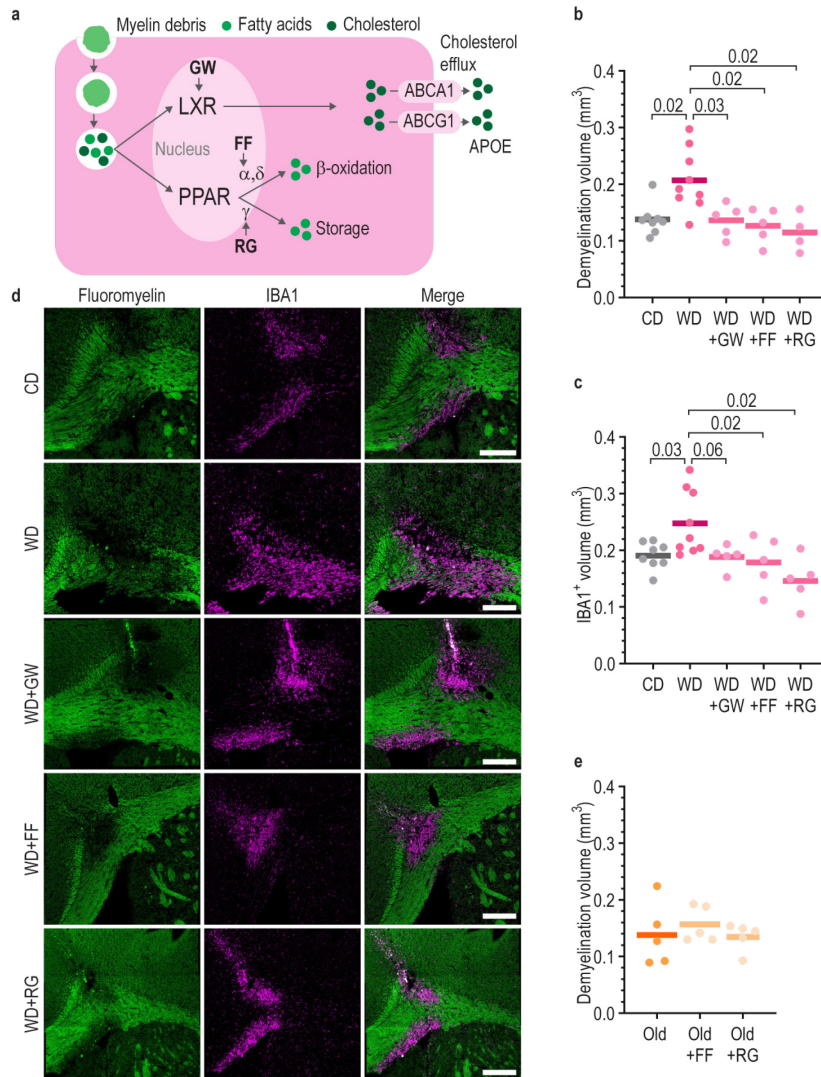


Figure 3.10: Stimulating lipid-sensing nuclear receptors in WD-fed mice improves lesion repair after demyelination. **a**, Diagram demonstrating two lipid processing pathways targeted in this study and the agonists used to do so. **b,c**, Quantification of demyelination (**b**) and IBA1⁺ (**c**) volume at 14 dpi in CD-, WD-, WD+GW-, WD+FF- and WD+RG-fed mice (one-way Brown-Forsythe and Welch ANOVA tests with multiple comparisons corrected by Dunnett T3 test). **d**, Images of corpus callosum lesions of all treatment groups at 14 dpi. Scale bar: 200 μ m. **e**, Quantification of the demyelination volume at 14 dpi in old, old+FF and old+RG mice. We observed no differences (one-way Brown-Forsythe and Welch ANOVA tests with multiple comparisons corrected by Dunnett T3 test). P-values below 0.1 and n numbers are indicated in the figure. Solid lines in the graphs indicate the mean. GW: GW3965, LXR agonist. FF: Fenofibrate, PPAR α agonist, RG: rosiglitazone, PPAR γ agonist, CD: control diet, WD: western diet, WD+GW: western diet supplemented with GW3965, WD+FF: western diet supplemented with fenofibrate, WF+RG: western diet supplemented with rosiglitazone, Old+FF: old mice fed fenofibrate-containing chow, Old+RG: old mice fed rosiglitazone-containing chow, dpi: days post injection.

2.4. Stimulation of LXR and PPAR pathways enhances lipid processing in microglia and macrophages

Our results showed that treatment of WD-fed mice with LXR and PPAR α/γ pathway agonists improved recovery from demyelination in these mice. To investigate whether this improvement was associated with better lipid processing in microglia and macrophages, we analysed the properties of microglia and macrophages in the demyelinated lesions of the different groups. Indeed, we found that the lesions of WD-fed mice treated with LXR and PPAR α/γ agonists contained lower numbers of myelin- and crystal-loaded IBA1⁺ cells (Fig. 3.11a-c). Furthermore, we analysed the area occupied by IBA1⁺ signal and found no differences between groups (Fig. 3.11d,f). However, it is important to note that the lesions of the group of WD-fed mice treated with rosiglitazone did not contain less cholesterol crystals and showed a clear trend to increased area occupied by IBA1⁺ signal, indicating that the improved remyelination abilities observed in this group were originated from different mechanisms as compared to the GW and fenofibrate treatments. Furthermore, we quantified the area occupied by LAMP1⁺ staining and found that the PPAR agonists decreased the reactivity of the endolysosomal system (Fig. 3.11e,f), although these differences were not statistically significant. Together, these results indicate that, indeed, stimulation of lipid processing in microglia and macrophages led to improved repair after demyelination and further point to a failure in the activation of lipid processing pathways in the phagocytic system of WD-fed mice.

To further examine these indications, we turned to genetic expression analysis. We isolated the demyelinated lesions of CD- and WD-fed mice both at 2 and 7 dpi. We chose these timepoints to be able to analyse the induction in mRNA expression of LXR and PPAR α/γ pathway targets caused by myelin intake. Interestingly, RT-qPCR analysis of the LXR target genes *ApoE*, *Abca1* and *Abcg1* indicated that the increase in expression from 2 to 7 dpi was smaller or inexistent in lesions from WD-fed mice when compared to those of CD-fed mice (Fig. 3.11g). Thus, it appeared that WD-fed mice were unable to induce the LXR pathway to the extent necessary for successful lipid processing. In addition, RT-qPCR analysis of the PPAR targets *Fabp4*, *Hmox1* and *Plin2* showed that the expression of these genes decreased from 2 to 7 dpi, and they tended to decrease to a higher extent in WD-fed mice (Fig. 3.11h). These results were puzzling, because it is known that these genes should be induced in microglia after myelin intake (Bogie et al., 2014b). However, these genes are also present in other glial cells in the CNS, and their decrease in lesions could be caused by the loss of such cells. Nevertheless, the pronounced decrease observed in WD-fed mice could point to insufficient expression of PPAR α/γ target genes that contributes to poor lipid processing in microglia and macrophages.

Hence, these results demonstrated that insufficient activation of the LXR pathway and, probably, insufficient amounts of PPAR α/γ pathway targets, underlies lipid processing failure in microglia and macrophages from WD-fed mice.

Results

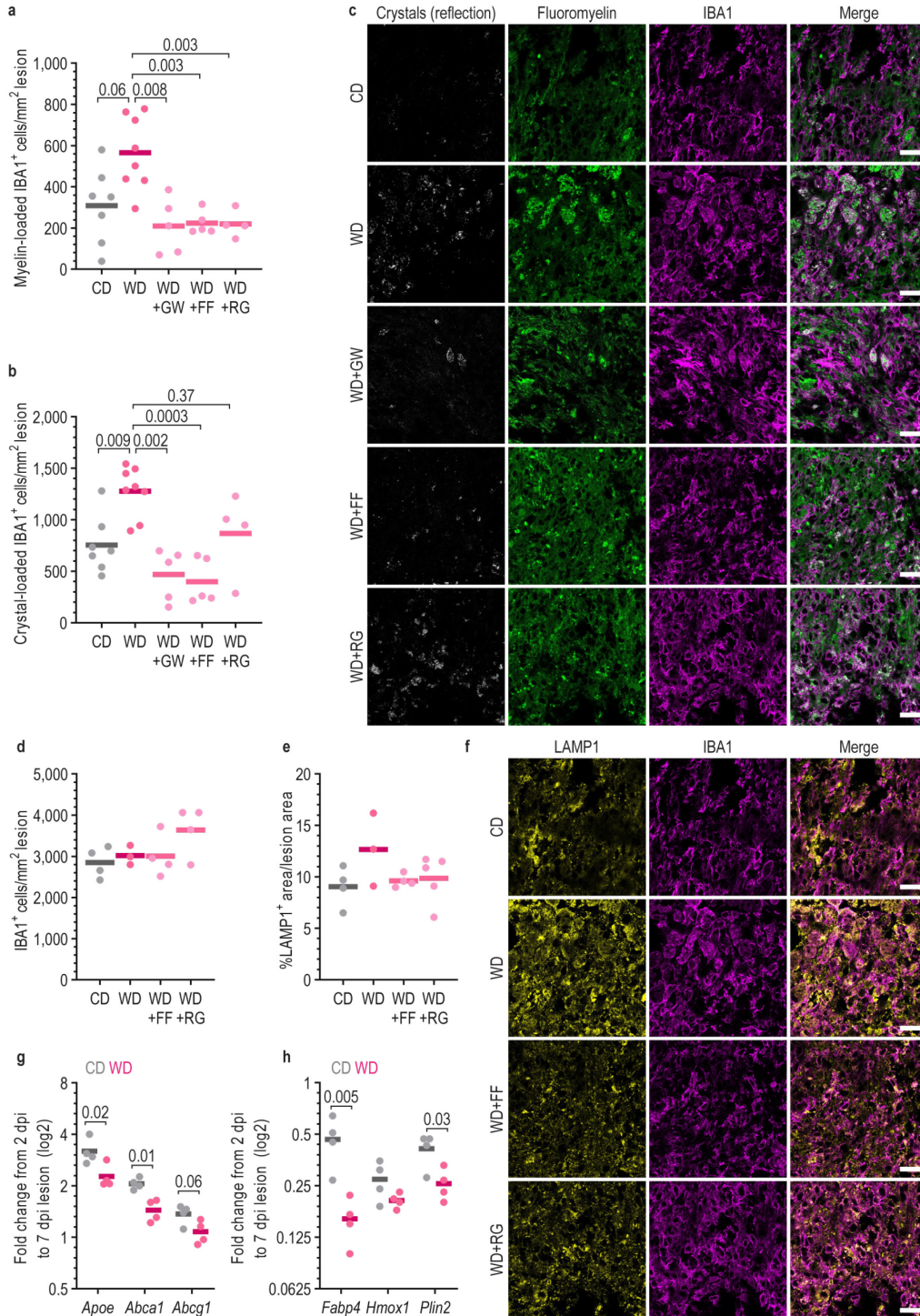


Figure 3.11: Stimulation of LXR and PPAR pathways improves lipid processing by microglia and macrophages in WD-fed mice. **a,b**, Quantification of the number of myelin- (**a**) and crystal- (**b**) loaded IBA1⁺ cells per mm² of lesion (one-way Brown-Forsythe and Welch ANOVA tests with multiple comparisons corrected by Dunnett T3 test). **c**, Images of the demyelinated lesion in the corpus callosum at 14 dpi exemplifying myelin- and crystal-loaded IBA1⁺ cells in all treatment groups. Scale bar: 20 μ m. **d,e**, Quantification of the number of IBA1⁺ cells (**d**) and the percentage area occupied by LAMP1⁺ signal (**e**) in the demyelinated lesions in CD-, WD-, WD+FF- and WD+RG-fed mice. We observed no significant differences (one-way Brown-Forsythe and Welch ANOVA tests with multiple comparisons corrected by Dunnett T3 test). **f**, Images of the demyelinated lesions

stained for the lysosomal marker LAMP1 and IBA1. Scale bar 20 μm . **g,h**, Quantification of the change in mRNA expression of the LXR targets *ApoE*, *Abca1* and *Abcg1* (**g**) and the PPAR targets *Fabp4*, *Hmox1* and *Plin2* (**h**) from 2 to 7 dpi lesions from CD and WD-fed mice (two-tailed Welch's t-test). P-values below 0.1 and n numbers are indicated in the figure. Solid lines in the graphs indicate the mean. CD: control diet, WD: western diet, WD+GW: western diet supplemented with GW3965, WD+FF: western diet supplemented with fenofibrate, WF+RG: western diet supplemented with rosiglitazone.

3. Why do microglia in WD-fed mice poorly induce the LXR pathway?

Our results led us to the conclusion that WD causes poor recovery from demyelinating injury due to impaired lipid processing function by microglia and macrophages that, in turn, arose from poor induction of the LXR pathway. Next, we were interested in understanding what caused microglia and macrophages in WD-fed mice to poorly induce this pathway.

3.1. Increased chromatin acetylation as the cause of poor LXR pathway induction

We first wondered whether epigenetic mechanisms could underlie the poor induction of the LXR pathway in WD-fed mice. Butyric acid can function as a HDAC inhibitor, thereby driving chromatin to a more relaxed, transcriptionally active state. Thus, the lower butyric acid production observed in WD-fed mice could lead to decreased acetylation of chromatin and poor transcriptional responses in microglia and macrophages. To investigate this hypothesis, we treated WD-fed and old mice with sodium butyrate by adding this in the drinking water from 5 days before LLC injection until the end of the experiment. Interestingly, this treatment led to smaller demyelination and IBA1⁺ volumes at 14 dpi both in WD-fed and in old mice (Fig. 3.12a-e). Hence, it appeared that promoting histone acetylation was beneficial for recovery from demyelinating injury. After these results, we realized that characterizing the epigenetic effects of WD and age on microglia was out of the scope of this project. Thus, this hypothesis was further pursued in more depth by my colleague Vini Tiwari.

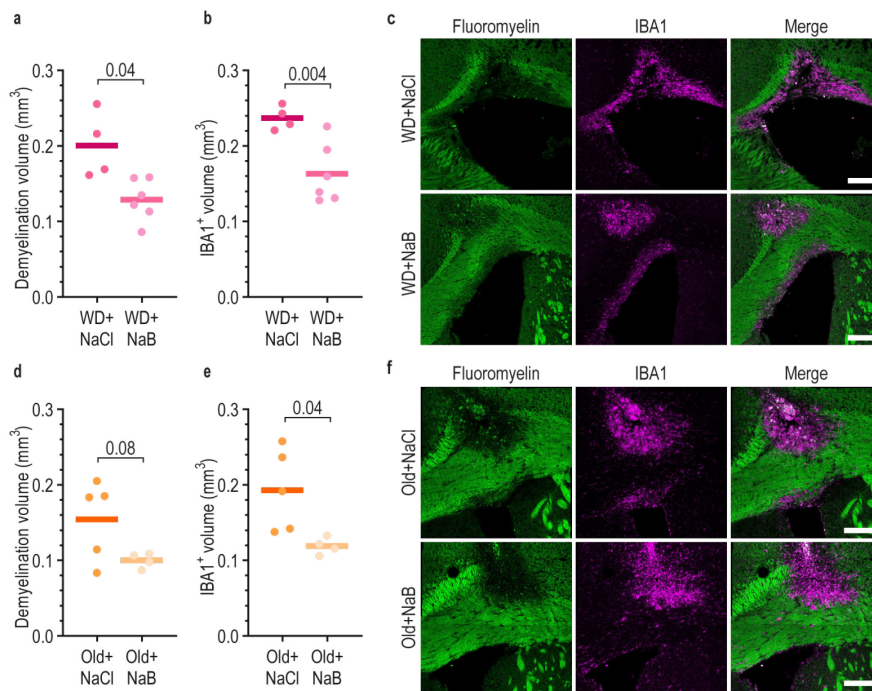


Figure 3.12: Sodium Butyrate treatment enhances lesion repair both in WD-fed mice and in old mice. **a,b**, Quantification of the demyelination (**a**) and the IBA1⁺ (**b**) volumes in WD-fed mice treated with sodium butyrate or with vehicle control (sodium chloride) at 14 dpi (two-tailed Welch's t-test). **c**, Images of demyelinated lesions in the corpus callosum at 14 dpi of WD-fed mice treated with sodium butyrate or vehicle control. Scale bar: 200 μm **d,e**, Quantification of the demyelination (**d**) and the IBA1⁺ (**e**) volumes in old mice treated with sodium butyrate or with vehicle control (sodium chloride) at 14 dpi (two-tailed Welch's t-test). **f**, Images of demyelinated lesions in the corpus callosum at 14 dpi of old mice treated with sodium butyrate or vehicle control. Scale bar: 200 μm. P-values below 0.1 and n numbers are indicated in the figure. Solid lines in the graphs indicate the mean.

NaCl: sodium chloride (vehicle control), NaB: sodium butyrate, WD: western diet, dpi: days post injection.

3.2. Are LXR ligands sufficiently produced in the lesions of WD-fed mice?

Next, we examined the production of the most common LXR ligands in the demyelinated lesions. For this, we used gas chromatography mass spectrometry (GC/MS) to quantify desmosterol, 24S-hydroxycholesterol and 27-hydroxycholesterol in lesions isolated at 4 and 7 dpi from CD- and WD-fed mice. We detected several differences between the timepoints and the diet groups. For example, the amounts of desmosterol, the most potent LXR ligand (Spann et al., 2012), increased significantly by 1.2-fold in lesions from WD-fed mice from 4 to 7 dpi, but not in the lesions from CD-fed mice (Fig. 3.13a). Moreover, the amounts of 24S-hydroxycholesterol were increased in both groups from 4 to 7 dpi (Fig. 3.13b), whereas the amounts of 27-hydroxycholesterol, the oxysterol with lowest quantity in the CNS, increased in lesions from CD-fed mice but not in the lesions from WD-fed mice (Fig. 3.13c). In short, these results showed that poor LXR pathway induction in WD-fed mice was not due to insufficient production of LXR ligands.

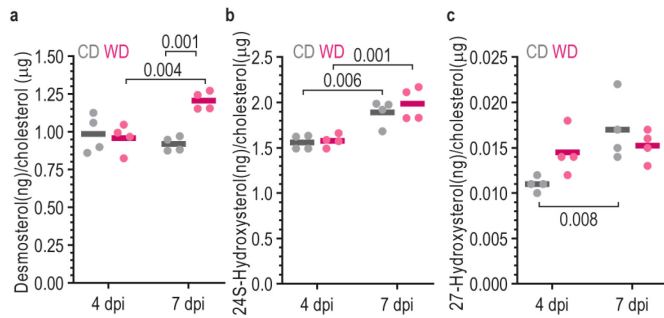


Figure 3.13: The differential production of endogenous LXR ligands does not explain the poor induction of the LXR pathway observed in WD-fed mice. a-c, Quantification of the amounts of the endogenous LXR agonists desmosterol (a), 24S-hydroxysterol (b) and 27-hydroxysterol (c) in the demyelinated lesions at 4 and 7 dpi in CD- and WD-fed mice. Each LXR

ligand was normalized to the cholesterol amounts in the same lesion (two-way ANOVA followed by multiple comparisons correction with Sidak test). Solid lines in the graphs indicate the mean. P-values below 0.1 and n numbers are indicated in the figure. dpi: days post injection, CD: control diet, WD: western diet.

3.3. Insufficient early-phase microglia activation upon demyelination in WD-fed mice

To successfully enter the resolving, lipid processing phase of inflammation, microglia and macrophages first need to enter a pro-inflammatory activation phase (Bogie et al., 2014a). To understand whether poor LXR pathway induction in microglia and macrophages from WD-fed mice was caused by poor initial pro-inflammatory activation, we examined demyelinating lesions at early timepoints after damage; at 2 and 4 dpi. We stained 4 dpi lesions with typical microglia activation markers such as MAC2, MHCII and CD68. Interestingly, we detected lower percentages of MAC2+IBA1⁺ and MHCII+IBA1⁺ phagocytes in the lesions of WD-fed mice (Fig. 3.14a,b,d,e). Despite a small trend, analysis of CD68 staining did not show significant differences between the groups (Fig. 3.14c,f).

Furthermore, we quantified by RT-qPCR the expression of the activation gene *Arg1* in 2 dpi lesions and found a strong trend to lower amounts of this activation gene in lesions from WD-fed mice (Fig. 3.14g). Finally, we used the ARG1-YFP x iNOS-tdTomato double-reporter mouse line to examine

the expression of these inflammatory activation markers in spinal cord lesions from CD- and WD-fed mice at 4 dpi. The quantification of the ARG1⁺IBA1⁺ area demonstrated a similar trend to impaired microglia and macrophage activation in WD-fed mice (Fig. 3.14h,i). Due to difficulties imaging the signal from iNOS, we decided not to quantify the differences in this protein. However, as judged by simple observation, the trend was similar to that observed for ARG1 (Fig. 3.14i).

Interestingly, these results point to an unresponsive state or a lack of plasticity by microglia in WD-fed mice, and contrast with the slight microglia activation we detected in WD-fed mice under unlesioned conditions.

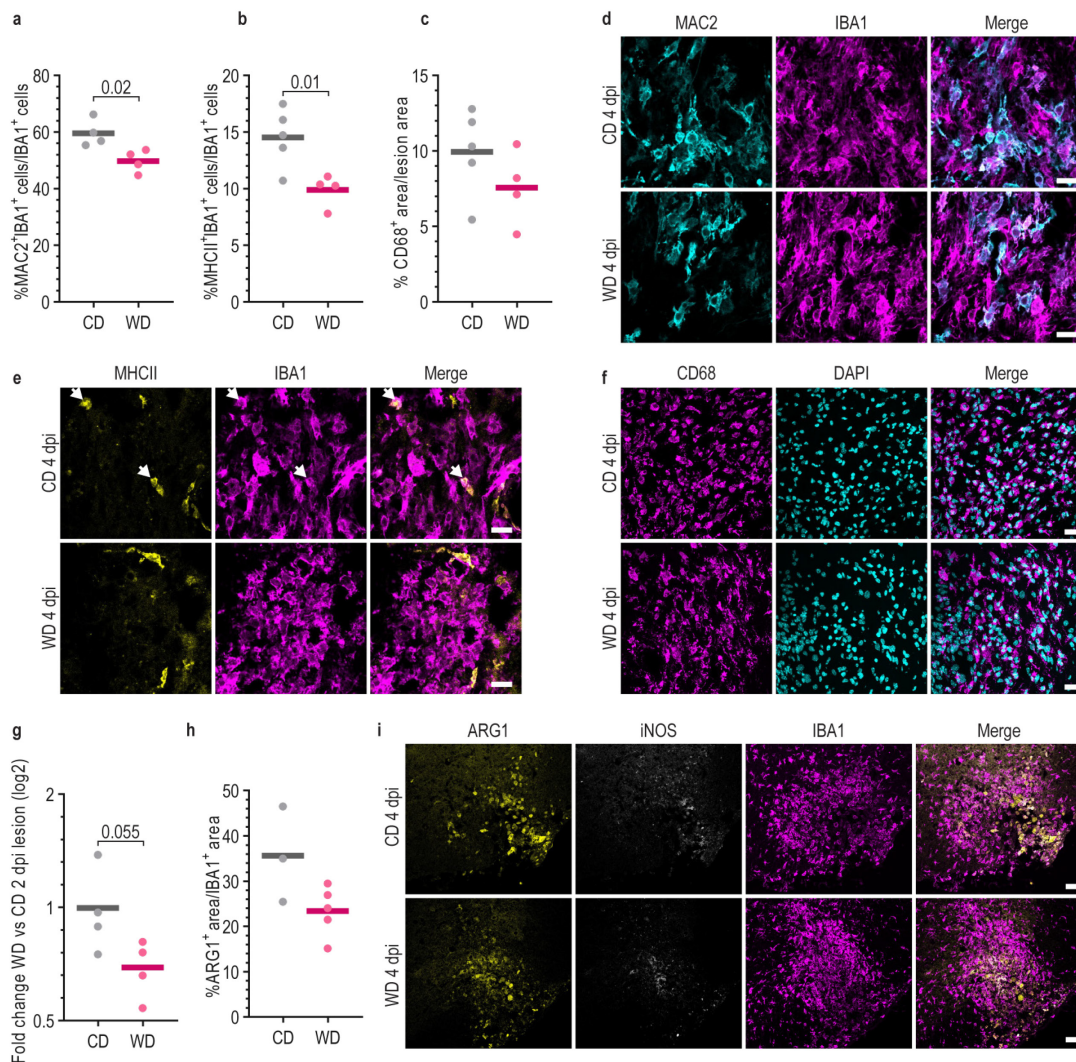


Figure 3.14: Microglia activation upon demyelination is impaired in WD-fed mice. **a,b**, Quantification of the percentage of MAC2⁺ (**a**) and MHCII⁺ (**b**) IBA1⁺ cells in 4 dpi lesions (two-tailed Welch's t-test). **d,e**, Images of demyelinated lesions at 4 dpi exemplifying MAC2⁺ (**d**) and MHCII⁺ (**e**) IBA1⁺ cells. Double-positive labelled cells are shown by white arrows. Scale bar: 20 μm. **c**, Quantification of the lesion area covered by CD68⁺ signal at 4 dpi in CD- and WD-fed mice. **f**, Images of demyelinated lesions at 4 dpi exemplifying CD68⁺ cells. Scale bar: 20 μm. **g**, Quantification of the mRNA expression of *Arg1* in 2 dpi lesions from CD- and WD-fed mice (two-tailed Welch's t-test). **h**, Quantification of the IBA1⁺ area of the lesion covered by ARG1⁺ staining. No significant differences were observed (two-tailed Welch's t-test). **i**, Images of demyelinated lesions in the spinal cord at 4 dpi from iNOS/ARG1 double reporter mice. The signals from ARG1, iNOS and IBA1 are

exemplified. Scale bar: 50 μm . P-values below 0.1 and n numbers are indicated in the figure. Solid lines in the graphs indicate the mean. CD: control diet, WD: western diet, dpi: days post injection.

3.4. TGF β signalling in the CNS of western diet-fed mice

Our results indicated poor activation upon demyelination by microglia and macrophages in WD-fed mice. To look for possible causes, we further searched into our transcriptomic results (see chapter 1.2.2. of Results). Interestingly, we had found that several genes related to the TGF β pathway were increased in microglia from WD-fed mice. In the CNS, TGF β determines microglia's homeostatic signature and keeps microglia in a resting state. Furthermore, in obesity, TGF β signalling seems to be increased not only in the circulation and adipose tissue but also in the CSF and hippocampus (Yan et al., 2014). Hence, we hypothesised that WD causes an increase in TGF β signalling that prevents microglia from responding upon demyelinating injury.

In mammals, the TGF β family is composed of three subtypes: TGF β 1, TGF β 2 and TGF β 3. *In vivo*, these subtypes have distinct properties and distribution. For instance, TGF β 1 is the predominant isoform expressed by the immune system and thus by microglia in the CNS, while TGF β 2 is more commonly expressed by astrocytes (Zhang et al., 2014). TGF β is synthesized from one single gene and includes an N-terminal pro-domain and a C-terminal domain that will form the mature cytokine after cleavage in the Golgi apparatus. Despite cleavage, the pro-domain and the cytokine domain remain non-covalently attached to each other and to milieu molecules (Qin et al., 2018), which prevents TGF β from interacting with its receptors and allows for TGF β to be stored inactive in the extracellular space (Shi et al., 2011).

TGF β signals by binding to tetrameric receptors consisting of two type I receptors (TGF β RI) and two type II receptors (TGF β RII). Both are serine/threonine kinase receptors, and upon ligand binding, TGF β RII phosphorylates the cytoplasmic domain of TGF β RI. This phosphorylated site then recruits SMAD proteins 2 and 3, which also get phosphorylated and activated. Phosphorylated SMAD2/3 then forms a trimeric complex with SMAD4 and translocates into the nucleus to bind SMAD-responsive elements and alter the transcriptional profile of the cell (Feng and Derynck, 2005). Apart from SMAD-mediated transcription, TGF β can activate MAPK, PI3K or RHO GTPases pathways (Zhang, 2009). TGF β negatively regulates its own signalling by promoting the transcription of SMAD7, which can prevent SMAD2/3 from binding to TGF β RI or promote TGF β RI degradation (Tang et al., 2004).

First, we confirmed that TGF β signalling was increased in the CNS of WD-fed mice by RT-qPCR analysis of the two most common TGF β ligands; *Tgfb1* and *Tgfb2* (Fig. 3.15a). Next, we examined the expression of the same genes separately in the white and grey matter of the brain and found a significantly increased amount of *Tgfb2* specifically in the white matter (Fig. 3.15b). Then, we analysed the expression of these genes in the demyelinated lesions at 2 dpi and found that the increased TGF β signalling was persistent at this early timepoint after demyelination, as demonstrated by increased expression of *Tgfb1* (Fig. 3.15c). We confirmed these findings by staining the demyelinated lesions at 4 dpi for pSMAD2, the active form of the TGF β R signalling protein SMAD2. Despite a similar

Results

number of cells in the lesion (Fig. 3.15e), the area occupied by pSMAD2 staining was higher in the lesions from WD-fed mice (Fig. 3.15d,f). To localize the source of TGF β in the lesions, we used RNA in situ hybridization to detect *Tgfb1* and *Tgfb2* mRNA molecules. In the lesioned areas, we found approximately 35% of *Tgfb1* and 20% of *Tgfb2* in microglia, while approximately only 10% of *Tgfb1* and 20% of *Tgfb2* was found in astrocytes (Fig. 3.15j,k).

Together, these findings provide evidence that WD increases TGF β signalling in the CNS and raise the question whether this is the underlying cause for impaired phagocyte activation and lipid processing in WD-fed mice.

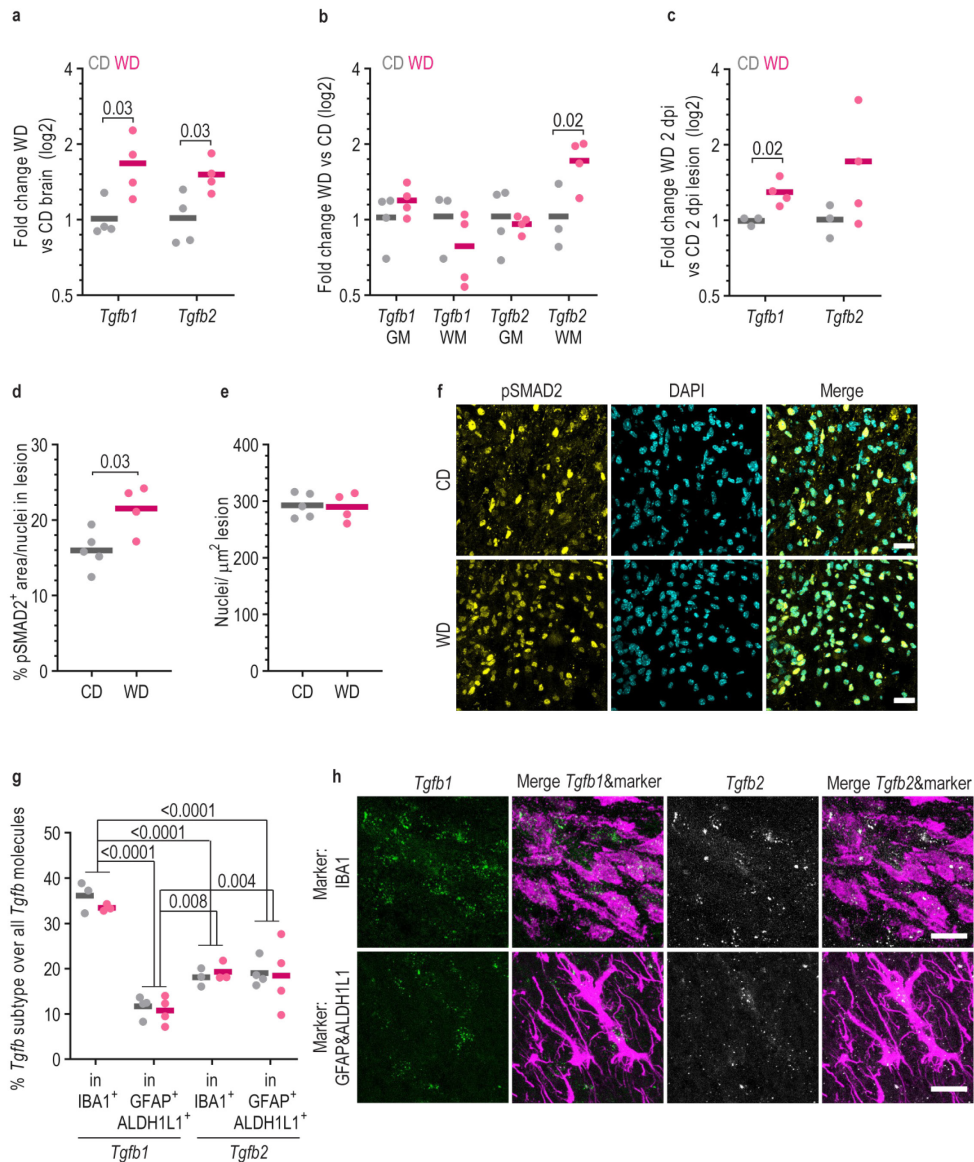


Figure 3.15: TGF β signalling is increased in WD-fed mice. **a**, Quantification of *Tgfb1* and *Tgfb2* expression in the brain (**a**), in the grey and white matter separately (**b**) and in the demyelinated lesion at 2 dpi (**c**) by RT-qPCR (two-tailed Welch's t-test). **d,e**, Quantification of the lesion area covered by pSMAD2 over the number of nuclei in the lesion (**d**) and the number of nuclei per μm^2 of lesion (**e**) in the demyelinated lesions at 4 dpi (two-tailed Welch's t-test). **f**, Images of demyelinated lesions at 4 dpi showing pSMAD2 and DAPI staining. Scale bar: 20 μm . **g**, Quantification of the percentage of *Tgfb1* and *Tgfb2* mRNA molecules in IBA1⁺ or in GFAP⁺ALDH1L1⁺ over the total number of *Tgfb1*

and *Tgfb2* mRNA molecules in a demyelinated lesion at 2 dpi (the differences among different localizations and different *Tgfb* subtypes was analysed by two-way ANOVA followed by multiple comparison correction by Tukey test). **h**, Images of the fluorescent in situ hybridization of *Tgfb1* and *Tgfb2* molecules and its location either within the protein staining of IBA1⁺ cells or GFAP⁺ALDH1L1⁺ cells. Scale bar: 20 μ m. Solid lines in the graphs indicate the mean. P-values below 0.1 and n numbers are indicated in the figure. CD: control diet, WD: western diet, dpi: days after injection.

3.5. TGF β blocks LXR target gene induction after myelin uptake

To understand if TGF β could block LXR pathway induction after myelin uptake in microglia, we needed to isolate the factors involved. Thus, we used an *in vitro* approach where we cultured primary microglia from p7-p10 C57BL/6J mice brains in medium with or without TGF β and examined the phagocytic uptake of myelin (Fig. 3.16a). Four and 24 hours after the myelin wash, we collected cell lysates for RT-qPCR analysis of the mRNA expression changes upon myelin intake. Confirming previous data (Bogie et al., 2012), myelin intake by microglia led to increased expression of *Abca1* and *Abcg1* both at 4 and 24 hours, while *ApoE* increased only after 24 hours (Fig. 3.16b,c grey dots). Notably, when TGF β was added to the medium, the induction of *Abca1* and *Abcg1* transcripts was repressed (Fig. 3.16b,c green dots), demonstrating that; indeed, TGF β had a repressive influence on the induction of the LXR pathway.

Furthermore, we analysed the effect of TGF β on the induction of PPAR target genes *Fabp4*, *Hmox1* and *Plin2* after myelin internalization. We found that only *Fabp4* and *Plin2* were induced in our paradigm, and only after 24 hours (Fig. 3.16d,e grey dots). TGF β had divergent effects on the induction of these genes: TGF β seemed to enhance the induction of *Fabp4*, while it appeared to repress the induction of *Plin2* (Fig. 3.16d,e green dots). Thus, we concluded that the influence of TGF β on the PPAR pathway was diverse and inconsistent, thereby further indicating that the effects of TGF β on the LXR pathway were more relevant.

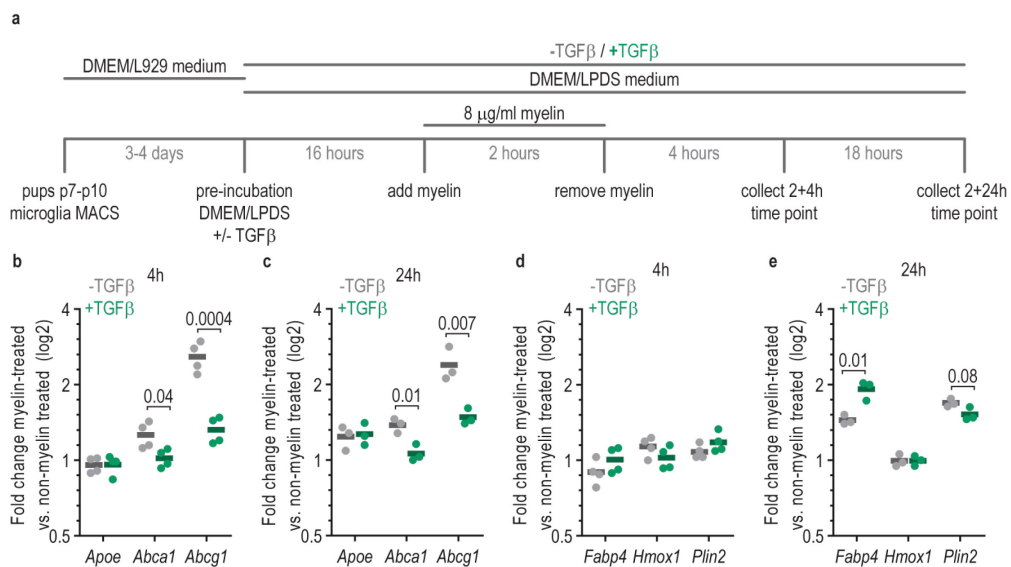


Figure 3.16: TGF β blocks LXR target gene induction after myelin uptake. **a**, Schematic representation of the *in vitro* experimental approach to analyse LXR pathway induction in microglia

Results

upon myelin treatment and TGF β treatment. **b,c**, Quantification of the increase in mRNA expression of *ApoE*, *Abca1* and *Abcg1* 4 hours (**b**) and 24 hours (**c**) after myelin phagocytosis with or without TGF β treatment (two-tailed Welch's t-test). **d,e**, Quantification of the increase in mRNA expression of *Fabp4*, *Hmox1* and *Plin2* 4 hours (**d**) and 24 hours (**e**) after myelin phagocytosis with or without TGF β treatment (two-tailed Welch's t-test). Solid lines in the graphs indicate the mean. P-values below 0.1 and n numbers are indicated in the figure. CD: control diet, WD: western diet, h: hours, dpi: days post injection, LPDS: lipoprotein-deficient serum, L929: L929 cell line-conditioned media.

4. Finding a way to rescue the phenotype

Our data provide evidence that WD-induced TGF β signalling suppresses the transcription of the machinery required for cholesterol efflux in microglia and macrophages after demyelinating injury. To confirm that this TGF β mediates the poor regeneration observed in WD-fed mice, we needed to either block TGF β signalling or promote microglia's early inflammatory response upon demyelination. We performed both approaches, which are explained in the following section.

4.1. Genetic deletion of *Tgfb2* in microglia of WD-fed mice promotes recovery from demyelinating injury

To determine whether WD-induced TGF β signalling was responsible for the poor recovery from demyelination observed in WD-fed mice, we used a microglia-specific conditional *Tgfb2* knock-out mouse line (*Tgfb2* KO). In this mouse line, deletion of *Tgfb2* occurs upon tamoxifen administration in cells expressing the *Cx3cr1* gene (Fig. 3.17a). *Tgfb2* KO (*Cx3cr1*^{CreERT/wt};*Tgfb2*^{fl/fl}) and *Tgfb2* controls (*Cx3cr1*^{wt/wt};*Tgfb2*^{fl/fl}) were fed WD for 4 weeks before injection to induce obesity. All mice were injected with tamoxifen 2 weeks prior to LLC injection and analysed 2 weeks after injection (14 dpi). Interestingly, we observed smaller volumes of demyelination lesion in *Tgfb2* KO mice compared to *Tgfb2* control mice (Fig. 3.17b,f). Furthermore, *Tgfb2* KO mice had reduced accumulation of IBA1⁺ phagocytes (Fig. 3.17c,f), less myelin-loaded IBA1⁺ cells (Fig. 3.17d,g) and less cholesterol crystallization within IBA1⁺ cells (Fig. 3.17e,g), indicating successful lipid processing of myelin debris.

Therefore, specific deletion of TGF β signalling in microglia enhanced lipid processing in these cells and resulted in improved remyelination in WD-fed mice. This observation highlighted once more the role of microglia in coordinating myelin regeneration and indicated that excess TGF β signalling was detrimental for microglia's pro-repair functions.

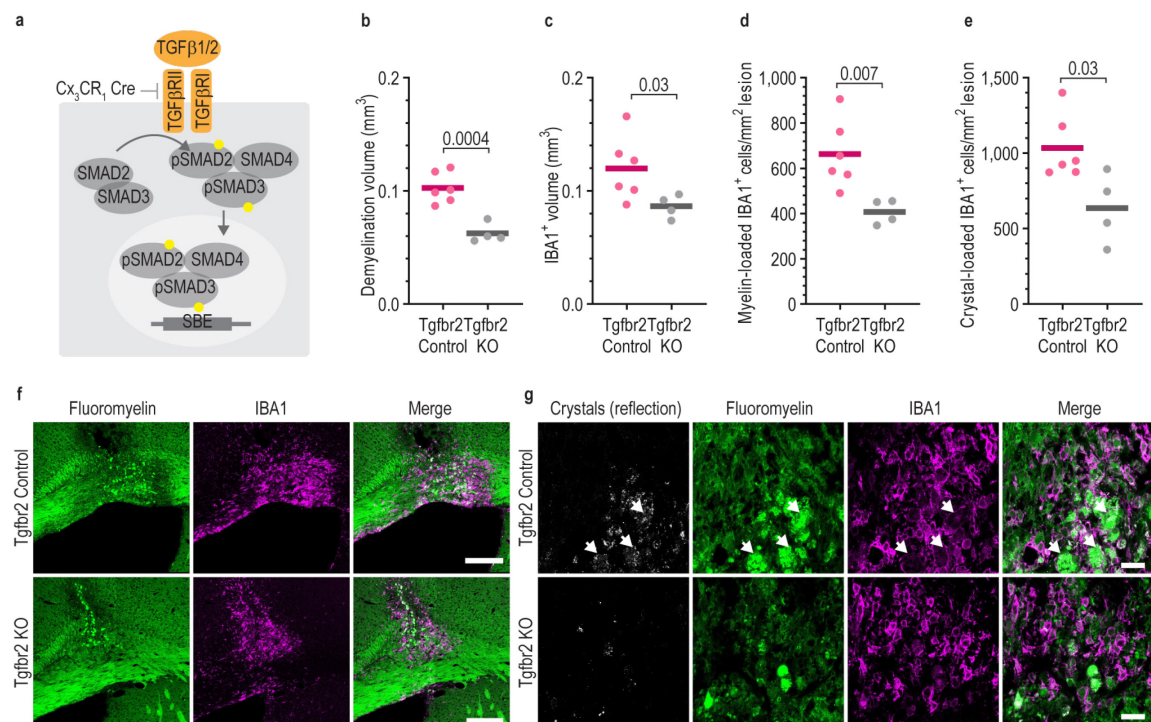


Figure 3.17 (previous page): Genetic deletion of the *Tgfb2* in microglia of WD-fed mice promotes recovery from demyelinating injury. **a**, Illustration to demonstrate the site of action of the conditional genetic knock-out in the TGF β pathway. **b, c**, Quantification of demyelination (**b**) and IBA1⁺ (**c**) volume at 14 dpi in *Cx3cr1^{CreERT};wt;Tgfb2^{fl/fl}* (Tgfb2 KO) or *Cx3cr1^{wt};wt;Tgfb2^{fl/fl}* (Control) mice treated with tamoxifen 14 days before lesion induction (two-tailed Welch's t-test). **d,e**, Quantification of the number of myelin- (**d**) and crystal- (**e**) loaded IBA1⁺ cells per mm² of lesion (two-tailed Welch's t-test). **f**, Images of corpus callosum lesions of *Cx3cr1 wt/wt* vs *Cx3cr1 Cre/wt* mice at 14 dpi. Scale bar: 200 μ m. **g**, Images of the demyelinated lesion in the corpus callosum at 14 dpi exemplifying myelin- and crystal-loaded IBA1⁺ cells in Tgfb2 KO and control mice. White arrows point to crystal- and myelin-loaded IBA1⁺ cells. Scale bar: 20 μ m. P-values below 0.1 and n numbers are indicated in the figure. Solid lines in the graphs indicate the mean. WD: western diet, dpi: days post injection, TGF β RI/II: TGF β receptor I and II, SBE: SMAD-binding elements.

4.2. Galunisertib treatment enhances microglia's reparative immune responses in WD-fed mice but not in old mice

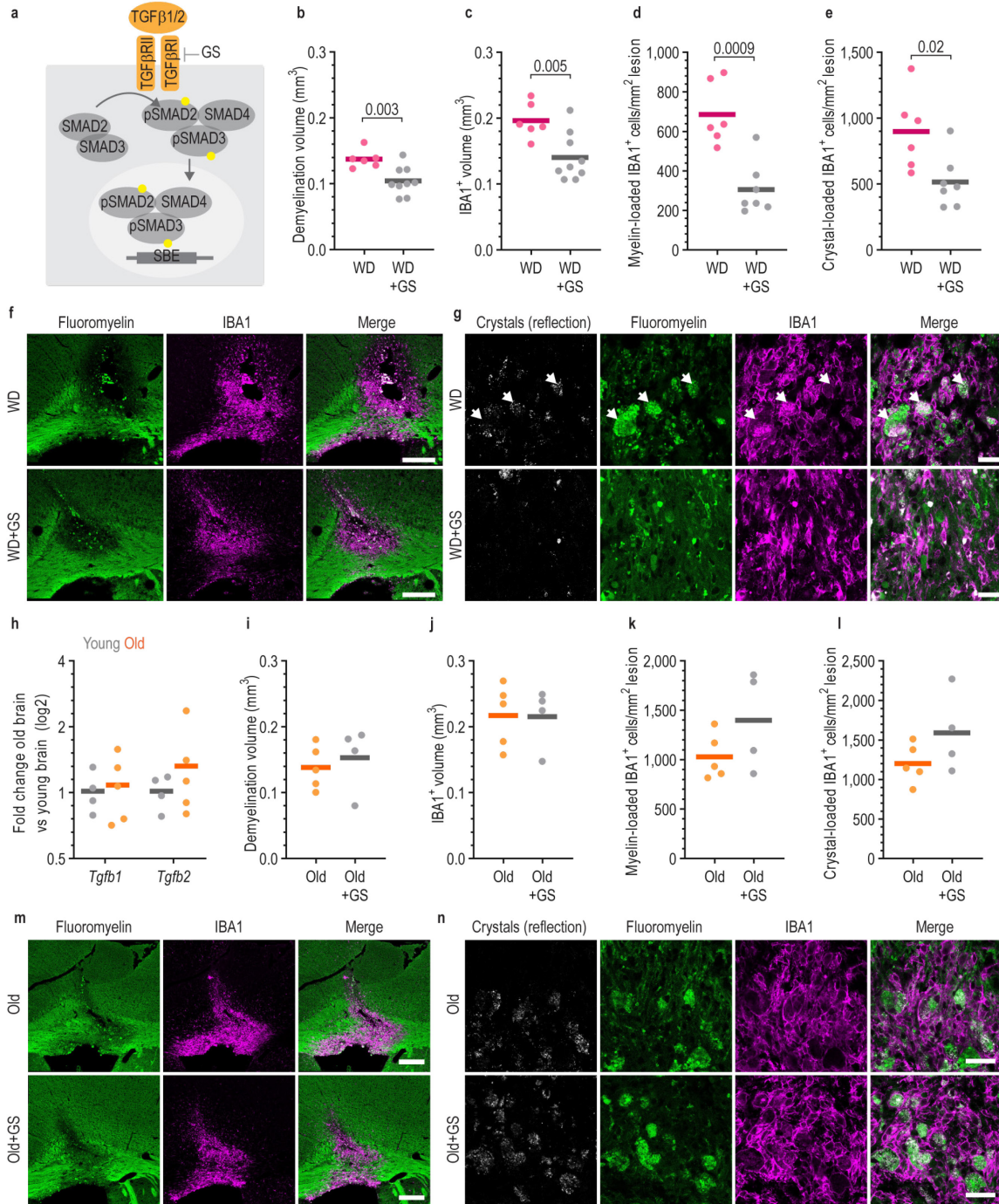
Next, we wanted to examine whether a pharmacological approach that blocks TGF β signalling could also have beneficial effects on recovery from demyelinating injury. We used galunisertib, a TGF β RI blocker currently under clinical trials for glioblastoma treatment (Seystahl et al., 2016), to treat WD-fed and old mice for the duration of the demyelinating injury (14 days) (Fig. 3.18a). In WD-fed mice, galunisertib treatment led to smaller demyelination volumes (Fig. 3.18b,f) and smaller accumulation of IBA1⁺ cells in the lesions (Fig. 3.18c,f). In addition, galunisertib enhanced lipid processing by microglia and macrophages, as the number of myelin-loaded (Fig. 3.18d,g) and crystal-loaded (Fig. 3.18e,g) IBA1⁺ cells was reduced in the lesions of these mice.

In old mice, we detected no differences in the expression of the *Tgfb1* and *Tgfb2* transcripts in the brain by RT-qPCR analysis (Fig. 3.18h). Accordingly, galunisertib treatment did not lead to improved regeneration, as demonstrated by similar demyelination volumes in both galunisertib-treated and vehicle-treated WD-fed mice (Fig. 3.18i,m). The extent of accumulation of IBA1⁺ cells (Fig. 3.18j,m) and the number of myelin-loaded (Fig. 3.18k,n) and crystal-loaded (Fig. 3.18l,n) IBA1⁺ cells were also comparable between both groups, indicating no enhancement of lipid processing in this case.

We concluded that indeed, a pharmacological approach to block TGF β signalling was beneficial for myelin debris clearance and recovery from demyelinating injury in WD-fed mice. Furthermore, we discovered that only when TGF β signalling is upregulated in the CNS (which is the case in WD-fed mice, but not in old mice), will the blockade of TGF β signalling improve myelin debris clearance in phagocytes and enhance recovery from demyelinating damage.

Figure 3.18 (next page): Blocking TGF β signalling with Galunisertib in WD-fed mice promotes recovery from demyelinating injury. **a**, Illustration to demonstrate the mode of action of Galunisertib (GS) in the TGF β pathway. **b,c**, Quantification of demyelination (**b**) and IBA1⁺ (**c**) volume at 14 dpi in WD-fed and WD+GS-fed mice (two-tailed Welch's t-test). **d,e**, Quantification of the number of myelin- (**d**) and crystal- (**e**) loaded IBA1⁺ cells per mm² of lesion (two-tailed Welch's t-test). **f**, Images of corpus callosum lesions of WD-fed and WD+GS-fed mice at 14 dpi. Scale bar: 200 μ m. **g**, Images of the demyelinated lesion in the corpus callosum at 14 dpi exemplifying myelin- and crystal-loaded IBA1⁺ cells in WD- and WD+GS-fed mice. White arrows point to crystal- and myelin-loaded IBA1⁺ cells. Scale bar: 20 μ m. **h**, Quantification of *Tgfb1* and *Tgfb2* expression in the brain of young and old mice by RT-qPCR (two-tailed Welch's t-test). **i,j**, Quantification of demyelination (**i**) and IBA1⁺ (**j**) volume at 14 dpi in old and old+GS mice. No significant differences were found (two-tailed Welch's t-test). **k,l**, Quantification of the number of myelin- (**k**) and crystal-

(l) loaded IBA1⁺ cells per mm² of lesion. No significant differences were found (two-tailed Welch's t-test). **m**, Images of corpus callosum lesions of old and old+GS mice at 14 dpi. Scale bar: 200 μ m. **n**, Images of the demyelinated lesion in the corpus callosum at 14 dpi exemplifying myelin- and crystal-loaded IBA1⁺ cells in old and old+GS mice. Scale bar: 20 μ m. P values below 0.1 and n numbers are indicated in the figure. Solid lines in the graphs indicate the mean. GS: Galunisertib, WD: western diet, dpi: days post injection, TGF β R1/II: TGF β receptor I and II, SBE: SMAD-binding elements.



4.3. Enhancing TREM2 activity improves lipid clearance by microglia and macrophages after demyelinating injury

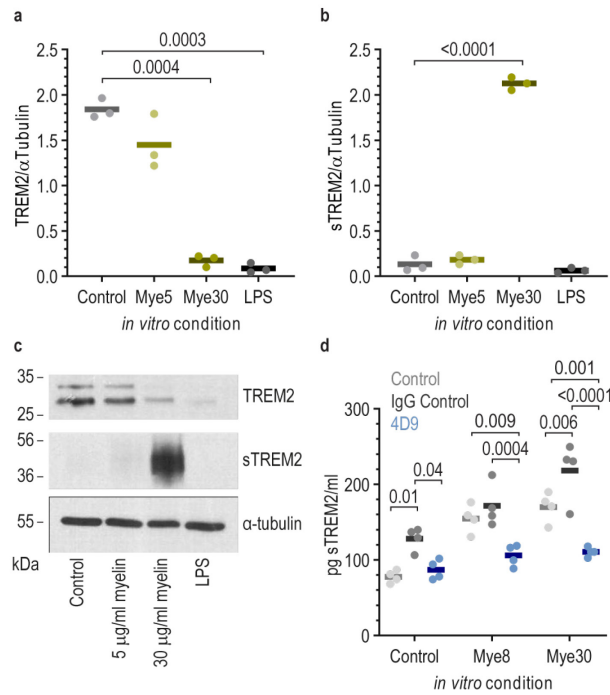
The functions of TGF β and TREM2 can be seen as two opposing factors governing microglia activation (Fig. 1.2) (Song and Colonna, 2018). In our study, blocking TGF β signalling was beneficial for repair, thus; we speculated that enhancing TREM2 could have similar effects. Indeed, a recent study using a chronic demyelination model showed that cholesterol efflux is defective in TREM2 KO microglia, leading to accumulation of cholesteryl esters in these cells upon myelin intake (Nugent et al., 2020). Hence, we hypothesised that enhancing TREM2 function could improve microglia's early inflammatory response, promote lipid processing by microglia and macrophages and act as a pro-regenerative therapy.

To enhance TREM2 function, we used an approach that prevents the termination of TREM2-induced signalling. Termination of TREM2 signalling is mediated by TREM2 cleavage, which releases a soluble TREM2 ectodomain (sTREM2) into the extracellular space (Kleinberger et al., 2014; Wunderlich et al., 2013), a process also named TREM2 shedding. Although the mechanism driving the cleavage is unknown, TREM2 cleavage leads to silencing of the pathway and subsequent suppression of lipid metabolism pathways necessary for beneficial microglia function.

First, we assessed how myelin debris intake by microglia influenced TREM2 shedding. For this, we treated primary microglia cultures with different myelin concentrations and determined the presence of full-length TREM2 (TREM2) and cleaved TREM2 (sTREM2) by western blot analysis. Treatment of microglia with high concentrations of myelin debris caused lipid overload in microglia, which was associated with a profound depletion of full-length TREM2 in microglial cell lysates (Fig. 3.19a,c) and an intense increase in sTREM2 in the supernatant (Fig. 3.19b,c). To prevent TREM2 shedding and thus enhance TREM2 function, we used a monoclonal antibody named 4D9 that was recently identified by Schlepckow et al. (Schlepckow et al., 2020). In this study, 4D9 potently inhibits TREM2 shedding and promotes the activation of phospho-SYK signalling. In our primary microglia cultures, 4D9 successfully prevented the TREM2 shedding caused by myelin debris intake (Fig. 3.19d), demonstrating that 4D9 was also functional in this context.

Figure 3.19 (next page): Myelin intake by microglia causes TREM2 shedding. a,b Quantification of the band density in western blots of TREM2-labelled (a) and sTREM2-labelled (b) bands normalized by the density of the bands labelled by α -tubulin. Microglia were treated with myelin for 24 hours (one-way Brown-Forsythe and Welch ANOVA tests with multiple comparisons corrected by Dunnett T3 test). c, Example images of the western blots used for quantification of TREM2 and sTREM2 densities. Molecular weight ladders are indicated on the left side. d, Quantification by ELISA of the amounts of sTREM2 found in the media in different conditions. Microglia were treated with 20 μ g/ml of 4D9 antibody or IgG isotype control for 16 hours, followed by 24 hours of myelin treatment (two-way ANOVA followed by multiple comparisons between groups within the same *in vitro* condition. Tukey test used for correction of multiple comparisons). P-values and n numbers are indicated in the figure. Solid lines in the graphs indicate the mean. sTREM2: soluble TREM2, Mye5: 5 μ g/ml myelin treatment, Mye8: 8 μ g/ml myelin treatment, Mye30: 30 μ g/ml myelin treatment, 4D9: TREM2 enhancing antibody.

Finding a way to rescue the phenotype



To examine whether 4D9 could promote lipid processing by microglia and macrophages and remyelination *in vivo*, we used 4D9 to treat WD-fed mice. For this, we induced focal demyelination in the spinal cord of WD-fed mice treated either with 4D9 antibody or an IgG isotype control for 14 days. Upon study termination, the injured spinal cords were collected to determine lipid loading in phagocytes by electron microscopy. We observed that the number of foam cells harbouring lipid droplets was reduced in 4D9-treated as compared to control antibody-treated WD-fed mice (Fig. 3.20a,b). To investigate whether TREM2 enhancement was also beneficial for aged-induced remyelination failure, we examined the effect of the 4D9 antibody on recovery from demyelinating injury in 12-month old mice. Old mice were treated with 4D9 or an isotype control antibody for 14 and 21 days. Numerous foam cells harbouring lipid droplets and needle-shaped cholesterol crystals, were found in isotype control antibody treated animals. Notably, we observed a marked reduction of foam cells in 4D9-treated mice (Fig. 3.20c,d). Finally, we determined the number of remyelinated axons on semithin sections and found that remyelination was significantly enhanced in 4D9-treated old mice as compared to isotype controls at 21 dpi (Fig. 3.20e,f).

Together, these findings indicate that promoting TREM2 function with a TREM2 enhancing antibody improves lipid processing by microglia and macrophages. These effects lead to improved remyelination in a model of remyelination failure such as 12-month old mice. Hence, a TREM2-enhancing antibody represents a potential novel therapy to improve recovery after demyelinating injury.

Results

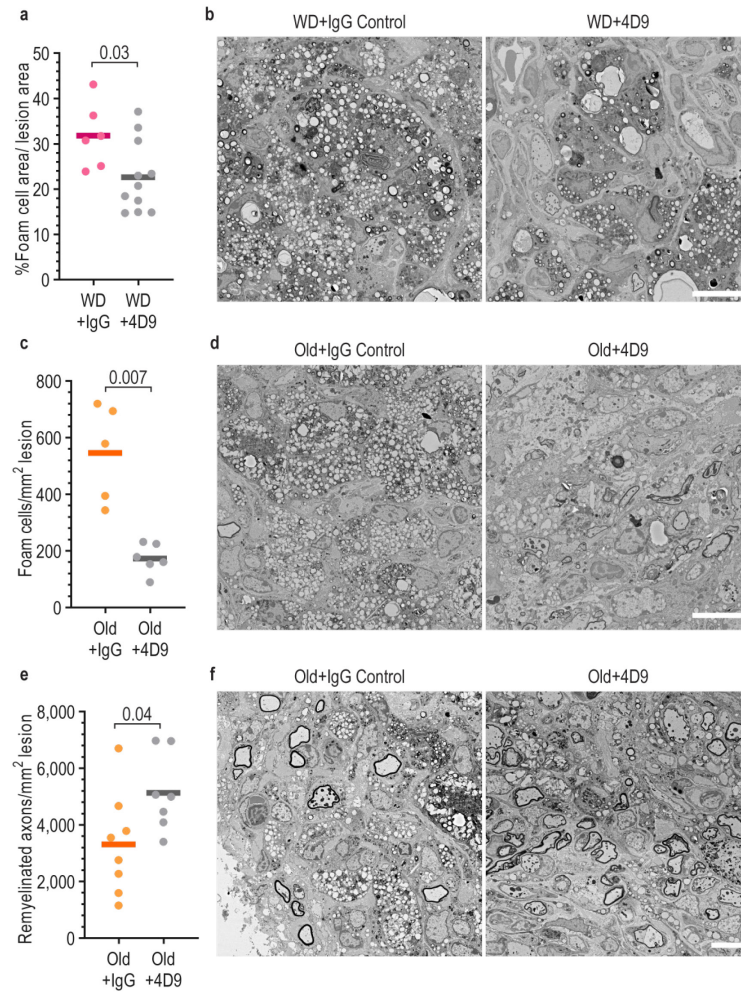


Figure 3.20: Treatment with the TREM2-activating monoclonal antibody 4D9 improves lipid clearance in phagocytes after demyelinating injury. **a**, Quantification of the percentage of lesion area occupied by foam cells at 14 dpi in WD-fed mice treated intraperitoneally with 100 mg/kgBW of 4D9 antibody or its isotype control at day 0, 3 and 7 after injection (two-tailed Welch's t-test). **b**, Electron microscopy images of the demyelinated lesions in the spinal cord at 14 dpi exemplifying foam cell accumulation within the lesion. Scale bar: 10 μ m. **c**, Quantification of the number of foam cells per mm² of lesion at 14 dpi in 12-month-old mice treated intraperitoneally with 100 mg/kgBW 4D9 antibody or its isotype control at day 0, 3, 7 after injection (two-tailed Welch's t-test). **d**, Electron microscopy images of the demyelinated lesions in the spinal cord at 14 dpi exemplifying foam cell accumulation within the lesion. Scale bar: 10 μ m. **e**, Quantification of the number of remyelinated axons per mm² of lesion at 21 dpi in 12-month-old mice treated intraperitoneally with 100 mg/kgBW of 4D9 antibody or its isotype control at day 0, 3, 7 and 14 after injection (two-tailed Welch's t-test). **f**, Electron microscopy images of the demyelinated lesions in the spinal cord at 21 dpi exemplifying remyelinated axons. Scale bar: 10 μ m. P-values below 0.1 and n numbers are indicated in the figure. Solid lines in the graphs indicate the mean. WD: western diet, IgG: control Immunoglobulin treatment. 4D9: TREM2-enhancing antibody.

Discussion

Our study focuses on the relation between diet, microglia function, lipid metabolism and remyelination. We explored how WD consumption alters microglia's pro-repair functions upon demyelinating injury in the CNS. Interestingly, we found that WD intake causes a decline in remyelination efficiency that mimics the effects of ageing. WD feeding results in an impaired ability of microglia to respond to and resolve the innate inflammatory process that occurs after myelin injury. This leads to an overwhelming of the phagocytic efflux capacities and excessive accumulation of cholesterol-rich myelin debris within microglia and macrophages, which results in the transition of cholesterol to crystals that further promote a maladaptive immune response. We found that stimulation of lipid processing pathways in microglia and macrophages using agonists of the LXR and PPAR α / γ pathways was sufficient to restore the capacity of WD-fed mice to resolve lipid accumulation in microglia and macrophages, providing evidence that these lipid clearance pathways are central in regulating phagocyte function during recovery from demyelinating injury.

To understand the molecular basis for nuclear lipid receptor unresponsiveness in WD-fed mice, we further studied how WD affects the brain and microglia function during homeostatic conditions. Surprisingly, we found that WD causes alterations in the brain lipid composition and a low degree of microglia activation in the white matter, which was associated with increased production of TGF β . Such excess TGF β prevented microglia activation and led to impaired LXR pathway activation and cholesterol efflux in microglia, thereby perturbing remyelination. Promoting microglia activation by either blocking TGF β signalling or promoting TREM2 function successfully improved remyelination efficiency.

Our findings can be summarized in three main conclusions that will be separately discussed. First, obese mice poorly regenerate myelin after toxin-induced demyelination due to deficient lipid processing by CNS macrophages. Second, excess TGF β signalling in the microglia of WD-fed mice causes insufficient microglia response and impaired cholesterol efflux, which ultimately lead to poor myelin regeneration. Third, WD feeding alters the lipid composition of the brain white and grey matter and is associated with microglia reactivity in the corpus callosum.

1. Remyelination is impaired in obese mice

1.1. WD intake and leptin deficiency cause poor myelin regeneration

Our findings using both WD-induced and genetically induced obesity models indicate that obesity impairs myelin regeneration in the CNS. Poor wound healing in peripheral tissues of obese mice models has been described previously (Fantuzzi and Faggioni, 2000; Goodson and Hunt, 1986; Tsuboi and Rifkin, 1990); however, our data offers the first indication that such impairment could be mirrored in the CNS. To better understand the role of WD in MS, it would be interesting to examine the influence of WD on other MS models, such as EAE. So far, feeding HFD to EAE models proved detrimental, while calorie restriction experiments were beneficial (Manzel et al., 2014), further

increasing the evidence for a detrimental role of obesity on MS. I am confident that mechanistic investigations of this influence will provide a better understanding of the risk factors for this disease. Furthermore, it remains to be elucidated whether and how obesity affects other diseases of the CNS such as AD, PD, HD or stroke. Thus far, the suggested mechanisms are driven by changes in the CNS vasculature, inflammation, oxidative stress and hormonal dysregulation (Awada et al., 2013; Naderali et al., 2009).

It is important to highlight that the persistently demyelinated lesions of WD-fed mice seemed to recapitulate the pathological hallmarks of old mice. In this study, we tested our hypotheses both in WD-fed mice and in old mice to understand whether similar mechanisms apply to both cohorts. Our results indicate that, indeed, similar mechanisms apply in some cases, but not all. Thus, a detailed transcriptomics analysis to understand the mechanisms of microglia response to LLC-induced demyelination under (1) healthy conditions, (2) WD consumption and (3) old age would be necessary to be able to compare which perturbed pro-repair mechanisms are shared and which are divergent between WD-fed mice and old mice. Such screening approach will provide us with a detailed view on which mechanisms are most relevant and hence, which elements to target.

Even though we have not specifically addressed the question of whether diets rich in specific types of lipids such as SFAs, PUFAs or ω 3- and ω 6-PUFAs also influence regeneration, other studies using different models of demyelination demonstrate that ω 3-PUFA-rich diets can prevent demyelination and enhance remyelination when compared to ω 6-PUFA-rich diets (Siegert et al., 2017; Torkildsen et al., 2009). Regarding the direct comparison between PUFA-rich and SFA-rich diets, nothing has been yet published. However, the WD is rich in SFAs and poor in PUFAs, indicating that a high SFA/PUFA ratio is detrimental for myelin regeneration. Various mechanisms might mediate the effects of these diets, yet one main mechanism currently under study is the production of lipid resolution mediators. These are PUFA-derived lipid species that promote inflammation resolution or catabasis; the coordinated and active process aimed at restoration of tissue integrity and function (Tabas, 2010; Viola and Soehnlein, 2015). It will be interesting to investigate the influence of PUFA- or SFA-rich diets on remyelination and the role of lipid resolution mediators in remyelination.

A remaining question is: does the changed lipidome in the brain cause impaired remyelination, or is this due to poor microglia function due to obesity-induced neuroinflammation? Unfortunately, it is extremely challenging to dissociate the WD-associated changes in the brain lipidome from the WD-induced neuroinflammation. We were able to replicate our results in WD-fed mice with leptin-deficient mice, suggesting that the poor regenerative response in obese mice is not only due to diet components, but rather due to obesity and its associated co-morbidities such as atherosclerosis and diabetes. However, we did not examine the brain lipidome of leptin-deficient mice, thus; we cannot discard that these mice might also have lipid profile changes in the brain that affect its regenerative capacity. Personally, I am inclined to think that although the changes in brain lipidome can potentially alter microglia function, it is chronic neuroinflammation which ultimately has a stronger influence on microglia function, but further experiments are necessary to achieve a better understanding of this question.

1.2. Impaired lipid processing by phagocytes as the underlying mechanism of poor myelin regeneration

Our results suggest an impairment of cholesterol efflux by microglia and macrophages as a possible shared mechanism of failure between WD-fed and old mice. Indeed, stimulation of the LXR pathway resulted in enhanced lipid clearance by microglia and macrophages and improved remyelination both in WD-fed and in old mice. Nevertheless, since this treatment was not cell-specific, we should consider the effects of this treatment on other cell types. For example, astrocytes are master regulators of cholesterol homeostasis in the brain. They are the main producers of cholesterol and lipoproteins and provide cholesterol to oligodendrocytes and neurons through LXR-dependent reverse cholesterol transport (Courtney and Landreth, 2016; Wang et al., 2002). Furthermore, the LXR pathway also regulates myelination, as demonstrated by myelination impairments in LXR-deficient mice (Wang et al., 2002). Likewise, LXR agonists stimulate oligodendrocytes differentiation and regulate the expression of myelin-related genes (Shackleford et al., 2013). Hence, it is plausible that the effects from systemic LXR agonism stem not only from the beneficial effects on microglia and macrophages but also on other glial cells. To discern whether the effects we observe are microglia-specific, we used a microglia-specific, inducible ABCA1/G1 double KO mouse line. These mice, whose cholesterol efflux pathway is blocked in microglia, demonstrate reduced remyelination and increased inflammation and crystal formation in demyelinated lesions (Cantuti-Castelvetri et al., 2018). However, more evidence would be necessary to demonstrate the specificity of this effect.

In addition, we should consider the effects of these treatments on the periphery. This is especially relevant for the treatment using fenofibrate and rosiglitazone on WD-fed mice. Both PPAR agonists have beneficial effects on lipid metabolism by improving liver, muscle and adipose tissue function. More importantly, fenofibrate efficiently decreased body weight in WD-fed and old mice in our set up. Hence, it is plausible to think that the beneficial effects on immune cell function and ultimately on repair that we observed in WD-fed mice could derive from a general improvement of health, i.e. from “treating obesity”. Even more, this could further explain why these drugs had a beneficial effect on WD-fed mice but not in old mice. Hence, we would need to perform further tests to demonstrate a central effect of these drugs in our paradigm, such as target engagement experiments or direct brain drug delivery experiments.

The anti-inflammatory effects of LXR and PPAR α/γ stimulation, mainly mediated by parallel inhibition of the AP1 and NF κ B pathways, could further contribute to the beneficial effects of LXR and PPAR α/γ agonism on WD-fed mice. Given the main role of inflammation resolution in lesion repair (Serhan, 2007; Viola and Soehnlein, 2015), it is possible that these anti-inflammatory effects drive inflammation resolution and thus, partially promote remyelination. Debris clearance and lipid processing are also essential steps for inflammation resolution, thereby making it difficult to dissect between the direct and indirect effects that these drugs might have on inflammation. Nevertheless, it would be worth to further examine the inflammatory profile of microglia in mice treated with LXR and PPAR α/γ agonists. Interestingly, we already have some hints that point to differential microglia and macrophage function upon rosiglitazone treatment, since the demyelinated lesions in these mice

seemed to accumulate higher numbers of microglia/MDMs (see chapter 2.4 of Results). A deeper understanding of the common mechanisms underlying the beneficial effects of LXR and PPAR α/γ stimulation could lead us to new ideas on how to promote a beneficial microglial response.

1.3. Translational potential of lipid-processing stimulating drugs

Despite the promising observations in basic research using LXR agonists, which seemed to indicate translational potential, most synthetic LXR agonists cause hepatotoxic side effects in humans that limit their clinical use (Fan et al., 2018). Specifically, apart from promoting cholesterol efflux, these drugs increase hepatic lipogenesis, hypertriglyceridemia and liver steatosis by inducing the expression of SREBP1c (Schultz et al., 2000). These effects are mostly attributed to LXR α ; thus, several alternatives are being proposed that could specifically target LXR β and prevent side effects. This is extremely challenging, since LXR α and β share 77% sequence homology in their ligand binding domain and have a highly flexible binding pocket, thereby making it difficult to find subtype-selective agonists (Molteni et al., 2007; Temml et al., 2014). Another strategy currently tested is to use desmosterol mimetics to stimulate the LXR pathway. Desmosterol is the most abundant natural LXR ligand in foam cells and, apart from binding and activating LXR, also inhibits SREBP processing (Spann et al., 2012). Furthermore, Muse et al. demonstrated that desmosterol strongly activates LXR and suppressed SREBP in mouse and human macrophages, while it has almost no activity on mouse or human hepatocytes (Muse et al., 2018). A very recent report also demonstrates beneficial effects of desmosterol mimetics on remyelination in mouse models of MS (Berghoff et al., *submitted*). Thus, it appears that an approach to target LXR that better resembles physiological conditions could be beneficial.

The use of PPAR α/γ agonists to stimulate pro-repair functions in microglia and macrophages to promote remyelination is slightly controversial. In our hands, agonism of PPAR α/γ pathways is only beneficial for WD-fed mice, not for old mice, indicating that we are targeting a mechanism only occurrent due to obesity, but not age. Furthermore, PPAR α/γ therapies have profound peripheral effects, thereby making their recommendation to MS patients slightly more challenging. Another member of the PPAR family, PPAR δ , is highly expressed in both mouse and human microglia and macrophages and is a key regulator of fat burning. Furthermore, it appears that the phosphatidylserine residues found in myelin can activate the PPAR δ pathway in phagocytes, as corroborated by the activation of PPAR δ in foam cells within active MS lesions (Bogie et al., 2014b). Hence, it will be interesting to examine whether PPAR δ activators could enhance pro-repair functions of phagocytes both in WD-fed mice and old mice.

Another possible drug target to stimulate lipid processing is the RXR. This is the common partner for heterodimerization of the LXR and PPARs, and its activation can have synergistic effects on these pathways. Indeed, a study by Natrajan et al. demonstrated that stimulation of the RXR using the agonist bexarotene led to improved myelin debris clearance in aged macrophages and reversed the gene expression profile in monocytes from MS patients to a more beneficial profile (Natrajan et al., 2015). In any case, it is clear that stimulating myelin clearance by phagocytes by activating the LXR/PPAR/RXR pathways is a feasible promising strategy to promote remyelination in MS.

2. Excess TGF β signalling perturbs cholesterol efflux

2.1. TGF β is increased in the brain of WD-fed mice

In our study, WD-fed mice have increased TGF β signalling in the CNS, rendering their microglia unable to respond to demyelination and leading to poor LXR pathway activation and impaired lipid processing. Therefore, our results indicate TGF β signalling can influence both inflammation and obesity. Indeed, TGF β signalling has a crucial role in regulating inflammation: *Tgfb1* knock-out mice die either at the embryonic or early postnatal stage from uncontrolled lymphocyte proliferation and autoimmunity that lead to multi-organ failure (Robertson and Rifkin, 2016). Interestingly, CNS-specific *Tgfb1* knock-out mice develop motor symptoms four to six months after birth (Lund et al., 2018). Likewise, loss of LRRC3, a milieu molecule uniquely associated with, and required for, integrin-dependent activation of TGF β 1 in macrophages and microglia, leads to ascending paraparesis characterized by demyelination and axonal loss that leads to death by five months of age (Qin et al., 2018). Furthermore, TGF β seems to play a role in the regulation of obesity: TGF β 1 levels are positively correlated to adiposity in rodents and to body mass index and fat mass in humans (Alessi et al., 2000; Yadav et al., 2011). Interestingly, systemic blockade of TGF β or genetic removal of SMAD3 protects from diet-induced obesity and diabetes in mouse models (Yadav et al., 2011).

Our results show that TGF β 1 and 2 are increased in the brain of WD-fed mice. A previous report measured TGF β 1 in the hippocampus and cerebrospinal fluid and found increased levels in HFD-fed and aged mice, which were recoverable by a two-month calorie-restrictive diet (Yan et al., 2014). Yet, no source or cause for the central increase in TGF β signalling have been identified. In the periphery, it has been suggested that circulating TNF α can increase *Tgfb* mRNA expression in the adipose tissue, which in turn can contribute to the stimulation of plasminogen activator inhibitor-1 secretion and to cardiovascular complications (Samad et al., 1997). Whether similar mechanisms occur in the CNS has not yet been investigated. In the CNS, TGF β is mainly produced by microglia, astrocytes and endothelial cells (Zhang et al., 2014). Considering that these cells might respond to obesity-related neuroinflammation and lipid changes, it is possible that they alter the expression of cytokines such as TGF β , thereby becoming the source of increased TGF β . Furthermore, circulating TGF β could also contribute to the effects we observed. To examine this, we could collect serum and cerebrospinal fluid from CD- and WD-fed mice to measure TGF β . Regarding the cause for excess TGF β production, our data support previous findings by Yan et al., where they speculate that TGF β signalling is initially triggered as an adaptive mechanism to normalize the inflammatory environment during a chronic inflammatory insult (Yan et al., 2014). To this end, it would be interesting to examine how different durations of WD feeding would affect TGF β signalling.

2.2. Excess TGF β signalling perturbs microglia's response to myelin damage

Our results indicate that the WD-induced increase in TGF β signalling impairs microglia's response to demyelination. In the uninjured CNS, TGF β tightly regulates microglia function by promoting a homeostatic, inactivated state. Indeed, deletion of the *Tgfb2* in microglia increases microglia density and alters microglia morphology in the retina (Ma et al., 2019) and in the brain (Buttgereit et al., 2016; Zöller et al., 2018). Further characterization of microglia devoid of *Tgfb2* demonstrated higher

expression of activation markers such as CD45, AXL, CD74, F4/80 and MHCII, downregulation of homeostatic markers such as Siglec-H and elevated expression of IL1 β , TNF α and CXCL10 (Buttgereit et al., 2016; Zöller et al., 2018), indicating that absence of TGF β 1 signalling leads to microglia activation. Thus, TGF β acts a “checkpoint mechanism” that ensures tight regulation of microglia responsiveness. As suggested by Deczkowska et al. (Deczkowska et al., 2018), such checkpoint mechanisms can limit the ability of microglia to protect the CNS in the context of chronic neuroinflammatory disease. For example, loss or mutations of the lipid-sensor TREM2, which is necessary to trigger microglia activation, prevent microglia from detecting and clustering around amyloid β plaques and damaged neurons (Wang et al., 2015), contributing to neurodegeneration. Likewise, the fractaline receptor CX₃CR1, which normally prevents microglia activation, hinders amyloid β clearance (Lee et al., 2010; Liu et al., 2010). In our study, obesity-induced excess TGF β signalling also leads to inappropriate microglia responses. Thus, our findings support the idea that checkpoint mechanisms can be detrimental in the context of chronic neuroinflammatory diseases.

The altered inflammation dynamics that we observed further support the established notion that the activation profile of microglia and MDMs must be dynamically regulated for efficient regeneration (Lloyd and Miron, 2019). Alterations of this dynamics due to pre-existing neuroinflammation, aberrant immune checkpoint mechanisms or slower phagocyte response inevitably result in impaired remyelination. Several studies have demonstrated that various macrophage populations are necessary to respond to demyelination and promote remyelination, and that the switch between them must be timely coordinated for successful repair (Lloyd et al., 2019; Miron et al., 2013; Ruckh et al., 2012; Vogel et al., 2013). In our model, enhancing microglia activation by antagonizing TGF β signalling in microglia or promoting TREM2 function improved remyelination in WD-fed and old mice. Furthermore, promoting lipid processing by inducing LXR and PPAR α/γ pathways proved beneficial for inflammation resolution and repair. Thus, our data underline the relevance of an early strong inflammatory response and the switch to a pro-resolving, lipid-processing response (Bogie et al., 2014a).

The inflammatory response to demyelination in WD-fed mice was delayed due to an excess in TGF β signalling, which led to impaired lipid processing by phagocytes. Therefore, in these mice the dynamics controlling the inflammatory response are completely dysregulated. When we examined the change in *Tgfb1* and *Tgfb2* transcripts between 2 and 7 dpi, we detected an increase in these transcripts in CD-fed mice. However, in WD-fed mice there was no change. Therefore, the normal cytokine dynamics are altered by a pre-existent alteration in TGF β levels. In order to further refine this hypothesis, it would be interesting to analyse the expression of various cytokines and activation markers in different timepoints after demyelination. In addition, it would be necessary to analyse the influence of our different intervention strategies (LXR/PPAR α/γ agonists, *tgfb2* knock-out, galunisertib and 4D9 antibody) in an early timepoint after damage (e.g. 4 dpi) to evaluate the influence of these treatments on the initial inflammatory response.

In this study, blocking TGF β signalling proved beneficial for myelin regeneration. Nonetheless, whether suppressing TGF β signalling is beneficial or detrimental for neurodegenerative disease

appears to be dependent on its source and cellular target. For instance, Endo et al. (Endo et al., 2015) report beneficial effects by demonstrating that astrocyte-derived TGF β 1 accelerates disease progression in ALS in mice due to impaired microglia activation, which reduces the neuroprotective properties of microglia. In addition, the rising levels of circulating TGF β known to occur with ageing seem to impair the ability of microglia to promote remyelination (Baror et al., 2019) and inhibiting TGF β signalling inhibited glial scar formation and promoted neurite outgrowth after vascular damage (Schachtrup et al., 2010). However, TGF β limited ischemic damage in a model of stroke (Doyle et al., 2010), and systemic administration of TGF β 1 decreased disease severity in EAE (Kuruvilla et al., 1991) and promoted oligodendrocyte maturation in the spinal cord after toxin-induced demyelination (Hamaguchi et al., 2019). Despite the apparent contradictions, which are expected from targeting a pleiotropic cytokine such as TGF β , we believe that neurological diseases characterized by a weak microglia response might benefit from furthering microglia activation through either the acute hindrance of TGF β signalling or the promotion of beneficial microglia activation by enhancing TREM2 signalling.

In MS, serum levels of TGF β 1 are augmented, especially during relapses, which might represent an endogenous pro-resolution mechanism to counteract ongoing immunoinflammatory events (Nicoletti et al., 1998). TGF β 1 expression can also be detected in the demyelinated lesions in MS patients and in the EAE model (De Groot et al., 1999; Issazadeh et al., 1995), further indicating an important role for this cytokine in MS. Considering the autoimmune nature of this disease, we are aware that inhibiting TGF β signalling in MS patients is not the most appropriate therapeutic strategy. That's why we have searched for alternative strategies to target the same checkpoint mechanism. Since TREM2 and TGF β control microglia response in opposite directions, we used the TREM2-enhancing antibody 4D9 to promote microglia activation independently of TGF β . Since this treatment was beneficial for both WD-fed and old mice, we believe that TREM2 could be a potential target for remyelination therapy. Our next step will be to treat EAE mice with the 4D9 antibody, to explore whether TREM2 stimulation will also prove beneficial in the context of an autoimmune demyelinating disease.

Lastly, it is important to note that TGF β also has an essential role in regulating scarring. During tissue wound repair, a scar might be formed to resolve the damage and restore the key functions of the tissue (Fawcett and Asher, 1999). In the CNS, injury almost always results in the formation of a glial scar, which includes multiple cellular and extracellular components (Bradbury and Burnside, 2019). This includes chronic MS lesions, characterized by astroglial scarring in the lesion centre. Such scarring is profoundly detrimental for lesion repair, as it inhibits axonal regeneration and remyelination (Silver and Miller, 2004). TGF β seems to promote glial scar formation by promoting the release of extracellular molecules by astrocytes (Schachtrup et al., 2010; Silver and Miller, 2004; Song et al., 2019). Hence, our strategy of blocking TGF β signalling might also prevent glial scar formation and thereby promote remyelination (Baror et al., 2019). In order to further examine this, we are interested in understanding how astrocytes react to demyelination in our model. In our experiments, we have observed a scar appearance in astrocytes at late timepoints after lesion (14-21

dp̄). Thus, it would be necessary to dissociate the role of TGFβ on microglia activation from the influence it might have on scarring.

2.3. TGFβ blocks the induction of the LXR pathway upon myelin intake

Our data indicate that TGFβ prevents the induction of the LXR pathway that normally occurs after myelin intake in microglia and suggest that TGFβ might have an influence on PPAR pathway activation too. Previous reports have investigated the relationship between TGFβ and PPARγ and have established that they maintain a bidirectional negative regulation. PPARγ seems to repress TGFβ partly through dephosphorylation of the transcription factor zinc finger 9 (ZF9) and partly through AP1 inhibition (Lee et al., 2008; Seung et al., 2006). On the other hand, there are several evidences that TGFβ can inhibit the expression of PPARγ and its target genes, although these effects seem to be rather pleiotropic and cell- and time-dependent (Ahdjoudj et al., 2002; Han et al., 2000; Kintscher et al., 2002; Lund et al., 2018; Mingui et al., 2003). Regarding LXR and TGFβ, very few reports have investigated their link so far. Some reports indicate that TGFβ stimulates the expression of *Abca1*, although this effect might not be mediated by LXR (Yin et al., 2010). One report suggested that the addition of TGFβ to foam cells derived from THP-1 macrophages induces the expression of *Abca1*, *Abcg1* and *Srb1* through activation of the LXRα pathway (Hu et al., 2010). However, in this case, TGFβ was added after the formation of foam cells, while, in our conditions, excess TGFβ is already existing in the environment before damage.

Another possibility would be that TGFβ indirectly affects the LXR/PPAR pathways. According to the model of biphasic temporal pattern of microglial and macrophage activation (see Fig. 1.4), the initial pro-inflammatory activation of these cells is required to posteriorly enter the lipid processing phase, where the LXR and PPAR pathways are activated. Since excess TGFβ in WD-fed mice prevents this first initial inflammatory activation, it indirectly also prevents the progression into the pro-resolving, lipid-processing phase. In this regard, this is in line with the beneficial effects observed by TREM2 stimulation. TREM2-dependent pathways are activated upon transformation of microglia into DAM, and these pathways upregulate genes that promote lysosomal function and lipid metabolism. Hence, enhancing TREM2 function is a way to compensate for the initial lack of inflammatory response and promote myelin clearance by phagocytes.

The precise mechanism by which TGFβ might be interfering with LXR/PPAR function is still an open question. At first, we considered the hypothesis that WD could drive epigenetic modifications on the LXR/PPAR DNA response elements through TGFβ. One report demonstrated that chromatin acetylation was required for microglia function in a model of AD (Datta et al., 2018), while another study showed that systemic inflammation induced by WD induced long-lasting trained immunity in myeloid cells through epigenetic modifications, including the closing of the genomic area containing the *Abca1* promoter (Christ et al., 2018). It was also shown that microglia also develop trained immunity upon several peripheral inflammatory stimulations by modifying their epigenome (Neher and Cunningham, 2019; Wendeln et al., 2018), suggesting that WD could have an influence on microglia function as well. In addition, our data demonstrate that the production of butyrate, which can act as an HDAC inhibitor, is decreased in the gut and that butyrate treatment was beneficial

for remyelination both in WD-fed and old mice. Thus, it would be relevant to evaluate the accessibility of the LXR and PPAR DNA response elements in microglia isolated from CD- and WD-fed mice by ATAC sequencing. Possibly, we could then further analyse the role of TGF β in modifying the epigenetic marks in these sites. In this regard, we will also analyse the influence of switching WD-fed mice to CD after 4 weeks of feeding, to examine whether the WD insult might cause epigenetic modifications on microglia that have long-lasting functional consequences on remyelination. Other epigenome-independent mechanisms might also be plausible, yet extremely challenging to find without previous screening. Further transcriptomic analysis will be necessary to understand the alterations caused by WD in microglia and trigger our imagination to elaborate new working hypothesis.

3. Western diet intake alters the brain lipidome and causes white matter neuroinflammation

3.1. The plasma lipid profile is profoundly altered by western diet intake

In humans, it is well described that obesity causes several changes in the plasma lipid profile. In rodents, changes in the plasma lipidome upon HFD have been previously reported (Eisinger et al., 2014; Li et al., 2014; Miao et al., 2015), however; how the high-fat, high-sugar and high-calorie properties of WD affect the plasma lipidome is still unknown. In our study, feeding WD to C57BL/6J male mice for 8-10 weeks caused profound changes in the lipid profile of plasma. We observed an increase in the content in CE and a decrease in the proportion of TAGs. These two lipid classes are responsible for lipid storage, which is known to be altered also in humans upon obesity (Quehenberger and Dennis, 2011). Furthermore, CE are the main component (50% of lipid content) of low-density lipoproteins (LDL). Hence, its higher content suggests that the plasma lipoprotein profile of WD-fed mice would be skewed to a high LDL profile. The analysis of the lipoprotein profile in plasma from WD-fed mice would provide further information in that direction and would contribute to our understanding of the alterations in whole-body lipid transport and storage. It was slightly surprising for us to observe lower proportions of TAGs in our analysis, since obesity is typically characterized by high TAG content in plasma (Quehenberger and Dennis, 2011). Despite these differences, our data clearly demonstrate alterations in lipid storage induced by WD intake.

The lipids in the plasma of WD-fed mice were also characterized by shorter length and increased saturation. This further confirms that the higher proportions of short-length fatty acids and lower proportions of polyunsaturated fatty acids (such as C18:2 and C18:3) in the WD directly influenced the lipid composition in plasma. Lower rates of PUFAs over SFAs are known to increase the risk for cardiometabolic disease (Quehenberger and Dennis, 2011; Tortosa-Caparrós et al., 2017; Yagi et al., 2017), and our study suggests that such alterations can also perturb regeneration in the brain.

In old mice, the alterations in the plasma lipidome were modest. We observed a decrease in DAG and a non-significant increase in CE, whereas the length and saturation of lipids was not altered. In addition, old mice had a higher total content of lipids in plasma (p value = 0.055). Hence, our data suggests that although WD has a more significant influence, age also causes a certain degree of lipid metabolism alterations in plasma. Alterations of the plasma lipidome with ageing have been previously reported both in humans (Frahnow et al., 2017; Ishikawa et al., 2014) and rats (Saito et al., 2014). Thus, further investigations would be required to better understand how age alters the lipid profile and whether there are some parallelisms between age-induced and WD-induced lipid metabolism alterations. In addition, it would be interesting to measure to content of free fatty acids in plasma both in WD-fed and in old mice. Free fatty acids are the most direct mediators between lipid metabolism alterations and inflammatory cascades in other organs, thus; their analysis would provide further information on how changes in the plasma lipidome can cause inflammatory alterations in the CNS.

3.2. The lipid alterations in plasma are associated with lipid alterations in the brain

We characterized the changes induced by WD on the brain lipidome and observed that the alterations found in plasma (i.e. shorter length, increased saturation) appear to be mirrored in the grey and white matter of the brain. Although the changes were not as extensive as in the plasma, they followed the same trend. These findings are relevant, since they are the first description of lipid alterations in the white and grey matter upon WD consumption. However, it is important to mention that other groups investigated similar questions. For example, Pakiet et al. described the influence of HFD on whole-brain lipid composition (Pakiet et al., 2019) and reported decreased content of the anti-inflammatory molecule eicosapentaenoic acid (EPA), thereby suggesting that altered inflammatory regulation could contribute to the impaired brain function upon HFD consumption. Additionally, other reports have focused on understanding the influence of diets rich in SFAs or PUFAs on the brain lipidome and documented modest but relevant differences (Elsherbiny et al., 2015; Giles et al., 2016; Valentini et al., 2018, Fitzner et al., *in revision*). Hence, it is clear that diet can influence the brain lipid composition. Nevertheless, it is now important to demonstrate whether the changes in lipid composition are involved in brain and cellular function. The highest lipid content in the brain is found in myelin, and changes in myelin lipid composition could affect its stability and, therefore; could potentially affect neuronal signalling and myelin remodelling and plasticity. Furthermore, alterations in the lipid composition of cellular membranes of microglia and astrocytes could contribute to the reactivity observed in these cells upon HFD or WD intake. For these reasons, it would be crucial to analyse the lipidome of single cell types isolated from the CNS. In a recent study, Nugent et al. analysed the lipidome of microglia and astrocytes isolated from healthy and demyelinated mouse brain (Nugent et al., 2020) and described an increase of cholesterol esters in microglia upon demyelination. Similar techniques and analyses could be applied in our model to determine how the cellular lipidome changes upon diet. Moreover, a combination of lipidomics and transcriptomics analysis from white and grey matter will allow a comprehensive understanding of how changes in lipid brain profiles correlate with cellular function.

One interesting question is the route of entry for the plasma lipids into the brain. Our preliminary data show lipid accumulation in the epithelial lining of the lateral ventricles and a diminished cover by astrocytic processes. This is associated with an increased accumulation of lipid particles in the microglia in the corpus callosum. Thus, the cerebrospinal fluid and the ventricular system are a potential route of lipid exchange between plasma and CNS. To determine whether other barriers such as the choroid plexus, the ventricular system and the perivascular spaces also show similar characteristics, it would be relevant to examine other CNS macrophages than microglia, i.e. perivascular macrophages, meningeal macrophages and choroid plexus macrophages, given their role in regulating the CNS barriers. In addition, the labelling of plasma lipids using stable isotope labelling (Triebel and Wenk, 2018) would allow the tracing of the diffusion of certain lipids from the plasma into the CNS.

To conclude, we show that WD feeding causes relevant changes in the lipid composition of the white and grey matters of the brain, and future studies will be needed to determine how these influence cellular function.

3.3. Lipid alterations associate with low-grade neuroinflammation in the white matter

The lipid alterations in the white matter caused by WD intake appear to be associated with microglia reactivity in the corpus callosum. Using several microglia activation markers, we observed a certain degree of inflammatory response, which we interpreted as low-grade microgliosis. To better characterize these small changes, it would be interesting to analyse the microglia transcriptome at a single-cell level so that we can describe which populations are altered by WD. Furthermore, we could compare the populations found in WD-fed mice to the ones in old mice, to determine whether there are any parallelisms in their response.

In all our experiments, we have analysed the influence of 8 to 10 weeks of WD consumption. However, different effects of WD and HFD are described dependent on the duration of the diet (Guillemot-Legris and Muccioli, 2017). Thus, it would be intriguing to understand how a short-term pulse of WD (i.e. 1 week) and a very long term WD challenge (i.e. 6-8 months) could affect microglia function in the white matter. In the literature, it is apparent that the first reaction from microglia to WD is highly reactive and skewed to classical pro-inflammation (i.e. including the secretion of cytokines such as IL6, TNF α and IL1 β). However, with time microglia appear to adapt to the new environment and start secreting factors demonstrating an alternatively activated or even anti-inflammatory profile (Baufeld et al., 2016; Guillemot-Legris and Muccioli, 2017; Kim et al., 2019; Miller and Spencer, 2014).

In short, microglia in the corpus callosum of WD-fed mice presented excessive lipid deposits and a certain degree of activation. Future transcriptomic analyses will provide more detailed information on the influence of WD on microglia function.

4. Conclusion

Together, our data delineate a model of how obesity might be disturbing microglia's response to damage in the white matter (Fig. 4.1). We suggest that the perturbed lipid homeostasis and low-grade inflammation prevailing in peripheral organs upon the consumption of a high-fat, high-sugar diet such as WD translates into alterations in the lipid composition of the brain white matter and into low-grade neuroinflammation characterized by modest microgliosis. In this context, chronic neuroinflammation triggers TGF β production to re-establish homeostasis, which is beneficial to oppose chronic neuroinflammation. However, upon acute damage to the CNS such as demyelination, excess TGF β prevents microglia's full activation, which results in poor cholesterol efflux and lipotoxicity. Therefore, even though phagocytes are recruited to the lesioned area, they cannot fully turn on the functional machinery necessary to cope with the damage. Thus, blocking TGF β signalling or promoting microglia activation through TREM2 could be ways to promote correct microglia activation and successful resolution of damage in the CNS.

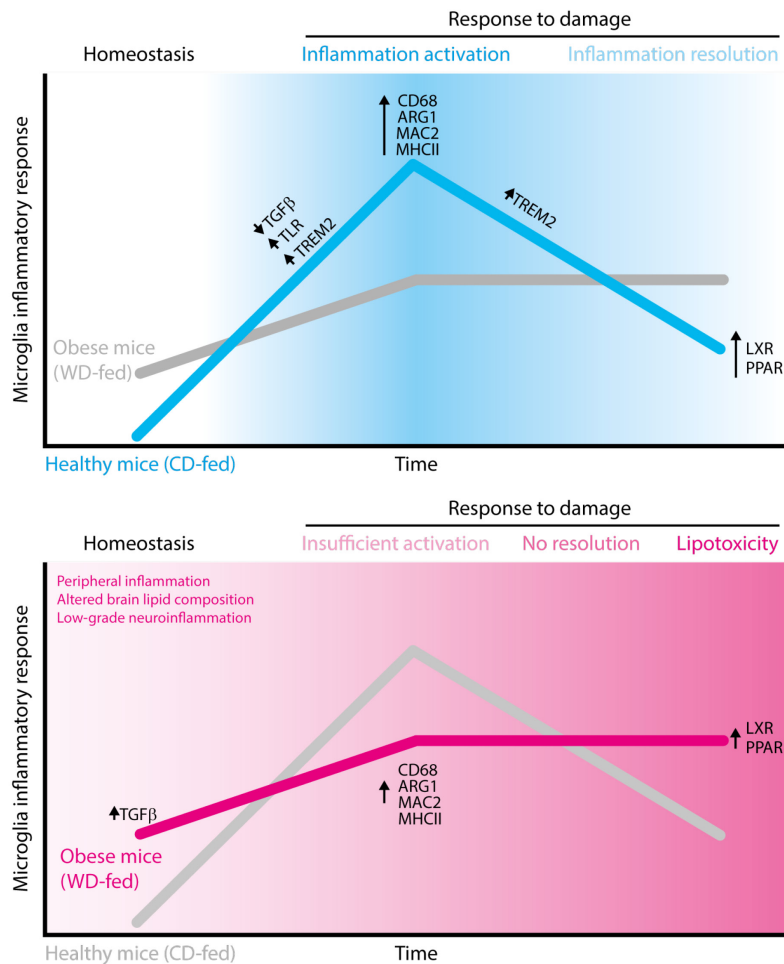


Figure 4.1: Working model of the influence of obesity on microglia's response to myelin damage. The top diagram illustrates the microglia response upon demyelinating damage in healthy mice, while the bottom diagram illustrates the response in obese mice. In healthy mice, damage triggers a potent inflammatory response by microglia, characterized by the expression of activation markers such as CD68, ARG1, MAC2 and MHCII. This inflammatory peak is necessary to then enter the inflammation resolution phase, where the LXR and PPAR pathways are activated to process

ingested lipids and to resolve inflammation. These processes are mediated by the activation of TLRs and TREM2, and the silencing of TGF β . In obese mice, microglia homeostasis is perturbed and associated with increased TGF β signalling. Due to the excess TGF β signalling, microglia from obese mice cannot respond as potently as they should, which renders them unable to enter the resolution phase and induces lipotoxicity and thus, failure to regenerate myelin.

Treatments that delay, prevent or reverse the progression phase are an unmet need in MS research. Large efforts have been directed into identifying strategies to promote the generation and differentiation of OPCs into pre- and myelinating oligodendrocytes to enhance endogenous remyelination. Currently, some treatments are finishing phase 2 clinical studies and report efficacy, thus; the prospect of licensed remyelinating treatments in MS looks increasingly feasible (Cunniffe and Coles, 2019). Here, we expand the spectrum of potential therapeutic strategies by uncovering central microglial checkpoint mechanisms as possible targets in promoting a reparative inflammatory response after demyelinating injury. Nevertheless, recent research raised doubts about the contribution of OPCs to remyelination in humans. Using an elegant ^{14}C -dating technique, Yeung et al. demonstrated that the oligodendrocytes in areas supposed to have undergone at least partial remyelination could not derive from new OPCs (Yeung et al., 2019). Concurrently, Jäkel et al. reported reduced OPC numbers in these same areas (Jäkel et al., 2019). These findings reveal a new dimension of complexity to the process of remyelination that challenges our view of remyelination in humans and force us to better examine how biological mechanisms unravelled using animal models translate into human disease.

In conclusion, our study further proves the detrimental influence that obesity can have on health and strengthens the evidences demonstrating that obesity can indeed also perturb CNS function. The implantation of a diet high in sugar, fat and calories (i.e. WD) in developed countries has led to endemic rates of obesity. According to the World Health Organization, worldwide obesity has nearly tripled since 1975, with 39% of adults older than 18 and over 340 million children and adolescents aged 5-19 being overweight in 2016. Several studies show an association between obesity in childhood and adolescence and the risk of developing MS and a high prevalence of obesity in MS patients (Altowaijri et al., 2017). Since obesity is preventable, our study emphasizes the need to establish strict diet guidelines not only for MS patients, but also for the general population. Furthermore, I believe ethical restrictions of market regulations should aim to facilitate the consumption of a health-promoting diet.

Appendix

1. Summary figures

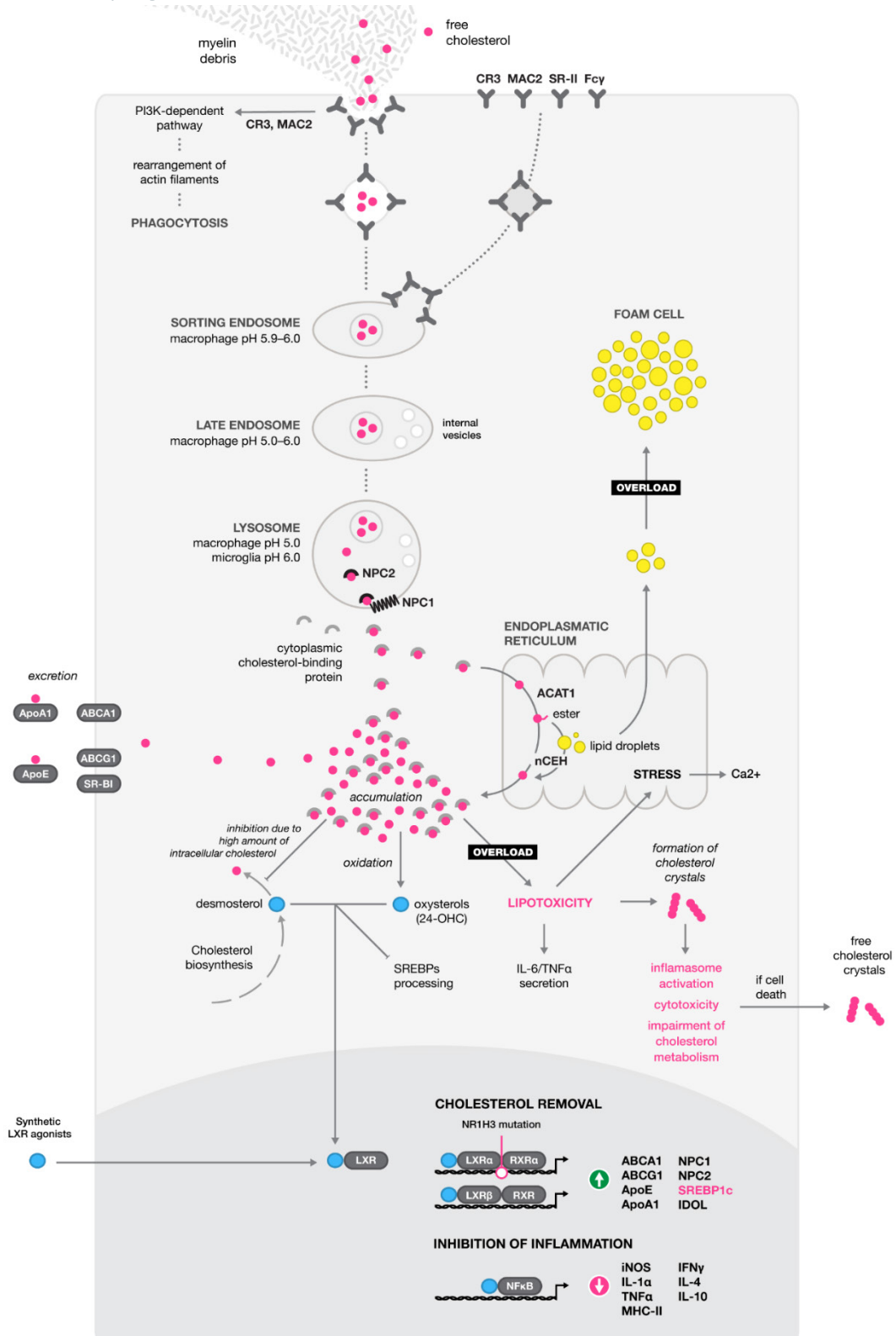


Figure 5.1 (previous page): Cellular processes triggered upon myelin debris intake. This figure illustrates the various steps performed by a phagocyte from myelin debris intake and processing to transcriptional changes via activation of the LXR pathway. Myelin debris are detected by several receptors, which stimulate PI3K-dependent signalling pathways to re-arrange the actin filaments and promote phagocytosis. At the late endosome stage, lysosomal hydrolases derived from the Golgi apparatus are incorporated into the phagosome and process myelin debris into its components, one of which is free cholesterol. Free cholesterol is transported out of the late endosome/lysosome through the cooperative action of NPC1 and NPC2, bound to a cytoplasmic cholesterol-binding protein, and trafficked to the endoplasmic reticulum. There, free cholesterol is esterified by ACAT1 and, together with fatty acids, incorporated into lipid droplets. An excessive accumulation of lipid droplets gives the cell a foam cell morphology. Free cholesterol can be de-esterified by nCEH, which liberates free cholesterol that can be then out flowed from macrophages through the transporters ABCA1 and ABCG1. Free cholesterol can also oxidised, thereby forming oxysterols, which are LXR agonists. Furthermore, free cholesterol inhibits cholesterol synthesis, thus causing the accumulation of desmosterol, another LXR agonist. Also, synthetic agonists can be incorporated into the cell and also bind the LXR. Ligand binding activates the heterodimer LXR-RXR and initiates the transcription of genes that promote cholesterol efflux from the cell. In parallel, inflammatory pathways are inhibited. If these lipid processing mechanisms are overloaded, unbuffered free cholesterol will accumulate in the cytoplasm and lead to lipotoxicity. This can associate with ER stress, further pro-inflammatory activation, and cholesterol crystallization, which eventually leads to necrotic cell death and the release of cholesterol crystals into the extracellular space. *Illustration created by Martin Krzywinski from a draft by Mar Bosch Queralt. For abbreviations, please see the list of abbreviations.*

Figure 5.2 (next page): Lipid processing by microglia and macrophages is the bottleneck for successful remyelination. This illustration summarizes the inflammatory response triggered upon myelin damage. Upon demyelination, microglia and macrophages are recruited to the area of damage, where they will take up myelin debris. Once myelin debris have been taken up, they need to be processed into the different myelin components. Cholesterol and free fatty acids present in myelin debris then activate the LXR and PPAR pathways, respectively. These will induce lipid processing and buffering by either promoting cholesterol efflux, lipid burning, or safe lipid storage in lipid droplets. If these pathways are correctly activated, inflammation will resolve and remyelination will occur. If, however, these pathways are not timely and properly activated, lipid overload will lead to lipotoxicity and microglia/macrophage malfunction. Thus, inflammation will not resolve, and remyelination will not occur. *Illustration created by Mar Bosch Queralt, with the assistance of Martin Krzywinski. For abbreviations, please see the list of abbreviations.*

2. Generation of recombinant anti-TREM2 antibodies

Isotype and 4D9 antibody materials were produced, characterized, and assessed for quality performed at Denali Therapeutics as reported in (Schlepckow et al., 2020). Wistar rats were immunized subcutaneously and intraperitoneally with a mixture of 70 µg recombinant his-tagged mouse TREM2 protein (aa19-171, Creative Biomart) in 500 µl PBS, 5 nmol CpG2006 (TIB MOLBIOL, Berlin, Germany), and 500 µl Incomplete Freund's adjuvant. Fusion of the myeloma cell line P3X63-Ag8.653 with the rat immune spleen cells was performed. Hybridoma supernatants were tested in an enzyme-linked immunoassay using biotinylated peptides (0.2µg/mL) bound to avidin-coated plates. The hybridoma cells of TREM2-reactive supernatants were cloned at least twice by limiting dilution. The IgG subclass was determined in an ELISA assay with mouse anti-rat kappa light chain antibodies as capture and HRP-coupled mouse anti-rat IgG subclass-specific antibodies for detection. Total RNA was extracted from the monoclonal antibody expressing hybridoma cells using QIAGEN RNeasy Plus Mini Kit (QIAGEN, Germantown, MD) following manufacturer's instructions. The extracted total RNA was used as template for 5'- RACE-ready cDNA synthesis (Takara Bio, Mountain View, CA). The heavy chain variable domain (VH) and the light chain variable domain (VK) of 4D9 were amplified separately by PCR using the 5'-RACE adaptor-specific forward primer, rat IgG or kappa constant-specific reverse primers. For VK domain amplification, a peptide nucleic acid oligo (CCTGTGGAGGAGGAGGATGCT-KK) was used to selectively amplify the functional kappa chain. The PCR products of VH and VK were purified and cloned into the pCR-TOPO vector (Invitrogen, Carlsbad, CA). The cloned vector was transformed into TOP10 *E. coli* (Invitrogen, Carlsbad, CA) by chemical transformation and selected on a LB agar plate containing 100 µg/mL carbenicillin. Sanger sequencing was done on bacteria colonies using the M13 forward and M13 reverse primers to sequence VH and VK of the 4D9 antibody. The polypeptide sequences of VH and VK were codon optimized for CHO cell expression and synthesized by Integrated DNA Technologies (Coralville, IA). The synthesized VH and VK fragments were cloned into the human IgG1 containing effector knock-out mutations (L234A, L235A, and P329G) and human kappa chain expression vectors, respectively. ExpiCHO cells (Gibco, Carlsbad, CA) were transfected with the antibody expression plasmids. The culture medium containing the expressed recombinant antibody was harvested 5 days after transfection. The recombinant antibody was purified by MabSelect SURE (GE Life Sciences, Pittsburgh, PA). The purity of 4D9 recombinant antibody was analysed by SDS-PAGE (NuPAGE 4-12% Bis-Tris, Invitrogen, Carlsbad, CA) and size exclusion chromatography (Tosoh TSKgel, Tosoh Biosciences, Japan).

The 4D9 antibody was sequenced and reformatted onto a human IgG1-effectorless backbone for cell culture experiments, and in a mouse backbone for mouse *in vivo* experiments (Schlepckow et al., 2020).

3. Custom-made macros in Fiji

Macro to measure consecutive lesion areas in one demyelinated lesion

This simple macro analyses the area and intensity of a region of interest (ROI) selected manually in consecutive images of a lesion from one mouse. The steps to achieve that are the following:

1. Create dialog for user to select the file to process.
2. Open file container or directory with single images and make a selection list with all images.
3. For each image, allow the user to select the ROI and measure the area and intensity of that ROI.
4. Save results and close.

```

/*
 * Macro for measuring the Area and intensity of Fluoromyelin positive filaments
 * in z tile scan stacks
 * Version with manual thresholding
 * Ioannis K. Alexopoulos
 */

// Create dialog, create save folders, and select file(s) to process
Dialog.create("Measure Lesion Area");
Dialog.addCheckbox("Save ROI Selections", true);
Dialog.addString("Name of saving folder: ", "_ResultsDem");
Dialog.show();

// Variables of Dialog
single_file=false;
SAVE_ROI=Dialog.getCheckbox();
save_folder=Dialog.getString();
sep = File.separator;

if (single_file)
{
    Filelist=newArray(1);
    Filelist[0] = File.openDialog("Select a file to process...");
    SourceDir=File.getParent(Filelist[0]);
    Filelist[0]=File.getName(Filelist[0]);
    SAVE_DIR=SourceDir;
}
else
{
    SourceDir = getDirectory("Choose source directory");
    Filelist=getFileList(SourceDir);
    SAVE_DIR=File.getParent(SourceDir);
    BASIC_NAME=File.getName(SourceDir);
}

// Remove Folders from Filelist array
tmp=newArray();
for(k=0;k<Filelist.length;k++)
{
    if (!File.isDirectory(SourceDir+"/"+Filelist[k]))
    {
        tmp = Array.concat(tmp,Filelist[k]);
    }
}
Filelist=tmp;
Array.sort(Filelist);

new_folder=SAVE_DIR + sep + save_folder;
File.makeDirectory(new_folder);
roiManager("reset");
run("Clear Results");
for (k=0;k<Filelist.length;k++)
{
    run("Bio-Formats Macro Extensions");
    Ext.setID(SourceDir+sep+Filelist[k]);
    Ext.getSeriesCount(SERIES_COUNT);
    FILE_PATH=SourceDir + sep + Filelist[k];

    for (i=0;i<SERIES_COUNT; i++)
    {
        options="open=["+ FILE_PATH + "] " + "autoscale color_mode=Default view=Hyperstack
stack_order=XYZCT " + "series_" + d2s(i+1,0);
        run("Bio-Formats Importer", options);
        FILE_NAME=File.getName(FILE_PATH);
        Ext.setSeries(i);
        Ext.getSeriesName(SERIES_NAMES);
    }
}

```

Appendix

```
SERIES_NAMES=replace(SERIES_NAMES, " ", "_");
SERIES_NAMES=replace(SERIES_NAMES, "/", "_");
SERIES_NAMES=replace(SERIES_NAMES, "\\(", "(");
SERIES_NAMES=replace(SERIES_NAMES, "\\)", ")");
SAVE_NAME=Filelist[k]+"_"+SERIES_NAMES;
rename(SAVE_NAME);
run("Enhance Contrast", "saturated=0.35");

//Select ROI to analyze
setTool("freehand");
waitForUser("Please select the region of lesion and press OK");
run("Set Measurements...", "area mean min shape integrated redirect=None decimal=3");
run("Measure");
roiManager("Add");
close();
}
}
saveAs("Results", new_folder+ sep +BASIC_NAME+"-Results+".txt");
run("Clear Results");
roiManager("save", new_folder+ sep + BASIC_NAME+"_Selections+".zip");
roiManager("reset");
run("Close All");
```

Macro to measure percentage of area covered and intensity of different signals

This macro analyses the area and intensity occupied by a particular signal in a ROI selected manually. The macro pasted here measures DAPI, crystals, myelin, lysosomes and macrophages, but a similar macro was used for several combinations of signals, such as CD68, PLIN2 or pSMAD2. In short, the steps to achieve this analysis are the following:

1. Create dialog for user to select the file(s) to process and the thresholding strategy (both manual and automatic options available). Also, the option is given to load a pre-selected ROI.
2. Open file container or directory with single images and make a selection list with all images.
3. For each image, convert the image to 32-Bit and allow the user to select the ROI. Then, allow the user to select a thresholding strategy to eliminate the tissue holes and measure the area occupied by the tissue. For each channel, allow the user to select a thresholding strategy to distinguish the positive signal from the background and measure the area and intensity of the thresholded signal. For the DAPI channel, allow the user to select a thresholding strategy to distinguish the positive signal from the background and quantify the number of particles of a certain size and circularity.
4. Save results and close.

Example given for measuring DAPI, crystals, myelin, lysosomes and macrophages. Variations of the same were used to analyse PLIN2, CD68 in lesions and GFAP, IBA1 in unlesioned samples.

```
*****
* Author Dr. Ioannis K. Alexopoulos
* The author of the macro reserve the copyrights of the original macro.
* However, you are welcome to distribute, modify and use the program under
* the terms of the GNU General Public License as stated here:
* (http://www.gnu.org/licenses/gpl.txt) as long as you attribute proper
* acknowledgement to the author as mentioned above.
* This program is distributed in the hope that it will be useful,
* but WITHOUT ANY WARRANTY; without even the implied warranty of
* MERCHANTABILITY or FITNESS FOR A PARTICULAR PURPOSE. See the
* GNU General Public License for more details.
*****
* Description of macro
* -----
* This macro is used to analyse crystals, lysosomes, myelin and macrophages in
* spinal cord lesions.
* It quantifies:
* 1. The area of the lesion (defined by the user and excluding tissue holes)
* 2. Number of nuclei in the lesion area
* 3. The area occupied by lysosomes as well as their mean intensity
* 4. The area occupied by crystals as well as their mean intensity
* 5. The area occupied by myelin as well as the mean intensity
* 6. The area occupied by macrophages as well as their mean intensity
*
* The output of the macro is:
```

Appendix

```
* a. The lesion ROI
* b. The results files (.txt)
* c. The tissue thresholded image (the image used to measure only tissue area)
* d. A five channel image:
*         C1=Crystals
*         C2=DAPI
*         C3=Lysosomes (Lamp1)
*         C4=Myelin
*         C5=Macrophages (Ibal)
*/

// Create dialog, create save folders, and select file(s) to process
ThresholdMethods=getList("threshold.methods");
Dialog.create("Parameters");
Dialog.addMessage("Quantify crystals, lysosomes myelin and macrophages within a lesion");
Dialog.addCheckbox("Analyse single image container file", true);
Dialog.addCheckbox("Load lesion ROI", false);

//Channels
Dialog.addNumber("Crystals Channel", 1);
Dialog.addNumber("DAPI Channel", 2);
Dialog.addNumber("Lysosome (Lamp1) Channel", 3);
Dialog.addNumber("Myelin Channel", 4);
Dialog.addNumber("Ibal Channel", 5);
Dialog.addString("Name of saving folder: ", "_Results");
Dialog.addCheckbox("Automatic Threshold", true);
Dialog.addChoice("Threshold Algorithm for crystals", ThresholdMethods);
Dialog.addChoice("Threshold Algorithm for DAPI", ThresholdMethods);
Dialog.addChoice("Threshold Algorithm for Lamp1", ThresholdMethods);
Dialog.addChoice("Threshold Algorithm for Myelin", ThresholdMethods);
Dialog.addChoice("Threshold Algorithm for Ibal", ThresholdMethods);
Dialog.show();

// Variables of Dialog
single_file=Dialog.getCheckbox();
LOAD_ROI=Dialog.getCheckbox();
CRYST_ch=Dialog.getNumber();
DAPI_ch=Dialog.getNumber();
LAMP1_ch=Dialog.getNumber();
MYELIN_ch=Dialog.getNumber();
IBAL_ch=Dialog.getNumber();
save_folder=Dialog.getString();
auto_thr=Dialog.getCheckbox();
Method_cryst=Dialog.getChoice();
Method_dapi=Dialog.getChoice();
Method_lamp1=Dialog.getChoice();
Method_myelin=Dialog.getChoice();
Method_ibal=Dialog.getChoice();

if(auto_thr)
{
    save_folder=save_folder+"_"+Method_ibal;
}else{
    save_folder=save_folder+"_ManualThr";
}
sep = File.separator;

if (single_file)
{
    Filelist=newArray(1);
    Filelist[0] = File.openDialog("Select a file to process...");
    SourceDir=File.getParent(Filelist[0]);
    Filelist[0]=File.getName(Filelist[0]);
    save_folder_name_add=Filelist[0];
    SAVE_DIR=SourceDir;
}else
{
    SourceDir = getDirectory("Choose source directory");
    Filelist=getFileList(SourceDir);
    SAVE_DIR=SourceDir;
    save_folder_name_add=File.getName(SourceDir);
}

save_folder=save_folder+"_"+save_folder_name_add;
// Remove Folders from Filelist array
tmp=newArray();
for(k=0;k<Filelist.length;k++)
{
    if (!File.isDirectory(SourceDir+"/"+Filelist[k]))
    {
        tmp = Array.concat(tmp,Filelist[k]);
    }
}
Filelist=tmp;

if(LOAD_ROI)
{
    LARGE_ROI_PATH = getDirectory("Select the folder containing the lesion ROIs");
```

Appendix

```

}

getDateAndTime(year, month, dayOfWeek, dayOfMonth, hour, minute, second, msec);
month=month+1;
save_folder=save_folder+"_"+year+"_"+month+"_"+dayOfMonth+"_"+hour+"_"+minute+"_"+second;
new_folder=SAVE_DIR + sep + save_folder;
File.makeDirectory(new_folder);
setBatchMode(true);
for (k=0;k<Filelist.length;k++)
{
    if(!endsWith(Filelist[k], sep))
    {
        run("Bio-Formats Macro Extensions");
        Ext.setId(SourceDir+sep+Filelist[k]);
        Ext.getSeriesCount(SERIES_COUNT);
        FILE_PATH=SourceDir + sep + Filelist[k];

        //Arrays for each serie
        SeriesNames=newArray(SERIES_COUNT);
        TotalArea_Lesion=newArray(SERIES_COUNT);
        Nuclei_count=newArray(SERIES_COUNT);
        Cryst_Area=newArray(SERIES_COUNT);
        Cryst_Mean=newArray(SERIES_COUNT);
        Lampl_Area=newArray(SERIES_COUNT);
        Lampl_Mean=newArray(SERIES_COUNT);
        Myelin_Area=newArray(SERIES_COUNT);
        Myelin_Mean=newArray(SERIES_COUNT);
        Ibal_Area=newArray(SERIES_COUNT);
        Ibal_Mean=newArray(SERIES_COUNT);

        for (i=0;i<SERIES_COUNT; i++)
        {
            options="open=["+ FILE_PATH + "]" + " " + "autoscale color_mode=Default
view=Hyperstack stack_order=XYCZT " + "series_"+d2s(i+1,0);
            run("Bio-Formats Importer", options);
            FILE_NAME=File.nameWithoutExtension;
            Ext.setSeries(i);
            Ext.getSeriesName(SERIES_NAMES);
            SERIES_NAMES=replace(SERIES_NAMES, " ", "_");
            SERIES_NAMES=replace(SERIES_NAMES, "/", "_");
            SERIES_NAMES=replace(SERIES_NAMES, "\\(", "(");
            SERIES_NAMES=replace(SERIES_NAMES, "\\)", ")");
            SeriesNames[i]=SERIES_NAMES;
            SAVE_NAME=FILE_NAME+"_"+SERIES_NAMES;
            rename(SAVE_NAME);
            run("32-bit");
            run("Gaussian Blur...", "sigma=1.5 stack");
            getDimensions(width, height, channels, slices, frames);
            if(slices>1)
            {
                run("Z Project...", "projection=[Max Intensity]");
                selectWindow(SAVE_NAME);
                close();
                selectWindow("MAX_"+SAVE_NAME);
                rename(SAVE_NAME);
            }
            Stack.setDisplayMode("composite");
            //Select ROI to analyze and measure Lesion area
            roiManager("reset");
            Stack.setChannel(CRYST_ch);
            run("Grays");
            Stack.setChannel(DAPI_ch);
            run("Cyan");
            Stack.setChannel(LAMP1_ch);
            run("Green");
            run("Enhance Contrast", "saturated=0.35");
            Stack.setChannel(MYELIN_ch);
            run("Magenta");
            run("Enhance Contrast", "saturated=0.35");
            Stack.setChannel(IBA1_ch);
            run("Yellow");
            run("Enhance Contrast", "saturated=0.35");
            Stack.setActiveChannels("011110");

            //Threshold out tissue "holes"
            selectWindow(SAVE_NAME);
            run("Duplicate...", "duplicate channels="+IBA1_ch+"");
            rename("temp");
            setBatchMode("show");
            waitForUser("Please select the threshold limits,press Apply and convert
background to NaN\nThen click OK for this message");
            setBatchMode("hide");

            selectWindow(SAVE_NAME);
            setTool("freehand");
            if(LOAD_ROI)
            {
                roiManager("Open", LARGE_ROI_PATH + sep + SAVE_NAME+"-
Lesion_ROI"+".zip" );

```

Appendix

```
}else
{
    setBatchMode("show");
    waitForUser("Please select the region of interest and press OK");
    roiManager("Add");
    setBatchMode("hide");
}
//Measure only tissue area (exclude "holes")
selectWindow("temp");
roiManager("Select", 0);
run("Set Measurements...", "area redirect=None decimal=3");
run("Measure");
TotalArea_Lesion[i]=getResult("Area", 0);
run("Clear Results");
selectWindow("temp");
saveAs("tif", new_folder+ sep +SAVE_NAME+"-Tissue_only");
run("Close");
selectWindow(SAVE_NAME);
roiManager("deselect");
run("Select None");
run("Clear Results");
run("Set Measurements...", "area mean redirect=None decimal=3");
run("Split Channels");
//Analyse Crystals Channel
selectWindow("C"+CRYST_ch+"-"+SAVE_NAME);
if(auto_thr)
{
    setAutoThreshold(Method_cryst+" dark");
    run("NaN Background");
}
else
{
    setBatchMode("show");
    waitForUser("Threshold Crystals channel\n\nPlease select the
threshold limits,press Apply and convert background to NaN\n\nThen click OK for this message");
    setBatchMode("hide");
}
roiManager("Select", 0);
run("Measure");
Cryst_Area[i]=getResult("Area", 0);
Cryst_Mean[i]=getResult("Mean", 0);
run("Clear Results");
//Analyse DAPI Channel
selectWindow("C"+DAPI_ch+"-"+SAVE_NAME);
run("8-bit");
if(auto_thr)
{
    setAutoThreshold(Method_dapi+" dark");
    run("NaN Background");
}
else
{
    setBatchMode("show");
    waitForUser("Threshold DAPI channel\n\nPlease select the threshold
limits and press Apply\n\nThen click OK for this message");
    setBatchMode("hide");
}
setOption("BlackBackground", true);
run("Convert to Mask");
run("Fill Holes");
run("Watershed");
roiManager("Select", 0);
run("Analyze Particles...", "size=4.00-Infinity display clear");
Nuclei_count[i]=nResults;
selectWindow("C"+DAPI_ch+"-"+SAVE_NAME);
run("32-bit");
run("Clear Results");
//Analyse Lamp1 Channel
selectWindow("C"+LAMP1_ch+"-"+SAVE_NAME);
if(auto_thr)
{
    setAutoThreshold(Method_lamp1+" dark");
    run("NaN Background");
}
else
{
    setBatchMode("show");
    waitForUser("Threshold Lamp1 channel\n\nPlease select the threshold
limits,press Apply and convert background to NaN\n\nThen click OK for this message");
    setBatchMode("hide");
}
roiManager("Select", 0);
run("Measure");
Lamp1_Area[i]=getResult("Area", 0);
Lamp1_Mean[i]=getResult("Mean", 0);
run("Clear Results");
//Analyse Myelin Channel
selectWindow("C"+MYELIN_ch+"-"+SAVE_NAME);
if(auto_thr)
{
    setAutoThreshold(Method_myelin+" dark");
```

Appendix

```

        run("NaN Background");
    }else
    {
        setBatchMode("show");
        waitForUser("Threshold Myelin channel\n\nPlease select the threshold
limits,press Apply and convert background to NaN\n\nThen click OK for this message");
        setBatchMode("hide");
    }
    roiManager("Select", 0);
    run("Measure");
    Myelin_Area[i]=getResult("Area", 0);
    Myelin_Mean[i]=getResult("Mean", 0);
    run("Clear Results");
    //Analyse Ibal Channel
    selectWindow("C"+IBAL_ch+"-"+SAVE_NAME);
    if(auto_thr)
    {
        setAutoThreshold(Method_ibal+" dark");
        run("NaN Background");
    }else
    {
        setBatchMode("show");
        waitForUser("Threshold Ibal channel\n\nPlease select the threshold
limits,press Apply and convert background to NaN\n\nThen click OK for this message");
        setBatchMode("hide");
    }
    roiManager("Select", 0);
    run("Measure");
    Ibal_Area[i]=getResult("Area", 0);
    Ibal_Mean[i]=getResult("Mean", 0);
    run("Clear Results");

    run("Merge Channels...", "c1=[C"+CRYST_ch+"-"+SAVE_NAME+"] c2=[C"+DAPI_ch+"-
"+SAVE_NAME+"] c3=[C"+LAMP1_ch+"-"+SAVE_NAME+"] c4=[C"+MYELIN_ch+"-"+SAVE_NAME+"] c5=[C"+IBAL_ch+"-
"+SAVE_NAME+"] create");
    Stack.setDisplayMode("composite");
    Stack.setChannel(CRYST_ch);
    run("Grays");
    Stack.setChannel(DAPI_ch);
    run("Cyan");
    Stack.setChannel(LAMP1_ch);
    run("Green");
    run("Enhance Contrast", "saturated=0.35");
    Stack.setChannel(MYELIN_ch);
    run("Magenta");
    run("Enhance Contrast", "saturated=0.35");
    Stack.setChannel(IBAL_ch);
    run("Yellow");
    saveAs("tif", new_folder+ sep +SAVE_NAME+"-Thresh");

    roiManager("Select",0);
    roiManager("save", new_folder+ sep + SAVE_NAME+"-Lesion_ROI+".zip");
    roiManager("reset");

    run("Close All");
}
roiManager("reset");
for (t=0;t<SERIES_COUNT; t++)
{
    run("Input/Output...", "jpeg=85 gif=-1 file=.xls copy_row save_column");
    setResult("Slice", t, SeriesNames[t]);
    setResult("Lesion Area [um^2]", t, TotalArea_Lesion[t]);

    setResult("Number of nuclei in lesion", t, Nuclei_count[t]);
    setResult("Crystals Area [um^2]", t, Cryst_Area[t]);
    setResult("Crystals mean intensity", t, Cryst_Mean[t]);

    setResult("Lysosomes Area [um^2]", t, Lamp1_Area[t]);
    setResult("Lysosomes mean intensity [um^2]", t, Lamp1_Mean[t]);

    setResult("Myelin Area [um^2]", t, Myelin_Area[t]);
    setResult("Myelin mean intensity", t, Myelin_Mean[t]);

    setResult("Macrophages Area [um^2]", t, Ibal_Area[t]);
    setResult("Macrophages mean intensity", t, Ibal_Mean[t]);

    updateResults();

    saveAs("Results", new_folder+ sep +FILE_NAME+"-Results+".txt");
    run("Clear Results");
}
}
setBatchMode(false);

```

Macro to quantify the signal from fluorescent in situ hybridization

This macro was used for quantification of particles positive for a certain RNA, labelled using FISH. The macro quantifies the number of positive particles in two different channels and the area occupied by a third channel (standard protein labelling by immunohistochemistry). Furthermore, it creates a mask out of the protein-labelled channel, and applies this onto the channels representing the RNA particles. Then, it quantifies the number of RNA particles contained in the particular protein staining. In our case, the RNA particles were always for *Tgfb1* and *Tgfb2*, and the protein staining was either labelling IBA1 (represented here) or GFAP. In short, the steps to achieve this analysis are the following:

1. Create dialog for user to select the file to process and the thresholding strategy for each channel (both manual and automatic options available). Also, the option is given to load a pre-selected ROI.
2. Open file container or directory with single images and make a selection list with all images.
3. For each image, convert the image to 32-Bit and allow the user to select the ROI. Then, allow the user to select a thresholding strategy to eliminate the tissue holes and measure the area occupied by the tissue. For the protein channel, allow the user to select a thresholding strategy to distinguish the positive signal from the background and measure the area and intensity of the thresholded signal. For the DAPI and RNA channels, allow the user to select a thresholding strategy to distinguish the positive signal from the background and quantify the number of particles of a certain size and circularity.
4. Convert the protein channel to 8-Bit and to a binary (0-1) mask. Use this mask to multiply each other channel (DAPI, RNA 1 and RNA 2) so that only the signal that falls into the positive pixels of the mask is considered. Then, quantify again the number of positive particles.
5. Save results and close.

```

/*****
* Author Mar Bosch-Queralt
* The author of the macro reserves the copyrights of the original macro.
* However, you are welcome to distribute, modify and use the program under
* the terms of the GNU General Public License as stated here:
* (http://www.gnu.org/licenses/gpl.txt) as long as you attribute proper
* acknowledgement to the author as mentioned above.
* This program is distributed in the hope that it will be useful,
* but WITHOUT ANY WARRANTY; without even the implied warranty of
* MERCHANTABILITY or FITNESS FOR A PARTICULAR PURPOSE. See the
* GNU General Public License for more details.
*****/
* Description of macro
* -----
* This macro is used to analyse:
* 1. dapi numbers,
* 2. area covered by and intensity of Ibal signal
* 3. number of TGFB1+ RNA molecules
* 4. number of TGFB2+ RNA molecules
* 5. number of dapi nuclei that are Ibal+
* 6. number of TGFB1+ RNA molecules within Ibal+ signal
* 7. number of TGFB2+ RNA molecules within Ibal+ signal
* in the unlesioned CC, unlesioned cortex, and lesioned CC
*
* It quantifies:
* 1. The area of the lesion (defined by the user and excluding tissue holes)
* 2. Number of nuclei in the ROI
* 3. area covered by and intensity and integrated density of Ibal signal
* 4. number of TGFB1+ RNA molecules
* 5. number of TGFB2+ RNA molecules
* 6. Number of DAPI nuclei in Ibal+ signal
* 7. number of TGFB1+ RNA molecules within Ibal+ signal
* 8. number of TGFB2+ RNA molecules within Ibal+ signal
*

```

Appendix

```
*
* The output of the macro is:
* a. The ROI
* b. The results files (.txt)
* c. A 4 channel image:
*         C1=DAPI
*         C2=Ibal
*         C3=TGFB1+ dots
*         C4=TGFB2+ dots
* d. One image: Ibal Mask
* e. A 3 channel image:
*         C1=DAPI in Ibal+
*         C2=TGFB1+ dots in Ibal+
*         C3=TGFB2+ dots in Ibal+
*/

// Create dialog, create save folders, and select file(s) to process
ThresholdMethods=getList("threshold.methods");
Dialog.create("Parameters");
Dialog.addMessage("Quantifying RNA Scope results");
Dialog.addCheckbox("Analyse single image container file", true);
Dialog.addCheckbox("Load lesion ROI", false);

//Channels
Dialog.addNumber("DAPI Channel", 1);
Dialog.addNumber("IBAL Channel", 2);
Dialog.addNumber("TGFB1 Channel", 3);
Dialog.addNumber("TGFB2 Channel", 4);
Dialog.addString("Name of saving folder: ", "_Results");
Dialog.addCheckbox("Automatic Threshold", true);
Dialog.addChoice("Threshold Algorithm for DAPI", ThresholdMethods);
Dialog.addChoice("Threshold Algorithm for IBAL", ThresholdMethods);
Dialog.addCheckbox("Automatic Threshold", true);
Dialog.addChoice("Threshold Algorithm for TGFB1", ThresholdMethods);
Dialog.addChoice("Threshold Algorithm for TGFB2", ThresholdMethods);

Dialog.show();

// Variables of Dialog
single_file=Dialog.getCheckbox();
LOAD_ROI=Dialog.getCheckbox();
DAPI_ch=Dialog.getNumber();
IBAL_ch=Dialog.getNumber();
TGFB1_ch=Dialog.getNumber();
TGFB2_ch=Dialog.getNumber();
save_folder=Dialog.getString();
auto_thr=Dialog.getCheckbox();
Method_DAPI=Dialog.getChoice();
Method_IBAL=Dialog.getChoice();
Method_TGFB1=Dialog.getChoice();
Method_TGFB2=Dialog.getChoice();

if(auto_thr)
{
    save_folder=save_folder+"_"+Method_DAPI+"_"+Method_IBAL+"_"+Method_TGFB1+"_"+Method_TGFB2;
}else{
    save_folder=save_folder+"_ManualThr";
}
sep = File.separator;

if (single_file)
{
    Filelist=newArray(1);
    Filelist[0] = File.openDialog("Select a file to process...");
    SourceDir=File.getParent(Filelist[0]);
    Filelist[0]=File.getName(Filelist[0]);
    save_folder_name_add=Filelist[0];
    SAVE_DIR=SourceDir;
}else
{
    SourceDir = getDirectory("Choose source directory");
    Filelist=getFileList(SourceDir);
    SAVE_DIR=SourceDir;
    save_folder_name_add=File.getName(SourceDir);
}

save_folder=save_folder+"_"+save_folder_name_add;

// Remove Folders from Filelist array
tmp=newArray();
for(k=0;k<Filelist.length;k++)
{
    if (!File.isDirectory(SourceDir+"/"+Filelist[k]))
    {
        tmp = Array.concat(tmp,Filelist[k]);
    }
}
}
```

Appendix

```
Filelist=tmp;

if(Load_ROI)
{
    LARGE_ROI_PATH = getDirectory("Select the folder containing the lesion ROIs");
}

getDateAndTime(year, month, dayOfWeek, dayOfMonth, hour, minute, second, msec);
month=month+1;
save_folder=save_folder+"_"+year+"_"+month+"_"+dayOfMonth+"_"+hour+"_"+minute+"_"+second;
new_folder=SAVE_DIR + sep + save_folder;
File.makeDirectory(new_folder);
setBatchMode(true);
for (k=0;k<Filelist.length;k++)
{
    if(!endsWith(Filelist[k], sep))
    {
        run("Bio-Formats Macro Extensions");
        Ext.setID(SourceDir+sep+Filelist[k]);
        Ext.getSeriesCount(SERIES_COUNT);
        FILE_PATH=SourceDir + sep + Filelist[k];

        //Arrays for each serie
        SeriesNames=newArray(SERIES_COUNT);
        TotalArea_ROI=newArray(SERIES_COUNT);
        DAPI_Count=newArray(SERIES_COUNT);
        IBA1_Area=newArray(SERIES_COUNT);
        IBA1_Mean=newArray(SERIES_COUNT);
        IBA1_IntegratedDen=newArray(SERIES_COUNT);
        TGFB1_Count=newArray(SERIES_COUNT);
        TGFB2_Count=newArray(SERIES_COUNT);
        DAPIIBA1_Count=newArray(SERIES_COUNT);
        TGFB1IBA1_Count=newArray(SERIES_COUNT);
        TGFB2IBA1_Count=newArray(SERIES_COUNT);

        for (i=0;i<SERIES_COUNT; i++)
        {
            options="open=["+ FILE_PATH + "] " + "autoscale color_mode=Default
view=Hyperstack stack_order=XYCZT " + "series_"+d2s(i+1,0);
            run("Bio-Formats Importer", options);

            FILE_NAME=File.nameWithoutExtension;
            Ext.setSeries(i);
            Ext.getSeriesName(SERIES_NAMES);
            SERIES_NAMES=replace(SERIES_NAMES, " ", "_");
            SERIES_NAMES=replace(SERIES_NAMES, "/", "_");
            SERIES_NAMES=replace(SERIES_NAMES, "\\(", "_");
            SERIES_NAMES=replace(SERIES_NAMES, "\\)", "_");
            SeriesNames[i]=SERIES_NAMES;
            SAVE_NAME=FILE_NAME+"_"+SERIES_NAMES;
            rename(SAVE_NAME);

            run("32-bit");
            run("Gaussian Blur...", "sigma=1.5 stack");
            getDimensions(width, height, channels, slices, frames);
            if(slices>1)
            {
                run("Z Project...", "projection=[Max Intensity]");
                selectWindow(SAVE_NAME);
                close();
                selectWindow("MAX_"+SAVE_NAME);
                rename(SAVE_NAME);
            }
            Stack.setDisplayMode("composite");

            //Select ROI to analyze and measure Lesion area
            roiManager("reset");
            Stack.setChannel(DAPI_ch);
            run("Cyan");
            Stack.setChannel(IBA1_ch);
            run("Magenta");
            run("Enhance Contrast", "saturated=0.35");
            Stack.setChannel(TGFB1_ch);
            run("Green");
            run("Enhance Contrast", "saturated=0.35");
            Stack.setChannel(TGFB2_ch);
            run("Yellow");
            run("Enhance Contrast", "saturated=0.35");
            Stack.setActiveChannels("11111");

            //Threshold out tissue holes and measure area ROI
            selectWindow(SAVE_NAME);
            run("Duplicate...", "duplicate channels="+IBA1_ch+"");
            rename("temp");
            setBatchMode("show");
            waitForUser("Please select the threshold limits,press Apply and convert
background to NaN\nThen click OK for this message. Bravo!");
            setBatchMode("hide");
        }
    }
}
```

Appendix

```
selectWindow(SAVE_NAME);
setTool("freehand");
if(LOAD_ROI)
{
    roiManager("Open",    LARGE_ROI_PATH    +    sep    +    SAVE_NAME+"-
Lesion_ROI"+" .zip" );
}
else
{
    setBatchMode("show");
    waitForUser("Please select the region of interest and press OK.
Efharisto!");
    roiManager("Add");
    setBatchMode("hide");
}
selectWindow("temp");
roiManager("Select", 0);
run("Set Measurements...", "area redirect=None decimal=3");
run("Measure");
TotalArea_ROI[i]=getResult("Area", 0);
run("Clear Results");
selectWindow("temp");
saveAs("tif", new_folder+ sep +SAVE_NAME+"-Tissue_only");
run("Close");
selectWindow(SAVE_NAME);
roiManager("deselect");
run("Select None");
run("Clear Results");
run("Set Measurements...", "area mean integrated redirect=None decimal=3");
run("Split Channels");

//Analyse DAPI Channel
selectWindow("C"+DAPI_ch+"-"+SAVE_NAME);
run("8-bit");
if(auto_thr)
{
    setAutoThreshold(Method_DAPI+" dark");
}
else
{
    setBatchMode("show");
    waitForUser("Threshold DAPI channel\n\nPlease select the threshold
limits and press Apply\nThen click OK for this message\nLooking good! Keep going...");
    setBatchMode("hide");
}
setOption("BlackBackground", true);
run("Convert to Mask");
run("Fill Holes");
run("Watershed");
roiManager("Select", 0);
run("Analyze Particles...", "size=4.00-Infinity display clear");
DAPI_Count[i]=nResults;
selectWindow("C"+DAPI_ch+"-"+SAVE_NAME);
run("32-bit");
run("Clear Results");

//Analyse Ibal Channel area and int
selectWindow("C"+IBAL_ch+"-"+SAVE_NAME);
if(auto_thr)
{
    setAutoThreshold(Method_IBA1+" dark");
    run("NaN Background");
}
else
{
    setBatchMode("show");
    waitForUser("Threshold IBA1 channel\n\nPlease select the threshold
limits,press Apply and convert background to NaN\nThen click OK for this message\nThank you, love!");
    setBatchMode("hide");
}
roiManager("Select", 0);
run("Measure");
IBAL_Area[i]=getResult("Area", 0);
IBAL_Mean[i]=getResult("Mean", 0);
IBAL_IntegratedDen[i]=getResult("IntDen", 0);
selectWindow("C"+IBAL_ch+"-"+SAVE_NAME);
run("32-bit");
run("Clear Results");

//Analyse TGFB1 Channel
selectWindow("C"+TGFB1_ch+"-"+SAVE_NAME);
run("8-bit");
if(auto_thr)
{
    setAutoThreshold(Method_TGFB1+" dark");
}
else
{
    setBatchMode("show");
```

Appendix

```

        waitForUser("Threshold TGFB1 channel\n\nPlease select the threshold
limits and press Apply\nThen click OK for this message\nEfharisto!");
        setBatchMode("hide");
    }
    setOption("BlackBackground", true);
    run("Convert to Mask");
    run("Fill Holes");
    run("Watershed");
    roiManager("Select", 0);
    run("Analyze Particles...", "size=0.80-Infinity circularity=0.50-1.00
display clear");

    TGFB1_Count[i]=nResults;
    selectWindow("C"+TGFB1_ch+"-"+SAVE_NAME);
    run("32-bit");
    run("Clear Results");

//Analyse TGFB2 Channel
selectWindow("C"+TGFB2_ch+"-"+SAVE_NAME);
run("8-bit");
if(auto_thr)
{
    setAutoThreshold(Method_TGFB2+" dark");
}
else
{
    setBatchMode("show");
    waitForUser("Threshold TGFB2 channel\n\nPlease select the threshold
limits and press Apply\nThen click OK for this message\nParakalo!");
    setBatchMode("hide");
}
setOption("BlackBackground", true);
run("Convert to Mask");
run("Fill Holes");
run("Watershed");
roiManager("Select", 0);
run("Analyze Particles...", "size=0.80-Infinity circularity=0.50-1.00
display clear");

    TGFB2_Count[i]=nResults;
    selectWindow("C"+TGFB2_ch+"-"+SAVE_NAME);
    run("32-bit");
    run("Clear Results");

//Making a Mask from Iba1 channel with values 1 and 0
selectWindow("C"+IBA1_ch+"-"+SAVE_NAME);
run("Duplicate...", "");
rename("IBA1_Mask");
run("8-bit");
setOption("BlackBackground", true);
run("Convert to Mask");
run("Fill Holes");
run("Subtract...", "value=254");

//Multiply DAPI by the Iba1 Mask and measure then the dots there
selectWindow("C"+DAPI_ch+"-"+SAVE_NAME);
run("Duplicate...", "");
rename("C"+DAPI_ch+"-DAPI-positive");
imageCalculator("Multiply create", "C"+DAPI_ch+"-DAPI-positive", "IBA1_Mask");

selectWindow("Result of C"+DAPI_ch+"-DAPI-positive");
run("8-bit");
roiManager("Select", 0);
run("Analyze Particles...", "size=4-Infinity display clear");
DAPIIBA1_Count[i]=nResults;
selectWindow("Result of C"+DAPI_ch+"-DAPI-positive");
run("Clear Results");

//Multiply TGFB1 by the Iba1 Mask and measure then the dots there
selectWindow("C"+TGFB1_ch+"-"+SAVE_NAME);
run("Duplicate...", "");
rename("C"+TGFB1_ch+"-TGFB1-positive");
imageCalculator("Multiply create", "C"+TGFB1_ch+"-TGFB1-
positive", "IBA1_Mask");

selectWindow("Result of C"+TGFB1_ch+"-TGFB1-positive");
run("8-bit");
roiManager("Select", 0);
run("Analyze Particles...", "size=0.8-Infinity circularity=0.50-1.00 display
clear ");

    TGFB1IBA1_Count[i]=nResults;
    selectWindow("Result of C"+TGFB1_ch+"-TGFB1-positive");
    run("Clear Results");

//Multiply TGFB2 by the Iba1 Mask and measure then the dots there
selectWindow("C"+TGFB2_ch+"-"+SAVE_NAME);
run("Duplicate...", "");
rename("C"+TGFB2_ch+"-TGFB2-positive");
```

Appendix

```
imageCalculator("Multiply", "C"+TGFB2_ch+"-TGFB2-
positive", "IBAl_Mask");

selectWindow("Result of C"+TGFB2_ch+"-TGFB2-positive");
run("8-bit");
roiManager("Select", 0);
run("Analyze Particles...", "size=0.8-Infinity circularity=0.50-1.00 display
clear ");

TGFB2IBAl_Count[i]=nResults;
selectWindow("Result of C"+TGFB2_ch+"-TGFB2-positive");
run("Clear Results");

//Finishing up
run("Merge Channels...", "c1=[C"+DAPI_ch+"-"+SAVE_NAME+"] c2=[C"+IBAl_ch+"-
"+SAVE_NAME+"] c3=[C"+TGFB1_ch+"-"+SAVE_NAME+"] c4=[C"+TGFB2_ch+"-"+SAVE_NAME+"] create");
Stack.setDisplayMode("composite");
Stack.setChannel(DAPI_ch);
run("Cyan");
Stack.setChannel(IBAl_ch);
run("Magenta");
run("Enhance Contrast", "saturated=0.35");
Stack.setChannel(TGFB1_ch);
run("Green");
run("Enhance Contrast", "saturated=0.35");
Stack.setChannel(TGFB2_ch);
run("Yellow");
run("Enhance Contrast", "saturated=0.35");
saveAs("tif", new_folder+ sep +SAVE_NAME+"-Thresh");

selectWindow("IBAl_Mask");
saveAs("tif", new_folder+ sep +SAVE_NAME+"-Mask");
run("Merge Channels...", "c1=[Result of C"+DAPI_ch+"-DAPI-positive]
c2=[Result of C"+TGFB1_ch+"-TGFB1-positive] c3=[Result of C"+TGFB2_ch+"-TGFB2-positive] create");
saveAs("tif", new_folder+ sep +SAVE_NAME+"-DAPI-TGFB1-TGFB2_Masked");

roiManager("Select", 0);
roiManager("save", new_folder+ sep + SAVE_NAME+"-ROI"+".zip");
roiManager("reset");

run("Close All");
}
roiManager("reset");
for (t=0;t<SERIES_COUNT; t++)
{
run("Input/Output...", "jpeg=85 gif=-1 file=.xls copy_row save_column");
setResult("Slice", t, SeriesNames[t]);
setResult("ROI Area [um^2]", t, TotalArea_ROI[t]);
setResult("Number of nuclei", t, DAPI_Count[t]);
setResult("IBAl Area [um^2]", t, IBAl_Area[t]);
setResult("IBAl mean intensity", t, IBAl_Mean[t]);
setResult("IBAl integrated density", t, IBAl_IntegratedDen[t]);
setResult("Number of TGFB1", t, TGFB1_Count[t]);
setResult("Number of TGFB2", t, TGFB2_Count[t]);
setResult("Number of DAPIIBAl", t, DAPIIBAl_Count[t]);
setResult("Number of TGFB1IBAl", t, TGFB1IBAl_Count[t]);
setResult("Number of TGFB2IBAl", t, TGFB2IBAl_Count[t]);

updateResults();
}
saveAs("Results", new_folder+ sep +FILE_NAME+"-Results"+".txt");
run("Clear Results");
}
}
setBatchMode(false);
```

Macro to quantify the signal from the reporter mouse line CX3CR1-GFP x CCR2-RFP

This macro was created to quantify the percentage area occupied by the different signals in the reporter mouse line CX3CR1-GFP x CCR2-RFP, plus the signal from a IBA1 staining. It quantifies the area occupied by a certain signal after thresholding and computes image calculations to also quantify the percentage area occupied by the overlap between different signal combinations. In short, the steps to achieve this analysis are the following:

1. Create dialog for user to select the file to process and the thresholding strategy for each channel (both manual and automatic options available). Also, the option is given to load a pre-selected ROI.

Appendix

2. Open file container or directory with single images and make a selection list with all images.
3. For each image, convert the image to 32-Bit and allow the user to select the ROI. For each channel, allow the user to select a thresholding strategy to distinguish the positive signal from the background and measure the area and intensity of the thresholded signal.
4. Multiply 32-bit-thresholded versions of different channels in order to generate 32-bit images with only the double-positive areas (for example: IBA1+CX3CR1+). Then, measure the percentage of total area occupied by this new signal.
5. Save results and close.

```
/*
*****
* Author Dr. Ioannis K. Alexopoulos
* The author of the macro reserve the copyrights of the original macro.
* However, you are welcome to distribute, modify and use the program under
* the terms of the GNU General Public License as stated here:
* (http://www.gnu.org/licenses/gpl.txt) as long as you attribute proper
* acknowledgement to the author as mentioned above.
* This program is distributed in the hope that it will be useful,
* but WITHOUT ANY WARRANTY; without even the implied warranty of
* MERCHANTABILITY or FITNESS FOR A PARTICULAR PURPOSE. See the
* GNU General Public License for more details.
*****
* Description of macro
* -----
* This macro is used to analyse the mouse spinal cord lesions.
* It quantifies:
* 1. The area of the lesion (defined by the user)
* 2. The area occupied by Ibal+ cells
* 3. The area occupied by CX3CR1+ cells
* 4. The area occupied by CCR2+ cells
* 5. The area occupied by Ibal+/CX3CR1+ cells
* 6. The area occupied by Ibal+/CCR2+ cells
* 7. The area occupied by Ibal+/CX3CR1+/CCR2+ cells
* 8. The area occupied by Ibal+/CX3CR1+/CCR2- cells
*
* The output of the macro is:
* a. The lesion ROI
* b. The results files (.txt)
* c. A seven channel image:
*      C1=Ibal+
*      C2=CX3CR1+
*      C3=CCR2+
*      C4=Ibal+/CX3CR1+
*      C5=Ibal+/CCR2+
*      C6=Ibal+/CX3CR1+/CCR2+
*      C7=Ibal+/CX3CR1+/CCR2-
*
*/

// Create dialog, create save folders, and select file(s) to process
ThresholdMethods=getList("threshold.methods");
Dialog.create("Parameters");
Dialog.addMessage("Quantify macrophages and microglia infiltration within a lesion");
Dialog.addCheckbox("Analyse single image container file", true);
Dialog.addCheckbox("Load lesion ROI", false);

//Channels
Dialog.addNumber("DAPI Channel", 1);
Dialog.addNumber("Ibal Channel", 2);
Dialog.addNumber("CX3CR1 Channel", 3);
Dialog.addNumber("CCR2 Channel", 4);
Dialog.addString("Name of saving folder: ", "_Results");
Dialog.addCheckbox("Automatic Threshold", true);
Dialog.addChoice("Threshold Algorithm for DAPI", ThresholdMethods);
Dialog.addChoice("Threshold Algorithm for Ibal", ThresholdMethods);
Dialog.addChoice("Threshold Algorithm for CX3CR1", ThresholdMethods);
Dialog.addChoice("Threshold Algorithm for CCR2", ThresholdMethods);
Dialog.addCheckbox("Dilate and fill Ibal mask", true);
Dialog.show();

// Variables of Dialog
single_file=Dialog.getCheckbox();
LOAD_ROI=Dialog.getCheckbox();
DAPI_ch=Dialog.getNumber();
IBA1_ch=Dialog.getNumber();
CX3CR1_ch=Dialog.getNumber();
CCR2_ch=Dialog.getNumber();
save_folder=Dialog.getString();
```

Appendix

```
auto_thr=Dialog.getCheckbox();
Method_dapi=Dialog.getChoice();
Method_ibal=Dialog.getChoice();
Method_CX3CR1=Dialog.getChoice();
Method_CCR2=Dialog.getChoice();
dilate_option=Dialog.getCheckbox();

if(auto_thr)
{
    save_folder=save_folder+"_"+Method_ibal;
}else{
    save_folder=save_folder+"_ManualThr";
}
sep = File.separator;

if (single_file)
{
    Filelist=newArray(1);
    Filelist[0] = File.openDialog("Select a file to process...");
    SourceDir=File.getParent (Filelist[0]);
    Filelist[0]=File.getName (Filelist[0]);
    save_folder_name_add=Filelist[0];
    SAVE_DIR=SourceDir;
}else
{
    SourceDir = getDirectory("Choose source directory");
    Filelist=getFileList (SourceDir);
    SAVE_DIR=SourceDir;
    save_folder_name_add=File.getName (SourceDir);
}

save_folder=save_folder+" "+save_folder_name_add;
// Remove Folders from Filelist array
tmp=newArray();
for(k=0;k<Filelist.length;k++)
{
    if (!File.isDirectory(SourceDir+"/"+Filelist[k]))
    {
        tmp = Array.concat(tmp,Filelist[k]);
    }
}
Filelist=tmp;

if(LOAD_ROI)
{
    LARGE_ROI_PATH = getDirectory("Select the folder containing the lesion ROIs");
}

getDateAndTime(year, month, dayOfWeek, dayOfMonth, hour, minute, second, msec);
month=month+1;
save_folder=save_folder+"_"+year+"_"+month+"_"+dayOfMonth+"_"+hour+"_"+minute+"_"+second;
new_folder=SAVE_DIR + sep + save_folder;
File.makeDirectory(new_folder);
setBatchMode(true);
for (k=0;k<Filelist.length;k++)
{
    if(!endsWith(Filelist[k], sep))
    {
        run("Bio-Formats Macro Extensions");
        Ext.setId(SourceDir+sep+Filelist[k]);
        Ext.getSeriesCount (SERIES_COUNT);
        FILE_PATH=SourceDir + sep + Filelist[k];

        //Arrays for each serie
        SeriesNames=newArray (SERIES_COUNT);
        TotalArea_Lesion=newArray (SERIES_COUNT);
        Ibal_Area=newArray (SERIES_COUNT);
        CX3CR1_Area=newArray (SERIES_COUNT);
        CCR2_Area=newArray (SERIES_COUNT);
        Ibal_CCR2_Area=newArray (SERIES_COUNT);
        Ibal_CX3CR1_Area=newArray (SERIES_COUNT);
        Ibal_CX3CR1_CCR2_Area=newArray (SERIES_COUNT);
        Ibal_CX3CR1_CCR2_neg_Area=newArray (SERIES_COUNT);

        for (i=0;i<SERIES_COUNT; i++)
        {
            options="open=["+ FILE_PATH + "]" + " " + "autoscale color_mode=Default
view=Hyperstack stack_order=XYCZT " + "series "+d2s(i+1,0);
            run("Bio-Formats Importer", options);
            FILE_NAME=File.nameWithoutExtension;
            Ext.setSeries(i);
            Ext.getSeriesName (SERIES_NAMES);
            SERIES_NAMES=replace (SERIES_NAMES, " ", "_");
            SERIES_NAMES=replace (SERIES_NAMES, "/", "_");
            SERIES_NAMES=replace (SERIES_NAMES, "\\(", "_");
            SERIES_NAMES=replace (SERIES_NAMES, "\\)", "_");
            SeriesNames[i]=SERIES_NAMES;
        }
    }
}
```

Appendix

```
SAVE_NAME=FILE_NAME+"_"+SERIES_NAMES;
rename(SAVE_NAME);
run("32-bit");
run("Gaussian Blur...", "sigma=1.5 stack");
getDimensions(width, height, channels, slices, frames);
if(slices>1)
{
    run("Z Project...", "projection=[Max Intensity]");
    selectWindow(SAVE_NAME);
    close();
    selectWindow("MAX_"+SAVE_NAME);
    rename(SAVE_NAME);
}
Stack.setDisplayMode("composite");

//Select ROI to analyze and measure Lesion area
roiManager("reset");

Stack.setChannel(DAPI_ch);
run("Cyan");
Stack.setChannel(IBA1_ch);
run("Grays");
run("Enhance Contrast", "saturated=0.35");
Stack.setChannel(CX3CR1_ch);
run("Green");
run("Enhance Contrast", "saturated=0.35");
Stack.setChannel(CCR2_ch);
run("Magenta");
run("Enhance Contrast", "saturated=0.35");

Stack.setActiveChannels("0110");
setTool("freehand");
if(LOAD_ROI)
{
    roiManager("Open", LARGE_ROI_PATH + sep + SAVE_NAME+"-
Lesion_ROI"+" .zip" );
}
else
{
    setBatchMode("show");
    waitForUser("Please select the region of interest and press OK");
    roiManager("Add");
    setBatchMode("hide");
}
roiManager("Select", 0);
run("Set Measurements...", "area redirect=None decimal=3");
run("Measure");
TotalArea_Lesion[i]=getResult("Area", 0);
run("Clear Results");

roiManager("deselect");
run("Select None");
run("Clear Results");
run("Set Measurements...", "area redirect=None decimal=3");
run("Split Channels");

//Analyse Ibal Channel
selectWindow("C"+IBA1_ch+"-"+SAVE_NAME);
if(auto_thr)
{
    setAutoThreshold(Method_ibal+" dark");
    run("NaN Background");
}
else
{
    setBatchMode("show");
    waitForUser("Please select the threshold limits,press Apply and
convert background to NaN\nThen click OK for this message");
    setBatchMode("hide");
}
roiManager("Select", 0);
run("Measure");
Ibal_Area[i]=getResult("Area", 0);
run("Clear Results");
selectWindow("C"+IBA1_ch+"-"+SAVE_NAME);
rename("C"+IBA1_ch+"-Ibal-positive");
run("Select None");
run("Duplicate...", "title=C"+IBA1_ch+"-positive-binary");
setOption("BlackBackground", true);
run("Make Binary");
if (dilate_option)
{
    run("Options...", "iterations=4 count=2 black do=Dilate stack");
    run("Close-", "stack");
    run("Fill Holes", "stack");
}
run("Divide...", "value=255.000");
run("32-bit");
setAutoThreshold("Default dark");
```

Appendix

```

run("NaN Background");

//Analyse Microglia-GFP Channel
selectWindow("C"+CX3CR1_ch+"-"+SAVE_NAME);
if(auto_thr)
{
    setAutoThreshold(Method_CX3CR1+" dark");
    run("NaN Background");
}
else
{
    setBatchMode("show");
    waitForUser("Please select the threshold limits,press Apply and
convert background to NaN\nThen click OK for this message");
    setBatchMode("hide");
}
roiManager("Select", 0);
run("Measure");
CX3CR1_Area[i]=getResult("Area", 0);
run("Clear Results");
selectWindow("C"+CX3CR1_ch+"-"+SAVE_NAME);
rename("C"+CX3CR1_ch+"-CX3CR1-positive");

//Analyse Macrophages-RFP Channel
selectWindow("C"+CCR2_ch+"-"+SAVE_NAME);
if(auto_thr)
{
    setAutoThreshold(Method_CCR2+" dark");
    run("NaN Background");
}
else
{
    setBatchMode("show");
    waitForUser("Please select the threshold limits,press Apply and
convert background to NaN\nThen click OK for this message");
    setBatchMode("hide");
}
roiManager("Select", 0);
run("Measure");
CCR2_Area[i]=getResult("Area", 0);
run("Clear Results");
selectWindow("C"+CCR2_ch+"-"+SAVE_NAME);
run("Select None");
rename("C"+CCR2_ch+"-CCR2-positive");
run("Duplicate...", "title=C"+CCR2_ch+"-binary");
setOption("BlackBackground", true);
run("Make Binary");
run("Divide...", "value=255.000");
run("Invert");
run("32-bit");
setAutoThreshold("Default dark");
run("NaN Background");
rename("C"+CCR2_ch+"-CCR2-negative");

imageCalculator("Multiply create 32-bit", "C"+IBA1_ch+"-positive-
binary", "C"+CCR2_ch+"-CCR2-positive");
selectWindow("Result of C"+IBA1_ch+"-positive-binary");
rename("Iba1-CCR2");
roiManager("Select", 0);
run("Measure");
Iba1_CCR2_Area[i]=getResult("Area", 0);
run("Clear Results");

//Iba1/CX3CR1+
imageCalculator("Multiply create 32-bit", "C"+IBA1_ch+"-positive-
binary", "C"+CX3CR1_ch+"-CX3CR1-positive");
selectWindow("Result of C"+IBA1_ch+"-positive-binary");
rename("Iba1-CX3CR1");
roiManager("Select", 0);
run("Measure");
Iba1_CX3CR1_Area[i]=getResult("Area", 0);
run("Clear Results");

//Iba1/CX3CR1+/CCR2+
imageCalculator("Multiply create 32-bit", "Iba1-CX3CR1", "C"+CCR2_ch+"-CCR2-
positive");

selectWindow("Result of Iba1-CX3CR1");
rename("Iba1-CX3CR1-CCR2");
roiManager("Select", 0);
run("Measure");
Iba1_CX3CR1_CCR2_Area[i]=getResult("Area", 0);
run("Clear Results");

//Iba1/CX3CR1+/CCR2-
imageCalculator("Multiply create 32-bit", "Iba1-CX3CR1", "C"+CCR2_ch+"-CCR2-
negative");

selectWindow("Result of Iba1-CX3CR1");
rename("Iba1-CX3CR1-CCR2_neg");
roiManager("Select", 0);
run("Measure");

```

Appendix

```
Iba1_CX3CR1_CCR2_neg_Area[i]=getResult("Area", 0);
run("Clear Results");

run("Merge Channels...", "c1=[C"+Iba1_ch+"-Iba1-positive]
c2=[C"+CX3CR1_ch+"-CX3CR1-positive] c3=[C"+CCR2_ch+"-CCR2-positive] c4=[Iba1-CX3CR1] c5=[Iba1-CCR2]
c6=[Iba1-CX3CR1-CCR2] c7=[Iba1-CX3CR1-CCR2_neg] create");
saveAs("tif", new_folder+ sep +SAVE_NAME+"-Thresh");

roiManager("Select",0);
roiManager("save", new_folder+ sep + SAVE_NAME+"-Lesion_ROI"+".zip");
roiManager("reset");

run("Close All");
}
roiManager("reset");
for (t=0;t<SERIES_COUNT; t++)
{
run("Input/Output...", "jpeg=85 gif=-1 file=.xls copy_row save_column");
getResult("Slice", t, SeriesNames[t]);
getResult("Lesion Area [um^2]", t, TotalArea_Lesion[t]);

getResult("Iba1+ Area [um^2]", t, Iba1_Area[t]);
getResult("CX3CR1+ Area [um^2]", t, CX3CR1_Area[t]);
getResult("CCR2+ Area [um^2]", t, CCR2_Area[t]);

getResult("Iba1+/CX3CR1+ Area [um^2]", t, Iba1_CX3CR1_Area[t]);
getResult("Iba1+/CCR2+ Area [um^2]", t, Iba1_CCR2_Area[t]);
getResult("Iba1+/CX3CR1+/CCR2+ Area [um^2]", t, Iba1_CX3CR1_CCR2_Area[t]);
getResult("Iba1+/CX3CR1+/CCR2- Area [um^2]", t, Iba1_CX3CR1_CCR2_neg_Area[t]);
updateResults();
saveAs("Results", new_folder+ sep +FILE_NAME+"-Results"+".txt");
run("Clear Results");
}
}
setBatchMode(false);
```

Macro to quantify the signal from the reporter mouse line ARG1-YFP x iNOS-tdTomato

This macro is very similar to the one used for the CX3CR1-GFP x CCR2-RFP mouse line. It was created to quantify the percentage area occupied by the different signals in the reporter mouse line ARG1-YFP x iNOS-tdTomato, plus the signal from a IBA1 staining. It quantifies the area occupied by a certain signal after thresholding and computes image calculations to also quantify the percentage area occupied by the overlap between different signal combinations. In short, the steps to achieve this analysis are the following:

1. Create dialog for user to select the file to process and the thresholding strategy for each channel (both manual and automatic options available). Also, the option is given to load a pre-selected ROI.
2. Open file container or directory with single images and make a selection list with all images.
3. For each image, convert the image to 32 Bit and allow the user to select the ROI. Then, allow the user to select a thresholding strategy to eliminate the tissue holes and measure the area occupied by the tissue. For each channel, allow the user to select a thresholding strategy to distinguish the positive signal from the background and measure the area and intensity of the thresholded signal.
4. Multiply 32-bit-thresholded versions of different channels to generate 32-bit images with only the double-positive areas (for example: iNOS⁺ARG1⁺). Then, measure the percentage of total area occupied by this new signal.
5. Save results and close.

```
/*
 * Author Dr. Ioannis K. Alexopoulos
 * The author of the macro reserve the copyrights of the original macro.
 * However, you are welcome to distribute, modify and use the program under
 * the terms of the GNU General Public License as stated here:
 * (http://www.gnu.org/licenses/gpl.txt) as long as you attribute proper
 * acknowledgement to the author as mentioned above.
 * This program is distributed in the hope that it will be useful,
```

Appendix

```
* but WITHOUT ANY WARRANTY; without even the implied warranty of
* MERCHANTABILITY or FITNESS FOR A PARTICULAR PURPOSE. See the
* GNU General Public License for more details.
*****
* Description of macro
* -----
* This macro is used to analyse the mouse spinal cord lesions.
* It quantifies:
* 1. The area of the lesion (defined by the user)
* 2. The area occupied by Ibal+ cells
* 3. The area occupied by Arginase+ cells
* 4. The area occupied by iNOS+ cells
* 5. The area occupied by Ibal+/Arginase+ cells
* 6. The area occupied by Ibal+/iNOS+ cells
* 7. The area occupied by Arginase+/iNOS+ cells
* 8. The area occupied by Ibal+/Arginase+/iNOS+ cells
*
* The output of the macro is:
* a. The lesion ROI
* b. The results files (.txt)
* c. The tissue thresholded image (the image used to measure only tissue area)
* d. A seven channel image:
*         C1=Ibal+
*         C2=Arginase+
*         C3=iNOS+
*         C4=Ibal+/Arginase+
*         C5=Ibal+/iNOS+
*         C6=Arginase+/iNOS+
*         C7=Ibal+/Arginase+/iNOS+
*/

// Create dialog, create save folders, and select file(s) to process
ThresholdMethods=getList("threshold.methods");
Dialog.create("Parameters");
Dialog.addMessage("Quantify macrophages and microglia infiltration within a lesion");
Dialog.addCheckbox("Analyse single image container file", true);
Dialog.addCheckbox("Load lesion ROI", false);

//Channels
Dialog.addNumber("DAPI Channel", 1);
Dialog.addNumber("Ibal Channel", 2);
Dialog.addNumber("Arginase Channel", 3);//Arginase
Dialog.addNumber("iNOS Channel", 4);//iNOS
Dialog.addString("Name of saving folder: ", " Results");
Dialog.addCheckbox("Automatic Threshold", true);
Dialog.addChoice("Threshold Algorithm for DAPI", ThresholdMethods);
Dialog.addChoice("Threshold Algorithm for Ibal", ThresholdMethods);
Dialog.addChoice("Threshold Algorithm for Arginase", ThresholdMethods);
Dialog.addChoice("Threshold Algorithm for iNOS", ThresholdMethods);
Dialog.addCheckbox("Dilate and fill Ibal mask", true);
Dialog.show();

// Variables of Dialog
single_file=Dialog.getCheckbox();
LOAD_ROI=Dialog.getCheckbox();
DAPI_ch=Dialog.getNumber();
IBAL_ch=Dialog.getNumber();
ARGINASE_ch=Dialog.getNumber();
iNOS_ch=Dialog.getNumber();
save_folder=Dialog.getString();
auto_thr=Dialog.getCheckbox();
Method_dapi=Dialog.getChoice();
Method_ibal=Dialog.getChoice();
Method_ARGINASE=Dialog.getChoice();
Method_iNOS=Dialog.getChoice();
dilate_option=Dialog.getCheckbox();

if(auto_thr)
{
    save_folder=save_folder+"_"+Method_ibal;
}else{
    save_folder=save_folder+"_ManualThr";
}
sep = File.separator;

if (single_file)
{
    Filelist=newArray(1);
    Filelist[0] = File.openDialog("Select a file to process...");
    SourceDir=File.getParent(Filelist[0]);
    Filelist[0]=File.getName(Filelist[0]);
    save_folder_name_add=Filelist[0];
    SAVE_DIR=SourceDir;
}else
{
    SourceDir = getDirectory("Choose source directory");
}
```

Appendix

```
Filelist=getFileList(SourceDir);
SAVE_DIR=SourceDir;
save_folder_name_add=File.getName(SourceDir);
}

save_folder=save_folder+"_"+save_folder_name_add;
// Remove Folders from Filelist array
tmp=newArray();
for(k=0;k<Filelist.length;k++)
{
    if (!File.isDirectory(SourceDir+"/"+Filelist[k]))
    {
        tmp = Array.concat(tmp,Filelist[k]);
    }
}
Filelist=tmp;

if(LOAD_ROI)
{
    LARGE_ROI_PATH = getDirectory("Select the folder containing the lesion ROIs");
}

getDateAndTime(year, month, dayOfWeek, dayOfMonth, hour, minute, second, msec);
month=month+1;
save_folder=save_folder+"_"+year+"_"+month+"_"+dayOfMonth+"_"+hour+"_"+minute+"_"+second;
new_folder=SAVE_DIR + sep + save_folder;
File.makeDirectory(new_folder);
setBatchMode(true);
for (k=0;k<Filelist.length;k++)
{
    if(!endsWith(Filelist[k], sep))
    {
        run("Bio-Formats Macro Extensions");
        Ext.setID(SourceDir+sep+Filelist[k]);
        Ext.getSeriesCount(SERIES_COUNT);
        FILE_PATH=SourceDir + sep + Filelist[k];

        //Arrays for each serie
        SeriesNames=newArray(SERIES_COUNT);
        TotalArea_Lesion=newArray(SERIES_COUNT);
        Ibal_Area=newArray(SERIES_COUNT);
        ARGINASE_Area=newArray(SERIES_COUNT);
        iNOS_Area=newArray(SERIES_COUNT);
        Ibal_ARGINASE_Area=newArray(SERIES_COUNT);
        Ibal_iNOS_Area=newArray(SERIES_COUNT);
        ARGINASE_iNOS_Area=newArray(SERIES_COUNT);
        Ibal_ARGINASE_iNOS_Area=newArray(SERIES_COUNT);
        Ibal_ARGINASE_iNOS_neg_Area=newArray(SERIES_COUNT);

        for (i=0;i<SERIES_COUNT; i++)
        {
            options="open=["+ FILE_PATH + "] " + "autoscale color_mode=Default
view=Hyperstack stack_order=XYCZT " + "series_"+d2s(i+1,0);
            run("Bio-Formats Importer", options);
            FILE_NAME=File.nameWithoutExtension;
            Ext.setSeries(i);
            Ext.getSeriesName(SERIES_NAMES);
            SERIES_NAMES=replace(SERIES_NAMES, " ", "_");
            SERIES_NAMES=replace(SERIES_NAMES, "/", "_");
            SERIES_NAMES=replace(SERIES_NAMES, "\\(", "(");
            SERIES_NAMES=replace(SERIES_NAMES, "\\)", ")");
            SeriesNames[i]=SERIES_NAMES;
            SAVE_NAME=FILE_NAME+"_"+SERIES_NAMES;
            rename(SAVE_NAME);
            run("32-bit");
            run("Gaussian Blur...", "sigma=1.5 stack");
            getDimensions(width, height, channels, slices, frames);
            if(slices>1)
            {
                run("Z Project...", "projection=[Max Intensity]");
                selectWindow(SAVE_NAME);
                close();
                selectWindow("MAX_"+SAVE_NAME);
                rename(SAVE_NAME);
            }
            Stack.setDisplayMode("composite");
            //Select ROI to analyze and measure Lesion area
            roiManager("reset");

            Stack.setChannel(DAPI_ch);
            run("Cyan");
            Stack.setChannel(IBA1_ch);
            run("Grays");
            run("Enhance Contrast", "saturated=0.35");
            Stack.setChannel(ARGINASE_ch);
            run("Green");
            run("Enhance Contrast", "saturated=0.35");
            Stack.setChannel(iNOS_ch);
```

Appendix

```
run("Magenta");
run("Enhance Contrast", "saturated=0.35");
Stack.setActiveChannels("0110");
//Threshold out tissue "holes"
selectWindow(SAVE_NAME);
run("Duplicate...", "duplicate channels="+IBAL_ch+"");
rename("temp");
setBatchMode("show");
waitForUser("Please select the threshold limits,press Apply and convert
background to NaN\nThen click OK for this message");
setBatchMode("hide");

selectWindow(SAVE_NAME);
setTool("freehand");
if(LOAD_ROI)
{
    roiManager("Open",    LARGE_ROI_PATH    +    sep    +    SAVE_NAME+"-
Lesion_ROI"+" .zip" );
}
else
{
    setBatchMode("show");
    waitForUser("Please select the region of interest and press OK");
    roiManager("Add");
    setBatchMode("hide");
}
//Measure only tissue area (exclude "holes")
selectWindow("temp");
roiManager("Select", 0);
run("Set Measurements...", "area redirect=None decimal=3");
run("Measure");
TotalArea_Lesion[i]=getResult("Area", 0);
run("Clear Results");
selectWindow("temp");
saveAs("tif", new_folder+ sep +SAVE_NAME+"-Tissue_only");
run("Close");
selectWindow(SAVE_NAME);
roiManager("deselect");
run("Select None");
run("Clear Results");
run("Set Measurements...", "area redirect=None decimal=3");
run("Split Channels");
//Analyse Ibal Channel
selectWindow("C"+IBAL_ch+"-"+SAVE_NAME);
if(auto_thr)
{
    setAutoThreshold(Method_ibal+" dark");
    run("NaN Background");
}
else
{
    setBatchMode("show");
    waitForUser("Please select the threshold limits,press Apply and
convert background to NaN\nThen click OK for this message");
    setBatchMode("hide");
}
roiManager("Select", 0);
run("Measure");
Ibal_Area[i]=getResult("Area", 0);
run("Clear Results");
selectWindow("C"+IBAL_ch+"-"+SAVE_NAME);
rename("C"+IBAL_ch+"-Ibal-positive");
run("Select None");
run("Duplicate...", "title=C"+IBAL_ch+"-positive-binary");
setOption("BlackBackground", true);
run("Make Binary");
if (dilate_option)
{
    run("Options...", "iterations=4 count=2 black do=Dilate stack");
    run("Close-", "stack");
    run("Fill Holes", "stack");
}
run("Divide...", "value=255.000");
run("32-bit");
setAutoThreshold("Default dark");
run("NaN Background");
//Analyse Arginase-YFP Channel
selectWindow("C"+ARGINASE_ch+"-"+SAVE_NAME);
if(auto_thr)
{
    setAutoThreshold(Method_ARGINASE+" dark");
    run("NaN Background");
}
else
{
    setBatchMode("show");
    waitForUser("Please select the threshold limits,press Apply and
convert background to NaN\nThen click OK for this message");
    setBatchMode("hide");
}
roiManager("Select", 0);
```

Appendix

```

run("Measure");
ARGINASE_Area[i]=getResult("Area", 0);
run("Clear Results");
selectWindow("C"+ARGINASE_ch+"-"+SAVE_NAME);
rename("C"+ARGINASE_ch+"-ARGINASE-positive");
//Analyse iNOS-tdTomato Channel
selectWindow("C"+iNOS_ch+"-"+SAVE_NAME);
if(auto_thr)
{
    setAutoThreshold(Method_iNOS+" dark");
    run("NaN Background");
}
else
{
    setBatchMode("show");
    waitForUser("Please select the threshold limits,press Apply and
convert background to NaN\nThen click OK for this message");
    setBatchMode("hide");
}
roiManager("Select", 0);
run("Measure");
iNOS_Area[i]=getResult("Area", 0);
run("Clear Results");
selectWindow("C"+iNOS_ch+"-"+SAVE_NAME);
run("Select None");
rename("C"+iNOS_ch+"-ARGINASE-positive");
run("Duplicate...", "title=C"+iNOS_ch+"-binary");
setOption("BlackBackground", true);
run("Make Binary");
run("Divide...", "value=255.000");
run("Invert");
run("32-bit");
setAutoThreshold("Default dark");
run("NaN Background");
rename("C"+iNOS_ch+"-iNOS-negative");

//Ibal+/Arginase+
imageCalculator("Multiply create 32-bit", "C"+IBal_ch+"-positive-
binary", "C"+ARGINASE_ch+"-ARGINASE-positive");
selectWindow("Result of C"+IBal_ch+"-positive-binary");
rename("Ibal-ARGINASE");
roiManager("Select", 0);
run("Measure");
Ibal_ARGINASE_Area[i]=getResult("Area", 0);
run("Clear Results");

//Ibal+/iNOS+
imageCalculator("Multiply create 32-bit", "C"+IBal_ch+"-positive-
binary", "C"+iNOS_ch+"-iNOS-positive");
selectWindow("Result of C"+IBal_ch+"-positive-binary");
rename("Ibal-iNOS");
roiManager("Select", 0);
run("Measure");
Ibal_iNOS_Area[i]=getResult("Area", 0);
run("Clear Results");

//iNOS+/Arginase+
imageCalculator("Multiply create 32-bit", "C"+iNOS_ch+"-iNOS-
positive", "C"+ARGINASE_ch+"-ARGINASE-positive");
selectWindow("Result of C"+iNOS_ch+"-iNOS-positive");
rename("iNOS-Arginase");
roiManager("Select", 0);
run("Measure");
iNOS_ARGINASE_Area[i]=getResult("Area", 0);
run("Clear Results");

//Ibal+/iNOS+/Arginase+
imageCalculator("Multiply create 32-bit", "Ibal-ARGINASE", "C"+iNOS_ch+"-
iNOS-positive");

selectWindow("Result of Ibal-ARGINASE");
rename("Ibal-ARGINASE-iNOS");
roiManager("Select", 0);
run("Measure");
Ibal_ARGINASE_iNOS_Area[i]=getResult("Area", 0);
run("Clear Results");

run("Merge Channels...", "c1=[C"+IBal_ch+"-Ibal-positive]
c2=[C"+ARGINASE_ch+"-ARGINASE-positive] c3=[C"+iNOS_ch+"-iNOS-positive] c4=[Ibal-iNOS] c5=[Ibal-
ARGINASE] c6=[iNOS-Arginase] c7=[Ibal-iNOS-ARGINASE] create");
saveAs("tif", new_folder+ sep +SAVE_NAME+"-Thresh");

roiManager("Select", 0);
roiManager("save", new_folder+ sep + SAVE_NAME+"-Lesion_ROI"+" .zip");
roiManager("reset");

run("Close All");
}
roiManager("reset");
for (t=0;t<SERIES_COUNT; t++)

```

Appendix

```
{
    run("Input/Output...", "jpeg=85 gif=-1 file=.xls copy_row save_column");
    setResult("Slice", t, SeriesNames[t]);
    setResult("Lesion Area [um^2]", t, TotalArea_Lesion[t]);

    setResult("Iba1+ Area [um^2]", t, Iba1_Area[t]);
    setResult("ARGINASE+ Area [um^2]", t, ARGINASE_Area[t]);
    setResult("iNOS+ Area [um^2]", t, iNOS_Area[t]);

    setResult("Iba1+/ARGINASE+ Area [um^2]", t, Iba1_ARGINASE_Area[t]);
    setResult("Iba1+/iNOS+ Area [um^2]", t, Iba1_iNOS_Area[t]);
    setResult("ARGINASE+/iNOS+ Area [um^2]", t, ARGINASE_iNOS_Area[t]);
    setResult("Iba1+/ARGINASE+/iNOS+ Area [um^2]", t,
Iba1_ARGINASE_iNOS_Area[t]);

    updateResults();
}
saveAs("Results", new_folder+ sep +FILE_NAME+"-Results+".txt");
run("Clear Results");
}
setBatchMode(false);
```

4. Protocols

Find in the following pages the detailed protocols of the most commonly used techniques of this study.

DNA isolation and PCR for genotyping

Lysis with NucleoSpin Tissue Kit

PROTOCOL

1. Add 200 μ L Buffer T1 and 25 μ L Proteinase K solution. Vortex to mix. Be sure that the samples are completely covered with lysis solution
Do not mix Buffer T1 and Proteinase K. And if you do, do not do it more than 10-15 min before addition to sample.
2. Incubate at 56 °C overnight. Use a shaking incubator, around 700-900 rpm.
3. Shortly vortex.
4. Centrifuge for 10 min at high speed (21000 xg) and transfer 200 μ L of supernatant to a new microcentrifuge tube (get rid of hairs, sometimes that will be difficult).
5. Add 200 μ L Buffer B3, vortex vigorously and incubate at 70 °C for 20 min at 1200 rpm.
If there are insoluble particles, centrifuge for 5 min at high speed (11000 xg) and transfer 200 μ L of supernatant to a new microcentrifuge tube.
6. Add 210 ethanol (96-100%) to the sample and vortex vigorously. Place elution buffer at 70 °C to warm up.
7. For each sample, place on NucleoSpin Tissue Column into a Collection Tube. Apply the sample to the column. Centrifuge for 1 min at 11000 xg. Discard collection Tube with flow-through and place the column in a new collection tube (provided)
8. Add 500 μ L Buffer BW. Centrifuge for 1 min at 11000 xg. Discard flow-through and place the column back into the collection tube.
9. Add 600 μ L Buffer B5 to the column and centrifuge for 1 min at 11000 xg. Discard flow-through and place the column back into the Collection Tube.
10. Centrifuge the column for 1 min at 11000 xg. Residual ethanol is removed during this step.
11. Place the NucleoSpin Tissue Column into a 1.5 mL microcentrifuge tube (not provided) and add 100 Buffer BE. Incubate at 70 °C for 2 min. Centrifuge 1 min at 11000 xg.

Mix for PCR:

25 μ L dream Taq Green PCR Master Mix (2X)

0.2 μ L of each primer (original concentration 100 μ M, final concentration 0.4 μ M)

X μ L DNA

To 50 μ L with nuclease-free Water

Component	For one well	For 35->40 wells
Dream Taq Green	25 μ L	1000 μ L
Primer CX3CR1cre Mainz fw (double amount)	0.4 μ L	16 μ L
Primer CX3CR1cre Mainz rev wt	0.2 μ L	8 μ L
Primer CX3CR1cre Mainz spec 1	0.2 μ L	8 μ L
Water	19.2 μ L	768 μ L
DNA	5 μ L in each well	

Standard IHC fluorescence

All procedures are performed at RT unless otherwise stated.

Day 1:

1. Incubate slides 30' at 37°C (bacterial incubator, must be DRY). This brings slides to RT and makes the sections stick even more on the glass slide.
2. Wash with PBS 3x10'
3. Permeabilization - wash with PBS+0,3% Triton X100 for 10' .
4. Wash 2x5' with PBS
5. Draw liquid blocker line with pap pen and let dry for 5 seconds before dipping it again into a solution (do not do this step before triton - even if they say that the pen resists... it doesn't!)
6. Incubate with mouse Fab fragments if any of the primary antibodies are produced in mouse, 1:100 in PBS, 1h, then wash 3x5' in PBS.
7. Incubate with **Blocking solution** (ready made in lab, PBS+2.5% BSA, 2.5% FCS and 2.5% fish gelatin - no triton because it messes up with lipid stainings. Add triton if better infiltration required and not looking for lipid stainings) for 1h - careful with timing when you have many slides!
8. Dip slides once in PBS
9. Prepare Primary Antibody in **Staining solution** (25% of Blocking Solution - no triton because it messes up with lipid stainings. Add triton if better infiltration required and not looking for lipid stainings).
10. Incubate Primary Antibody overnight at 4°C

Day 2:

11. Take slides out of fridge and incubate primary antibody for 1h
12. Wash 3x10' with PBS (each staining separately)
13. Dilute Secondary Antibody in Staining Solution
14. Incubate Secondary Antibody for 2h (alternatively: Overnight at 4°C)
15. Wash 3x10' with PBS (each staining separately)
16. Prepare Fluoromyelin and DAPI in PBS
17. Incubate Fluoromyelin and DAPI for 15'
18. Wash with PBS 3x10' (important washing step)
19. Dilute LipidTOX in PBS.
20. Incubate with LipidTOX for 30'. (LipidTOX shouldn't be washed!)
21. Dip once in H₂O to remove salts
22. Dry
23. Mount with Mowiol
24. Dry
25. Check staining! ;)

L929 cell line preparation

Cells are kept in 10% DMSO in the media (which depends on the cell line). DMSO protects the membranes, but it is toxic so we should get rid of it before plating the cells.

Serum helps cells recover after thawing, makes it easier to plate them and expand them so that they recover well. I should not do the experiments right away on those cells, because cells are in shock.

L929 are fibroblasts (they will form nice epithelia), and they are tumor cells, so they accumulate mutations.

Solutions:

- Media: DMEM+ 1% P/S + 1% Sodium Pyruvate → filtrate sterile (because sodium pyruvate is common stock).
- Add serum just before use, 10% (5mL serum, 45 mL medium) - into a separate aliquot (50 mL) of medium, not into the stock bottle - avoid contamination.

Pre do:

1. Warm up media

Protocol:

2. Take frozen tube from liquid N2 storage: our rack is n. 7! Tube is labelled "L929 cells, P(X)" - this X will be the number of passages already undergone by this line.
3. Thaw cells by shaking tube in 37 °C until it is liquid (water bath should not touch the lid).
4. Transfer cells (2 mL) to a 15 mL tube.
5. Add 9 mL warm media very slowly - by reclining pipette on the wall of the tube (not surface but more deep inside) and going at low speed.
6. Spin down at 300 xg for 10' at RT - intention: get rid of all the DMSO.
7. We plate in flasks (orange cap with filter. If it did not have holes with the filter, it would be necessary to keep the lid lose so that cells get the correct CO₂ concentration).
8. Label flasks with my name, the cell's name and the passage number (freezing and thawing counts as one passage as well!
9. We obtain a bit pellet from the centrifuge. Discard supernatant with pump.
10. Resuspend pellet in 1 mL new media and then add 9 mL more.
11. Put the 10 mL with the cells in the flask (10 mL/flask, 30mL/flask in the bigger ones). Pipette again more media into the same plastic pipette to completely wash cells off the pipette.
12. Check cells under microscope and decide whether they are too many and we therefore have to put them in a bigger flask or not.
13. Shake flasks a little - avoid touching neck.
14. To the incubator!

To passage cells 1 to 4:

1. Remove media of the flask.
2. Add 5 mL for small, 10 mL for big flask of media without serum (with pyruvate) - this will wash serum off
3. Close and shake
4. Remove these 5 or 10 ml
5. Add 1.5 mL for small, 3 mL for big flask of Trypsin + EDTA mix, shake strongly
6. Hit repeatedly with the hand surface to de-attach the cells. Have a look under the microscope to confirm that cells are floating.
7. Add 2-3 volumes of media with serum (5 mL for small, 10 mL for big flask)
8. Flush on the wall of the flask to detach cells
9. Transfer all liquid to 15 mL tube
10. Centrifuge 300x for 10', resuspend in 1 mL of media
11. Prepare media + FCS
12. Prepare 4 flasks and label them. Add 12 mL for small, 30 mL for big flask of media in each flask
13. Add 250 µL of the resuspended stuff in each flask.

The cells should be passaged again 1:4. Then:

- Wait until 100% confluence and change the media.
- Wait 1 week.
- Collect the medium, filter it, aliquot in 10 mL aliquots and keep frozen.

To freeze cells:

Freeze them when they have around 70% confluence (never at 100% because they would downregulate their proliferation machinery). Each cell line has its specific properties - check instructions online.

We leave the cells in medium for around one week and collect the medium they produce, which we use at 10-20% in the medium for microglia.

Myelin isolation protocol

Standardised protocol followed at AG Simons in the Göttingen Lab

Materials

- Waste Bottle
- 10 and 25 mL pipettes (many)
- Centrifuge tubes (Beckman Coulter, REF 326823)
- 20 mL syringes
- Big needles (green)
- Ice bucket
- Rack for 50 mL falcons
- HEPES Buffer, sucrose solutions, sterile filtered
- ddH₂O sterile filtered
- glass vase to balance (100 mL vase)
- Filter tips 1 mL and p20
- Ultracentrifuge
- Rotor and buckets for μ Ultracentrifuge (SW32Ti in BMC).
- Forceps
- Pipette P1000 and P20

Before start

- Prepare **Buffers**: filtrate sterile in cell culture hood
 - o 10 mM HEPES (1 mol=238.31 g) in ddH₂O → 2.38 g HEPES in 1 L ddH₂O
- Prepare **Sucrose solutions** in different molarities, in the Buffer just prepared. Place in ice once done. Prepare fresh everytime, maximum keep 1-2 days at 4°C.
 - o 0.35 M sucrose (1 mol = 342.3 g) → 29.95 g for 250 mL, 59.9 g for 500 mL
 - o 0.85 M sucrose (1 mol = 342.3 g) → 72.74 g for 250 mL, 145.48 g for 500 mL
- ** do not dissolve in full volume of buffer. If, e.g. preparing 100 mL, just fill it up with buffer until 50 mL. Then, when shaken, the sucrose dissolves and makes it increase in volume. Once dissolved, add buffer volume up to 100 mL.
- Filter some ddH₂O (approx. 1.5 L needed for 6 big tubes)
- (In BMC!) Fill tubes up with EtOH to make them more sterile and wash them. Remove EtOH after a while and re-use it. Dry tubes well with Kimtech tissue.

Brain extraction and tissue homogenisation

1. Use adult male mice (we used 8 wo mice).
2. Dislocate head and cut off. Remove brain and spinal cord.
3. (optional) Wash brain and spinal cord in PBS in a culture dish in order to remove blood.
4. Possible: freeze brains on dry ice if later use predicted. 3 brains and 2 spinal cords per each tube.
5. Add HEPES solution (2 mL) to the tube with brains+SC under cell culture hood
6. Homogenise tissue: perform with sonicator (3rd floor). Button to turn on is in the front lower part. Recall program 13. Press “start” to run. Program takes 40s. Check for pieces, and run again if there are still some.
7. Keep tubes on ice.
8. Go to BMC.

Myelin from non-myelin separation

9. Turn on centrifuge, turn vacuum on and set temperature to 4°C.
10. Make sure to clean tubes with EtOH before using them. They are plastic, in theory not reusable, but we reuse them as long as they do not have cracks.
11. Add 15 mL of 0.35 M sucrose into each tube.
12. Cut needle tip so that it is not sharp (clean scissors in EtOH).
13. Fill tubes up with 15 mL of 0.85 M sucrose from the bottom of the tube, using a long needle and a big syringe (approx. 20 mL syringe), thereby creating a gradient. Perform slowly and with great care not to mix the two phases. Handle the tubes with care from here on in order to avoid mixing.
 - ** *Ensure that syringe is full of liquid before inserting it into the tube and insert the liquid, in order to avoid bubbles.*
14. Transfer tubes to buckets with forceps.
 - ** *avoid scratching buckets with forceps - changes weight!*
15. Add the 2 mL of homogenate on top of the tube by laying pipette tip on the side of the tube.
16. Weight buckets with tube inside and without lid. Weigh one, add 1 mL of 0.35M sucrose to this one, then zero balance, and then adjust all others. Balance all tubes by adding 0.35 M sucrose on the top of the tube so that all tubes have the same weight (only ± 0.01 g is allowed).
 - ** *if we over-adjust and add too much liquid, we can always remove a bit and transfer it into another tube (as long as all myelin is the same).*
17. Close lids by turning and pressing until number of lid and bucket are in front of each other.
18. Centrifuge at 25000 rpm (for SW32Ti) for 38' at 4°C.
 - o Acceleration: set to slow.
 - o Deceleration: set to slow.
19. Collect white interphases (as shown in figure) into new tubes (same tubes as before, also cleaned). To do so, aspirate the myelin part by staying with the pipette tip at the surface of the myelin phase and rotating slowly.

Washing steps

20. Fill tubes up with ice-cold ddH₂O (pipette up and down a bit if liquid is not homogenous) - water osmotically breaks myelin membranes.
21. Again, place tubes in the buckets and balance them.
22. Centrifuge for 18' at 4°C at 25000 rpm (for SW32Ti). Acceleration and deceleration set at max.
23. Discard supernatant with 25 mL pipette and pipette boy. Be careful μ L because the pellet is quite loose - there will be more washing steps, so it is better to keep some water in there than to lose pellet!
24. Add 2 mL of ice-cold ddH₂O in each tube and resuspend pellet thoroughly with the 1 mL pipette. Add water until almost f μ L, dry tubes and transfer to buckets, and balance all tubes.
25. Centrifuge for 18' at 4°C at 10000 rpm (for SW32Ti). Acceleration and deceleration set at fast.
26. Repeat steps 22-24.

Myelin purification

1. Discard supernatant with 25 mL pipette and pipette boy. Be careful because the pellet is still quite loose.
2. Resuspend in 2 mL 0.35 M sucrose in each tube.
3. Fill another round of tubes up with 15 mL of 0.35 M sucrose.
4. Then add 0.85 M sucrose from the bottom of the tube, using a long needle and a big syringe (approx. 20 mL syringe), thereby creating a gradient. Perform slowly and with great care not to mix the two phases. This time it is a bit harder to see the two phases but it is still manageable. Handle the tubes with care from here on in order to avoid mixing.
5. Add the re-suspended myelin on top of the tubes by laying pipette tip on the side.
6. Centrifuge at 25000 rpm (for SW32Ti) for 38' at 4°C.
 - o Acceleration: set to slow.
 - o Deceleration: set to slow.
7. Again, aspirate the white interphase that contains the purified myelin and transfer into new tube. To do so, collect the myelin interphase with the 1 mL pipette. At this point, myelin is sticky and it sticks to the walls of the tube, so be careful to get it all.
8. Fill in tube with ice-cold ddH₂O - first only 2 mL to mix with myelin, then fill tube up.
9. Transfer tubes into buckets, balance buckets.
10. Centrifuge for 18' at 4°C at 25000 rpm (for SW32Ti). Acceleration and deceleration set at maximum.
11. Discard supernatant by decantation.
12. Add 2 mL of ice-cold ddH₂O in each tube and resuspend pellet thoroughly with the 1 mL pipette. Add water until almost full, dry tubes and transfer to buckets, and balance all tubes.
13. Centrifuge for 18' at 4°C at 10000 rpm (for SW32Ti). Acceleration and deacceleration set at fast.
14. Discard pellet with 25 mL pipette and pipette boy - pellet is quite loose!
15. Repeat steps 37-39.
16. Keep pellets on ice, cover tubes with Parafilm cleaned with Ethanol, go back to lab.
17. Resuspend pellet in 500 µL of 4°C HEPES Buffer under the hood. Pool all myelin in one 15 mL tube. Add 500 µL of HEPES Buffer more to the tubes to really clean them and get all the myelin.
18. Use 27G needle to break the remaining myelin pieces.
19. Freeze myelin at -20°C (if you want to go home and sleep. Otherwise, simply continue).

Myelin protein quantification

20. Thaw myelin and sonicate it (Program 13, twice). This resuspends really all pieces.
21. Use BSA for creating the standardised curve in HEPES Buffer. Create different concentrations of BSA (1, 0.8, 0.6, 0.4, 0.2, 0.1, 0.05 mg/ml) and transfer 10 µL of each into a flat 96-well plate, in triplicates.
22. Transfer 10 µL Hepes Buffer into also three of the wells.
23. Dilute myelin 1:3 in a separate tube and also transfer 10 µL in plate.
24. Add 200 µL of Biorad Protein Assay Dye Reagent Concentrate, diluted 1:5 in ddH₂O.
25. 3'-4' of incubation with the dye
26. Measure concentrations in the Höglinger Lab and extrapolate in curve using regression line. Take care that R² is high enough (more than 0.9!).
 - o Omega software - magda user - run
 - o Plate out, put plate in, plate in
 - o Manage protocol - bradford - edit
 - o Wavelength 595 - set up layout
 - o Start measurement - recheck - confirm
 - o Say yes to "no concentration values"
 - o The program runs, then finishes when noise stops. Plate out!
 - o Where is it saved? In Mars - Exit Omega to enter Mars
 - o Open Mars (Omega_Data Analysis) - magda - run
 - o Ignore error
 - o Double click to open the last run program (make sure it is the date and time correct)
 - o Have raw and blank correct options
 - o Export excel and save

*** Take into account that proteins degrade over time so the concentration might have to be re-checked!*

Comments

- Be always VERY SAFE when using an Ultracentrifuge:
 - o Balance tubes to the ±0.01 g.
 - o Fill tubes up as much as possible - leave approximately 2-3 mm free in the small SW60 tubes, and approx. 5 mm in the big SW20 tubes.
 - o Fill up first tube balance with 1 mL more of solution, then all tubes have less weight and liquid has to be added to reach the wanted weight - makes balancing easy peasy.
 - o Move rotor always with its base, because it is really not balancable without it. Put it into the centrifuge in a straight fashion (without the base of course).
 - o Each rotor has its buckets, make sure you use the correct ones!
 - o Keep numbers: bucket to lid and to position in the rotor.
 - o Double check correct positioning of tubes in rotor by pulling them downwards and sideways.
 - o Switch vacuum off everytime we want to open the ultracentrifuge, and on again once it is closed.
 - o Double check correct positioning of rotor in centrifuge by assuring that we hear the click and by turning the rotor manually.
 - o Decrease the acceleration and deceleration of the rotor when working with gradients so as to avoid initial or final mixing of tube content.
 - o Stay in the room until the centrifugation reaches 3000 rpm to ensure that everything runs smoothly.
 - o Turn tubes open with the help of forceps in order to avoid breaking lid hook.
 - o Protocol can be stopped anytime you have a pelleted, by adding a bit of buffer and freezing it in dry ice.
- The more diluted myelin is, the better the yield and the quality are going to be (?).

Appendix

How does the centrifuge work:

- On: side switch
- PuLL handle and slide open lid
- Put in the rotor with the buckets
- Close
- Set up speed, time and temp (press enter after entering the value)
- Set up accel and decel
- Pres start (vacuum starts automatically)
- To finish: press vacuum to turn it off, wait until there is no number under vacuum which means there is no vacuum, then open lid again and remove rotor
- Leave lid open when finished?

MACS cultures of microglia

Protocol adapted for GentleMACS Dissociator with Heaters - 02.08.2019

Performed with:
Experiment date:

Materials:

- Animals: P7-10 C57BL/6 wild-type pups - count on 1 million cells/pup
- 2 or 3 brains per C tube (depending on how big the brains are - for >p9, use 2 brains/C tube.)
- gentleMACS C tubes and LS columns
- Neural Dissociation Kit (P) (Miltenyi Biotec, order No. 130-092-628)
- Enzyme A aliquots stored at -20 °C (Reconstitute 1 vial of Enzyme A with 1 mL of Buffer A. Do not vortex.)
- Anti-CD11b MicroBeads, human and mouse (Miltenyi Biotec)
- DMEM/pyruvate medium at RT: DMEM containing 1 mM sodium pyruvate (1%)
- DMEM/FCS medium at RT: DMEM containing 10% FCS, 1 mM sodium pyruvate (1%) and 1% pen/strep (prepare little, like 30 mL)
- 10 mL of L929-conditioned medium
- DMEM/FCS/L929 medium: 10 mL of L929-conditioned medium + 40 mL of DMEM/FCS medium

Solutions:

Solution	Theoretical amounts	Quantity for today
DMEM + Pyruvate	500 mL DMEM 5 mL Sodium Pyruvate (1mM) Lasts 2-3 weeks	
DMEM/FCS	10 mL of Fetal/Bovine Calf Serum (FCS/BCS) 1 mL PenStrep 89 mL of DMEM/Py Filtrate sterile (due to FCS/BCS). Lasts 2-3 weeks.	200 mL is what is normally needed for 4 pups.
DMEM/FCS/L929	40 mL of DMEM/FCS 10 mL of L929-conditioned medium Prepare only what needed for the day.	50 mL is what is normally needed for 4 pups.
Enzyme Mix1	Enzyme P (-20°C) 50µl Buffer X (+4°C) 1900µL PER BRAIN → mix and pre-heated in waterbath.	
Enzyme Mix2	Buffer Y (+4°C) 20µl Enzyme A (-20°C) 10µl PER BRAIN → keep at R.T till use.	

Prepare:

1. Dissection Hood: turn on UV light and expose all instruments to it for 30' (dissection dishes and all tools, big scissor, medium sized curved forceps, tissue-pinchers and 2 thin pointy straight forceps). Cover hood with papers with ethanol.
2. Prepare the Enzyme Mix 1 for 2 brains in 2 C tubes (see table). Pre-heat Enzyme Mix 1 at 37°C for 10-15 min.
3. Prepare media
4. Coat the coverslips with Poly-L-Lysine (PLL) for 1 h. Wash twice with PBS. (Add DMEM/FCS medium.)

Dissociate tissue:

5. Decapitate the pups. Flush all heads, instruments and hands with EtOH.
6. Cut the scalp in the middle and flap aside. Cut the skull and uncover the brain. Transfer 2 brains to 1 dish.
7. Chop the brain tissue with a blade into a tiny mush.
8. Under a cell culture hood, transfer 2 brains to each C tube containing enzyme mix 1: put forceps in 70% EtOH for 1', then let dry, then use them to transfer the mush into the C tubes.
9. Add 30 µL of enzyme mix 2 into the C tube.
10. Close the lid tightly. Attach the C tubes upside down onto the sleeve of gentleMACS Octo Dissociator with heaters (flat side to flat side).
11. Run gentleMACS program **37C_NTDK_1**. (it takes around 20 min)
12. Centrifuge at 300 ×g for 5 min at RT (protocol says briefly). Aspirate most of the supernatant carefully (loose pellet).
13. Filtering and washing of cells (1 filter for each 2 mL - for each brain):
14. Resuspend the pellet in 1 mL of DMEM/pyruvate medium per C tube by pipetting 5 times (*pressing the pipette at the bottom of the Falcon. Avoid bubbles*). Then add 9 mL more.
15. Place 70µm cell strainers on 50mL Falcons. Apply 3 mL of DMEM to wash, then 5 mL of cell suspension to each cell strainer. Lift the cell strainer to get the last drops of cell suspension.
16. Wash with 2 mL of DMEM/pyruvate medium.
17. Place new cell strainers on the same Falcons. Repeat procedure.
18. Centrifuge the cell suspension at 300 ×g for 10 min at RT. (Meanwhile wash coated plates with PBS?)
19. Aspirate most of the supernatant carefully. Resuspend the cells in 1 mL of DMEM/pyruvate medium first, and then top up to 20 mL of DMEM/pyruvate medium per tube.
20. Count the number of brighter round cells (usually several hundred cells per 16-square grid). Calculate the total number ($n \times 10^7$) of cells in 20 mL. Averaged the cell suspension in 2 Falcons.

Dilute the cells 1/10 for counting in media. Number of cells per mL = total number of cells counted/number of 16 square grids counted × 10⁴. Total number of cells: multiply for the dilution factor and the total volume.

MACS of microglia using anti-CD11b MicroBeads

1. Centrifuge the cell suspension at 300 ×g for 10 min at RT.
2. Aspirate the supernatant carefully. For each 10⁷ cells, add 90 μL of DMEM/FCS medium (serum is necessary to block unspecific binding) and 10 μL of anti-CD11b MicroBeads. Mix well (do not vortex). Incubate on ice for 15 min.
3. For each 10⁷ cells, wash with 2 mL of DMEM/FCS medium (simply add volume?). Centrifuge at 300 ×g for 10 min at 4 °C.
4. Aspirate all the supernatant carefully. Resuspend the pellet in 500μL of DMEM/FCS medium per 10⁷ cells.
5. Place the LS columns on the magnet, the flaps of column facing outside. Activate the column by passing 3 mL of DMEM/FCS medium through it. Collected the flow-through in Falcons labeled “waste”.
6. Prepare Falcons for “unlabeled cells”. Apply the cell suspension onto the column. Collected the flow-through containing unlabeled cells, which could be used for the isolation of OPCs.
7. Wash the column 3 times with 3 mL of DMEM/FCS medium.
8. Prepare a 15mL Falcon for each column. Take the column from the magnet and place it into a 15mL Falcon. Apply 5 mL of DMEM/FCS/L929 medium onto the column, and immediately flush out the labeled cells by pushing the plunger into the column.
9. Count the cell number. (Do not dilute the cells.) A good yield from 8 brains is 8×10⁶ cells. Plate accordingly.
 - 12 well plate: plate 100-150K cells/well
 - 24 well plate: plate around 100K cells/well
 - 48 well plate: plate 80K cells/well
10. Keep the cells in DMEM/FCS/L929 until they have the desired density for experiments. Switch the media at least once a week (preferred: once every 3-4 days).

Keep 2 pups/tube

Divide each tube in 18 wells of a 24-well-plate.

Microglia isolation from adult mice

Protocol established by and learnt from AG Tahirovic (Alessio+Laura). I added my own modifications to eliminate all myelin debris.

Date this was run:

Sample this protocol was run on:

Reagent and instrument requirements

- HBSS with Mg²⁺ and Ca²⁺, no phenol red (Gibco, 14025-100).
- HBSS without Mg²⁺ and Ca²⁺, no phenol red.
- HEPES (Roth, HN78.2)
- Bovine Serum Albumin lyophilized powder, ≥96% (Sigma A2153)
- Percoll™ (GE Health Care 17-0891-01)
- DMEM
- Fetal Calf Serum or Bovine Serum.
- D-PBS without Mg, Ca.
- CD11b MicroBeads, MACS
- Neuronal Tissue dissociation Kit (P) (130-092-628) (MACS)
- 15 and 50 ml tubes (falcon tubes with blue lid)
- 15 ml tubes, fully transparent (Sigma Aldrich, CLS430053-500EA)
- Sterile cell strainer 70µm
- Fire-polished Pasteur pipettes with decreasing tip diameters (3/animal). They must have a long thin part and a cotton filter (VWR, 612-1799)
- Suction cups for the Pasteur Pipettes (2 ml)
- Enzyme Mix1 and Enzyme Mix2 (freshly prepared)
- Sterile instruments - especially, 1 forceps with fine sharp straight tip and 1 forceps with very fine curved tip.
- 6 cm dishes
- Waterbath at 37°C.
- Stereoscope with light from top.
- Waste bottle.

Reagent and material preparation

- Stock Solutions are prepared when Kit arrives and aliquots are stored at -20°C or +4°C (Enzyme P and A are stored at -20°C)
- Bring Percoll and DMEM+FCS to room temperature to prepare the Percoll solutions and shake them well!
- Turn on UV light in hood and disinfect the dissection tools there.
- Prepare the following solutions:

Solution	Theoretical amounts	Quantity for today
MACS (PBS+0,5% BSA) Buffer	100 mL 1x PBS 0,5g BSA Approx. 30 mL per brain, filtrate sterile (holds for 1 month). Pre-prepare!	
HBSS without Mg ²⁺ , Ca ²⁺ + 7mM HEPES	500 mL HBSS w/o 0,834 g HEPES filtrate sterile (should hold long time). Pre-prepare!	
HBSS with Mg ²⁺ , Ca ²⁺ + 7mM HEPES	500 mL HBSS with 0,834 g HEPES filtrate sterile (should hold long time). Pre-prepare!	
4% BSA in ddH ₂ O	100 mL ddH ₂ O 4 g BSA filter sterile (should hold long time). Pre-prepare!	
DMEM + 2% FCS/FBS	100 mL DMEM 2,04 mL FCS/FBS/BS. Approx. 30 mL per 4 brains (one day). Filtrate sterile (due to FBS). Prepare fresh each day!	
37% Percoll	3.15 mL of DMEM+FCS 1.85 mL Percoll 5 mL total per brain	
70% Percoll	1.2 mL of DMEM+FCS 2.8 mL of Percoll 4 mL total per brain	
Enzyme Mix1	Enzyme P (+4°C) 50µl Buffer X (+4°C) 1900µl PER BRAIN → mix and pre-heated in waterbath.	
Enzyme Mix2	Buffer Y (+4°C) 20µl Enzyme A (-20°C) 10µl PER BRAIN → keep at R.T till use.	

- Fire-polish 2 sets of 3 sizes of Pasteur Pipettes: 1st size is original size, 2nd is half of original, 3rd is really thin - I kept the first ones I used as example. Then, coat them with 4% BSA by pipetting up and down.
- Prepare 4x 6cm dish and 4 tubes with 4 ml HBSSw/o+HEPES.

Steps to follow:

Manual dissociation

1. Perfuse mouse with ice-cold PBS, isolate brain, transfer to tube with HBSS w/o and keep in ice.

Appendix

1. In a glass dish, drop the HBSS solution and the brain, cut out the cerebellum and the olfactory bulb (not used) and separate the two hemispheres. Clean the brain from the most prominent meninges, especially in the area ("pocket") where the midbrain covers the hippocampus. Then transfer the cleaned hemispheres to the clean dish. Do this for all brains.
2. Then, cut the brain into small pieces with the forceps in HBSS. Approx. Size: 2mmx2mm? Don't cut too small. Technique: take piece with one forcep, do knife move with other forcep.
3. Transfer the pieces with a 5ml glass pipette into a clear 15ml tube (let the pieces precipitate and use the supernatant to take the left pieces in the dish). Do not do up and down!
4. Let the brain pieces precipitate down to the tube. Then aspirate and discard the supernatant with the 5mL pipette carefully - no need to remove it completely.
5. Add 1950µl of preheated enzyme mix 1, mix gently by shaking tube, without completely turning it, do not vortex!
6. Incubate for 15min at 37°C in the waterbath (shake the tube every 5 minutes) - do not do in incubator, it breaks too much!
7. Add 30µl of Enzyme Mix2 to the sample and mix gently, do not vortex!
8. Dissociate tissue mechanically using the wide-tipped, fire-polished Pasteur pipette and pipetting up and down 10 times; avoid air bubbles. It will not completely dissociate the tissue, but that is okay. Do not overdo.
9. Incubate at 37°C for 10min in the waterbath (shake the tube every 5 minutes).
10. Centrifuge for a short pulse the tubes in order to bring all material down.
11. Dissociate tissue mechanically using again the wide-tipped pipette and then the other two fire-polished pipettes in decreasing diameter. Pipette slowly up and down 10 times with each pipette, or as long as tissue pieces are still observable. Avoid formation of air bubbles. Do not overdo the dissociation. Around 10 times for the first two sizes, and around 15-20 for the last are enough. Only very small pieces of mostly white matter will remain unbroken¹.
12. Incubate at 37°C for 10min in the waterbath (shake the tube every 5 minutes), or in the shaker in the incubator.
13. Apply 5ml of HBSS through a 70µm cell strainer, placed on a 50ml tube (to condition the cell strainer).
14. Pipette up and down 5 times with smallest glass pipette, then apply cell suspension through the cell strainer with the fire-polished glass pipette with the smallest tip opening.
15. Add 5ml of HBSS into the tube where the sample was and apply it through the cell strainer to wash it. Some pieces, mostly of white matter, will remain in the filter.
16. Discard cell strainer and centrifuge at 300xg for 10min at 4°C². Aspirate supernatant completely with the 10mL pipette.
17. Resuspend cells in 1ml of HBSS Buffer (with!) slowly and well, then add 9 ml HBSS buffer.

Magnetic labeling of neural cells

18. You should count cells, but I assume 30 million.
19. Centrifuge cell suspension at 300 xg for 10min at 4°C. Aspirate supernatant completely.
20. Resuspend cell pellet in 270 µL MACS Buffer+30 µL CD11b Beads per brain. Make mix first and then add to each tube! (otherwise liquid stays on wall of tube). For 4.5 brains: 1215 µL MACS Buffer+ 135 µL CD11b Beads.
21. Mix well with the P200 at 200 µL (do not vortex) and incubate for 15min in the fridge. Shake every 5 minutes very slowly (done with the rack)⁴.
22. Wash cells by adding 6 ml of MACS buffer, make sure they mix⁵, and centrifuge at 300xg for 10min. Discard supernatant completely.
23. Resuspend cells in 500 µL MACS buffer.

Magnetic separation (use LS columns).

24. Place column in the magnetic field of the MACS Separator.
25. Prepare column by rinsing with 3mL MACS buffer.
26. Apply cell suspension onto the column.
27. Perform washing steps by adding MACS buffer 3x with 3 mL of MACS Buffer.
28. Remove column from the separator and place it on a fresh 15ml CLEAR collection tube. Do one sample at a time⁶!
29. Pipette 5 ml MACS buffer onto the column and flush out the cells by firmly pushing the plunger into the column (one sample at a time!).
30. Determine cell number
We count: (average) $\times 10.000 =$ cells/mL $\times 2\text{mL} =$ total microglia after the isolation
31. Centrifuge at 300xg for 15 minutes at 4°C and aspirate the supernatant carefully (with 1mL pipette).
If for the desired application you are not measuring lipids or possible myelin debris don't play a role, stop the protocol here, wash the sample with PBS, and flash-freeze the pellet.

Percoll gradient separation

32. Resuspend cells in 37% Percoll. 5 mL 37% Percoll per tube.
33. Overlay the layer of 70% Percoll (4 ml in a clear tube) carefully with the sample in 37% Percoll. It is very important to be very slow! How: first shake a bit the tubes with 70% Percoll so that it gets a bit wet around the liquid interface. Then, keep tube with 70% Percoll in your left hand, in an angle of approx. 30° C from the horizontal. With the right hand, aspirate the cells (diluted in the 37% Percoll) in a 10 ml Pipette with the Pipet boy. Put end of pipette quite close to 70% Percoll solution in the tube. Then start to very slowly push the solution of 37% out of the pipette. As the tube is filling, retract the pipette accordingly, so that it never directly touches the solution but it is always close to it.
34. Let all tubes rest for 5' in the ice.
35. Centrifuge at 500 x g for 30' at 4° without brake or acceleration.
What you obtain here is, from top to bottom: Myelin debris, 37% Percoll, Cells, 70% Percoll.
36. Discard the myelin debris located at the top by aspirating it from the very top (until like the 7 ml mark!?).
37. With a 1 ml pipette, collect cells from the cloudy interface between 70% and 37% Percoll into a new 15 mL clear tube. Be very slow and never move the pipette tip fast!
38. Add DMEM+2% FBS to the solution obtained. Add twice the amount of liquid that was collected. Make sure that the added DMEM and the solution with the cells mix well! Pipette up and down with the 1 ml pipette⁸.
39. Centrifuge 400 g for 15' at 4°C. The pellet is not super clear, but it is there!
40. Discard supernatant but keep it in a tube. Resuspend the pellet very well and transfer into 0.5 mL of PBS (once resuspending, the pellet is indeed seeable, you see that it de-attaches and mixes!). Transfer to an autoclaved epi tube.

Appendix

1. Centrifuge the supernatant tubes again - and process following same protocol to see if I see a pellet at the epi tubes⁹.
2. Centrifuge the epi tubes at 400 g for 15' at 4°C (table top centrifuge).
3. Discard supernatant completely, resuspend in 510 µL of PBS, take aliquots for cell counting and keep tubes in ice.
4. Transfer 10 µL into the Neubauer Chamber (mix well to avoid chunks!).
We count: $(\text{total number of cells}/4) \times 10.000 = \text{cells/mL} \times 0,50 \text{ mL} = \text{total microglia after myelin removal}$
5. Aliquot sample if needed (requires a lot of pipetting!)
6. Centrifuge again all tubes at 800xg for 15' at 4°C. Completely withdraw and discard supernatant. Carefully clean tube walls with cotton tipped stick to discard all liquid. Snap-freeze the pellet in liquid N₂.

Comments:

1. Don't overdo the manual dissociation. Some very small pieces were left in the end, and remained on the strainer once filtering, but that is okay. The pieces were mostly white matter. That weird gellyish whitish substance didn't form.
2. Start centrifuging at 4°C right after filtering.
3. Use autoclaved epi tubes and pipette tips all the way through.
4. While incubating the cells with the beads, shake the tubes every 5 minutes. The tubes were kept in the rack, and I shook them very smoothly while still in the rack.
5. Make sure the 2 ml washing MACS Buffer after the labelling mixes with the rest of the sample.
6. Transfer the column onto the new clear tube and flushed the cells out one sample at a time (transfer column onto new tube, add 2 ml MACS Buffer, flush. Then next sample).
7. When counting the cells after the MACS Column isolation, the cells might be quite coagulated, forming chunks. You should not really count those (meaning I counted maybe 1 or 2 cells for each chunk).
8. It is important to ensure that the added DMEM+FCS mixes well with the solution containing the cells after Percoll gradient centrifugation!
9. It is a good idea to process the supernatants from the first centrifugation after taking cells from Percoll gradient, but there was absolutely no pellet at the epi tube.
10. The pellet while you work with the single cell suspension is really lose, so be careful.
11. To check: clean the counting chamber not with ethanol but with water! Ethanol might be killing the cells??? Many cells were dead in the counting chamber last time, be careful with that!

Microglia isolation from adult mice for RNA analysis

Protocol established by and learnt from AG Tahirovic (Alessio+Laura). I added my own modifications to really eliminate all myelin debris. Adapted to RNA with help from Minhui's protocol and Shima's advice.

Date this was run:

Sample this protocol was run on:

Reagent and instrument requirements

- HBSS with Mg²⁺ and Ca²⁺, no phenol red (Gibco, 14025-100).
- HEPES (Roth, HN78.2)
- Bovine Serum Albumin lyophilized powder, ≥96% (Sigma A2153)
- Percoll™ (GE Health Care 17-0891-01)
- DMEM
- Fetal Calf Serum or Bovine Serum.
- D-PBS without Mg, Ca.
- CD11b MicroBeads, MACS
- Neuronal Tissue dissociation Kit (P) (130-092-628) (MACS)
- 50 ml tubes (falcon tubes with blue lid)
- 15 ml tubes, fully transparent (Sigma Aldrich, CLS430053-500EA)
- Sterile cell strainer 40µm
- Fire-polished Pasteur pipettes with decreasing tip diameters (3/animal). They must have a long thin part and a cotton filter.
- Suction cups for the Pasteur Pipettes (5 ml?)
- Enzyme Mix1 and Enzyme Mix2 (freshly prepared)
- Sterile instruments - especially, 2 forceps with fine sharp straight tip.
- 6 cm dishes
- Waterbath at 37°C.
- Stereoscope.
- Waste bottle.
- RNase Zap to clean surfaces and instruments.

Reagent and material preparation

- Stock Solutions are prepared when Kit arrives and aliquots are stored at -20°C or +4°C.
- Bring Percoll and DMEM+FCS to room temperature and shake them well!
- Turn on UV light in hood and disinfect the dissection tools there. Also with **RNase ZAP!**
- Prepare the following solutions:

Solution	Theoretical amounts	Quantity for today
MACS (PBS+0,5% BSA)	Buffer 100 mL 1x PBS 0,5g BSA Approx. 30 mL per brain, filtrate sterile (holds for 1 month).	done.
HBSS + 7mM HEPES	500 mL HBSS 0,834 g HEPES filtrate sterile (should hold long time).	done
4% BSA in ddH ₂ O	100 mL ddH ₂ O 4 g BSA filter sterile (should hold long time).	Already done
Enzyme Mix1	Enzyme P (+4°C) 50µl Buffer X (+4°C) 1900µL PER BRAIN → mix and pre-heated in waterbath.	250 µL Enzyme P 9500 µL Buffer X
Enzyme Mix2 (prepare during experiment)	Buffer Y (+4°C) 20µl Enzyme A (-20°C) 10µl PER BRAIN → keep at R.T till use.	100 µL Buffer Y 50 µL Enzyme A
DMEM + 2% FCS/FBS (prepare during experiment)	100 mL DMEM 2,04 mL FCS/FBS. Approx. 30 mL per 4 brains (one day)	50 mL DMEM 1,02 mL FCS/FBS
37% Percoll (prepare during experiment)	3.15 mL of DMEM+FCS 1.85 mL Percoll 5 mL total per 2 brains	9,45 mL DMEM+FCS 5,55 mL Percoll
70% Percoll (prepare during experiment)	1.2 mL of DMEM+FCS 2.8 mL of Percoll 4 mL total per 2 brains	3.6 mL DMEM 8.4 mL Percoll

- Fire-polish 3 sizes of Pasteur Pipettes: 1st size is original size, 2nd is half of original, 3rd is really thin - I kept the first ones I used as example. Then, coat them with 4% BSA by pipetting up and down.
- Prepare 8x 6cm dish with 3ml HBSS+HEPES (2 per sample: one to isolate the brain and clean it from the meninges and the other one for the cleaned hemispheres and cut them in pieces). 4 dishes with 3 mL HBSS, 4 dishes with 6 mL HBSS.

Steps to follow:

Manual dissociation

1. Sacrifice mouse with CO₂ and remove the mouse brain. Determine the weight (should not be more than 400mg per tube) by subtracting the weight of the empty dishes. Keep dishes on ice ALWAYS, also while dissecting meninges (smaller dish within bigger dish).

Appendix

1. Cut out the cerebellum and the olfactory bulb (not used) and separate the two hemispheres. Clean the brain from meninges, especially in the area ("pocket") where the midbrain covers the hippocampus (and transfer to the clean dish) and cut the brain into small pieces with the forceps in HBSS. Approx. Size: 2mmx2mm? Technique: take piece with one forcep, do knife move with other forcep.
2. Transfer the pieces with a 5ml pipette into a clear 15ml tube (let the pieces precipitate and use the supernatant to take the left pieces in the dish). Do not do up and down! Centrifuge a very short pulse just to bring all pieces down.
3. Aspirate and discard the supernatant with the 5mL pipette carefully.
4. Add 1950µl of preheated enzyme mix 1, mix gently by shaking tube by tipping its bottom, without completely turning it, do not vortex! 2 mL per tube, slightly pipette up and down with the 5 mL pipette only once to "resuspend" the tissue after the centrifuge pulse.
5. Incubate for 15min at 37°C in the waterbath, shake the tube every 5 minutes.
6. Add 30µl of Enzyme Mix2 to the sample and mix gently, do not vortex!
7. Dissociate tissue mechanically using the wide-tipped, fire-polished Pasteur pipette and pipetting up and down 10 times; avoid air bubbles.
8. Incubate at 37°C for 10min and shake the tube every 5 minutes.
9. Dissociate tissue mechanically using again the wide-tipped pipette and then the other two fire-polished pipettes in decreasing diameter. Pipette slowly up and down 10 times with each pipette, or as long as tissue pieces are still observable. Avoid formation of air bubbles. Pipette up and down while touching with the end of the pipette to the bottom of the tube around 5x.
10. Incubate at 37°C for 10min and shake the tube from time to time.
11. Apply 5ml of HBSS through a 40µm cell strainer, placed on a 50ml tube (to condition the cell strainer).
12. Apply cell suspension through the cell strainer.
13. Add 5ml of HBSS into the tube where the sample was and apply it through the cell strainer to wash it. Lift strainer to get last drops.
14. Discard cell strainer, move to bench and centrifuge at 400xg for 10min at 4°C. Aspirate supernatant completely with the 10mL pipette. *Meanwhile: clean bench with RNase ZAP!*
15. Resuspend cells in 10ml HBSS buffer for further applications

Magnetic labeling of neural cells - From here on, keep both cells and solutions always on ice (except Percoll?)

16. Determine cell number (dilute 1:4 with Trypan blue - 15µL tripan blue+5µL cell suspension) - very difficult to count! Assume 20-30 million cells! Always consider you have around 5 million cells more when calculating the buffer and beads volume.
We count: $x \times 4 \text{ (tripan blue dilution)} \times 10.000 = \text{cells/mL} \times 10\text{mL} = \text{total cells before isolation}$
17. Centrifuge cell suspension at 400xg for 10min at 4°C. Aspirate supernatant completely (count the cells during the centrifugation)
18. When working with mouse cells, resuspend cell pellet in 90µl of MACS buffer per 10⁷ total cells and add 10µl of CD11b (Microglia) MicroBeads per 10⁷ total cells (mix up-down with the 200 µL pipette).
Do for 3x10⁷ cells → 270 µL MACS Buffer, 30 µL CD11b Beads PER BRAIN. Make mix first and then add to each tube! (otherwise liquid stays on wall of tube).
19. Mix well, do not vortex and incubate for 15min in the fridge. Shake every 5 minutes.
20. Wash cells by adding 2ml of MACS buffer and centrifuge at 400xg for 10min. Discard supernatant completely.
21. Resuspend cells in 1mL MACS buffer.

Magnetic separation (use LS columns).

22. Place column in the magnetic field of the MACS Separator.
23. Prepare column by rinsing with 3mL MACS buffer.
24. Apply cell suspension onto the column.
25. Perform washing steps by adding MACS buffer 3x with 1mL (this is different from the MACS protocol itself, where it says 3x with 3 mL).
26. Remove column from the separator and place it on a fresh 15ml CLEAR collection tube.
27. Pipette 2ml MACS buffer onto the column and flush out the cells by firmly pushing the plunger into the column (one sample at a time).
28. Determine cell number (dilute 1:2 with Trypan blue)
We count: $x \times 2 \text{ (Trypan blue dilution)} \times 10.000 = \text{cells/mL} \times 2\text{mL} = \text{million total cells after isolation}$
29. Centrifuge at 400xg for 2 minutes at 4°C and aspirate the supernatant carefully (with 1mL pipette).

Percoll gradient separation

30. Resuspend cells in 37% Percoll. 5 mL 37% Percoll per tube & brain.
31. Overlay the layer of 70% Percoll carefully with the sample in 37% Percoll. It is very important to be very slow!
How: first shake a bit the tubes with 70% Percoll so that it gets a bit wet around the liquid interface. Then, keep tube with 70% Percoll in your left hand, in an angle of approx. 30°C from the horizontal. With the right hand, aspirate the cells (diluted in the 37% Percoll) in a 10 ml Pipette with the Pipet boy. Put end of pipette quite close to 70% Percoll solution in the tube. Then start to very slowly push the solution of 37% out of the pipette. As the tube is filling, retract the pipette accordingly, so that it never directly touches the solution but it is always close to it.
32. Centrifuge at 500 x g for 30' at 4°, brake=0 and acceleration=0. **Result:** top to bottom: Myelin debris, 37% Percoll, Cells, 70% Percoll.
33. Discard the myelin debris located at the top by aspirating it from the very top (just like 1 mL).
34. With a 1 ml pipette, collect cells from the cloudy interface between 70% and 37% Percoll into a new 15 mL normal tube (blue cap). Be very slow and never move the pipette tip fast! Collect like 2 mL, restrict yourself to the cell interface!
35. Add DMEM+2% FBS to the solution obtained. Add twice the amount of liquid that was collected.
36. Centrifuge 800 g for 15' at 4°C. It might be hard to see the pellet!

Appendix

1. Discard supernatant but keep it in a tube. Resuspend pellet into 0,51 mL of PBS and count cells. Transfer to an epi tube.

<u>Sample 1:</u>	x 10.000=	milion cells/mL x 0,21mL=	total cells after myelin removal
<u>Sample 2:</u>	x 10.000=	milion cells/mL x 0,21mL=	total cells after myelin removal
<u>Sample 3:</u>	x 10.000=	milion cells/mL x 0,21mL=	total cells after myelin removal
<u>Sample 4:</u>	x 10.000=	milion cells/mL x 0,21mL=	total cells after myelin removal

2. Centrifuge the epi tubes at 400 g for 15' at 4°C (table top centrifuge).

3. Centrifuge the supernatant tubes again - check for Pellet!

4. Discard supernatant, resuspend in 500 µL of RTL Buffer for around 500,000 cells.

5. Snap-freeze sample in liquid Nitrogen.

RNA isolation Protocol

Performed on:

Samples:

Observations:

- Always read the RNeasy plus mini kit protocols before starting
- Centrifuge always at 20-25 °C
- The centrifuge has no 15'' option, so all centrifugations are minimum 30'' long
- Very low ratios of A260/230 are normal because of some component of the RLT buffer that stays there - not a problem for qPCR.
- Kit: RNeasy Plus Mini
- After centrifugation, carefully remove the RNeasy spin column from the collection tube so that the column does not contact the flow-through. Be sure to empty the collection tube completely.

Prepare the kit

- I added 44 mL of 100% Ethanol (the one super pure for RNA!) to the RPE Buffer.
- Considering the samples you have on that day, prepare an aliquot of the buffer RLT Plus with Beta-mercaptoethanol (B-ME, C2H6OS, ART Nr 4227.3 Roth) In this case, I had 8 samples, and 600 µL per sample are needed → 5 mL of RLT+50 µL of B-ME.
- Prepare the 70% Ethanol necessary: 10 samples + 350 µL 70%EtOH/sample =3500 µL →prepare 6 mL of 70% Ethanol, using the 100% Ethanol for RNA and the RNase-free water (4.2 mL of 100% EtOH, 1.8 mL of RNase free water)

Isolate RNA - RNeasy Plus mini kit

Maximal amount of starting material:

- Animal cells: 10⁷
- Animal tissue: 30 mg
- Yeast: 5x10⁷
- Plant tissues: 100 mg
- Filamentous fungi: 100 mg

Disrupt and homogenize tissue:

1. Add 350 µL of **RLT Buffer** into each tube - re-suspend sample.
Note: use 600 µL of RLT Buffer for 20 to 30 mg of tissue, use 350 µL of RLT Buffer for less than 20 mg of tissue.
2. Set the P1000 Pipette to 350 µL and pipette up and down the RLT Buffer containing the sample, so that you homogenize the sample. Pipette also up and down against the wall of the tube to really dissociate the tissue.
3. Transfer all the liquid onto a **QIAshredder spin column** placed in a 2 ml collection tube (supplied), and centrifuge for 2 min at maximum speed.
4. Remove the column and cover tube with the lids. Make sure that the tubes are labelled. **Centrifuge the lysate** for 3 min at maximum speed.
5. Carefully remove the "supernatant" by pipetting and transfer it to a **gDNA Eliminator spin column** placed in a 2 mL collection tube (supplied).
6. Centrifuge for 30s at 12000 g. Discard the column, save the flow-through.

Isolate RNA

7. Add 350 µL of 70% EtOH to flow-through. Mix and immediately transfer (all liquid (700 µL) and any precipitate) onto an **RNeasy spin column** placed in a 2 mL collection tube (Supplied).
8. Centrifuge 15s at 12000 g.
9. Discard flow-through. Add 700 µL **Buffer RW1** to the RNeasy spin column.
10. Close the lid gently and centrifuge for 15'' at 12000 xg to wash the spin column membrane.
11. Discard the flow-through. Reuse the collection tube in next step. Add 500 µL **Buffer RPE** to the RNeasy spin column.
12. Close the lid gently and centrifuge for 15'' at 12000 xg to wash the spin column membrane.
13. Discard the flow-through. Reuse the collection tube in next step. Add 500 µL **Buffer RPE** to the RNeasy spin column. Close the lid gently, and centrifuge for 2 min at 12000 xg to wash the spin column membrane.
The long centrifugation dries the spin column membrane, ensuring that no ethanol is carried over during RNA elution. Residual ethanol may interfere with downstream reactions.
14. **Optional(DO IT!):** Place the RNeasy spin column in a new 2 ml tube and centrifuge at full speed for 1 min.
Perform this step to eliminate any possible carryover of Buffer RPE, or if residual flow-through remains on the outside of the RNeasy spin column after step 9.
15. Place the RNeasy spin column in a new 1.5 mL collection tube (supplied, looks like a normal one). Add 30µL **RNase-free water directly** (means making sure that the drop goes onto the membrane and not to the side of the tube) to the spin column membrane. Incubate for 5 min.
Note: The volume of elution depends on the amount of RNA expected. You can use between 30 to 50 µL - use less volume when less RNA is expected!
16. Centrifuge for 1 min at 12000 xg to elute the RNA.
Note: careful when placing tubes in centrifuge - lids of 1.5 mL tubes should not overlap or they will break! Split in two centrifugation rounds if necessary.
17. Use the eluate from step 16-17 to **elute again the RNA from the membrane** by simply aspirating the elute and adding it again directly to the spin column membrane. Incubate again for 5 min and centrifuge for 1 min at 12000g.
Note: you can either use the same elute or another volume of water - again, depending on RNA concentration wanted.

Determine the RNA yield

We use the NanoDrop Spectrophotometer for determining RNA yield. This is based on Absorbance.

Absorbance at 260 nm provides total nucleic acid content, while absorbance at 280 nm determines sample purity. Since free nucleotides, RNA, ssDNA and sdDNA absorb at 260 nm, they all contribute to the total absorbance of the sample.

Appendix

- 230 nm - chemicals
- 260 nm - nucleic acids
- 280 nm - proteins

Procedure

1. The sensor is very sensitive, so do not touch it directly (not even with the pipette tip).
2. Wash the Nanodrop sensor: Put 1 μL of RNase free water on top of the sensor, close the Nanodrop and open again, wipe with a tissue (both parts, "lid" too!!). Do this three times.
3. Open Software: Nanodrop 2000, choose nucleic acid. Choose RNA as sample and write sample name.
4. Run blank: add 1 μL of RNase free water to the sensor and run the blank.
5. Measure sample: pipette up and down the sample with the RNA, and add 1 μL of the RNA sample onto Nanodrop detector.
6. Wash the sensor 1x or 2x between samples.
7. When finished, wash the Nanodrop sensor again just like in step 2.
8. At software: reports, export \rightarrow save file to USB Stick.

Results:

- Ratio A260/A280 of around 2 is considered pure (more nucleic acids than proteins).
- Ratio A260/A230 should also be around 2 (more nucleic acids than chemicals) - in trizol isolation method this is going to be worse than in the column method.

Save the file that the software gives you by exporting the project - select all samples - and combine it in a excel file!

Aliquot the samples in 2 small red tubes, each with approx. 13 μL of liquid

The art of producing cDNA

Performed:

Samples:

First-strand cDNA Synthesis

Using SuperScript III First-Strand Synthesis System for RT-PCR - see the protocol online for more details.

Material:

- SuperScript III First-Strand Synthesis System for RT-PCR, cat 18080-051, Invitrogen (kept -20°C)
- RNase ZAP to clean surfaces
- Autoclaved 1.5 mL tubes
- Sterile filter tips all sizes
- Epi Rack

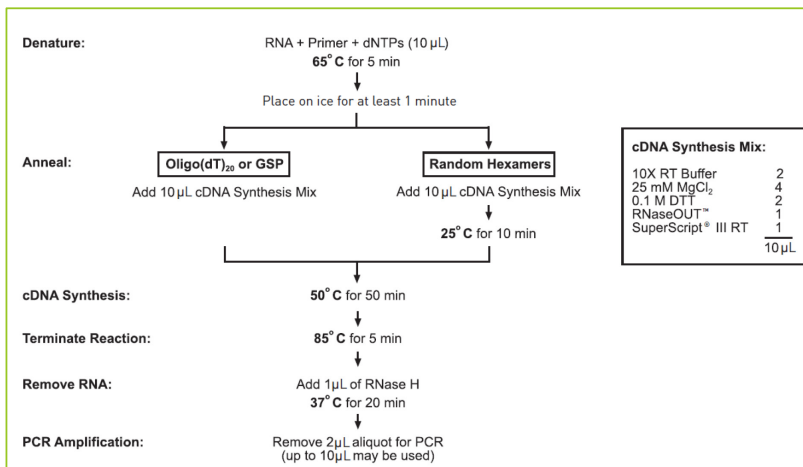
Details of kit:

- Made to detect targets from 100 bp to >12 kb.
- Amount of starting material required can vary from 1 pg to 5 ug of total RNA (we normally use 1 ug), or 1 pg to 500 ng of poly(A)⁺RNA. For >5 ug total RNA, increase reaction volumes and amount of SuperScript III RT proportionally.
- Small amounts of genomic DNA in the RNA preparation may be amplified along with the target cDNA. If your application requires removal of all genomic DNA from your RNA preparation, we recommend using DNase I, Amplification Grade (catalog n. 18068-015).
- Primers:
 - o **Random hexamers:** it is the most typical. Most nonspecific priming method, typically used when the mRNA is difficult to copy in its entirety and when you want to screen for many genes. With this method, all primers confer specificity during PCR. To maximize the size of cDNA, you should determine the ratio of random hexamers to RNA empirically for each RNA preparation. However, for most applications 50 ng of random hexamers per 5 ug total RNA is adequate.
 - o **Oligo(dT):** more specific priming method, used to hybridize to 3' poly(A) tails, which are found in the vast majority of eukaryotic mRNAs. Since poly(A)⁺ RNA constitutes approximately 1% to 2% of total RNA, the amount and complexity of cDNA is considerably less than with random hexamers. This is recommended when performing RT-PCR for new mRNA targets, because the product it produces is more consistent. However, one has to be careful because since the primers bind the poly A, the polymerase will start at the poly A, and there might be many base-pairs separating the polyA from the actual coding sequence, and if the polymerase falls off the RNA before it has reached the coding sequence, this coding sequence will actually not get converted to cDNA!
**One can also do a mix of random hexamers + oligo(dT)20.*
 - o **Gene-specific primer:** then you basically only convert to cDNA your gene of interest. Most specific.

Preparation:

- Ice bucket with ice
- Transfer all tubes of the kit into the ice to thaw - it takes a while! Exception: RNase OUT and the SuperScript III RT, which should stay at -20°C until just before use (and when you do need them, keep them in the yellow container for frozen samples).
- Transfer tubes with RNA to the ice.
- Mix and briefly centrifuge each component before use. You can vortex, EXCEPT: enzymes, DNA, RNA and primers, which should NEVER be vortexed.
- Clean with RNase ZAP: bench, hands, pipettes, epi rack, lids of tubes before opening them (spray RNase ZAP on tissue and use that to wipe tubes, pipettes and so on).
- Calculate amount of RNA to be added: normally, Ludo adds 1 ug of RNA.
- Prepare heater at 65°C

Protocol:



Appendix

- RNA calculations:** We want to add between 100 ng and 1 µg of total RNA into the reaction → make calculations. Anyway, it is not so important to be very precise with the amount of RNA added in the beginning because the qPCR already controls the initial amount - you can control for the initial differences in material quantity. Simply try to keep it constant.
- Combine the following in an autoclaved 1.5 mL tube:

Component	Amount / tube	For test samples:	For control samples:
Up to 5 µg total RNA	n µL		
Primer*	1 µL		
10 mM dNTP mix	1 µL		
DEPC-treated water	To 10 µL		

- *Use Random Hexamers. There are other options, but the random hexamers is best for our application.
- Incubate the tubes at 65 °C for 5', then place on ice for at least 1 min. Change the thermoblock to 50 °C.
 - Prepare the following cDNA Synthesis Mix, adding each component in the indicated order. MIX WELL!

Component	Amount 1x	For Today (+RT)	For Today (-RT)
10X RT buffer	2 µL		
25 mM MgCl ₂	4 µL		
0.1 M DTT	2 µL		
RNase OUT (40 U/µL)	1 µL		
SuperScript III RT (200 U/µL)	1 µL		-
DEPC-treated water	1 µL	-	

- Add 10 µL of cDNA Synthesis Mix to each RNA/primer mixture, mix gently (up and down, don't vortex) and incubate as follows:
 - Random hexamer primed: 10 min at 25 °C (on the bench), followed by 50 min at 50 °C. Prepare block at 85 °C.
 - Oligo(dT)₂₀ or GSP primed: 50 min at 50 °C.
- Terminate the reactions at 85 °C for 5'. Chill on ice for 5'. Prepare block at 37 °C.
- Collect the reactions by brief centrifugation. Add 1 µL of RNase H to each tube and incubate the tubes for 20 min at 37 °C.
- cDNA synthesis reaction can be stored at -30 °C to -10 °C or used for PCR immediately (keep on ice if wanted to use for PCR, simply put into the freezer if you want to store it).

Controls

It is generally better to have your own tissue for positive control. This should be RNA from tissue you know definitely has the genes. Also on this control RNA and in one of the samples, a non-RT control should be added.

Control Reactions

The control RNA provided with this system consists of total HeLa RNA (10 ng/µL). The sense and antisense control primers provided with this kit are designed from the human β-actin gene and produce a 353-bp RT-PCR product.

Sense primer: 5'-GCTCG TCGTC GACAA CGGCT C-3'

Antisense primer: 5'-CAAAC ATGAT CTGGG TCATC TTCTC-3'

Use the following protocol for both plus and minus RT control reactions:

- Dilute the total HeLa RNA to 100pg/µL with DEPC-treated water.
- Prepare the RNA/primer mixtures in sterile 0.2- or 0.5-mL tubes as follows:

Component	+ RT Control	- RT Control
Diluted total HeLa RNA (100 pg/µL)	1 µL	1 µL
Oligo(dT) ₂₀	1 µL	1 µL
10 mM dNTP mix	1 µL	1 µL
DEPC-treated water	7 µL	7 µL

- Incubate the samples at 65 °C for 5 min, then place them on ice for at least 1 min. Collect the contents by brief centrifugation and add the following:

Component	+ RT Control	- RT Control
10X RT buffer	2 µL	2 µL
25 mM MgCl ₂	4 µL	4 µL
0.1 M DTT	2 µL	2 µL
RNaseOUT™ (40 U/µL)	1 µL	1 µL
SuperScript® III RT (200 U/µL)	1 µL	-
DEPC-treated water	-	1 µL

- Mix the tubes gently and collect the reactions by brief centrifugation.
- Incubate the samples at 50 °C for 50 min.
- Terminate the reactions at 85 °C for 5 min. Chill on ice.
- Collect the reactions by brief centrifugation. Add 1 µL of RNase H to each tube and incubate for 20 min at 37 °C.

*For First Strand cDNA Synthesis of Transcripts with High GC Content, see Invitrogen protocol.

- Prepare a PCR mixture for each control reaction. For each control reaction, add the following to a 0.2-mL tube sitting on ice:

Component	Volume
DEPC-treated water	38.1 µL
10X PCR buffer minus Mg ²⁺	5 µL
50 mM MgCl ₂	1.5 µL
10 mM dNTP mix	1 µL
Control sense primer (10 µM)	1 µL
Control antisense primer (10 µM)	1 µL
cDNA from control RNA	2 µL
Taq DNA polymerase (5 units/µL)	0.4 µL
Final volume	50 µL

- Mix the contents of the tube. Centrifuge briefly to collect the reaction components.
- Place reaction mixture in preheated (94 °C) thermal cycler. Perform an initial denaturation step: 94 °C for 2 min.
- Perform 40 cycles of PCR:

Denature	94 °C for 15 sec
Anneal	55 °C for 30 sec
Extend	68-72 °C for 1 min

Note: For slow-ramping thermal cyclers, follow manufacturer's directions.
- Upon completion, maintain reactions at 4 °C.
- Analyze 10 µL of each reaction, using agarose gel electrophoresis and ethidium bromide staining. For the + RT Control, a 353-bp band, corresponding to at least 25 ng of product, should be visible. For the - RT Control, the same band should be ≤50% in intensity when compared to the + RT Control.

qPCR particularities

General protocol for: PowerUP SYBR Green Master Mix - **always check** the User Guide before starting (find it as a printed copy in Protocols folder)

Guidelines:

- Use 1-10 ng single-stranded cDNA or 10-100 ng gDNA per reaction
- Four replicates of each reaction are recommended (we sue 3)
- Reaction mixes can be prepared depending upon experimental requirements. Scale the components according to the number of reactions and include 10% overage
- If using smaller reaction volumes, scale all components proportionally. Reaction volumes less than 10 μL are not recommended.
- Using no template control (NTC) reactions can be used to identify PCR contamination. NTC reactions contain all reaction components except sample and therefore should not return a Ct value \rightarrow this we do with the noRT control!

Before you begin:

1. Clean bench with EtOH
2. Thaw all components in ice - SYBR Green Master Mix, Primer Mixes and cDNA. Takes a long time! Sometimes leave at RT for a bit and move back to ice.... Important is, that none of the components stays for too long at RT.
3. Prepare the cDNA: dilution 1:10 recommended, but one can modify it a bit in case of very small RNA amounts.
4. Keep the SYBR green and any tubes made with that covered - protect fluorescence.
5. Mix absolutely very tube before use by pipetting up and down the whole volume.

Set up the PCR reactions:

1. Prepare the appropriate number of reactions, plus 10% coverage (10 μL /well for 384 well-plate):
 - a. For optimal performance in Fast and Standard modes, use 300-800 nM for each primer - we used 300 nM in the first testings and worked.
 - b. Use 1-10 ng cDNA or 10-100 ng gDNA for each reaction

Component	Volume (10 μL /well)	Volume (20 μL /well)
PowerUp™ SYBR™ Green Master Mix (2X)	5 μL	10 μL
Forward and reverse primers ^[1]	Variable	Variable
DNA template + Nuclease-Free Water ^[2]	Variable	Variable
Total	10 μL	20 μL

2. Centrifuge briefly in case of any liquid on the tube walls, then mix thoroughly by pipetting up and down the whole volume **right before use**.
3. Transfer the appropriate volume of each reaction to each well of an optical plate (9 μL /well for 384 well plate) - to the wall
4. Transfer 1 μL of the corresponding cDNA to each well - put tip all the way to bottom of well.
5. Cover plate and centrifuge with a plate centrifuge (AG Haass) for 1 minutes at 1000 rpm.

PCR can be performed on the reaction plate up to 24h after completing the set-up, when stored at RT (?????????)

Set up and run the real-time PCR instrument

1. Place the reaction plate in the RT-PCR instrument
2. Use fast cycling mode:

Table 3 Fast cycling mode (primer $T_m \geq 60^\circ\text{C}$)

Step	Temperature	Duration	Cycles
UDG activation	50°C	2 minutes	Hold
Dual-Lock™ DNA polymerase	95°C	2 minutes	Hold
Denature	95°C	1 second ^[1] or 3 seconds ^[2]	40
Anneal/extend	60°C	30 seconds	

^[1] When using a QuantStudio™ Real-Time PCR System or a ViiA™ 7 Real-Time PCR System.

^[2] When using a 7500 Fast Real-Time PCR System, StepOnePlus™ Real-Time PCR System, or StepOne™ Real-Time PCR System.

Appendix

Example:

Primers:

1. Fabb4_2
2. Cd36_1
3. Hmox1_2
4. Plin2_2 (target genes)
5. CYC1,

Samples: cDNA from tgfb9 cond 1.1 - 1.12 + NO RT (2.1-2.12 another day, 3.1-3.12 another day, 4.1-4.12 another day) (14 samples total). 3 replicates of each

TOTAL: 195 wells

Prepare cDNAs:

Already ready (1:10 dilution)

Prepare primer mixes:

Of each primer mix you need enough for 39 wells -> calculate for 45.

Component	1 well	45 wells
MasterMix SYBR Green	5 μ L	225 μ L
Primers (both together at a concentration of 5 μ M each)	0.6 (final concentration 300 nM)	27 μ L
Nuclease-free water	3.4	153 μ L
DNA Template	Add 1 μ L in each well	Add at each well
TOTAL VOLUME PER WELL	10 μL	

Mix well and share 9 μ L of primer mix to each well (with the step-pipette!)

Then mix well cDNA and add 1 μ L of cDNA per well (change pipette every time!)

Special things:

- qPCR run at the AG Dichgans machine - newer machine
- Primer mixes from Mar
- Performed by Agata/Mar

References

- Aggarwal, S., Yurlova, L., and Simons, M. (2011). Central nervous system myelin: structure, synthesis and assembly. *Trends Cell Biol.* *21*, 585–593.
- Aguilera, C.M., Gil-Campos, M., Cañete, R., and Gil, Á. (2008). Alterations in plasma and tissue lipids associated with obesity and metabolic syndrome. *Clin. Sci.* *114*, 183–193.
- Aguzzi, A., Barres, B.A., and Bennett, M.L. (2013). Microglia: Scapegoat, saboteur, or something else? *Science* (80-.). *339*, 156–161.
- Ahdjoudj, S., Lasmoles, F., Holy, X., Zerath, E., and Marie, P.J. (2002). Transforming Growth Factor β 2 Inhibits Adipocyte Differentiation Induced by Skeletal Unloading in Rat Bone Marrow Stroma. *J. Bone Miner. Res.* *17*, 668–677.
- Ajami, B., Bennett, J.L., Krieger, C., Tetzlaff, W., and Rossi, F.M.V. (2007). Local self-renewal can sustain CNS microglia maintenance and function throughout adult life. *Nat. Neurosci.* *10*, 1538–1543.
- Ajami, B., Bennett, J.L., Krieger, C., McNagny, K.M., and Rossi, F.M.V. (2011). Infiltrating monocytes trigger EAE progression, but do not contribute to the resident microglia pool. *Nat. Neurosci.* *14*, 1142–1149.
- Ajami, B., Samusik, N., Wieghofer, P., Ho, P.P., Crotti, A., Bjornson, Z., Prinz, M., Fantl, W.J., Nolan, G.P., and Steinman, L. (2018). Single-cell mass cytometry reveals distinct populations of brain myeloid cells in mouse neuroinflammation and neurodegeneration models. *Nat. Neurosci.* *21*.
- Al-Lahham, S., Roelofsen, H., Rezaee, F., Weening, D., Hoek, A., Vonk, R., and Venema, K. (2012). Propionic acid affects immune status and metabolism in adipose tissue from overweight subjects. *Eur. J. Clin. Invest.* *42*, 357–364.
- Al-Lahham, S.H., Roelofsen, H., Priebe, M., Weening, D., Dijkstra, M., Hoek, A., Rezaee, F., Venema, K., and Vonk, R.J. (2010). Regulation of adipokine production in human adipose tissue by propionic acid. *Eur. J. Clin. Invest.* *40*, 401–407.
- Alessi, M.C., Bastelica, D., Morange, P., Berthet, B., Leduc, I., Verdier, M., Geel, O., and Juhan-Vague, I. (2000). Plasminogen activator inhibitor 1, transforming growth factor- β 1, and BMI are closely associated in human adipose tissue during morbid obesity. *Diabetes* *49*, 1374–1380.
- Altowajiri, G., Fryman, A., and Yadav, V. (2017). Dietary Interventions and Multiple Sclerosis. *Curr. Neurol. Neurosci. Rep.* *17*, 28.
- Arvin, K.L., Han, B.H., Du, Y., Lin, S.Z., Paul, S.M., and Holtzman, D.M. (2002). Minocycline markedly protects the neonatal brain against hypoxic-ischemic injury. *Ann. Neurol.* *52*, 54–61.
- Askew, K., Li, K., Olmos-Alonso, A., Garcia-Moreno, F., Liang, Y., Richardson, P., Tipton, T., Chapman, M.A., Riecken, K., Beccari, S., et al. (2017). Coupled Proliferation and Apoptosis Maintain the Rapid Turnover of Microglia in the Adult Brain. *Cell Rep.* *18*.
- Awada, R., Parimisetty, A., and Lefebvre dHellencourt, C. (2013). Influence of Obesity on Neurodegenerative Diseases. In *Neurodegenerative Diseases*, (InTech), p.
- Barcellos, L. (2016). Obesity and Multiple Sclerosis Susceptibility: A Review. *J. Neurol. Neuromedicine* *1*, 1–5.
- Baror, R., Neumann, B., Segel, M., Chalut, K.J., Fancy, S.P.J., Schafer, D.P., and Franklin, R.J.M. (2019). Transforming growth factor-beta renders ageing microglia inhibitory to oligodendrocyte generation by CNS progenitors. *Glia* *67*, 1374–1384.
- Basu-Modak, S., Braissant, O., Escher, P., Desvergne, B., Honegger, P., and Wahli, W. (1999). Peroxisome proliferator-activated receptor β regulates acyl-CoA synthetase 2 in reaggregated rat brain cell cultures. *J. Biol. Chem.* *274*, 35881–35888.
- Baufeld, C., Osterloh, A., Prokop, S., Miller, K.R., and Heppner, F.L. (2016). High-fat diet-induced brain region-specific phenotypic spectrum of CNS resident microglia. *Acta Neuropathol.* *132*, 361–375.
- Baumann, N., and Pham-Dinh, D. (2001). Biology of oligodendrocyte and myelin in the mammalian central nervous system. *Physiol. Rev.* *81*, 871–927.
- Belbasis, L., Bellou, V., Evangelou, E., Ioannidis, J.P.A., and Tzoulaki, I. (2015). Environmental risk factors and multiple sclerosis: An umbrella review of systematic reviews and meta-analyses. *Lancet Neurol.* *14*.
- Bennett, F.C., Bennett, M.L., Yaqoob, F., Mulinyawe, S.B., Grant, G.A., Hayden Gephart, M., Plowey, E.D., and Barres, B.A. (2018). A Combination of Ontogeny and CNS Environment Establishes Microglial Identity. *Neuron*.
- Bennett, M.L., Bennett, F.C., Liddel, S.A., Ajami, B., Zamanian, J.L., Fernhoff, N.B., Mulinyawe, S.B., Bohlen, C.J., Adil, A., Tucker, A., et al. (2016). New tools for studying microglia in the mouse and human CNS. *Proc. Natl. Acad. Sci. U. S. A.*
- Berer, K., Gerdes, L.A., Cekanaviciute, E., Jia, X., Xiao, L., Xia, Z., Liu, C., Klotz, L., Stauffer, U., Baranzini, S.E., et al. (2017). Gut microbiota from multiple sclerosis patients enables spontaneous autoimmune encephalomyelitis in mice. *Proc. Natl. Acad. Sci. U. S. A.* *114*, 10719–10724.
- Berghoff, S.A., Spieth, L., Sun, T., Hosang, L., Schlaphoff, L., Dükling, T., Depp, C., Winchenbach, J., Neuber, J., Ewers, D., et al. (2020) Phase and cell-type specific post-squalene sterol synthesis coordinates inflammation and remyelination. Submitted.
- Bernardo, A., and Minghetti, L. (2006). PPAR-gamma agonists as regulators of microglial activation and brain inflammation. *Curr. Pharm. Des.* *12*, 93–109.
- den Besten, G., Bleeker, A., Gerding, A., van Eunen, K., Havinga, R., van Dijk, T.H., Oosterveer, M.H., Jonker, J.W., Groen, A.K., Reijngoud, D.-J., et al. (2015). Short-Chain Fatty Acids Protect Against High-Fat Diet-Induced Obesity via a PPAR γ -Dependent Switch From Lipogenesis to Fat Oxidation. *Diabetes* *64*, 2398–2408.
- Bhasin, M., Wu, M., and Tsirka, S.E. (2007). Modulation of microglial/macrophage activation by macrophage inhibitory factor (TKP) or tuftsin (TKPR) attenuates the disease course of experimental autoimmune encephalomyelitis. *BMC Immunol.* *8*, 10.
- De Biase, L.M., Schuebel, K.E., Fuszfeld, Z.H., Jair, K., Hawes, I.A., Cimbrot, R., Zhang, H.Y., Liu, Q.R., Shen, H., Xi, Z.X., et al. (2017). Local Cues Establish and Maintain Region-Specific Phenotypes of Basal Ganglia Microglia. *Neuron* *95*, 341–356.e6.
- Biber, K., Neumann, H., Inoue, K., and Boddeke, H.W.G.M. (2007). Neuronal “On” and “Off” signals control microglia. *Trends Neurosci.* *30*, 596–602.
- Biber, K., Owens, T., and Boddeke, E. (2014). What is microglia neurotoxicity (Not)? *Glia* *62*, 841–854.

References

- Blakemore, W.F., and Franklin, R.J.M. (2008). Remyelination in experimental models of toxin-induced demyelination. *Curr. Top. Microbiol. Immunol.* *318*, 193–212.
- Bloemen, J.G., Olde Damink, S.W.M., Venema, K., Buurman, W.A., Jalan, R., and Dejong, C.H.C. (2010). Short chain fatty acids exchange: Is the cirrhotic, dysfunctional liver still able to clear them? *Clin. Nutr.* *29*, 365–369.
- Boadu, E., Bilbey, N.J., and Francis, G.A. (2008). Cellular cholesterol substrate pools for adenosine-triphosphate cassette transporter A1-dependent high-density lipoprotein formation. *Curr. Opin. Lipidol.* *19*, 270–276.
- Bogie, J.F.J., Timmermans, S., Huynh-Thu, V.A., Irrthum, A., Smeets, H.J.M., Gustafsson, J.-Å., Steffensen, K.R., Mulder, M., Stinissen, P., Hellings, N., et al. (2012). Myelin-derived lipids modulate macrophage activity by liver X receptor activation. *PLoS One* *7*, e44998.
- Bogie, J.F.J., Stinissen, P., and Hendriks, J.J.A. (2014a). Macrophage subsets and microglia in multiple sclerosis. *Acta Neuropathol.* *128*, 191–213.
- Bogie, J.F.J., Jorissen, W., Mailleux, J., Nijland, P.G., Zelcer, N., Vanmierlo, T., Van Horsen, J., Stinissen, P., Hellings, N., and Hendriks, J.J.A. (2014b). Myelin alters the inflammatory phenotype of macrophages by activating PPARs. *Acta Neuropathol. Commun.* *2*, 43.
- Bohlen, C.J., Bennett, F.C., Tucker, A.F., Collins, H.Y., Mulinyawe, S.B., and Barres, B.A. (2017). Diverse Requirements for Microglial Survival, Specification, and Function Revealed by Defined-Medium Cultures. *Neuron* *94*, 759–773.e8.
- Bordet, R., Ouk, T., Petrault, O., Gelé, P., Gautier, S., Laprais, M., Deplanque, D., Duriez, P., Staels, B., Fruchart, J.C., et al. (2006). PPAR: A new pharmacological target for neuroprotection in stroke and neurodegenerative diseases. In *Biochemical Society Transactions*, pp. 1341–1346.
- Boven, L.A., Van Meurs, M., Van Zwam, M., Wierenga-Wolf, A., Hintzen, R.Q., Boot, R.G., Aerts, J.M., Amor, S., Nieuwenhuis, E.E., and Laman, J.D. (2006). Myelin-laden macrophages are anti-inflammatory, consistent with foam cells in multiple sclerosis. *Brain* *129*, 517–526.
- Bradbury, E.J., and Burnside, E.R. (2019). Moving beyond the glial scar for spinal cord repair. *Nat. Commun.* *10*, 1–15.
- Buckman, L.B., Thompson, M.M., Moreno, H.N., and Ellacott, K.L.J. (2013). Regional astrogliosis in the mouse hypothalamus in response to obesity. *J. Comp. Neurol.* *521*, 1322–1333.
- Buckman, L.B., Hasty, A.H., Flaherty, D.K., Buckman, C.T., Thompson, M.M., Matlock, B.K., Weller, K., and Ellacott, K.L.J. (2014). Obesity induced by a high-fat diet is associated with increased immune cell entry into the central nervous system. *Brain. Behav. Immun.* *35*, 33–42.
- Bueno, L., de Alwis, D.P., Pitou, C., Yingling, J., Lahn, M., Glatt, S., and Trocóniz, I.F. (2008). Semi-mechanistic modelling of the tumour growth inhibitory effects of LY2157299, a new type I receptor TGF- β kinase antagonist, in mice. *Eur. J. Cancer* *44*, 142–150.
- Butovsky, O., Landa, G., Kunis, G., Ziv, Y., Avidan, H., Greenberg, N., Schwartz, A., Smirnov, I., Pollack, A., Jung, S., et al. (2006). Induction and blockage of oligodendrogenesis by differently activated microglia in an animal model of multiple sclerosis. *J. Clin. Invest.* *116*, 905–915.
- Butovsky, O., Siddiqui, S., Gabriely, G., Lanser, A.J., Dake, B., Murugaiyan, G., Doykan, C.E., Wu, P.M., Gali, R.R., Iyer, L.K., et al. (2012). Modulating inflammatory monocytes with a unique microRNA gene signature ameliorates murine ALS. *J. Clin. Invest.* *122*, 3063–3087.
- Butovsky, O., Jedrychowski, M.P., Moore, C.S., Cialic, R., Lanser, A.J., Gabriely, G., Koeglsperger, T., Dake, B., Wu, P.M., Doykan, C.E., et al. (2014). Identification of a unique TGF- β -dependent molecular and functional signature in microglia. *Nat. Neurosci.* *17*, 131–143.
- Buttgereit, A., Lelios, I., Yu, X., Vrohings, M., Krakoski, N.R., Gautier, E.L., Nishinakamura, R., Becher, B., and Greter, M. (2016). Sall1 is a transcriptional regulator defining microglia identity and function. *Nat. Immunol.* *17*, 1397–1406.
- Canfora, E.E., Jocken, J.W., and Blaak, E.E. (2015). Short-chain fatty acids in control of body weight and insulin sensitivity. *Nat. Rev. Endocrinol.* *11*, 577–591.
- Cantuti-Castelvetri, L., Fitzner, D., Bosch-Queralt, M., Weil, M.-T., Su, M., Sen, P., Ruhwedel, T., Mitkovski, M., Trendelenburg, G., Lütjohann, D., et al. (2018). Defective cholesterol clearance limits remyelination in the aged central nervous system. *Science* *359*, 684–688.
- Castellano, B., Bosch-Queralt, M., Almolda, B., Villacampa, N., and González, B. (2016). Purine signaling and microglial wrapping. *Cell. Mol. Life Sci.* *373*, 117–127.
- Cermenati, G., Brioschi, E., Abbiati, F., Melcangi, R.C., Caruso, D., and Mitro, N. (2013). Liver X receptors, nervous system, and lipid metabolism. *J. Endocrinol. Invest.* *36*, 435–443.
- Chari, D.M. (2007). Remyelination in multiple sclerosis. *Int. Rev. Neurobiol.* *79*, 589–620.
- Chawla, A., Barak, Y., Nagy, L., Liao, D., Tontonoz, P., and Evans, R.M. (2001). PPAR- γ dependent and independent effects on macrophage-gene expression in lipid metabolism and inflammation. *Nat. Med.* *7*, 48–52.
- Cheray, M., and Joseph, B. (2018). Epigenetics control microglia plasticity. *Front. Cell. Neurosci.* *12*.
- Chinetti, G., Lestavel, S., Bocher, V., Remaley, A.T., Neve, B., Torra, I.P., Teissier, E., Minnich, A., Jaye, M., Duverger, N., et al. (2001). PPAR- α and PPAR- γ activators induce cholesterol removal from human macrophage foam cells through stimulation of the ABCA1 pathway. *Nat. Med.* *7*, 53–58.
- Chistiakov, D.A., Bobryshev, Y. V., and Orekhov, A.N. (2016). Macrophage-mediated cholesterol handling in atherosclerosis. *J. Cell. Mol. Med.* *20*, 17–28.
- Chiu, I.M., Morimoto, E.T.A., Goodarzi, H., Liao, J.T., O’Keeffe, S., Phatnani, H.P., Muratet, M., Carroll, M.C., Levy, S., Tavazoie, S., et al. (2013). A neurodegeneration-specific gene-expression signature of acutely isolated microglia from an amyotrophic lateral sclerosis mouse model. *Cell Rep.* *4*, 385–401.
- Chrast, R., Saher, G., Nave, K.-A., and Verheijen, M.H.G. (2011). Lipid metabolism in myelinating glial cells: lessons from human inherited disorders and mouse models. *J. Lipid Res.* *52*, 419–434.
- Christ, A., Günther, P., Lauterbach, M.A.R., Duester, P., Biswas, D., Pelka, K., Scholz, C.J., Oosting, M., Haendler, K., Bäßler, K., et al. (2018). Western Diet Triggers NLRP3-Dependent Innate Immune Reprogramming. *Cell* *172*, 162–175.e14.
- Cohen, M., Matcovitch, O., David, E., Barnett-Itzhaki, Z., Keren-Shaul, H., Blecher-Gonen, R., Jaitin, D.A., Sica, A., Amit, I., and Schwartz, M. (2014). Chronic exposure to TGF- β 1 regulates myeloid cell inflammatory response in an IRF-7-dependent manner. *EMBO J.* *33*, 2906–2921.
- Collins, J.L., Binz, J.G., Plunket, K.D., Morgan, D.G., Beaudet, E.J., Whitney, K.D., Kliewer, S. a., Willson, T.M., Fivush, A.M., Watson, M. a., et al. (2002). Identification of a nonsteroidal liver X receptor agonist through parallel array synthesis of tertiary amines. *J. Med. Chem.* *45*, 1963–1966.

- Court, F.A., and Alvarez, J. (2016). Glial Cells in Health and Disease of the CNS.
- Courtney, R., and Landreth, G.E. (2016). LXR Regulation of Brain Cholesterol: From Development to Disease. *Trends Endocrinol. Metab.*
- Cronk, J.C., Filiano, A.J., Louveau, A., Marin, I., Marsh, R., Ji, E., Goldman, D.H., Smirnov, I., Geraci, N., Acton, S., et al. (2018). Peripherally derived macrophages can engraft the brain independent of irradiation and maintain an identity distinct from microglia. *J. Exp. Med.*
- Cui, G., Qin, X., Wu, L., Zhang, Y., Sheng, X., Yu, Q., Sheng, H., Xi, B., Zhang, J.Z., and Zang, Y.Q. (2011). Liver X receptor (LXR) mediates negative regulation of mouse and human Th17 differentiation. *J. Clin. Invest.* *121*, 658–670.
- Cummins, C.L., and Mangelsdorf, D.J. (2006). Liver X receptors and cholesterol homeostasis: spotlight on the adrenal gland. *Biochem. Soc. Trans.* *34*, 1110–1113.
- Cunniffe, N., and Coles, A. (2019). Promoting remyelination in multiple sclerosis. *J. Neurol.* 1–15.
- Dalby, M.J., Ross, A.W., Walker, A.W., and Morgan, P.J. (2017). Dietary Uncoupling of Gut Microbiota and Energy Harvesting from Obesity and Glucose Tolerance in Mice. *Cell Rep.* *21*, 1521–1533.
- Datta, M., Staszewski, O., Raschi, E., Frosch, M., Hagemeyer, N., Tay, T.L., Blank, T., Kreutzfeldt, M., Merkler, D., Ziegler-Waldkirch, S., et al. (2018). Histone Deacetylases 1 and 2 Regulate Microglia Function during Development, Homeostasis, and Neurodegeneration in a Context-Dependent Manner. *Immunity* *48*, 514–529.e6.
- Davalos, D., Grutzendler, J., Yang, G., Kim, J. V, Zuo, Y., Jung, S., Littman, D.R., Dustin, M.L., and Gan, W.-B. (2005). ATP mediates rapid microglial response to local brain injury in vivo. *Nat. Neurosci.* *8*, 752–758.
- De, J., Guerrero-García, J., Carrera-Quintanar, L., Ivette López-Roa, R., Laura Márquez-Aguirre, A., Rojas-Mayorquín, A.E., and Ortuño-Sahagún, D. (2016). Review Article Multiple Sclerosis and Obesity: Possible Roles of Adipokines. *Hindawi.Com.*
- Deczkowska, A., Amit, I., and Schwartz, M. (2018). Microglial immune checkpoint mechanisms. *Nat. Neurosci.* *21*.
- Döring, A., Sloka, S., Lau, L., Mishra, M., van Minnen, J., Zhang, X., Kinniburgh, D., Rivest, S., and Yong, V.W. (2015). Stimulation of monocytes, macrophages, and microglia by amphotericin B and macrophage colony-stimulating factor promotes remyelination. *J. Neurosci.* *35*, 1136–1148.
- Doyle, K.P., Cekanaviciute, E., Mamer, L.E., and Buckwalter, M.S. (2010). TGF β signaling in the brain increases with aging and signals to astrocytes and innate immune cells in the weeks after stroke. *J. Neuroinflammation* *7*, 62.
- Dressel, U., Allen, T.L., Pippal, J.B., Rohde, P.R., Lau, P., and Muscat, G.E.O. (2003). The Peroxisome Proliferator-Activated Receptor $\beta/8$ Agonist, GW501516, Regulates the Expression of Genes Involved in Lipid Catabolism and Energy Uncoupling in Skeletal Muscle Cells. *Mol. Endocrinol.* *17*, 2477–2493.
- Duewell, P., Kono, H., Rayner, K.J., Sirois, C.M., Vladimer, G., Bauernfeind, F.G., Abela, G.S., Franchi, L., Nuñez, G., Schnurr, M., et al. (2010). LETTERS NLRP3 inflammasomes are required for atherogenesis and activated by cholesterol crystals. *Nature* *464*.
- Edwards, P.A., Kast, H.R., and Anisfeld, A.M. (2002). BAREing it all: the adoption of LXR and FXR and their roles in lipid homeostasis. *J. Lipid Res.* *43*, 2–12.
- Eisinger, K., Liebisch, G., Schmitz, G., Aslanidis, C., Krautbauer, S., and Buechler, C. (2014). Lipidomic Analysis of Serum from High Fat Diet Induced Obese Mice. *Int. J. Mol. Sci.* *15*, 2991–3002.
- Ejsing, C.S., Sampaio, J.L., Surendranath, V., Duchoslav, E., Ekroos, K., Klemm, R.W., Simons, K., and Shevchenko, A. (2009). Global analysis of the yeast lipidome by quantitative shotgun mass spectrometry. *Proc. Natl. Acad. Sci. U. S. A.* *106*, 2136–2141.
- Ellrichmann, G., Thöne, J., Lee, D.-H., Rupec, R.A., Gold, R., and Linker, R.A. (2012). Constitutive activity of NF-kappa B in myeloid cells drives pathogenicity of monocytes and macrophages during autoimmune neuroinflammation. *J. Neuroinflammation* *9*, 15.
- Elsherbiny, M.E., Goruk, S., Monckton, E.A., Richard, C., Brun, M., Emar, M., Field, C.J., and Godbout, R. (2015). Long-term effect of docosahexaenoic acid feeding on lipid composition and brain fatty acid-binding protein expression in rats. *Nutrients* *7*, 8802–8817.
- Endo, F., Komine, O., Fujimori-Tonou, N., Katsuno, M., Jin, S., Watanabe, S., Sobue, G., Dezawa, M., Wyss-Coray, T., and Yamanaka, K. (2015). Astrocyte-Derived TGF- β 1 Accelerates Disease Progression in ALS Mice by Interfering with the Neuroprotective Functions of Microglia and T Cells. *Cell Rep.* *11*, 592–604.
- Erny, D., Hrabě de Angelis, A.L., Jaitin, D., Wieghofer, P., Staszewski, O., David, E., Keren-Shaul, H., Mhalkaiov, T., Jakobshagen, K., Buch, T., et al. (2015). Host microbiota constantly control maturation and function of microglia in the CNS. *Nat. Neurosci.* *18*, 965–977.
- Fabbrini, E., Mohammed, B.S., Magkos, F., Korenblat, K.M., Patterson, B.W., and Klein, S. (2008). Alterations in Adipose Tissue and Hepatic Lipid Kinetics in Obese Men and Women With Nonalcoholic Fatty Liver Disease. *Gastroenterology* *134*, 424–431.
- Fan, J., Qi Zhao, R., Parro, C., Zhao, W., Chou, H.Y., Robert, J., Deeb, T.Z., Raynoschek, C., Barichievy, S., Engkvist, O., et al. (2018). Small molecule inducers of ABCA1 and apoE that act through indirect activation of the LXR pathway. *J. Lipid Res.* *59*, 830–842.
- Fantuzzi, G., and Faggioni, R. (2000). Leptin in the regulation of immunity, inflammation, and hematopoiesis. *J. Leukoc. Biol.* *68*, 437–446.
- Fawcett, J.W., and Asher, R.A. (1999). The glial scar and central nervous system repair. *Brain Res. Bull.* *49*, 377–391.
- Feinstein, D.L., Galea, E., Gavriluyk, V., Brosnan, C.F., Whitacre, C.C., Dumitrescu-Ozimek, L., Landreth, G.E., Pershadsingh, H.A., Weinberg, G., and Heneka, M.T. (2002). Peroxisome Proliferator-Activated Receptor- α Agonists Prevent Experimental Autoimmune Encephalomyelitis. *Ann Neurol* *51*, 694–702.
- Feng, X.-H., and Derynck, R. (2005). SPECIFICITY AND VERSATILITY IN TGF- β SIGNALING THROUGH SMADS. *Annu. Rev. Cell Dev. Biol.* *21*, 659–693.
- Ferguson, B., Matyszak, M.K., Esiri, M.M., and Perry, V.H. (1997). Axonal damage in acute multiple sclerosis lesions. *Brain* *120 (Pt 3)*, 393–399.
- Fitzner, D., Penkert, H., Bader, J.M., Bergner, C.G., Su, M., Weil, M.T., Surma, M.A., Klose, C., Simons, M. (2020). Cell type- and brain region-resolved mouse brain lipidome. *Cell reports*, submitted.
- Fleck, A.-K., Schuppan, D., Wiendl, H., and Klotz, L. (2017). Gut–CNS-Axis as Possibility to Modulate Inflammatory Disease Activity—Implications for Multiple Sclerosis. *Int. J. Mol. Sci.* *18*, 1526.

References

- Floris, S., Blezer, E.L.A., Schreibelt, G., Döpp, E., Van Der Pol, S.M.A., Schadee-Eestermans, I.L., Nicolay, K., Dijkstra, C.D., and De Vries, H.E. (2004). Blood-brain barrier permeability and monocyte infiltration in experimental allergic encephalomyelitis: A quantitative MRI study. *Brain* *127*, 616–627.
- Fowler, A.J., Sheu, M.Y., Schmuth, M., Kao, J., Fluhr, J.W., Rhein, L., Collins, J.L., Willson, T.M., Mangelsdorf, D.J., Elias, P.M., et al. (2003). Liver X receptor activators display anti-inflammatory activity in irritant and allergic contact dermatitis models: liver-X-receptor-specific inhibition of inflammation and primary cytokine production. *J. Invest. Dermatol.* *120*, 246–255.
- Frahnow, T., Osterhoff, M.A., Hornemann, S., Kruse, M., Surma, M.A., Klose, C., Simons, K., and Pfeiffer, A.F.H. (2017). Heritability and responses to high fat diet of plasma lipidomics in a twin study. *Sci. Rep.* *7*, 1–11.
- Franklin, R.J.M., and Ffrench-Constant, C. (2008). Remyelination in the CNS: from biology to therapy. *Nat. Rev. Neurosci.* *9*, 839–855.
- Franklin, R.J.M., and Ffrench-Constant, C. (2017). Regenerating CNS myelin - From mechanisms to experimental medicines. *Nat. Rev. Neurosci.*
- Fu, S., Yang, L., Li, P., Hofmann, O., Dicker, L., Hide, W., Lin, X., Watkins, S.M., Ivanov, A.R., and Hotamisligil, G.S. (2011). Aberrant lipid metabolism disrupts calcium homeostasis causing liver endoplasmic reticulum stress in obesity. *Nature* *473*, 528–531.
- Galatro, T.F., Holtman, I.R., Lerario, A.M., Vainchtein, I.D., Brouwer, N., Sola, P.R., Veras, M.M., Pereira, T.F., Leite, R.E.P., Möller, T., et al. (2017). Transcriptomic analysis of purified human cortical microglia reveals age-associated changes. *Nat. Neurosci.* *20*.
- Galea, I., Felton, L.M., Waters, S., van Rooijen, N., Perry, V.H., and Newman, T.A. (2008). Immune-to-brain signalling: The role of cerebral CD163-positive macrophages. *Neurosci. Lett.* *448*, 41–46.
- Gautier, E.L., Shay, T., Miller, J., Greter, M., Jakubzick, C., Ivanov, S., Helft, J., Chow, A., Elpek, K.G., Gordonov, S., et al. (2012). Gene-expression profiles and transcriptional regulatory pathways that underlie the identity and diversity of mouse tissue macrophages. *Nat. Immunol.* *13*, 1118–1128.
- Geissmann, F., Manz, M.G., Jung, S., Sieweke, M.H., Merad, M., and Ley, K. (2010). Development of monocytes, macrophages, and dendritic cells. *Science* *327*, 656–661.
- Gilardi, F., Viviani, B., Galmozzi, A., Boraso, M., Bartesaghi, S., Torri, A., Caruso, D., Crestani, M., Marinovich, M., and de Fabiani, E. (2009). Expression of sterol 27-hydroxylase in glial cells and its regulation by liver X receptor signaling. *Neuroscience* *164*, 530–540.
- Gilden, D.H. (2005). Infectious causes of multiple sclerosis. *Lancet Neurol.* *4*, 195–202.
- Giles, C., Takechi, R., Mellett, N.A., Meikle, P.J., Dhaliwal, S., and Mamo, J.C. (2016). The effects of long-term saturated fat enriched diets on the brain lipidome. *PLoS One* *11*, e0166964.
- Ginhoux, F., Greter, M., Leboeuf, M., Nandi, S., See, P., Gokhan, S., Mehler, M.F., Conway, S.J., Ng, L.G., Stanley, E.R., et al. (2010). Fate mapping analysis reveals that adult microglia derive from primitive macrophages. *Science* *330*, 841–845.
- Gitik, M., Liraz-Zaltsman, S., Oldenborg, P.A., Reichert, F., and Rotshenker, S. (2011). Myelin down-regulates myelin phagocytosis by microglia and macrophages through interactions between CD47 on myelin and SIRP α (signal regulatory protein- α) on phagocytes. *J. Neuroinflammation* *8*, 24.
- Godbout, J.P., Chen, J., Abraham, J., Richwine, A.F., Berg, B.M., Kelley, K.W., and Johnson, R.W. (2005). Exaggerated neuroinflammation and sickness behavior in aged mice following activation of the peripheral innate immune system. *FASEB J.* *19*, 1329–1331.
- Goddard, E.T., Fischer, J., and Schedin, P. (2016). A portal vein injection model to study liver metastasis of breast cancer. *J. Vis. Exp.* *2016*, 1–10.
- Goldmann, T., Wieghofer, P., Müller, P.F., Wolf, Y., Varol, D., Yona, S., Brendecke, S.M., Kierdorf, K., Staszewski, O., Datta, M., et al. (2013). A new type of microglia gene targeting shows TAK1 to be pivotal in CNS autoimmune inflammation. *Nat. Neurosci.* *16*, 1618–1626.
- Goldmann, T., Wieghofer, P., Jordão, M.J.C., Prutek, F., Hagemeyer, N., Frenzel, K., Amann, L., Staszewski, O., Kierdorf, K., Krueger, M., et al. (2016). Origin, fate and dynamics of macrophages at central nervous system interfaces. *Nat. Immunol.* *17*.
- Goldschmidt, T., Antel, J., König, F.B., Brück, W., and Kuhlmann, T. (2009). Remyelination capacity of the MS brain decreases with disease chronicity. *Neurology* *72*, 1914–1921.
- Goodson, W.H., and Hunt, T.K. (1986). Wound collagen accumulation in obese hyperglycemic mice. *Diabetes* *35*, 491–495.
- Gosselin, D., Link, V.M., Romanoski, C.E., Fonseca, G.J., Eichenfield, D.Z., Spann, N.J., Stender, J.D., Chun, H.B., Garner, H., Geissmann, F., et al. (2014). Environment drives selection and function of enhancers controlling tissue-specific macrophage identities. *Cell* *159*.
- Gosselin, D., Skola, D., Coufal, N.G., Holtman, I.R., Schlachetzki, J.C.M., Sajti, E., Jaeger, B.N., O'Connor, C., Fitzpatrick, C., Pasillas, M.P., et al. (2017). An environment-dependent transcriptional network specifies human microglia identity. *Science* (80-.). *356*.
- Grabert, K., Michoel, T., Karavolos, M.H., Clohisey, S., Baillie, J.K., Stevens, M.P., Freeman, T.C., Summers, K.M., and McColl, B.W. (2016). Microglial brain region-dependent diversity and selective regional sensitivities to aging. *Nat. Neurosci.* *19*.
- Graeber, M.B., and Streit, W.J. (2010). Microglia: biology and pathology. *Acta Neuropathol.* *119*, 89–105.
- Grajchen, E., Hendriks, J.J.A., and Bogie, J.F.J. (2018). The physiology of foamy phagocytes in multiple sclerosis. *Acta Neuropathol. Commun.* *6*, 124.
- GrandPré, T., Nakamura, F., Vartanian, T., and Strittmatter, S.M. (2000). Identification of the Nogo inhibitor of axon regeneration as a Reticulon protein. *Nature* *403*, 439–444.
- Gregor, M.F., and Hotamisligil, G.S. (2011). Inflammatory Mechanisms in Obesity. *Annu. Rev. Immunol.* *29*, 415–445.
- De Groot, C., Montagne, L., Barten, A., Sminia, P., and Van der Valk, P. (1999). Expression of transforming growth factor (TGF)- β 1, - β 2, and - β 3 isoforms and TGF- β type I and type II receptors in multiple sclerosis lesions and human adult astrocyte cultures. *J Neuropathol Exp Neurol* *174*–187.
- Guillemot-Legrès, O., and Muccioli, G.G. (2017). Obesity-Induced Neuroinflammation: Beyond the Hypothalamus. *Trends Neurosci.* *40*, 237–253.
- Hagemeyer, N., Hanft, K.-M., Akriditou, M.-A., Unger, N., Park, E.S., Stanley, · E Richard, Staszewski, · Ori, Dimou, · Leda, and Marco Prinz, · Microglia contribute to normal myelinogenesis and to oligodendrocyte progenitor maintenance during adulthood. *Acta Neuropathol.*
- Hamaguchi, M., Muramatsu, R., Fujimura, H., Mochizuki, H.,

References

- Kataoka, H., and Yamashita, T. (2019). Circulating transforming growth factor- β 1 facilitates remyelination in the adult central nervous system. *Elife* 8.
- Hammond, T.R., Dufort, C., Dissing-Olesen, L., Giera, S., Young, A., Wysoker, A., Walker, A.J., Gergits, F., Segel, M., Nemesh, J., et al. (2019). Single-Cell RNA Sequencing of Microglia throughout the Mouse Lifespan and in the Injured Brain Reveals Complex Cell-State Changes. *Immunity* 50, 253–271.e6.
- Han, J., Hajjar, D.P., Tauras, J.M., Feng, J., Gotto, A.M., and Nicholson, A.C. (2000). Transforming growth factor- β 1 (TGF- β 1) and TGF- β 2 decrease expression of CD36, the type B scavenger receptor, through mitogen-activated protein kinase phosphorylation of peroxisome proliferator-activated receptor- γ . *J. Biol. Chem.* 275, 1241–1246.
- Hanisch, U.-K., and Kettenmann, H. (2007). Microglia: active sensor and versatile effector cells in the normal and pathologic brain. *Nat. Neurosci.* 10, 1387–1394.
- Hargrave, S.L., Davidson, T.L., Lee, T.J., and Kinzig, K.P. (2015). Brain and behavioral perturbations in rats following Western diet access. *Appetite* 93, 35–43.
- Hedström, A.K., Olsson, T., and Alfredsson, L. (2012). High body mass index before age 20 is associated with increased risk for multiple sclerosis in both men and women. *Mult. Scler. J.* 18, 1334–1336.
- Heinz, S., Benner, C., Spann, N., Bertolino, E., Lin, Y.C., Laslo, P., Cheng, J.X., Murre, C., Singh, H., and Glass, C.K. (2010). Simple Combinations of Lineage-Determining Transcription Factors Prime cis-Regulatory Elements Required for Macrophage and B Cell Identities. *Mol. Cell* 38, 576–589.
- Henderson, A.P.D., Barnett, M.H., Parratt, J.D.E., and Prineas, J.W. (2009). Multiple sclerosis: Distribution of inflammatory cells in newly forming lesions. *Ann. Neurol.* 66, 739–753.
- Hendriks, J.J.A., Teunissen, C.E., de Vries, H.E., and Dijkstra, C.D. (2005). Macrophages and neurodegeneration. *Brain Res. Brain Res. Rev.* 48, 185–195.
- Heneka, M.T., and Landreth, G.E. (2007). PPARs in the brain. *Biochim. Biophys. Acta - Mol. Cell Biol. Lipids* 1771, 1031–1045.
- Heppner, F.L., Greter, M., Marino, D., Falsig, J., Raivich, G., Hövelmeyer, N., Waisman, A., Rüllicke, T., Prinz, M., Priller, J., et al. (2005). Experimental autoimmune encephalomyelitis repressed by microglial paralysis. *Nat. Med.* 11, 146–152.
- Herzog, R., Schwudke, D., Schuhmann, K., Sampaio, J.L., Bornstein, S.R., Schroeder, M., and Shevchenko, A. (2011). A novel informatics concept for high-throughput shotgun lipidomics based on the molecular fragmentation query language. *Genome Biol.* 12, R8.
- Hinks, G.L., and Franklin, R.J. (2000). Delayed changes in growth factor gene expression during slow remyelination in the CNS of aged rats. *Mol. Cell. Neurosci.* 16, 542–556.
- Holtman, I.R., Raj, D.D., Miller, J.A., Schaafsma, W., Yin, Z., Brouwer, N., Wes, P.D., Möller, T., Orre, M., Kamphuis, W., et al. (2015). Induction of a common microglia gene expression signature by aging and neurodegenerative conditions: a co-expression meta-analysis. *Acta Neuropathol. Commun.* 3, 31.
- Hong, C., and Tontonoz, P. (2014). Liver X receptors in lipid metabolism: opportunities for drug discovery. *Nat. Rev. Drug Discov.* 13, 433–444.
- Hong, S., Beja-Glasser, V.F., Nfonoyim, B.M., Frouin, A., Li, S., Ramakrishnan, S., Merry, K.M., Shi, Q., Rosenthal, A., Barres, B.A., et al. (2016). Complement and microglia mediate early synapse loss in Alzheimer mouse models. *Science* (80-.). 352, 712–716.
- Van Hove, H., Martens, L., Scheyltjens, I., De Vlaminck, K., Pombo Antunes, A.R., De Prijck, S., Vandamme, N., De Schepper, S., Van Isterdael, G., Scott, C.L., et al. (2019). A single-cell atlas of mouse brain macrophages reveals unique transcriptional identities shaped by ontogeny and tissue environment. *Nat. Neurosci.* 22, 1021–1035.
- Hoving, L.R., Heijink, M., van Harmelen, V., van Dijk, K.W., and Giera, M. (2018a). GC-MS analysis of short-chain fatty acids in feces, cecum content, and blood samples. In *Methods in Molecular Biology*, (Humana Press Inc.), pp. 247–256.
- Hoving, L.R., Heijink, M., van Harmelen, V., van Dijk, K.W., and Giera, M. (2018b). GC-MS analysis of medium- and long-chain fatty acids in blood samples. In *Methods in Molecular Biology*, (Humana Press Inc.), pp. 257–265.
- Hsu, T.M., and Kanoski, S.E. (2014). Blood-brain barrier disruption: mechanistic links between Western diet consumption and dementia. *Front. Aging Neurosci.* 6, 88.
- Hu, Y.W., Wang, Q., Ma, X., Li, X.X., Liu, X.H., Xiao, J., Liao, D.F., Xiang, J., and Tang, C.K. (2010). TGF- β 1 up-regulates expression of ABCA1, ABCG1 and SR-BI through liver X receptor α signaling pathway in THP-1 macrophage-derived foam cells. *J. Atheroscler. Thromb.* 17, 493–502.
- Hubler, M.J., and Kennedy, A.J. (2016). Role of lipids in the metabolism and activation of immune cells. *J. Nutr. Biochem.* 34, 1–7.
- Huitinga, I., van Rooijen, N., de Groot, C.J., Uitdehaag, B.M., and Dijkstra, C.D. (1990). Suppression of experimental allergic encephalomyelitis in Lewis rats after elimination of macrophages. *J. Exp. Med.* 172, 1025–1033.
- Huitinga, I., Damoiseaux, J.G., Döpp, E.A., and Dijkstra, C.D. (1993). Treatment with anti-CR3 antibodies ED7 and ED8 suppresses experimental allergic encephalomyelitis in Lewis rats. *Eur. J. Immunol.* 23, 709–715.
- Hyong, A., Jadhav, V., Lee, S., Tong, W., Rowe, J., Zhang, J.H., and Tang, J. (2008). Rosiglitazone, a PPAR gamma agonist, attenuates inflammation after surgical brain injury in rodents. *Brain Res.* 1215, 218–224.
- Ingersoll, M.A., Spanbroek, R., Lottaz, C., Gautier, E.L., Frankenberger, M., Hoffmann, R., Lang, R., Haniffa, M., Collin, M., Tacke, F., et al. (2010). Comparison of gene expression profiles between human and mouse monocyte subsets. *Blood* 115.
- Ishikawa, M., Maekawa, K., Saito, K., Senoo, Y., Urata, M., Murayama, M., Tajima, Y., Kumagai, Y., and Saito, Y. (2014). Plasma and serum lipidomics of healthy white adults shows characteristic profiles by subjects' gender and age. *PLoS One* 9.
- Issazadeh, S., Ljungdahl, A., Höjeberg, B., Mustafa, M., and Olsson, T. (1995). Cytokine production in the central nervous system of Lewis rats with experimental autoimmune encephalomyelitis: dynamics of mRNA expression for interleukin-10, interleukin-12, cytolysin, tumor necrosis factor alpha and tumor necrosis factor beta. *J. Neuroimmunol.* 61, 205–212.
- Ito, A., Hong, C., Rong, X., Zhu, X., Tarling, E.J., Hedde, P.N., Gratton, E., Parks, J., and Tontonoz, P. (2015). LXRs link metabolism to inflammation through Abca1-dependent regulation of membrane composition and TLR signaling. *Elife* 4, 1–23.
- Jäkel, S., Agirre, E., Mendanha Falcão, A., van Bruggen, D., Lee, K.W., Knuesel, I., Malhotra, D., French-Constant, C., Williams, A., and Castelo-Branco, G. (2019). Altered human oligodendrocyte heterogeneity in multiple sclerosis. *Nature* 566, 543–547.
- Janowski, B.A., Willy, P.J., Devi, T.R., Falck, J.R., and Mangelsdorf, D.J. (1996). An oxysterol signalling pathway

References

- mediated by the nuclear receptor LXR alpha. *Nature* *383*, 728–731.
- Jeffery, N.D., and Blakemore, A.F. (1995). Remyelination of mouse spinal cord axons demyelinated by local injection of lysolecithin. *Journal of Neurocytology* *24*, 775–781.
- Jeon, T. II, and Osborne, T.F. (2012). SREBPs: Metabolic integrators in physiology and metabolism. *Trends Endocrinol. Metab.* *23*, 65–72.
- Jiang, Z., Jiang, J.X., and Zhang, G.-X. (2014). Macrophages: a double-edged sword in experimental autoimmune encephalomyelitis. *Immunol. Lett.* *160*, 17–22.
- Jordão, M.J.C., Sankowski, R., Brendecke, S.M., Sagar, Locatelli, G., Tai, Y.H., Tay, T.L., Schramm, E., Armbruster, S., Hagemeyer, N., et al. (2019). Neuroimmunology: Single-cell profiling identifies myeloid cell subsets with distinct fates during neuroinflammation. *Science* (80-.). *363*.
- Joseph, S.B., Castrillo, A., Laffitte, B.A., Mangelsdorf, D.J., and Tontonoz, P. (2003). Reciprocal regulation of inflammation and lipid metabolism by liver X receptors. *Nat. Med.* *9*, 213–219.
- Kainu, T., Kononen, J., Enmark, E., Gustafsson, J.A., and Pelto-Huikko, M. (1996). Localization and ontogeny of the orphan receptor OR-1 in the rat brain. *J. Mol. Neurosci.* *7*, 29–39.
- Kálin, S., Heppner, F.L., Bechmann, I., Prinz, M., Tschöp, M.H., and Yi, C.-X. (2015). Hypothalamic innate immune reaction in obesity. *Nat. Rev. Endocrinol.* *11*, 339–351.
- Kaminska, B., Mota, M., and Pizzi, M. (2016). Signal transduction and epigenetic mechanisms in the control of microglia activation during neuroinflammation. *Biochim. Biophys. Acta - Mol. Basis Dis.* *1862*, 339–351.
- Kanoski, S.E., and Davidson, T.L. (2011). Western diet consumption and cognitive impairment: Links to hippocampal dysfunction and obesity. *Physiol. Behav.* *103*, 59–68.
- Karlsson, H.K., Tuulari, J.J., Hirvonen, J., Lepomäki, V., Parkkola, R., Hiltunen, J., Hannukainen, J.C., Soinio, M., Pham, T., Salminen, P., et al. (2013). Obesity is associated with white matter atrophy: A combined diffusion tensor imaging and voxel-based morphometric study. *Obesity* *21*, 2530–2537.
- Katz, S.S., Shipley, G.G., and Small, D.M. (1976). Physical chemistry of the lipids of human atherosclerotic lesions. Demonstration of a lesion intermediate between fatty streaks and advanced plaques. *J. Clin. Invest.* *58*, 200–211.
- Keren-Shaul, H., Spinrad, A., Weiner, A., Matcovitch-Natan, O., Dvir-Szternfeld, R., Ulland, T.K., David, E., Baruch, K., Lara-Astaiso, D., Toth, B., et al. (2017). A Unique Microglia Type Associated with Restricting Development of Alzheimer's Disease. *Cell* *169*, 1276–1290.e17.
- Kettenmann, H., Hanisch, U.-K., Noda, M., and Verkhratsky, A. (2011). Physiology of microglia. *Physiol. Rev.* *91*, 461–553.
- Kidani, Y., and Bensinger, S.J. (2012). Liver X receptor and peroxisome proliferator-activated receptor as integrators of lipid homeostasis and immunity. *Immunol Rev* *249*, 72–83.
- Kierdorf, K., and Prinz, M. (2013). Factors regulating microglia activation. *Front. Cell. Neurosci.* *7*, 44.
- Kierdorf, K., Erny, D., Goldmann, T., Sander, V., Schulz, C., Perdiguero, E.G., Wieghofer, P., Heinrich, A., Riemke, P., Hölscher, C., et al. (2013). Microglia emerge from erythromyeloid precursors via Pu.1- and Irf8-dependent pathways. *Nat. Neurosci.* *16*, 273–280.
- Kigerl, K.A., Gensel, J.C., Ankeny, D.P., Alexander, J.K., Donnelly, D.J., and Popovich, P.G. (2009). Identification of two distinct macrophage subsets with divergent effects causing either neurotoxicity or regeneration in the injured mouse spinal cord. *J. Neurosci.* *29*, 13435–13444.
- Kim, E., and Cho, S. (2016). Microglia and Monocyte-Derived Macrophages in Stroke. *Neurotherapeutics* *13*, 702–718.
- Kim, J. V., Kang, S.S., Dustin, M.L., and McGavern, D.B. (2009). Myelomonocytic cell recruitment causes fatal CNS vascular injury during acute viral meningitis. *Nature* *457*, 191–195.
- Kim, J.D., Yoon, N.A., Jin, S., and Diano, S. (2019). Microglial UCP2 Mediates Inflammation and Obesity Induced by High-Fat Feeding. *Cell Metab.*
- Kintscher, U., Wakino, S., Bruemmer, D., Goetze, S., Graf, K., Hsueh, W.A., and Law, R.E. (2002). TGF- β 1 induces peroxisome proliferator-activated receptor γ 1 and γ 2 expression in human THP-1 monocytes. *Biochem. Biophys. Res. Commun.* *297*, 794–799.
- Kleinberger, G., Yamanishi, Y., Suárez-Calvet, M., Czirr, E., Lohmann, E., Cuyvers, E., Struyfs, H., Pettkus, N., Weninger-Weinzierl, A., Mazaheri, F., et al. (2014). TREM2 mutations implicated in neurodegeneration impair cell surface transport and phagocytosis. *Sci. Transl. Med.* *6*, 243ra86.
- Klineova, S., and Lublin, F.D. (2018). Clinical course of multiple sclerosis. *Cold Spring Harb. Perspect. Med.* *8*.
- Kotroneo, A., Velagapudi, V.R., Yetukuri, L., Westerbacka, J., Bergholm, R., Ekroos, K., Makkonen, J., Taskinen, M.R., Orešič, M., and Yki-Järvinen, H. (2009). Serum saturated fatty acids containing triacylglycerols are better markers of insulin resistance than total serum triacylglycerol concentrations. *Diabetologia* *52*, 684–690.
- Kotter, M.R. (2006). Myelin Impairs CNS Remyelination by Inhibiting Oligodendrocyte Precursor Cell Differentiation. *J. Neurosci.* *26*, 328–332.
- Kotter, M.R., Setzu, A., Sim, F.J., Van Rooijen, N., and Franklin, R.J.M. (2001). Macrophage depletion impairs oligodendrocyte remyelination following lysolecithin-induced demyelination. *Glia* *35*, 204–212.
- Krasemann, S., Madore, C., Cialic, R., Baufeld, C., Calcagno, N., El Fatimy, R., Beckers, L., O'Loughlin, E., Xu, Y., Fanek, Z., et al. (2017). The TREM2-APOE Pathway Drives the Transcriptional Phenotype of Dysfunctional Microglia in Neurodegenerative Diseases. *Immunity* *47*, 566–581.e9.
- Kuruwilla, A.P., Shah, R., Hochwald, G.M., Liggitt, H.D., Palladino, M.A., and Thorbecke, G.J. (1991). Protective effect of transforming growth factor β 1 on experimental autoimmune diseases in mice. *Proc. Natl. Acad. Sci. U. S. A.* *88*, 2918–2921.
- Van Der Laan, L.J.W., Ruuls, S.R., Weber, K.S., Lodder, I.J., Döpp, E.A., and Dijkstra, C.D. (1996). Macrophage phagocytosis of myelin in vitro determined by flow cytometry: Phagocytosis is mediated by CR3 and induces production of tumor necrosis factor- α and nitric oxide. *J. Neuroimmunol.* *70*, 145–152.
- Lampron, A., Larochelle, A., Laflamme, N., Préfontaine, P., Plante, M.-M., Sánchez, M.G., Yong, V.W., Stys, P.K., Tremblay, M.-E., and Rivest, S. (2015). Inefficient clearance of myelin debris by microglia impairs remyelinating processes. *J. Exp. Med.* *212*, 481–495.
- Langer-Gould, A., Brara, S.M., Beaber, B.E., and Koebnick, C. (2013). Childhood obesity and risk of pediatric multiple sclerosis and clinically isolated syndrome. *Neurology* *80*, 548–552.
- Langley, M.R., Yoon, H., Kim, H.N., Choi, C. II, Simon, W., Kleppe, L., Lanza, I.R., LeBrasseur, N.K., Matveyenko, A., and Scarisbrick, I.A. (2020). High fat diet consumption results in mitochondrial dysfunction, oxidative stress, and

References

- oligodendrocyte loss in the central nervous system. *Biochim. Biophys. Acta - Mol. Basis Dis.* *1866*, 165630.
- Lasselain, J., Magne, E., Beau, C., Aubert, A., Dexpert, S., Carrez, J., Layé, S., Forestier, D., Ledaguenel, P., and Capuron, L. (2016). Low-grade inflammation is a major contributor of impaired attentional set shifting in obese subjects. *Brain. Behav. Immun.* *58*, 63–68.
- Lavin, Y., Winter, D., Blecher-Gonen, R., David, E., Keren-Shaul, H., Merad, M., Jung, S., and Amit, I. (2014). Tissue-resident macrophage enhancer landscapes are shaped by the local microenvironment. *Cell* *159*.
- Lee, S.D., and Tontonoz, P. (2015). Liver X receptors at the intersection of lipid metabolism and atherogenesis. *Atherosclerosis* *242*, 29–36.
- Lee, C.H., Kim, H.D., Shin, S.M., and Kim, S.G. (2008). A Novel Mechanism of PPAR γ Regulation of TGF β 1: Implication in Cancer Biology. *PPAR Res.* *2008*.
- Lee, C.H., Shin, S.H., Kang, G.M., Kim, S., Kim, J., Yu, R., and Kim, M.S. (2019). Cellular source of hypothalamic macrophage accumulation in diet-induced obesity. *J. Neuroinflammation* *16*, 221.
- Lee, S., Varvel, N.H., Konerth, M.E., Xu, G., Cardona, A.E., Ransohoff, R.M., and Lamb, B.T. (2010). CX3CR1 deficiency alters microglial activation and reduces beta-amyloid deposition in two Alzheimer's disease mouse models. *Am. J. Pathol.* *177*, 2549–2562.
- Lehmann, J.M., Kliewer, S. a, Moore, L.B., Smith-Oliver, T. a, Oliver, B.B., Su, J.L., Sundseth, S.S., Winegar, D. a, Blanchard, D.E., Spencer, T. a, et al. (1997). Activation of the nuclear receptor LXR by oxysterols defines a new hormone response pathway. *J. Biol. Chem.* *272*, 3137–3140.
- Lí, Q., and Barres, B.A. (2018). Microglia and macrophages in brain homeostasis and disease. *Nat. Rev. Immunol.* *18*.
- Lí, F., Jiang, C., Larsen, M.C., Bushkofsky, J., Krausz, K.W., Wang, T., Jefcoate, C.R., and Gonzalez, F.J. (2014). Lipidomics Reveals a Link between CYP11B1 and SCD1 in Promoting Obesity. *J. Proteome Res.* *13*, 2679–2687.
- Lí, Q., Cheng, Z., Zhou, L., Darmanis, S., Neff, N.F., Okamoto, J., Gulati, G., Bennett, M.L., Sun, L.O., Clarke, L.E., et al. (2019). Developmental Heterogeneity of Microglia and Brain Myeloid Cells Revealed by Deep Single-Cell RNA Sequencing. *Neuron* *101*, 207–223.e10.
- Lí, W.-W., Setzu, A., Zhao, C., and Franklin, R.J.M. (2005). Minocycline-mediated inhibition of microglia activation impairs oligodendrocyte progenitor cell responses and remyelination in a non-immune model of demyelination. *J. Neuroimmunol.* *158*, 58–66.
- Liddel, S.A., Guttenplan, K.A., Clarke, L.E., Bennett, F.C., Bohlen, C.J., Schirmer, L., Bennett, M.L., Münch, A.E., Chung, W.S., Peterson, T.C., et al. (2017). Neurotoxic reactive astrocytes are induced by activated microglia. *Nature* *541*.
- Liebisch, G., Binder, M., Schifferer, R., Langmann, T., Schulz, B., and Schmitz, G. (2006). High throughput quantification of cholesterol and cholesteryl ester by electrospray ionization tandem mass spectrometry (ESI-MS/MS). *Biochim. Biophys. Acta - Mol. Cell Biol. Lipids* *1761*, 121–128.
- Linnartz-Gerlach, B., Bodea, L.G., Klaus, C., Ginolhac, A., Halder, R., Sinkkonen, L., Walter, J., Colonna, M., and Neumann, H. (2019). TREM2 triggers microglial density and age-related neuronal loss. *Glia* *67*, 539–550.
- Liu, Y., Hao, W., Letiembre, M., Walter, S., Kulanga, M., Neumann, H., and Fassbender, K. (2006). Suppression of microglial inflammatory activity by myelin phagocytosis: role of p47-PHOX-mediated generation of reactive oxygen species. *J. Neurosci.* *26*, 12904–12913.
- Liu, Y., Colby, J.K., Zuo, X., Jaoude, J., Wei, D., and Shureiqi, I. (2018). The Role of PPAR- δ in Metabolism, Inflammation, and Cancer: Many Characters of a Critical Transcription Factor. *Int. J. Mol. Sci.* *19*, 3339.
- Liu, Z.W., Faraguna, U., Cirelli, C., Tononi, G., and Gao, X.B. (2010). Direct evidence for wake-related increases and sleep-related decreases in synaptic strength in rodent cortex. *J. Neurosci.* *30*, 8671–8675.
- Lloyd, A.F., and Miron, V.E. (2016). Cellular and Molecular Mechanisms Underpinning Macrophage Activation during Remyelination. *Front. Cell Dev. Biol.* *4*, 60.
- Lloyd, A.F., and Miron, V.E. (2019). The pro-remyelination properties of microglia in the central nervous system. *Nat. Rev. Neurol.* *15*, 447–458.
- Lloyd, A.F., Davies, C.L., Holloway, R.K., Labrak, Y., Ireland, G., Carradori, D., Dillenburger, A., Borger, E., Soong, D., Richardson, J.C., et al. (2019). Central nervous system regeneration is driven by microglia necroptosis and repopulation. *Nat. Neurosci.* *22*.
- Locatelli, G., Theodorou, D., Kendirli, A., Jordão, M.J.C., Staszewski, O., Phulphagar, K., Cantuti-Castelvetri, L., Dagkalis, A., Bessis, A., Simons, M., et al. (2018). Mononuclear phagocytes locally specify and adapt their phenotype in a multiple sclerosis model. *Nat. Neurosci.* *21*, 1196–1208.
- London, A., Cohen, M., and Schwartz, M. (2013). Microglia and monocyte-derived macrophages: Functionally distinct populations that act in concert in CNS plasticity and repair. *Front. Cell. Neurosci.* *7*, 34.
- Lu, W., Bhasin, M., and Tsirka, S.E. (2002). Involvement of tissue plasminogen activator in onset and effector phases of experimental allergic encephalomyelitis. *J. Neurosci.* *22*, 10781–10789.
- Lublin, F.D., Reingold, S.C., Cohen, J.A., Cutter, G.R., Sorensen, P.S., Thompson, A.J., Wolinsky, J.S., Balcer, L.J., Banwell, B., Barkhof, F., et al. (2014). Defining the clinical course of multiple sclerosis: The 2013 revisions. *Neurology* *83*.
- Lund, H., Pieber, M., Parsa, R., Grommisch, D., Ewing, E., Kular, L., Han, J., Zhu, K., Nijssen, J., Hedlund, E., et al. (2018). Fatal demyelinating disease is induced by monocyte-derived macrophages in the absence of TGF- β signaling. *Nat. Immunol.* *19*, 435–441.
- Luo, X.-G., Ding, J.-Q., and Chen, S.-D. (2010). Microglia in the aging brain: relevance to neurodegeneration. *Mol. Neurodegener.* *5*, 12.
- Ma, W., Silverman, S.M., Zhao, L., Villamil, R., Campos, M.M., Amaral, J., and Wong, W.T. (2019). Absence of TGF β signaling in retinal microglia induces retinal degeneration and exacerbates choroidal neovascularization. *Elife* *8*.
- Mancino, A., Termanini, A., Barozzi, I., Ghisletti, S., Ostuni, R., Prosperini, E., Ozato, K., and Natoli, G. (2015). A dual cis-regulatory code links IRF8 to constitutive and inducible gene expression in macrophages. *Genes Dev.* *29*, 394–408.
- Manzel, A., Müller, D.N., Hafler, D.A., Erdman, S.E., Linker, R.A., and Kleiweietfeld, M. (2014). Role of “western diet” in inflammatory autoimmune diseases. *Curr. Allergy Asthma Rep.* *14*, 1–8.
- Marín-Teva, J.L., Cuadros, M. a, Martín-Oliva, D., and Navascués, J. (2011). Microglia and neuronal cell death. *Neuron Glia Biol.* *7*, 25–40.
- Mass, E., Ballesteros, I., Farlik, M., Halbritter, F., Günther, P., Crozet, L., Jacome-Galarza, C.E., Händler, K., Klughammer, J., Kobayashi, Y., et al. (2016). Specification of tissue-resident

- macrophages during organogenesis. *Science* (80-.). 353.
- Masuda, T., Sankowski, R., Staszewski, O., Böttcher, C., Amann, L., Sagar, Scheiwe, C., Nessler, S., Kunz, P., van Loo, G., et al. (2019). Spatial and temporal heterogeneity of mouse and human microglia at single-cell resolution. *Nature* 566, 388–392.
- Matarese, G., Carrieri, P.B., Montella, S., De Rosa, V., and La Cava, A. (2010). Leptin as a metabolic link to multiple sclerosis. *Nat. Rev. Neurol.* 6, 455–461.
- Matcovitch-Natan, O., Winter, D.R., Giladi, A., Aguilar, S.V., Spinrad, A., Sarrazin, S., Ben-Yehuda, H., David, E., González, F.Z., Perrin, P., et al. (2016). Microglia development follows a stepwise program to regulate brain homeostasis. *Science* (80-.). 353.
- Maxfield, F.R. (2014). Role of endosomes and lysosomes in human disease. *Cold Spring Harb. Perspect. Biol.* 6, a016931.
- Mejia, R.O.S., Ona, V.O., Li, M., and Friedlander, R.M. (2001). Minocycline Reduces Traumatic Brain Injury-mediated Caspase-1 Activation, Tissue Damage, and Neurological Dysfunction. *Neurosurgery* 48, 1393–1401.
- Miao, H., Chen, H., Pei, S., Bai, X., Vaziri, N.D., and Zhao, Y.Y. (2015). Plasma lipidomics reveal profound perturbation of glycerophospholipids, fatty acids, and sphingolipids in diet-induced hyperlipidemia. *Chem. Biol. Interact.* 228, 79–87.
- Milanski, M., Arruda, A.P., Coope, A., Ignacio-Souza, L.M., Nunez, C.E., Roman, E.A., Romanatto, T., Pascoal, L.B., Caricilli, A.M., Torsoni, M.A., et al. (2012). Inhibition of hypothalamic inflammation reverses diet-induced insulin resistance in the liver. *Diabetes* 61, 1455–1462.
- Miller, A.A., and Spencer, S.J. (2014). Obesity and neuroinflammation: A pathway to cognitive impairment. *Brain Behav. Immun.* 42, 10–21.
- Mingui, F., Jifeng, Z., Yimin, L., Xiaojun, Z., Luning, Z., Mushtaq, A., and Markus, U EHRENGRUBER Yuqing E, C. (2003). Early stimulation and late inhibition of peroxisome proliferator-activated receptor γ (PPAR γ) gene expression by transforming growth factor β in human aortic smooth muscle cells: role of early growth-response factor-1 (Egr-1), activator protein 1 (AP1) a.
- Miron, V.E., Boyd, A., Zhao, J.-W., Yuen, T.J., Ruckh, J.M., Shadrach, J.L., van Wijngaarden, P., Wagers, A.J., Williams, A., Franklin, R.J.M., et al. (2013). M2 microglia and macrophages drive oligodendrocyte differentiation during CNS remyelination. *Nat. Neurosci.* 16, 1211–1218.
- Mokry, L.E., Ross, S., Ahmad, O.S., Forgetta, V., Smith, G.D., Leong, A., Greenwood, C.M.T., Thanassoulis, G., and Richards, J.B. (2015). Vitamin D and Risk of Multiple Sclerosis: A Mendelian Randomization Study. *PLoS Med.* 12, e1001866.
- Molteni, V., Li, X., Nabakka, J., Liang, F., Wityak, J., Koder, A., Vargas, L., Romeo, R., Mitro, N., Mak, P.A., et al. (2007). N-Acylthiadiazolines, a New Class of Liver X Receptor Agonists with Selectivity for LXR β . *J. Med. Chem.* 50, 4255–4259.
- de Monasterio-Schrader, P., Jahn, O., Tenzer, S., Wichert, S.P., Patzig, J., and Werner, H.B. (2012). Systematic approaches to central nervous system myelin. *Cell. Mol. Life Sci.* 69, 2879–2894.
- Moore, K.J., and Tabas, I. (2011). Macrophages in the Pathogenesis of Atherosclerosis. *Cell* 145, 341–355.
- Morrison, J.H., and Baxter, M.G. (2012). The ageing cortical synapse: Hallmarks and implications for cognitive decline. *Nat. Rev. Neurosci.* 13, 240–250.
- Mosher, K.I., and Wyss-Coray, T. (2015). Go with your gut: Microbiota meet microglia. *Nat. Neurosci.* 18, 930–931.
- Mosser, D.M., and Edwards, J.P. (2008). Exploring the full spectrum of macrophage activation. *Nat. Rev. Immunol.* 8, 958–969.
- Mount, C.W., and Monje, M. (2017). Wrapped to Adapt Experience-Dependent Myelination. *Neuron* 95.
- Moutinho, M., Nunes, M.J., Gomes, A.Q., Gama, M.J., Cedazo-Minguez, A., Rodrigues, C.M.P., Björkhem, I., and Rodrigues, E. (2015). Cholesterol 24S-Hydroxylase Overexpression Inhibits the Liver X Receptor (LXR) Pathway by Activating Small Guanosine Triphosphate-Binding Proteins (sGTPases) in Neuronal Cells. *Mol. Neurobiol.* 51, 1489–1503.
- Mrdjen, D., Pavlovic, A., Hartmann, F.J., Schreiner, B., Utz, S.G., Leung, B.P., Lelios, I., Heppner, F.L., Kipnis, J., Merkler, D., et al. (2018). High-Dimensional Single-Cell Mapping of Central Nervous System Immune Cells Reveals Distinct Myeloid Subsets in Health, Aging, and Disease. *Immunity* 48, 380-395.e6.
- Munger, K.L., Chitnis, T., and Ascherio, A. (2009). Body size and risk of MS in two cohorts of US women. *Neurology* 73, 1543–1550.
- Murray, P.J., and Wynn, T.A. (2011). Protective and pathogenic functions of macrophage subsets. *Nat. Rev. Immunol.* 11, 723–737.
- Muse, E.D., Yu, S., Edillor, C.R., Tao, J., Spann, N.J., Troutman, T.D., Seidman, J.S., Henke, A., Roland, J.T., Ozeki, K.A., et al. (2018). Cell-specific discrimination of desmosterol and desmosterol mimetics confers selective regulation of LXR and SREBP in macrophages. *Proc. Natl. Acad. Sci. U. S. A.* 115, E4680–E4689.
- Naderali, E.K., Ratcliffe, S.H., and Dale, M.C. (2009). Obesity and Alzheimer's disease: a link between body weight and cognitive function in old age. *Am. J. Alzheimers. Dis. Other Dement.* 24, 445–449.
- Nahrendorf, M., Swirski, F.K., Aikawa, E., Stangenberg, L., Wurdinger, T., Figueiredo, J.L., Libby, P., Weissleder, R., and Pittet, M.J. (2007). The healing myocardium sequentially mobilizes two monocyte subsets with divergent and complementary functions. *J. Exp. Med.* 204, 3037–3047.
- Natrajan, M.S., Fuente, A.G. De, Crawford, A.H., Linehan, E., Johnson, K.R., Wu, T., Fitzgerald, D.C., and Ricote, M. (2015). Retinoid X receptor activation reverses age-related deficiencies in myelin debris phagocytosis and remyelination. 1–17.
- Nave, K.A. (2010). Myelination and the trophic support of long axons. *Nat. Rev. Neurosci.* 11, 275–283.
- Neher, J.J., and Cunningham, C. (2019). Priming Microglia for Innate Immune Memory in the Brain. *Trends Immunol.* 40.
- Nelissen, K., Mulder, M., Smets, I., Timmermans, S., Smeets, K., Ameloot, M., and Hendriks, J.J. a (2012). Liver X receptors regulate cholesterol homeostasis in oligodendrocytes. *J. Neurosci. Res.* 90, 60–71.
- Neumann, B., Baror, R., Zhao, C., Segel, M., Dietmann, S., Rawji, K.S., Foerster, S., McClain, C.R., Chalut, K., van Wijngaarden, P., et al. (2019). Metformin Restores CNS Remyelination Capacity by Rejuvenating Aged Stem Cells. *Cell Stem Cell* 25, 473-485.e8.
- Nicoletti, F., Di Marco, R., Patti, F., Reggio, E., Nicoletti, A., Zaccone, P., Stivala, F., Meroni, P.L., and Reggio, A. (1998). Blood levels of transforming growth factor-beta 1 (TGF- β 1) are elevated in both relapsing remitting and chronic progressive multiple sclerosis (MS) patients and are further augmented by treatment with interferon-beta 1b (IFN- β 1b). *Clin. Exp. Immunol.* 113, 96–99.
- Nikić, I., Merkler, D., Sorbara, C., Brinkoetter, M., Kreutzfeldt, M., Bareyre, F.M., Brück, W., Bishop, D., Misgeld, T., and

References

- Kerschensteiner, M. (2011). A reversible form of axon damage in experimental autoimmune encephalomyelitis and multiple sclerosis. *Nat. Med.* *17*, 495–499.
- Nimmerjahn, A., Kirchhoff, F., and Helmchen, F. (2005). Resting microglial cells are highly dynamic surveillants of brain parenchyma in vivo. *Science* *308*, 1314–1318.
- Nonaka, G., and Kishimoto, Y. (1979). Levels of cerebroside, sulfatides, and galactosyl diglycerides in different regions of rat brain. Change during maturation and distribution in subcellular fractions of gray and white matter of sheep brain. *Biochim. Biophys. Acta* *572*, 432–441.
- Norris, G.T., and Kipnis, J. (2019). Immune cells and CNS physiology: Microglia and beyond. *J. Exp. Med.* *216*.
- Norton, W.T., and Poduslo, S.E. (1973). Myelination in rat brain: changes in myelin composition during brain maturation. *J. Neurochem.* *21*, 759–773.
- Nugent, A.A., Lin, K., van Lengerich, B., Lianoglou, S., Przybyla, L., Davis, S.S., Llapashtica, C., Wang, J., Kim, D.J., Xia, D., et al. (2020). TREM2 Regulates Microglial Cholesterol Metabolism upon Chronic Phagocytic Challenge. *Neuron* *105*.
- Orre, M., Kamphuis, W., Osborn, L.M., Melief, J., Kooijman, L., Huitinga, I., Klooster, J., Bossers, K., and Hol, E.M. (2014). Acute isolation and transcriptome characterization of cortical astrocytes and microglia from young and aged mice. *Neurobiol. Aging* *35*, 1–14.
- Pakiet, A., Jakubiak, A., Czumaj, A., Sledzinski, T., and Mika, A. (2019). The effect of western diet on mice brain lipid composition. *Nutr. Metab.* *16*, 81.
- Panatier, A., and Robitaille, R. (2012). The soothing touch: microglial contact influences neuronal excitability. *Dev. Cell* *23*, 1125–1126.
- Park, J., Wang, Q., Wu, Q., Mao-Draayer, Y., and Kim, C.H. (2019). Bidirectional regulatory potentials of short-chain fatty acids and their G-protein-coupled receptors in autoimmune neuroinflammation. *Sci. Rep.* *9*, 8837.
- Patani, R., Balaratnam, M., Vora, A., and Reynolds, R. (2007). Remyelination can be extensive in multiple sclerosis despite a long disease course. *Neuropathol. Appl. Neurobiol.* *33*, 277–287.
- Patrikios, P., Stadelmann, C., Kutzelnigg, A., Rauschka, H., Schmidbauer, M., Laursen, H., Soelberg Sorensen, P., Brück, W., Lucchinetti, C., Lassmann, H., et al. (2006). Remyelination is extensive in a subset of multiple sclerosis patients. *Brain* *129*, 3165–3172.
- Perez, F., and Granger, B.E. (2007). IPython: A System for Interactive Scientific Computing. *Comput. Sci. Eng.* *9*, 21–29.
- Pfeiffer, S.E., Warrington, A.E., and Bansal, R. (1993). The oligodendrocyte and its many cellular processes. *Trends Cell Biol.* *3*, 191–197.
- Phillips, M.C. (2014). Molecular mechanisms of cellular cholesterol efflux. *J. Biol. Chem.* *289*, 24020–24029.
- Piccio, L., Stark, J.L., and Cross, A.H. (2008). Chronic calorie restriction attenuates experimental autoimmune encephalomyelitis. *J. Leukoc. Biol.* *84*, 940–948.
- Pietiläinen, K.H., Sysi-Aho, M., Rissanen, A., Seppänen-Laakso, T., Yki-Järvinen, H., Kaprio, J., and Orešič, M. (2007). Acquired obesity is associated with changes in the serum lipidomic profile independent of genetic effects - A monozygotic twin study. *PLoS One* *2*.
- Plemel, J.R., Michaels, N.J., Weishaupt, N., Caprariello, A. V., Kcough, M.B., Rogers, J.A., Yukseloglu, A., Lim, J., Patel, V. V., Rawji, K.S., et al. (2018). Mechanisms of lysophosphatidylcholine-induced demyelination: A primary lipid disrupting myelinopathy. *Glia* *66*.
- Plemel, J.R., Stratton, J.A., Michaels, N.J., Rawji, K.S., Zhang, E., Sinha, S., Baaklini, C.S., Dong, Y., Ho, M., Thorburn, K., et al. (2020). Microglia response following acute demyelination is heterogeneous and limits infiltrating macrophage dispersion. *Sci. Adv.* *6*, eaay6324.
- Poliani, P.L., Wang, Y., Fontana, E., Robinette, M.L., Yamanishi, Y., Gilfillan, S., and Colonna, M. (2015). TREM2 sustains microglial expansion during aging and response to demyelination. *J. Clin. Invest.* *125*, 2161–2170.
- Ponomarev, E.D., Shriver, L.P., Maresz, K., and Dittel, B.N. (2005). Microglial cell activation and proliferation precedes the onset of CNS autoimmunity. *J. Neurosci. Res.* *81*, 374–389.
- Prinz, M. (2014). Microglia and monocytes: molecularly defined. *Acta Neuropathol.* *128*, 317–318.
- Prinz, M., and Priller, J. (2014). Microglia and brain macrophages in the molecular age: from origin to neuropsychiatric disease. *Nat. Rev. Neurosci.* *15*, 300–312.
- Prinz, M., and Priller, J. (2017). The role of peripheral immune cells in the CNS in steady state and disease. *Nat. Neurosci.* *20*.
- Prinz, M., Erny, D., and Hagemeyer, N. (2017). Ontogeny and homeostasis of CNS myeloid cells. *Nat. Immunol.* *18*.
- Prinz, M., Jung, S., and Priller, J. (2019). Microglia Biology: One Century of Evolving Concepts. *Cell* *179*, 292–311.
- Procaccini, C., Pucino, V., De Rosa, V.D., Marone, G., and Matarese, G. (2014). Neuro-endocrine networks controlling immune system in health and disease. *Front. Immunol.* *5*.
- Qin, Y., Garrison, B.S., Ma, W., Wang, R., Jiang, A., Li, J., Mistry, M., Bronson, R.T., Santoro, D., Franco, C., et al. (2018). A Milieu Molecule for TGF- β Required for Microglia Function in the Nervous System. *Cell* *174*.
- Quehenberger, O., and Dennis, E.A. (2011). The human plasma lipidome. *N. Engl. J. Med.* *365*, 1812–1823.
- Raj, D., Yin, Z., Breur, M., Doorduyn, J., Holtman, I.R., Olah, M., Mantingh-Otter, I.J., Van Dam, D., De Deyn, P.P., den Dunnen, W., et al. (2017). Increased white matter inflammation in aging- and alzheimer's disease brain. *Front. Mol. Neurosci.* *10*, 206–206.
- Raji, C.A., Ho, A.J., Parikshak, N.N., Becker, J.T., Lopez, O.L., Kuller, L.H., Hua, X., Leow, A.D., Toga, A.W., and Thompson, P.M. (2010). Brain structure and obesity. *Hum. Brain Mapp.* *31*, 353–364.
- Ransohoff, R.M., Hafler, D.A., and Lucchinetti, C.F. (2015). Multiple sclerosis—a quiet revolution. *Nat. Rev. Neurol.* *11*, 134–142.
- Ravichandran, K.S. (2010). Find-me and eat-me signals in apoptotic cell clearance: progress and conundrums. *J. Exp. Med.* *207*, 1807–1817.
- Rawji, K.S., and Yong, V.W. (2013). The benefits and detriments of macrophages/microglia in models of multiple sclerosis. *Clin. Dev. Immunol.* *2013*, 948976.
- Rawji, K.S., Mishra, M.K., Michaels, N.J., Rivest, S., Stys, P.K., and Yong, V.W. (2016). Immunosenescence of microglia and macrophages: Impact on the ageing central nervous system. *Brain*.
- Rigamonti, E., Helin, L., Lestavel, S., Mutka, A.L., Lepore, M., Fontaine, C., Bouhelle, M.A., Bultel, S., Fruchart, J.C., Ikonen, E., et al. (2005). Liver X receptor activation controls intracellular cholesterol trafficking and esterification in human macrophages. *Circ. Res.* *97*, 682–689.

References

- Robertson, I.B., and Rifkin, D.B. (2016). Regulation of the bioavailability of TGF- β and TGF- β -related proteins. *Cold Spring Harb. Perspect. Biol.* *8*.
- van Rossum, D., Hilbert, S., Strassenburg, S., Hanisch, U.-K., and Brück, W. (2008). Myelin-phagocytosing macrophages in isolated sciatic and optic nerves reveal a unique reactive phenotype. *Glia* *56*, 271–283.
- Rószter, T., Menéndez-Gutiérrez, M.P., Cedenilla, M., and Ricote, M. (2013). Retinoid X receptors in macrophage biology. *Trends Endocrinol. Metab.* *24*, 460–468.
- Ruckh, J.M., Zhao, J.W., Shadrach, J.L., Van Wijngaarden, P., Rao, T.N., Wagers, A.J., and Franklin, R.J.M. (2012). Rejuvenation of regeneration in the aging central nervous system. *Cell Stem Cell* *10*, 96–103.
- Sadler, R., Cramer, J. V., Heindl, S., Kostidis, S., Betz, D., Zuurbier, K.R., Northoff, B.H., Heijink, M., Goldberg, M.P., Plautz, E.J., et al. (2020). Short-chain fatty acids improve poststroke recovery via immunological mechanisms. *J. Neurosci.* *40*, 1162–1173.
- Saederup, N., Cardona, A.E., Croft, K., Mizutani, M., Cotleur, A.C., Tsou, C.-L., Ransohoff, R.M., and Charo, I.F. (2010). Selective Chemokine Receptor Usage by Central Nervous System Myeloid Cells in CCR2-Red Fluorescent Protein Knock-In Mice. *PLoS One* *5*, e13693.
- Saeed, S., Quintin, J., Kerstens, H.H.D., Rao, N.A., Aghajani-fah, A., Matarese, F., Cheng, S.C., Ratter, J., Berentsem, K., Van Der Ent, M.A., et al. (2014). Epigenetic programming of monocyte-to-macrophage differentiation and trained innate immunity. *Science* (80-.). *345*.
- Safaiyan, S., Kannaiyan, N., Snaidero, N., Brioschi, S., Biber, K., Yona, S., Edinger, A.L., Jung, S., Rossner, M.J., and Simons, M. (2016). Age-related myelin degradation burdens the clearance function of microglia during aging. *Nat. Neurosci.* *19*, 995–998.
- Safaiyan, S., Besson-Girard, S., Schifferer, M., Kaya, T., Liu, L., Usifo, F., Ji, H., Kannaiyan, N., Rossner, M.F., Gokce, O., Simons, M. (2020). White matter aging drives microglial diversity. *Nature Neuroscience*, submitted.
- Saito, K., Ishikawa, M., Murayama, M., Urata, M., Senoo, Y., Toyoshima, K., Kumagai, Y., Maekawa, K., and Saito, Y. (2014). Effects of sex, age, and fasting conditions on plasma lipidomic profiles of fasted sprague-dawley rats. *PLoS One* *9*.
- Samad, F., Yamamoto, K., Pandey, M., and Loskutoff, D.J. (1997). Elevated expression of transforming growth factor- β in adipose tissue from obese mice. *Mol. Med.* *3*, 37–48.
- Sampaio, J.L., Gerl, M.J., Klose, C., Ejsing, C.S., Beug, H., Simons, K., and Shevchenko, A. (2011). Membrane lipidome of an epithelial cell line. *Proc. Natl. Acad. Sci. U. S. A.* *108*, 1903–1907.
- Sawcer, S., Hellenthal, G., Pirinen, M., Spencer, C.C.A., Patsopoulos, N.A., Moutsianas, L., Dilthey, A., Su, Z., Freeman, C., Hunt, S.E., et al. (2011). Genetic risk and a primary role for cell-mediated immune mechanisms in multiple sclerosis. *Nature* *476*, 214–219.
- Schachtrup, C., Ryu, J.K., Helmrick, M.J., Vagena, E., Galanakis, D.K., Degen, J.L., Margolis, R.U., and Akassoglou, K. (2010). Fibrinogen triggers astrocyte scar formation by promoting the availability of active TGF- β after vascular damage. *J. Neurosci.* *30*, 5843–5854.
- Schafer, D.P., Lehrman, E.K., and Stevens, B. (2013). The “quad-partite” synapse: Microglia-synapse interactions in the developing and mature CNS. *Glia* *61*, 24–36.
- Schindelin, J., Arganda-Carreras, I., Frise, E., Kaynig, V., Longair, M., Pietzsch, T., Preibisch, S., Rueden, C., Saalfeld, S., Schmid, B., et al. (2012). Fiji: an open-source platform for biological-image analysis. *Nat. Methods* *9*, 676–682.
- Schlepckow, K., Monroe, K.M., Kleinberger, G., Cantuti-Castelvetri, L., Parhizkar, S., Xia, D., Willem, M., Werner, G., Pettkus, N., Brunner, B., et al. (2020). Enhancing protective microglial activities with a dual function <sc>TREM</sc> 2 antibody to the stalk region. *EMBO Mol. Med.* e11227.
- Schmidt, S. V., Krebs, W., Ulas, T., Xue, J., Baßler, K., Günther, P., Hardt, A.-L., Schultze, H., Sander, J., Klee, K., et al. (2016). The transcriptional regulator network of human inflammatory macrophages is defined by open chromatin. *Cell Res.* *26*, 151–170.
- Schultz, J.R., Tu, H., Luk, A., Repa, J.J., Medina, J.C., Li, L., Schwendner, S., Wang, S., Thoolen, M., Mangelsdorf, D.J., et al. (2000). Role of LXRs in control of lipogenesis. *Genes Dev.* *14*, 2831–2838.
- Schulz, C., Perdiguero, E.G., Chorro, L., Szabo-Rogers, H., Cagnard, N., Kierdorf, K., Prinz, M., Wu, B., Jacobsen, S.E.W., Pollard, J.W., et al. (2012). A lineage of myeloid cells independent of myb and hematopoietic stem cells. *Science* (80-.). *335*, 86–90.
- Schur, E.A., Melhorn, S.J., Oh, S.K., Lacy, J.M., Berkseth, K.E., Guyenet, S.J., Sonnen, J.A., Tyagi, V., Rosalynn, M., De Leon, B., et al. (2015). Radiologic evidence that hypothalamic gliosis is associated with obesity and insulin resistance in humans. In *Obesity*, (Blackwell Publishing Inc.), pp. 2142–2148.
- Schwartz, M., Kipnis, J., Rivest, S., and Prat, A. (2013). How do immune cells support and shape the brain in health, disease, and aging? *J. Neurosci.* *33*, 17587–17596.
- Serhan, C.N. (2007). Resolution phase of inflammation: novel endogenous anti-inflammatory and proresolving lipid mediators and pathways. *Annu. Rev. Immunol.* *25*, 101–137.
- Setzu, A., Lathia, J.D., Zhao, C., Wells, K., Rao, M.S., Ffrench-Constant, C., and Franklin, R.J.M. (2006). Inflammation stimulates myelination by transplanted oligodendrocyte precursor cells. *Glia* *54*, 297–303.
- Seung, J.L., Eun, K.Y., and Sang, G.K. (2006). Peroxisome proliferator-activated receptor- γ and retinoic acid X receptor α represses the TGF β 1 gene via PTEN-mediated p70 ribosomal S6 kinase-1 inhibition: Role for Z β 9 dephosphorylation. *Mol. Pharmacol.* *70*, 415–425.
- Seystahl, K., Wick, W., and Weller, M. (2016). Therapeutic options in recurrent glioblastoma-An update. *Crit. Rev. Oncol. Hematol.* *99*, 389–408.
- Shackleford, G., Makoukji, J., Grenier, J., Liere, P., Meffre, D., and Massaad, C. (2013). Differential regulation of Wnt/beta-catenin signaling by Liver X Receptors in Schwann cells and oligodendrocytes. *Biochem. Pharmacol.* *86*, 106–114.
- Shechter, R., Miller, O., Yovel, G., Rosenzweig, N., London, A., Ruckh, J., Kim, K.W., Klein, E., Kalchenko, V., Bendel, P., et al. (2013). Recruitment of Beneficial M2 Macrophages to Injured Spinal Cord Is Orchestrated by Remote Brain Choroid Plexus. *Immunity* *38*, 555–569.
- Shen, S., Sandoval, J., Swiss, V. a, Li, J., Dupree, J., Franklin, R.J.M., and Casaccia-Bonnel, P. (2008). Age-dependent epigenetic control of differentiation inhibitors is critical for remyelination efficiency. *Nat. Neurosci.* *11*, 1024–1034.
- Shi, M., Zhu, J., Wang, R., Chen, X., Mi, L., Walz, T., and Springer, T.A. (2011). Latent TGF- β structure and activation. *Nature* *474*, 343–351.
- Shields, S. a, Gilson, J.M., Blakemore, W.F., and Franklin, R.J. (1999). Remyelination occurs as extensively but more slowly in old rats compared to young rats following gliotoxin-induced CNS demyelination. *Glia* *28*, 77–83.

References

- Siebert, E., Paul, F., Rothe, M., and Weylandt, K.H. (2017). The effect of omega-3 fatty acids on central nervous system remyelination in fat-1 mice. *BMC Neurosci.* *18*.
- Sierra, A., Gottfried-Blackmore, A.C., McEwen, B.S., and Bulloch, K. (2007). Microglia derived from aging mice exhibit an altered inflammatory profile. *Glia* *55*, 412–424.
- Sierra, A., Encinas, J.M., Deudero, J.J.P., Chancey, J.H., Enikolopov, G., Overstreet-Wadiche, L.S., Tsirka, S.E., and Miletic-Savatic, M. (2010). Microglia shape adult hippocampal neurogenesis through apoptosis-coupled phagocytosis. *Cell Stem Cell* *7*, 483–495.
- Sierra, A., Castro, F. De, Juan, R., and Ram, S. (2016). The “Big-Bang” for Modern Glial Biology: Translation and Comments on Pío del R. Horta 1919 Series of Papers on Microglia. *Glia* *1801*–1840.
- Silver, J., and Miller, J.H. (2004). Regeneration beyond the glial scar. *Nat. Rev. Neurosci.* *5*, 146–156.
- Sim, F.J., Zhao, C., Penderis, J., and Franklin, R.J.M. (2002). The age-related decrease in CNS remyelination efficiency is attributable to an impairment of both oligodendrocyte progenitor recruitment and differentiation. *J. Neurosci.* *22*, 2451–2459.
- Šišková, Z., and Tremblay, M.-È. (2013). Microglia and synapse: interactions in health and neurodegeneration. *Neural Plast.* *2013*, 425845.
- Smith, M.E. (2001). Phagocytic properties of microglia in vitro: Implications for a role in multiple sclerosis and EAE. *Microsc. Res. Tech.* *54*, 81–94.
- Song, W.M., and Colonna, M. (2018). The identity and function of microglia in neurodegeneration. *Nat. Immunol.*
- Song, G., Yang, R., Zhang, Q., Chen, L., Huang, D., Zeng, J., Yang, C., and Zhang, T. (2019). TGF- β Secretion by M2 Macrophages Induces Glial Scar Formation by Activating Astrocytes In Vitro. *J. Mol. Neurosci.* *69*, 324–332.
- De Souza, C.T., Araujo, E.P., Bordin, S., Ashimine, R., Zollner, R.L., Boschero, A.C., Saad, M.J.A., and Velloso, L.A. (2005). Consumption of a Fat-Rich Diet Activates a Proinflammatory Response and Induces Insulin Resistance in the Hypothalamus. *Endocrinology* *146*, 4192–4199.
- Spann, N.J., and Glass, C.K. (2013). Sterols and oxysterols in immune cell function. *Nat. Immunol.* *14*, 893–900.
- Spann, N.J., Garmire, L.X., McDonald, J.G., Myers, D.S., Milne, S.B., Shibata, N., Reichart, D., Fox, J.N., Shaked, I., Heudobler, D., et al. (2012). Regulated accumulation of desmosterol integrates macrophage lipid metabolism and inflammatory responses. *Cell* *151*, 138–152.
- Squarzone, P., Oller, G., Hoeffel, G., Pont-Lezica, L., Rostaing, P., Low, D., Bessis, A., Ginhoux, F., and Garel, S. (2014). Microglia Modulate Wiring of the Embryonic Forebrain. *Cell Rep.* *8*, 1271–1279.
- Stadelmann, C., Timmler, S., Barrantes-Freer, A., and Simons, M. (2019). Myelin in the Central Nervous System: Structure, Function, and Pathology. *Physiol. Rev.* *99*, 1381–1431.
- Stence, N., Waite, M., and Dailey, M.E. (2001). Dynamics of microglial activation: a confocal time-lapse analysis in hippocampal slices. *Glia* *33*, 256–266.
- Stout, R.D., Jiang, C., Matta, B., Tietzel, I., Watkins, S.K., and Suttles, J. (2005). Macrophages Sequentially Change Their Functional Phenotype in Response to Changes in Microenvironmental Influences. *J. Immunol.* *175*, 342–349.
- Streit, W.J. (2006). Microglial senescence: does the brain’s immune system have an expiration date? *Trends Neurosci.* *29*, 506–510.
- Stys, P.K., Zamponi, G.W., Van Minnen, J., and Geurts, J.J.G. (2012). Will the real multiple sclerosis please stand up? *Nat. Rev. Neurosci.* *13*, 507–514.
- Surma, M.A., Herzog, R., Vasilj, A., Klose, C., Christinat, N., Morin-Rivron, D., Simons, K., Masoodi, M., and Sampaio, J.L. (2015). An automated shotgun lipidomics platform for high throughput, comprehensive, and quantitative analysis of blood plasma intact lipids. *Eur. J. Lipid Sci. Technol.* *117*, 1540–1549.
- Swinnen, N., Smolders, S., Avila, A., Notelaers, K., Paesen, R., Ameloot, M., Brône, B., Legendre, P., and Rigo, J.M. (2013). Complex invasion pattern of the cerebral cortex by microglial cells during development of the mouse embryo. *Glia* *61*, 150–163.
- Sysi-Aho, M., Ermolov, A., Gopalacharyulu, P. V., Tripathi, A., Seppänen-Laakso, T., Maukonen, J., Mattila, I., Ruohonen, S.T., Vähätalo, L., Yetukuri, L., et al. (2011). Metabolic Regulation in Progression to Autoimmune Diabetes. *PLoS Comput. Biol.* *7*, e1002257.
- Tabas, I. (2010). Macrophage death and defective inflammation resolution in atherosclerosis. *Nat. Rev. Immunol.* *10*, 117.
- Tabas, I., and Bornfeldt, K.E. (2016). Macrophage Phenotype and Function in Different Stages of Atherosclerosis. *Circ. Res.* *118*, 653–667.
- Takahashi, K., Rochford, C.D.P., and Neumann, H. (2005). Clearance of apoptotic neurons without inflammation by microglial triggering receptor expressed on myeloid cells-2. *J. Exp. Med.* *201*, 647–657.
- Takahashi, K., Prinz, M., Stagi, M., Chechneva, O., and Neumann, H. (2007). TREM2-transduced myeloid precursors mediate nervous tissue debris clearance and facilitate recovery in an animal model of multiple sclerosis. *PLoS Med.* *4*, e124.
- Tall, A.R., and Yvan-Charvet, L. (2015). Cholesterol, inflammation and innate immunity. *Nat. Rev. Immunol.* *15*, 104–116.
- Tang, Y., Tytler, E.M., Vickers, S.M., and Yang, L. (2004). Smad4 Protein Stability Is Regulated by Ubiquitin Ligase SCF β -TrCP1. *Artic. J. Biol. Chem.*
- Tchkonina, T., Morbeck, D.E., Von Zglinicki, T., Van Deursen, J., Lustgarten, J., Scoble, H., Khosla, S., Jensen, M.D., and Kirkland, J.L. (2010). Fat tissue, aging, and cellular senescence. *Aging Cell* *9*, 667–684.
- Temml, V., Voss, C. V., Dirsch, V.M., and Schuster, D. (2014). Discovery of new liver X receptor agonists by pharmacophore modeling and shape-based virtual screening. *J. Chem. Inf. Model.* *54*, 367–371.
- Thaler, J.P., Yi, C.X., Schur, E.A., Guyenet, S.J., Hwang, B.H., Dietrich, M.O., Zhao, X., Sarruf, D.A., Izgur, V., Maravilla, K.R., et al. (2012). Obesity is associated with hypothalamic injury in rodents and humans. *J. Clin. Invest.* *122*, 153–162.
- Thion, M.S., Low, D., Silvin, A., Chen, J., Grisel, P., Schulte-Schrepping, J., Blecher, R., Ulas, T., Squarzone, P., Hoeffel, G., et al. (2018). Microbiome Influences Prenatal and Adult Microglia in a Sex-Specific Manner. *Cell* *172*.
- Topping, D.L., and Clifton, P.M. (2001). Short-chain fatty acids and human colonic function: Roles of resistant starch and nonstarch polysaccharides. *Physiol. Rev.* *81*, 1031–1064.
- Torkildsen, Ø., Brunborg, L.A., Thorsen, F., Mørk, S.J., Stangel, M., Myhr, K.M., and Bø, L. (2009). Effects of dietary intervention on MRI activity, de- and remyelination in the cuprizone model for demyelination. *Exp. Neurol.* *215*, 160–166.

- Tortosa-Caparrós, E., Navas-Carrillo, D., Marín, F., and Orenes-Piñero, E. (2017). Anti-inflammatory effects of omega 3 and omega 6 polyunsaturated fatty acids in cardiovascular disease and metabolic syndrome. *Crit. Rev. Food Sci. Nutr.* *57*, 3421–3429.
- Traversari, C., Sozzani, S., Steffensen, K.R., and Russo, V. (2014). LXR-dependent and -independent effects of oxysterols on immunity and tumor growth. *Eur. J. Immunol.* *44*, 1896–1903.
- Triebel, A., and Wenk, M.R. (2018). Analytical considerations of stable isotope labelling in lipidomics. *Biomolecules* *8*.
- Tsuboi, R., and Rifkin, D.B. (1990). Recombinant basic fibroblast growth factor stimulates wound healing in healing-impaired db/db mice. *J. Exp. Med.* *172*, 245–251.
- Vaknin, I., Kunis, G., Miller, O., Butovsky, O., Bukshpan, S., Beers, D.R., Henkel, J.S., Yoles, E., Appel, S.H., and Schwartz, M. (2011). Excess Circulating Alternatively Activated Myeloid (M2) Cells Accelerate ALS Progression While Inhibiting Experimental Autoimmune Encephalomyelitis. *PLoS One* *6*, e26921.
- Valdearcos, M., Robblee, M.M., Benjamin, D.I., Nomura, D.K., Xu, A.W., and Koliwad, S.K. (2014). Microglia Dictate the Impact of Saturated Fat Consumption on Hypothalamic Inflammation and Neuronal Function. *Cell Rep.* *9*, 2124–2139.
- Valdearcos, M., Douglass, J.D., Robblee, M.M., Dorfman, M.D., Stifler, D.R., Bennett, M.L., Gerritse, I., Fasnacht, R., Barres, B.A., Thaler, J.P., et al. (2017). Microglial Inflammatory Signaling Orchestrates the Hypothalamic Immune Response to Dietary Excess and Mediates Obesity Susceptibility. *Cell Metab.*
- Valentini, K.J., Pickens, C.A., Wiesinger, J.A., and Fenton, J.I. (2018). The effect of fish oil supplementation on brain DHA and EPA content and fatty acid profile in mice. *Int. J. Food Sci. Nutr.* *69*, 705–717.
- Valledor, A.F. (2005). The innate immune response under the control of the LXR pathway. *Immunobiology* *210*, 127–132.
- Valledor, A.F., Hsu, L.-C., Ogawa, S., Sawka-Verhelle, D., Karin, M., and Glass, C.K. (2004). Activation of liver X receptors and retinoid X receptors prevents bacterial-induced macrophage apoptosis. *Proc. Natl. Acad. Sci. U. S. A.* *101*, 17813–17818.
- Viola, J., and Soehnlein, O. (2015). Atherosclerosis – A matter of unresolved inflammation. *Semin. Immunol.* *27*, 184–193.
- Vogel, D.Y., Vereyken, E.J., Glim, J.E., Heijnen, P.D., Mocton, M., van der Valk, P., Amor, S., Teunissen, C.E., van Horsen, J., and Dijkstra, C.D. (2013). Macrophages in inflammatory multiple sclerosis lesions have an intermediate activation status. *J. Neuroinflammation* *10*, 35.
- Vrieze, A., Van Nood, E., Holleman, F., Salojarvi, J., Kootte, R.S., Bartelsman, J.F.W.M., Dallinga-Thie, G.M., Ackermans, M.T., Serlie, M.J., Oozeer, R., et al. (2012). Transfer of intestinal microbiota from lean donors increases insulin sensitivity in individuals with metabolic syndrome. *Gastroenterology* *143*.
- Vrieze, A., Out, C., Fuentes, S., Jonker, L., Reuling, I., Kootte, R.S., Van Nood, E., Holleman, F., Knaapen, M., Romijn, J.A., et al. (2014). Impact of oral vancomycin on gut microbiota, bile acid metabolism, and insulin sensitivity. *J. Hepatol.* *60*, 824–831.
- Wake, H., Moorhouse, A.J., Jinno, S., Kohsaka, S., and Nabekura, J. (2009). Resting microglia directly monitor the functional state of synapses in vivo and determine the fate of ischemic terminals. *J. Neurosci.* *29*, 3974–3980.
- Wang, C., Popescu, D.C., Wu, C., Zhu, J., Macklin, W., and Wang, Y. (2010). In Situ Fluorescence Imaging of Myelination. *J. Histochem. Cytochem.* *58*, 611–621.
- Wang, L., Schuster, G.U., Hultenby, K., Zhang, Q., Andersson, S., and Gustafsson, J.-A. (2002). Liver X receptors in the central nervous system: from lipid homeostasis to neuronal degeneration. *Proc. Natl. Acad. Sci. U. S. A.* *99*, 13878–13883.
- Wang, Y., Cella, M., Mallinson, K., Ulrich, J.D., Young, K.L., Robinette, M.L., Gilfillan, S., Krishnan, G.M., Sudhakar, S., Zinselmeyer, B.H., et al. (2015). TREM2 lipid sensing sustains the microglial response in an Alzheimer's disease model. *Cell* *160*.
- Wells, J.E.A., Hurlbert, R.J., Fehlings, M.G., and Yong, V.W. (2003). Neuroprotection by minocycline facilitates significant recovery from spinal cord injury in mice. *Brain* *126*, 1628–1637.
- Wendeln, A.-C., Degenhardt, K., Kaurani, L., Gertig, M., Ulas, T., Jain, G., Wagner, J., Häslér, L.M., Wild, K., Skodras, A., et al. (2018). Innate immune memory in the brain shapes neurological disease hallmarks. *Nature* *556*.
- Whitmer, R.A., Gunderson, E.P., Barrett-Connor, E., Quesenberry, C.P., and Yaffe, K. (2005). Obesity in middle age and future risk of dementia: A 27 year longitudinal population based study. *Br. Med. J.* *330*, 1360–1362.
- Williams, K., Ulvestad, E., Waage, A., Antel, J.P., and McLaurin, J. (1994). Activation of adult human derived microglia by myelin phagocytosis in vitro. *J. Neurosci. Res.* *38*, 433–443.
- Wong, K., Noubade, R., Manzanillo, P., Ota, N., Foreman, O., Hackney, J.A., Friedman, B.A., Pappu, R., Scarce-Levie, K., and Ouyang, W. (2017). Mice deficient in NRROS show abnormal microglial development and neurological disorders. *Nat. Immunol.* *18*, 633–641.
- Wunderlich, P., Glebov, K., Kemmerling, N., Tien, N.T., Neumann, H., and Walter, J. (2013). Sequential proteolytic processing of the triggering receptor expressed on myeloid cells-2 (TREM2) protein by ectodomain shedding and γ -secretase-dependent intramembranous cleavage. *J. Biol. Chem.* *288*, 33027–33036.
- Xu, J., Wagoner, G., Douglas, J.C., and Drew, P.D. (2009). Liver X receptor agonist regulation of Th17 lymphocyte function in autoimmunity. *J. Leukoc. Biol.* *86*, 401–409.
- Xu, P., Li, D., Tang, X., Bao, X., Huang, J., Tang, Y., Yang, Y., Xu, H., and Fan, X. (2013). LXR agonists: new potential therapeutic drug for neurodegenerative diseases. *Mol. Neurobiol.* *48*, 715–728.
- Xue, J., Schmidt, S. V., Sander, J., Draffehn, A., Krebs, W., Quester, I., De Nardo, D., Gohel, T.D., Emde, M., Schmidleithner, L., et al. (2014). Transcriptome-based network analysis reveals a spectrum model of human macrophage activation. *Immunity* *40*, 274–288.
- Yadav, H., Quijano, C., Kamaraju, A.K., Gavrilova, O., Malek, R., Chen, W., Zervas, P., Zhigang, D., Wright, E.C., Stuelten, C., et al. (2011). Protection from Obesity and Diabetes by Blockade of TGF- β /Smad3 Signaling. *Cell Metab.* *14*, 67–79.
- Yagi, S., Fukuda, D., Aihara, K.I., Akaike, M., Shimabukuro, M., and Sata, M. (2017). n-3 polyunsaturated fatty acids: Promising nutrients for preventing cardiovascular disease. *J. Atheroscler. Thromb.* *24*, 999–1010.
- Yamasaki, R., Lu, H., Butovsky, O., Ohno, N., Rietsch, A.M., Cialic, R., Wu, P.M., Doykan, C.E., Lin, J., Cotleur, A.C., et al. (2014). Differential roles of microglia and monocytes in the inflamed central nervous system. *J. Exp. Med.* *211*, 1533–1549.
- Yan, J., Zhang, H., Yin, Y., Li, J., Tang, Y., Purkayastha, S., Li, L., and Cai, D. (2014). Obesity- and aging-induced excess of central transforming growth factor- β potentiates diabetic development via an RNA stress response. *Nat. Med.* *20*, 1001–1008.
- Yang, X., Lamia, K.A., and Evans, R.M. (2007). Nuclear

- receptors, metabolism, and the circadian clock. *Cold Spring Harb. Symp. Quant. Biol.* *72*, 387–394.
- Yeung, M.S.Y., Djelloul, M., Steiner, E., Bernard, S., Salehpour, M., Possnert, G., Brundin, L., and Frisén, J. (2019). Dynamics of oligodendrocyte generation in multiple sclerosis. *Nature* *566*, 538–542.
- Yi, C.X., Tschöp, M.H., Woods, S.C., and Hofmann, S.M. (2012). High-fat-diet exposure induces IgG accumulation in hypothalamic microglia. *DMM Dis. Model. Mech.* *5*, 686–690.
- Yin, K., Liao, D. fang, and Tang, C.K. (2010). ATP-binding membrane cassette transporter A1 (ABCA1): A possible link between inflammation and reverse cholesterol transport. *Mol. Med.* *16*, 438–449.
- Young, K.M., Psachoulia, K., Tripathi, R.B., Dunn, S.J., Cossell, L., Attwell, D., Tohyama, K., and Richardson, W.D. (2013). Oligodendrocyte dynamics in the healthy adult CNS: Evidence for myelin remodeling. *Neuron* *77*.
- Zhang-Gandhi, C.X., and Drew, P.D. (2007). Liver X receptor and retinoid X receptor agonists inhibit inflammatory responses of microglia and astrocytes. *J. Neuroimmunol.* *183*, 50–59.
- Zhang, Y.E. (2009). Non-Smad pathways in TGF- β signaling. *Cell Res.* *19*, 128–139.
- Zhang, M., Lv, X.Y., Li, J., Xu, Z.G., and Chen, L. (2008). The characterization of high-fat diet and multiple low-dose streptozotocin induced type 2 diabetes rat model. *Exp. Diabetes Res.* *2008*, 704045.
- Zhang, Y., Proenca, R., Maffei, M., Barone, M., Leopold, L., and Friedman, J.M. (1994). Positional cloning of the mouse obese gene and its human homologue. *Nature* *372*, 425–432.
- Zhang, Y., Chen, K., Sloan, S.A., Bennett, M.L., Scholze, A.R., O’Keefe, S., Phatnani, H.P., Guarnieri, P., Caneda, C., Ruderisch, N., et al. (2014). An RNA-sequencing transcriptome and splicing database of glia, neurons, and vascular cells of the cerebral cortex. *J. Neurosci.* *34*, 11929–11947.
- Zhao, C., Li, W., and Franklin, R.J.M. (2006). Differences in the early inflammatory responses to toxin-induced demyelination are associated with the age-related decline in CNS remyelination. *J. Neurosci.* *27*, 1298–1307.
- Zolezzi, J.M., Santos, M.J., Bastías-Candia, S., Pinto, C., Godoy, J.A., and Inestrosa, N.C. (2017). PPARs in the central nervous system: roles in neurodegeneration and neuroinflammation. *Biol. Rev.* *92*, 2046–2069.
- Zöller, T., Schneider, A., Kleimeyer, C., Masuda, T., Potru, P.S., Pfeifer, D., Blank, T., Prinz, M., and Spittau, B. (2018). Silencing of TGF β signalling in microglia results in impaired homeostasis. *Nat. Commun.* *9*, 1–13.
- Zrzavy, T., Hametner, S., Wimmer, I., Butovsky, O., Weiner, H.L., and Lassmann, H. (2017). Loss of “homeostatic” microglia and patterns of their activation in active multiple sclerosis. *Brain* *140*, 1900–1913.

List of figures

Introduction:

Figure 1.1: Microglia cover the entire brain parenchyma.

Figure 1.2: DAM represent a unique response to various neuropathologies.

Figure 1.3: Remyelination re-establishes myelin sheaths around demyelinated axons.

Figure 1.4: Illustration of the model of biphasic temporal pattern of microglial and macrophage activation.

Materials and Methods:

Figure 2.1: Experimental paradigm used to induce obesity by diet.

Figure 2.2: Timeline used for pharmacological treatments.

Figure 2.3: Timeline used for pharmacological treatments and induction of knock-outs.

Figure 2.4: Microglia are the predominant CNS macrophage present in lysolecithin-driven demyelinated lesions.

Results:

Figure 3.1: The plasma lipidome is profoundly altered by western diet.

Figure 3.2: The plasma lipidome is not altered by age.

Figure 3.3: Western diet feeding alters the brain lipidome of mice.

Figure 3.4: Microglia in the white matter are altered by western diet feeding.

Figure 3.5: The ventricle wall could be a site for lipid trafficking into the CNS.

Figure 3.6: The transcriptome of microglia is altered by western diet

Figure 3.7: Analysis of the epigenome of microglia resulted in similar results in all genes.

Figure 3.8: Obesity impairs lesion recovery after demyelinating injury.

Figure 3.9: Persistently demyelinated lesions in WD-fed mice contain lipid-loaded microglia.

Figure 3.10: Stimulating lipid-sensing nuclear receptors in WD-fed mice improves lesion repair after demyelination.

Figure 3.11: Stimulation of LXR and PPAR pathways improves lipid processing by microglia and macrophages in WD-fed mice.

Figure 3.12: Sodium Butyrate treatment enhances lesion repair both in WD-fed mice and in old mice.

Figure 3.13: The differential production of endogenous LXR ligands does not explain the poor induction of the LXR pathway observed in WD-fed mice.

Figure 3.14: Microglia activation upon demyelination is impaired in WD-fed mice.

Figure 3.15: TGF β signalling is increased in WD-fed mice.

Figure 3.16: TGF β blocks LXR target gene induction after myelin uptake.

Figure 3.17: Genetic deletion of the Tgfbr2 in microglia of WD-fed mice promotes recovery from demyelinating injury.

Figure 3.18: Blocking TGF β signalling with Galunisertib in WD-fed mice promotes recovery from demyelinating injury.

Figure 3.19: Myelin intake by microglia causes TREM2 shedding.

Figure 3.20: Treatment with TREM2-activating monoclonal antibody 4D9 improves lipid clearance in phagocytes after demyelinating injury.

Discussion:

Figure 4.1: Working model of the influence of obesity on microglia's response to myelin damage.

Appendix:

Figure 5.1: Cellular processes triggered upon myelin debris intake.

Figure 5.2: Lipid processing by microglia and macrophages is the bottleneck for successful remyelination.

List of tables

Table 1: Name, source and purpose of all mouse lines used in this study.

Table 2: Species, concentration and catalogue details of all primary antibodies used in this study.

Table 3: Application and catalogue details of all commercial kits used in this study.

Table 4: Sequence details of all primers used for genotyping.

Table 5: Sequence details of all primers used for RT-qPCR analysis.

Table 6: Application and source of all software used in this study.

List of abbreviations

ABCA1: ATP-binding cassette transporter A1	CNS: Central nervous system
ABCG1: ATP-binding cassette transporter G1	CR3: Complement receptor 3
ACAT1: Acyl coenzyme A cholesterol acyltransferase 1	CSF1: Colony Stimulating Factor 1
AD: Alzheimer's Disease	CSF1R: Colony Stimulating Factor 1 Receptor
ALS: Amyotrophic Lateral Sclerosis	CX3CR1: CX3C chemokine receptor 1, also known as fractalkine receptor or G-protein coupled receptor 13
AP1: Activator Protein 1	DAG: diacylglycerol
APOA1: Apolipoprotein A1	DAM: disease- or degeneration- associated microglia
APOE: Apolipoprotein E	DAMP: damage-associated molecular pattern
ARG1: Arginase 1	DDSA: Dodecenylsuccinic acid anhydride
ATACseq: Assay for Transposase-Accessible Chromatin using sequencing	DIO: diet-induced obesity
BCS: bovine calf serum	DMP-30: 2,4,6-Tris(dimethylaminomethyl)phenol
BDNF: Brain-derived Neurotrophic Factor	Dpi: days post injection
BSA: bovine serum albumin	E8: embryonic day 8
C1q: Complement Component 1q	EAE: experimental autoimmune encephalomyelitis
CCL2: Chemokine (C-C motif) Ligand 2	EM: electron microscopy
CCR2: Chemokine (C-C motif) Receptor 2	EPA: eicosapentaenoic acid
CD11b: Cluster of differentiation molecule 11b, Integrin α M	FCGRI: Fc gamma receptor I
CD11c: Cluster of differentiation molecule 11c, also known as ITGAX, Integrin α X	FF: fenofibrate
CD14: Cluster of differentiation 14	FFAR2: free fatty acid receptor 2
CD16/32: Cluster of differentiation 16/32, Fc receptor	GC-MS: gas chromatography-mass spectrometry
CD16: Cluster of differentiation 16, Fc γ RIII	GFAP: Glial Fibrillary Acidic Protein
CD172a: Cluster of differentiation, also known as signal-regulatory protein alpha SIRP α	GLUT1: Glucose transporter 1
CD200: Cluster of differentiation 200, also named OX-2 membrane glycoprotein	GTP: Guanosinotriphosphat
CD200R: Cluster of differentiation 200 receptor	HAT: Histone acyltransferase
CD206: Cluster of differentiation 206, mannose receptor	HD: Huntington's disease
CD22: Cluster of differentiation 22, also known SIGLEC-2	HDAC: Histone deacetylase
CD36: Cluster of differentiation 36, also known as scavenger receptor class B member 3	HDL: High density lipoprotein
CD4: Cluster of differentiation 4	HexCer: hexosylceramide
CD45: Cluster of differentiation 45, also known protein tyrosine phosphatase receptor type C	HFD: High fat diet
CD47: Cluster of differentiation 47, also named integrin associated protein	HLA-DR: Human Leukocyte Receptor – DR isotype
CE: cholesterol ester	HMGB1: High mobility group box 1
Cer: ceramide	IBA1: Ionized calcium-binding adapter molecule 1, also known as allograft inflammatory factor 1, AIF1
Chol: cholesterol	IGF1: Insulin growth factor 1
CL: cardiolipin	IKK β : Inhibitor of nuclear factor kappa-B kinase subunit beta
CLEC7A: C-type lectin domain family 7 member A or Dectin-1	IL1 α : Interleukin 1 α
	IL1 β : Interleukin 1 β
	IL34: Interleukin 34
	iNOS: inducible nitric oxide synthase
	IRF8: Interferon Regulatory Factor 8
	IRS: Insulin Receptor Substrate
	KO: knock out

List of abbreviations

LAMP1: Lysosomal-associated membrane protein 1	PI: phosphatidylinositol
LDL: Low density lipoprotein	PI3K: Phosphoinositide 3-kinase
LF: Lipofuscin	PLIN: Perilipin
LLC: lysolecithin	PMT: photo multiplier tubes
LPA: lyso-phosphatidate	PNS: Peripheral Nervous System
LPC: lyso-phosphatidylcholine	PPAR: Peroxisome Proliferator Activator Receptor
LPE: lyso-phosphatidylethanolamine	PS: phosphatidylserine
LPG: lyso-phosphatidylglycerol	PUFA: polyunsaturated fatty acids
LPI: lyso-phosphatidylinositol	RG: rosiglitazone
LPS: Lipopolysaccharide	ROS: Reactive Oxygen Species
LPS: lyso-phosphatidylserine	RXR: Retinoid X Receptor
LXR: Liver X Receptor	SCFA: Short-Chain Fatty Acid
Ly6c: Lymphocyte antigen 6 c	scRNAseq: single-cell RNA sequencing
MAC2: Also known as Galectin 3	SFA: saturated fatty acids
MAFB: V-maf musculoaponeurotic fibrosarcoma oncogene	SM: sphingomyelin
MAPK: mitogen-activated protein kinase	SPP1: secreted phosphoprotein 1
MCSF: macrophage colony stimulating factor	SRBI: scavenger receptor BI
M-CSF: macrophage colony stimulating factor	SREBP: sterol regulatory element-binding protein
MDMs: monocyte-derived macrophages	SREBP1c: sterol regulatory element-binding protein 1c
MEF2C: myocyte-specific enhancer factor 2C	SRII: scavenger receptor II
MgnD: Microglial neurodegenerative phenotype	STAT1: signal transducer and activator of transcription 1
MHCII: Major histocompatibility complex II	TAG: triacylglycerol
MMP12: Matrix metalloproteinase-12	TGFBRI and II: transforming growth factor β receptor I and II
MNA: methylnadic anhydride	TGF β : transforming growth factor β
MS: Multiple Sclerosis	Th1: T helper cell 1
MSMS: tandem mass spectrometry	Th17: T helper cell 17
MYD88: Myeloid differentiation primary response 88	TLR: toll like receptor
nCEH and nCEH1: neutral cholesterol ester hydrolase 1	TMEM119: transmembrane protein 119
NF κ B: nuclear factor kappa-light-chain-enhancer of activated B cells	TNF α : tumour necrosis factor α
NGF: neural growth factor	TREM2: triggering receptor expressed on myeloid cells 2
NPC1: Niemann Pick Disease type C intracellular cholesterol transporter 1	UCP2: uncoupling protein 2
NPC2: Niemann Pick Disease type C intracellular cholesterol transporter 2	UFAs: unsaturated fatty acids
NRROS: Negative Regulator of Reactive Oxygen Species	WD: western diet
OPCs: Oligodendrocyte Precursor Cells	ZF9: Zinc finger transcription factor 9
P14: postnatal 14	
PA: phosphatidate	
PAMP: pathogen-associated molecular pattern	
PC: phosphatidylcholine	
PC: phosphatidylcholine	
PD: Parkinson's disease	
PDGF α : Platelet-derived Growth Factor α	
PE: phosphatidylethanolamine	
PE: phosphatidylethanolamine	
PG: phosphatidylglycerol	

List of publications

Bosch-Queralt M, Cantuti-Castelvetri L, Damkou A, Schifferer M, Schlepckow K, Alexopoulos I, Lütjohann D, Klose C, Vaculčíaková L, Masuda T, Prinz M, M. Monroe K, Di Paolo G, Lewcock JW, Haass C, Simons M. Diet-dependent regulation of TGF β impairs reparative innate immune responses after demyelinating injury. *Nature Metabolism*, *in revision*.

Cantuti-Castelvetri L*, Fitzner D*, **Bosch-Queralt M**, Weil MT, Su M, Sen P, Ruhwedel T, Mitkovski M, Trendelenburg G, Lütjohann D, Möbius W, Simons M. Defective cholesterol clearance limits remyelination in the aged central nervous system. *Science*, 2018.

B. Castellano, **M. Bosch-Queralt**, B. Almolda, N. Villacampa and B. Gonzalez. Purine signalling and microglial wrapping. In: *Glial cells in health and disease*. Rommy von Bernhardt and Jaime Eugén (Eds) *Advances in Experimental Medicine and Biology* (Springer), 2016.

Copyright of figures taken from publications

SPRINGER NATURE LICENSE
TERMS AND CONDITIONS
Mar 19, 2020

This Agreement between Steinkirchnerstr. 35 ("You") and Springer Nature ("Springer Nature") consists of your license details and the terms and conditions provided by Springer Nature and Copyright Clearance Center.

License Number	4792350599659
License date	Mar 19, 2020
Licensed Content Publisher	Springer Nature
Licensed Content Publication	Nature Immunology
Licensed Content Title	The identity and function of microglia in neurodegeneration
Licensed Content Author	Wilbur M. Song et al
Licensed Content Date	Sep 24, 2018
Type of Use	Thesis/Dissertation
Requestor type	academic/university or research institute
Format	print and electronic
Portion	figures/tables/illustrations
Number of figures/tables/illustrations	1
High-res required	no
Will you be translating?	no
Circulation/distribution	1 - 29
Author of this Springer Nature content	no
Title	Obesity perturbs microglia function
Institution name	DZNE
Expected presentation date	Apr 2020
Portions	Figure 1
Requestor Location	Mar Bosch Queralt Steinkirchnerstr. 35 München, 81475 Germany Attn: Mar Bosch Queralt
Total	0.00 EUR
Terms and Conditions	

Springer Nature Customer Service Centre GmbH Terms and Conditions

This agreement sets out the terms and conditions of the licence (the **Licence**) between you and **Springer Nature Customer Service Centre GmbH** (the **Licensor**). By clicking 'accept' and completing the transaction for the material (**Licensed Material**), you also confirm your acceptance of these terms and conditions.

1. Grant of License

1. The Licensor grants you a personal, non-exclusive, non-transferable, world-wide licence to reproduce the Licensed Material for the purpose specified in your order only. Licences are granted for the specific use requested in the order and for no other use, subject to the conditions below.
2. The Licensor warrants that it has, to the best of its knowledge, the rights to license reuse of the Licensed Material. However, you should ensure that the material you are requesting is original to the Licensor and does not carry the copyright of another entity (as credited in the published version).

3. If the credit line on any part of the material you have requested indicates that it was reprinted or adapted with permission from another source, then you should also seek permission from that source to reuse the material.

2. Scope of Licence

1. You may only use the Licensed Content in the manner and to the extent permitted by these Ts&Cs and any applicable laws.
2. A separate licence may be required for any additional use of the Licensed Material, e.g. where a licence has been purchased for print only use, separate permission must be obtained for electronic re-use. Similarly, a licence is only valid in the language selected and does not apply for editions in other languages unless additional translation rights have been granted separately in the licence. Any content owned by third parties are expressly excluded from the licence.
3. Similarly, rights for additional components such as custom editions and derivatives require additional permission and may be subject to an additional fee. Please apply to Journalpermissions@springernature.com/bookpermissions@springernature.com for these rights.
4. Where permission has been granted **free of charge** for material in print, permission may also be granted for any electronic version of that work, provided that the material is incidental to your work as a whole and that the electronic version is essentially equivalent to, or substitutes for, the print version.
5. An alternative scope of licence may apply to signatories of the [STM Permissions Guidelines](#), as amended from time to time.

3. Duration of Licence

1. A licence for is valid from the date of purchase ('Licence Date') at the end of the relevant period in the below table:

Scope of Licence	Duration of Licence
Post on a website	12 months
Presentations	12 months
Books and journals	Lifetime of the edition in the language purchased

4. Acknowledgement

1. The Licensor's permission must be acknowledged next to the Licensed Material in print. In electronic form, this acknowledgement must be visible at the same time as the figures/tables/illustrations or abstract, and must be hyperlinked to the journal/book's homepage. Our required acknowledgement format is in the Appendix below.

5. Restrictions on use

1. Use of the Licensed Material may be permitted for incidental promotional use and minor editing privileges e.g. minor adaptations of single figures, changes of format, colour and/or style where the adaptation is credited as set out in Appendix 1 below. Any other changes including but not limited to, cropping, adapting, omitting material that affect the meaning, intention or moral rights of the author are strictly prohibited.
2. You must not use any Licensed Material as part of any design or trademark.
3. Licensed Material may be used in Open Access Publications (OAP) before publication by Springer Nature, but any Licensed Material must be removed from OAP sites prior to final publication.

6. Ownership of Rights

1. Licensed Material remains the property of either Licensor or the relevant third party and any rights not explicitly granted herein are expressly reserved.

7. Warranty

IN NO EVENT SHALL LICENSOR BE LIABLE TO YOU OR ANY OTHER PARTY OR ANY OTHER PERSON OR FOR ANY SPECIAL, CONSEQUENTIAL, INCIDENTAL OR INDIRECT DAMAGES, HOWEVER CAUSED, ARISING OUT OF OR IN CONNECTION WITH THE DOWNLOADING, VIEWING OR USE OF

THE MATERIALS REGARDLESS OF THE FORM OF ACTION, WHETHER FOR BREACH OF CONTRACT, BREACH OF WARRANTY, TORT, NEGLIGENCE, INFRINGEMENT OR OTHERWISE (INCLUDING, WITHOUT LIMITATION, DAMAGES BASED ON LOSS OF PROFITS, DATA, FILES, USE, BUSINESS OPPORTUNITY OR CLAIMS OF THIRD PARTIES), AND WHETHER OR NOT THE PARTY HAS BEEN ADVISED OF THE POSSIBILITY OF SUCH DAMAGES. THIS LIMITATION SHALL APPLY NOTWITHSTANDING ANY FAILURE OF ESSENTIAL PURPOSE OF ANY LIMITED REMEDY PROVIDED HEREIN.

8. **Limitations**

1. **BOOKS ONLY:** Where 'reuse in a dissertation/thesis' has been selected the following terms apply: Print rights of the final author's accepted manuscript (for clarity, NOT the published version) for up to 100 copies, electronic rights for use only on a personal website or institutional repository as defined by the Sherpa guideline (www.sherpa.ac.uk/romeo/).

9. **Termination and Cancellation**

1. Licences will expire after the period shown in Clause 3 (above).
2. Licensee reserves the right to terminate the Licence in the event that payment is not received in full or if there has been a breach of this agreement by you.

Appendix 1 — Acknowledgements:

For Journal Content:

Reprinted by permission from [the Licensor]: [Journal Publisher (e.g. Nature/Springer/Palgrave)] [JOURNAL NAME] [REFERENCE CITATION (Article name, Author(s) Name), [COPYRIGHT] (year of publication)

For Advance Online Publication papers:

Reprinted by permission from [the Licensor]: [Journal Publisher (e.g. Nature/Springer/Palgrave)] [JOURNAL NAME] [REFERENCE CITATION (Article name, Author(s) Name), [COPYRIGHT] (year of publication), advance online publication, day month year (doi: 10.1038/sj.[JOURNAL ACRONYM].)

For Adaptations/Translations:

Adapted/Translated by permission from [the Licensor]: [Journal Publisher (e.g. Nature/Springer/Palgrave)] [JOURNAL NAME] [REFERENCE CITATION (Article name, Author(s) Name), [COPYRIGHT] (year of publication)

Note: For any republication from the British Journal of Cancer, the following credit line style applies:

Reprinted/adapted/translated by permission from [the Licensor]: on behalf of Cancer Research UK: : [Journal Publisher (e.g. Nature/Springer/Palgrave)] [JOURNAL NAME] [REFERENCE CITATION (Article name, Author(s) Name), [COPYRIGHT] (year of publication)

For Advance Online Publication papers:

Reprinted by permission from The [the Licensor]: on behalf of Cancer Research UK: [Journal Publisher (e.g. Nature/Springer/Palgrave)] [JOURNAL NAME] [REFERENCE CITATION (Article name, Author(s) Name), [COPYRIGHT] (year of publication), advance online publication, day month year (doi: 10.1038/sj.[JOURNAL ACRONYM])

For Book content:

Reprinted/adapted by permission from [the Licensor]: [Book Publisher (e.g. Palgrave Macmillan, Springer etc) [Book Title] by [Book author(s)] [COPYRIGHT] (year of publication)

Other Conditions: Version 1.2

Questions? customercare@copyright.com or +1-855-239-3415 (toll free in the US) or +1-978-646-2777.

Acknowledgements

I would like to thank my supervisor Prof. Mikael Simons for the opportunity to join his research group for my doctoral studies, for his scientific guidance and fruitful discussions. Furthermore, I would like to thank Prof. Thomas Misgeld, Prof. Antje Grosche and Dr. Arthur Liesz for their scientific input into my project in their role as thesis advisor committee. Further thanks go to Prof. Christine Stadelmann-Nessler for her constant support and trust and for agreeing to review this dissertation. Also, I would like to thank Prof. Mikael Simons, Prof. Thomas Misgeld, Dr. Florence Bareyre and Dr. Conny Kopp-Scheinflug for finding the time and energy to evaluate my thesis defense.

Special gratitude goes also to the Graduate School for Systemic Neuroscience, for providing me with a social community, a clear path and invaluable support. I also want to send a heartfelt thank you to Boehringer Ingelheim Fonds for inestimable support, which went way beyond funding. I will forever cherish everything I have learnt and, especially, everyone I have met, during my time as a BIF fellow. Special thanks go also to Martin Krzywinski for teaching us his expertise in scientific illustration design and actively helping me design better figures.

I would like to thank everyone who has collaborated in this project. Alkmini, thank you for your hard work and constant scientific curiosity. I firmly believe that teaching others makes oneself a better scientist, and I have you to thank for that. Ludo, thank you for the endless advice you have given me and for sharing your results with me. Martina and Georg, thank you for being the best at what you do, and for pushing through in tight times. Kerstin, thank you for constant support and inspiration. We miss you! Giannis, thank you for allowing me to learn microscopy from one who cares to be as good as possible. I truly believe your help and precious advice made my project run smooth and efficiently. Agata, thank you for coming into our lab and releasing some weight off my shoulders. Lenka, thank you for supporting and guiding my intuition and making the volume analysis such an easy quantification. Aleks, thank you for your professionalism and excitement during our collaborations. I want to also thank Nirmal Kannaiyan and Moritz Rossner, Martin Giera, Dieter Lütjohann, Doron Merkler and Nicolas Page, Kai Schlepckow and Christian Haass, our collaborators at Denali and, finally, our collaborators at Lipotype, for the fruitful collaborations. Further thanks go to Takahiro Masuda and Marco Prinz for providing us with the Tgfb2 KO line. Finally, I would really like to appreciate the hard work that our animal facility has done all these years for me. Vanessa, Krystyna, Ekrem, Ljiljana, Michelle, Peggy, Steffi, Claudia, Anne and Manu, thank you for your help and patience; you made the work in the facility so nice and uncomplicated.

I am very grateful to all my lab colleagues for their sense of humour, attitude and ambition, which are always a source of inspiration. Martina and Lili, thank you for being great friends and confidants, thank you for your help at any time with any topic, and thank you for the evenings of release... at best with some chocolate souffle to accompany the desperation. Alkmini, thank you for listening to me, accompanying me, helping me, cheering me up in a time when I most needed it, and thank you

Acknowledgements

for your questions that keep me on my feet. Ludo, thank you for all the teaching and discussions. Agata, I am grateful for your technical help, but, especially, for your efficiency, coolness and straightforwardness, which came like a breath of fresh air. Thank you Shima, for teaching me everything you know about our favourite cell, and Maria, for your endless curiosity – expressed in the way of many questions. Chaitali, thank you for accompanying us in the very beginning, for your cute animal videos and your amazing laugh. Thank you Minou, for your patience and vision. Jana, danke für deine Geduld und deinen unermüdlichen Einsatz. And finally, thank you to the new generation: Nico, Seiji, Gary, Vini, Alix and Jianping – you guys brought new, fresh, cheerful energy to us!

Many more people accompanied me during these years. Caterina, thank you for your unique cute adorable personality, for expanding my world, and for understanding me like no one else. Johanna and Laura, thank you for the jokes, the gossip and the laughing. Maryam, thank you for your personal and scientific advice, but mostly, thank you for being the kindest soul on this planet and my very good friend. Gemma, és increïble que el destí ens portés tan a prop una de l'altra, moltes gràcies per fer-me un lloc en el teu apretat horari sempre que ho he necessitat, per tots els consells, però sobretot per ser una petita part de Catalunya a l'institut. Judit, gràcies per tenir sempre preparat un comentari graciós, donant-li així un toc catalanet a qualsevol cosa – encara que sigui catalanet de “Barna”. Becky, thank you for being my SCFA literature referent, for teaching me and for all the ommm. Lukas, thank you for sharing with me the PhD representative experience and for showing me what it really means to be involved. Johanna, Gregor, Michaela, Isa, David, Felix, Florian, Robert and Lars, thank you for being the coolest BIF fellows and an infinite source of inspiration. Pau, gràcies pels vespres de descans i de desfogament, de despotricar i intentar arreglar un món inarreglable. Gemmeta i Mimi, gràcies per venir-me a veure amb notícies tan especials, i per donar-me els ànims que em faltaven per encarar la recta final.

Ich möchte mich auch bei meiner “Ritteburg-Familie” bedanken. Ihr habt euch immer um mich gekümmert, habt mich immer zum Lachen gebracht, und habt an mich geglaubt, und dafür bin ich wirklich dankbar. Ritteburg wird für mich immer eine Inspirations- und Friedensquelle sein!

Tinc la gran sort de ser part d'una gran família amb persones meravelloses. Gràcies avieta, per totes les espelmes, gràcies Margarita per venir fins a Munich a veure'm, gràcies Miri pel teu positivisme, gràcies padrina, pel teu carinyo que m'arriba a molts quilòmetres de distància, Abel pel teu genuí interès en el que estudio i als nens més guapos del món per la seva energia positiva. I moltes, moltes gràcies als que són el meu pilar des de sempre i fins sempre: pares, nenes i Uri. Gràcies per les incomptables visites (algunes sorpresa i tot) i per tota l'ajuda. Però sobretot, gràcies per creure en mi i per estimar-me a través de la distància.

I, finalment, moltes gràcies a l'Erik! Dia a dia, m'has escoltat, m'has animat, m'has fet veure la realitat quan jo me n'allunyava, i m'has empès a ser millor – ho valoro com un gran tresor. Finalment, ens acostem al moment de començar la nostra pròpia aventura, junts, i em manquen paraules per descriure les ganes que en tinc.

Affidavit/Eidesstattliche Versicherung

I hereby confirm that the dissertation “Diet-dependent regulation of TGF β impairs reparative innate immune responses after demyelination” is the result of my own work and that I have only used sources or materials listed and specified in the dissertation.

Hiermit versichere ich an Eides statt, dass ich die vorliegende Dissertation „Diet-dependent regulation of TGF β impairs reparative innate immune responses after demyelination“ selbstständig angefertigt habe, mich außer der angegebenen keiner weiteren Hilfsmittel bedient und alle Erkenntnisse, die aus dem Schrifttum ganz oder annähernd übernommen sind, als solche kenntlich gemacht und nach ihrer Herkunft unter Bezeichnung der Fundstelle einzeln nachgewiesen habe.

Munich, date/*München, den*

Signature/*Unterschrift*

Author contributions

We hereby declare that the following authors contributed to the results of this study in the following manner:

Alkmini Damkou processed and analysed the samples from the CX3CR1-GFPxCCR2-RFP mice, the samples from the ARG1-YFP x iNOS-tdTomato mice, the activation markers MAC2 and MHCII at 4 dpi and the galunisertib-treated old mice. Furthermore, she performed the RT-qPCR analysis of TGF β transcripts in WM/GM samples and in brains from old/young mice and the FISH analysis of TGF β ligands in lesions from CD- and WD-fed mice.

Ludovico Cantuti-Castelvetri performed, processed and analysed the *in vitro* experiments with the 4D9 antibody and the *in vivo* experiments with 4D9-treated old mice, and performed the injections for the 4D9-treated WD-fed mice.

Aleksandra Mezydło performed the injections on the CX3CR1-GFP x CCR2-RFP mice and the ARG1-YFP x iNOS-tdTomato mice.

Kai Schlepckow analysed the supernatant of 4D9-treated microglia by ELISA assay.

Kathryn M. Monroe, Gilbert Di Paolo and Joseph W. Lewcock from Denali Therapeutics developed and provided us with the 4D9 antibody.

Lenka Vaculčíaková wrote the iPython script to compute the lesion volume from the different lesion areas.

Ioannis Alexopoulos assisted with image acquisition and wrote several custom-made Fiji macros for image analysis.

Martina Schifferer processed and imaged electron microscopy samples.

Georg Kislinger provided technical assistance for processing and imaging of electron microscopy samples.

Kerstin Karg provided technical assistance for processing and imaging of electron microscopy samples.

Agata Rhomberg provided technical assistance with RNA isolation and RT-qPCR analysis.

Christian Klose from Lipotype GmbH analysed the plasma and brain samples for lipidomics.

Dieter Lütjohann analysed the samples for quantification of oxysterols and desmosterols.

Martin Giera analysed the short- and medium-chain fatty acids in the caecum and portal vein blood plasma samples.

Nicolas Page and Doron Merkler analysed the chromatin status of microglia by ATACseq.

Author contributions

Nirmal Kannaiyan and Moritz J. Rossner analysed the transcriptomic profile of microglia by bulk RNAseq and performed the subsequent bioinformatic and statistical analysis.

All other experiments, sample preparations, sample processing, sample analysis, statistical analysis and data visualization were performed by Mar Bosch Queralt.

Yours faithfully,

Mar Bosch Queralt

Prof. Mikael Simons

Date, Place